Fiberwise Hyperbolic Invariant Tori in quasiperiodically forced skew product systems

Jordi-Lluís Figueras Romero

Universitat de Barcelona

Memòria presentada per aspirar al grau de
Doctor en Matemàtiques per la Universitat de Barcelona.

Certifico que aquesta memòria ha estat
realitzada per Jordi-Lluís Figueras Romero
i dirigida per mi.
Barcelona 4 d'Abril de 2011.

Àlex Haro Provinciale

A tots els que m'heu ensenyat
que el treball és el més important.
Tota la resta derivarà d'ell.

Abstract:

In this thesis we study fiberwise hyperbolic invariant tori (FHIT) in quasiperiodic skew product systems. These invariant objects are robust and persists under small perturbations. The thesis can be splitted in two main parts: In the first part it is studied several bifurcations of FHIT in 2D, and 3D, area, and volume, preserving skew products. It is presented old and new breakdown mechanisms, which are compared and contrasted. In the second part it is studied how to perform rigorous numerics to validate the existence of FHIT. We apply these validation techniques in the verge of breakdown of FHIT in several scenarios.

Abstract:

En aquesta tesi s'estudien tors invariants fibrats hiperbòlics (FHIT) en sistemes skew product forçats quasiperiòdicament. Aquests tenen la propietat que són robustos i romanen sota perturbacions petites. La tesi es pot dividir en dues parts: En la primera part s'estudia diferents tipus de bifurcacions en sistemes 2D i 3D. Són presentats vells i nous mecanismes de trencament. Aquests són comparats i contrastats. En la segona part s'estudia com es pot realitzar numèric rigorós per a validar l'existència de FHIT. Aquestes tècniques de validació són aplicades en FHIT prop de trencament en diversos escenaris.

Acknowledgments

First of all, I want to acknowledge my Phd. advisor Àlex Haro for his guideance, his patience, his warm friendship and for encouraging me all the time. I'm extremely proud, and it is an honour, to be his first scientific son.

The whole Group of Dynamical Systems in Barcelona has helped me a lot. I want to mention Carles Simó, who has been always aware of my research and he has always forcing me to go further in my research. I don't know how many cigarretes we have smoked outside the Bunker while discussing mathematics! Angel Jorba has been very kind with me and has helped me a lot, with special emphasis all the fruitful discussions about computer science and its applications in dynamical systems. Alejandra Gonzalez for her support, for her fruitful discussions and for her proofreadings of my papers and this thesis. Joaquim Puig for his judgements and fruitful discussions. Arturo Vieiro and Joan Carles Tatjer for helping me in my lectures in this final stage. Also, to all the research people in the Departament de Matemàtica Aplicada i Anàlisi at Universitat de Barcelona: Ernest Fontich, Gerard Gómez, Jordi Villadelprat, Jaume Timoneda, Pau Rabassa, Bharti Pridhnani, Elona Agora, Ariadna Farrés, Marta Canadell, Jordi Canela, Ruben Berenguel...

On August 2011 I spent three months in the University of Austin, at Texas, under the guideance of Professor Rafael de la Llave. That three months were incredible! I learned, discussed and enjoyed a lot. Thank you very much, Rafa. I met there Hector Lomelí and Maciej Capiński, who shared with me their friendship and mathematical knowledge.

I'm in debt with Marko Lindner, who invited me one week in TU Chemnitz. He shared his knowledge with me and made the stage very fruitful and comfortable.

I would like to thank to Professor Warwick Tucker for his support in this end stage of my Phd.

Finally I would like to thank to all my friends, specially Joan, Lluritu, Martí, Enric, Alga, Monky, Cubi, Tesa... for supporting me, and some of my teachers in high school: Pilar Cerdà, Júlia Ruiz and Toni Riobot. Also, to my families Figueras Romero and Villalonga Pons. We have suffered several hard episodes during these years but we have (almost) recovered from all. All of you have helped me a lot during all these years. Specially, my mother, wherever is, and my father, who sacrificed, at a high cost, all he had for his kids. And Joana, thank you very much for being at my side all the time.

Contents

Introduction

The long term behaviour of a dynamical system is organized by its invariant objects. Hence, it is important to understand which invariant objects persist under perturbations of the system, provide results about their existence, regularity and dependence with respect to parameters, and classify their bifurcations and mechanisms of breakdown. In this thesis, we address these questions for a particular class of dynamical systems and invariant objects. The systems we consider are quasiperiodically forced, that is coupled with an irrational rotation, and the invariant objects are invariant tori carrying such an irrational rotation. These tori are the response to the quasiperiodic forcing and are geometrically described as graphs of the state variables over the coupled angles describing the quasiperiodic motion [Sta97]. It is known that persistence (in open sets of parameters) of invariant manifolds is closely related to the concept of normal hyperbolicity [Fen72, HPS77, Mañ78, Sac65]. Here we consider an analogous concept, tailored for skew products over rotations. Hence, the invariant tori we consider are fiberwise hyperbolic (FHIT). Roughly speaking, a continuous invariant torus (with graph form) is fiberwise hyperbolic if the linearized dynamics on the normal bundle is exponentially dichotomic: the normal bundle splits into stable and unstable bundles on which the dynamics is uniformly contracting and expanding, respectively. Notice that the tangent dynamics is dominated by the normal dynamics, since the former presents zero Lyapunov exponents. This fact implies that fiberwise hyperbolic tori are robust and persist (in open sets of parameters) and are as smooth as the system [HdlL06c]. We observe that KAM techniques lead to results of persistence (in Cantor sets of parameters) of response tori under weaker conditions [BHS96], but often fiberwise hyperbolic tori appear in open gaps of the parameter space [BHJ$^+$03] (see [HdlL07] for numerical explorations of these normal-internal resonances, including the appearance of fiberwise hyperbolic tori whose invariant manifolds have non-orientable invariant manifolds).

In particular, we consider examples in which tori smoothly bifurcate and examples in which tori break non-smoothly. One main goal is to define good observables to study different types of bifurcations. The non-smooth breakdown phenomenon has been extensively studied in the literature in the context of the Strange Non-chaotic Attractors (SNA), since their discovery in [GOPY84] (and even before in [Her83]), in which an attracting smooth torus bifurcates into an attracting object of complicated geometry (not even continuous) but still carrying a non-chaotic (in fact quasiperiodic) dynamics. This extremely interesting behaviour aroused considerable interest in theoretical physics. It was considered as a prelude

of chaotic behaviour, and there was an explosion of numerical and experimental studies reporting of mechanisms of formation of those objects (see [FKP06, PNR01] and references therein). Further theoretical studies rigorously explaining and mathematically proving some of these mechanisms have been considered in the mathematical literature (see e.g. [BO96, Bje09, HP06, Jäg09, Kel96, Sta99, SS00]). In contrast to the attention that attractors have received, there are only a very few numerical studies on the mechanisms of breakdown of saddle-type invariant tori [HdlL06a, HdlL07]. These are cases in which computation of invariant tori and their whiskers (the invariant bundles) is computationally difficult. We also study what happens after the bifurcations, with special emphasis to the nature of the invariant objects that remain after the bifurcations.

We consider also the existence question of FHIT, even in cases in which the systems are very far from the perturbative regime and the tori are about to break. It is presented a new methodology to provide rigorous Computer-Assisted Proofs (CAPs) of the existence and (local) uniqueness of fiberwise hyperbolic invariant tori in quasiperiodically forced systems. A key point of the CAPs is to formulate the invariance of FHIT in functional terms [HdlL06c]. Applications of CAPs in functional analysis to dynamical system problems have a long history that goes back to the proof of the Feigenbaum conjecture in unimodal maps [Lan82, Lan87], the proof of the universality in the period-doubling cascade for area-preserving maps [EKW84], the proof of the existence of the strange attractor in the Lorenz equations [Tuc02], and, more recently, the proof of the existence of critical invariant tori (supporting the renormalization group picture) in Hamiltonian systems [Koc08]. See also the inspiring chapter 7 in [dlL01] and the review [KSW96]. The common denominator in these proofs is to propose a functional equation to be satisfied by the relevant object, to find an approximate solution of it, and to prove the existence of the true solution of the functional equation in a suitable Banach space by checking the bounds provided by a fixed point theorem (usually using a Newton-like method). For the porposes of the validation of FHIT, a natural Banach space for parametrizing tori and considering the invariance equation is the space of continuous periodic functions, endowed with the supremum norm. We note that, since there is a bootstrap in the regularity of fiberwise hyperbolic tori, and since they are in fact as smooth as the system [HdlL06c], we only consider C^0 norms. Let us mention that, in the examples mentioned in this paragraph, the differentials of the corresponding functionals are compact operators, which have a relatively simple spectrum. In contrast, the spectrum of the operators arising in the problems presented here is a set of annuli centered at 0 [Mat68, CL99] (the inner annuli could be a disk if the dynamical system is non-reversible). Hence, checking the applicability of Newton's method is equivalent to checking that 1 is not in the spectrum, and this is just rephrasing the condition of fiberwise hyperbolicity.

Summarizing, this thesis has two main goals: to study the possible breakdown routes of FHIT, and to give rigorous tools to perform computer-assisted proofs in order to prove the existence of these objects.

The thesis has been organized in several chapters.

1.- Theoretical framework of FHIT.
The theoretical framework of FHIT in skew product systems over irrational rigid rotations is described. These are nonlinear maps of the form

$$\begin{array}{rccc}(F,\omega)\colon & \mathbb{R}^n\times\mathbb{T} & \longrightarrow & \mathbb{R}^n\times\mathbb{T}\\ & (z,\theta) & \longrightarrow & (F(z,\theta),\theta+\omega)\end{array}$$

where ω is an irrational number. An invariant torus is the graph of a (continuous) map $K\colon\mathbb{T}\longrightarrow\mathbb{R}^n$ that satisfies the invariance equation

$$F(K(\theta),\theta)=K(\theta+\omega).$$

We say that an invariant torus is a Fiberwise Hyperbolic Invariant Torus (FHIT) if the infinitesimal normal dynamics around it is uniformly hyperbolic. That is, its associated linear cocycle

$$\begin{array}{rccc}(D_zF,\omega)\colon & \mathbb{R}^n\times\mathbb{T} & \longrightarrow & \mathbb{R}^n\times\mathbb{T}\\ & (v,\theta) & \longrightarrow & (D_zF(K(\theta),\theta)v,\theta+\omega)\end{array}$$

leaves invariant a Whitney sum of fiber bundles $E^u\oplus E^s$ such that their dynamics are exponentially expanding in E^u (unstable bundle), and exponentially contracting in E^s (stable bundle), respectively.

We briefly describe the dynamical properties of linear cocycles. This description helps us to understand the dynamics around an invariant torus, which is important in order to give a classification of the possible breakdowns and also for the design of the computer-aided proofs.

We also explore the relations between the dynamical properties of the FHIT with the functional properties of these objects, and study the important ideas around the spectral properties of FHIT, such as the Mather spectrum. This functional setting helps us to state the robustness of these objects.

Finally, we introduce the concept of discrete Schrödinger operartor. This will appear several times during the thesis binded with the gradient flow of some nonlinear functionals. These gradient flows will be a key point in order to understand and classify the possible routes to breakdown of invariant tori in area preserving skew product systems.

2.- Breakdown routes of FHIT in area preserving skew products.
In this chapter we describe, explore and compare several mechanisms of breakdown of invariant tori in area preserving skew products. This exploration has been done by approximating the (quasiperiodic) invariant tori by periodic orbits: we replace the irrational rotation of the skew product system by a rational partial convergent, so an invariant torus is approximated by periodic orbits. For each breakdown scenario introduced here, we perform this computation for a wide range of partial convergents, trying to capture the imporant observables, such as the maximal Lyapunov exponent, minimum distance between their invariant bundles, etc. The mechanisms described are the smooth bifurcation, the non-smooth breakdown and the

folding breakdown. The first one is completely understood (using normal form techniques), see [BHS96],[HdlL07]; and the second one is recent, first discovered in [HdlL07]. To the best of our knowledge the third one is new.

The smooth bifurcation, or saddle to elliptic bifurcation, is the transition of a FHIT torus to an elliptic torus with higher dimensional invariant tori. Both Lyapunov exponent and minimum distance between invariant bundles go to zero as the bifurcation occurs. This bifurcation is well understood using KAM techniques, see [BHS96].

The non-smooth breakdown satisfies that, while the minimum distance between the invariant bundles goes to zero as it approaches the breakdown, the Lyapunov exponent and the maximal distance between the invariant bundles remain positive, which is apparently counter-intuitive. Also, the maximum slope of the torus remains bounded at the breadown. We detect that, after the breakdown, an invariant object persists, which is no longer a continuous invariant torus.

The folding breakdown shares some similarities with the non-smooth breakdown: the minimum distance between the invariant bundles goes to zero as it approaches the breakdown, while the Lyapunov exponent and the maximal distance between the invariant bundles remain positive. But, while the invariant torus approaches the breakdown, its slope gets bigger: at the breakdown the slope is "*infinity*". After the breakdown it is observed that, for every computed partial convergent, the periodic orbit does not describe a graph of a continuous map, but they still form part of an invariant curve. These curves are folded with respect to the torus variables. If we replace one partial convergent by another, we observe that the folded curves differ only on the number of folding points, and it is observed that it remains almost the same object. After a massive exploration of these folded curves, we conjecture that they approximate an invariant object for the quasiperiodic rotation. We emphasize that this object cannot be a measurable curve, and it retains hyperbolicity properties.

3.- Fractalization route of FHIT in volume preserving skew products.
In this chapter we present the fractalization route of FHIT in volume preserving skew products. This mechanism, in which a torus is gradually destroyed without the collision with a nearby object, had been observed in dissipative systems [Kan84, HdlL06a, JT08] in the context of the existence of SNA. We have unified this mechanism, both in the dissipative and conservative case: the fractalization route can be explained in terms of the Mather spectrum associated to the invariant curves.

The fractalization route described in this chapter is presented with a numerical example in a 3D skew product system. The computation of the invariant curves is done using the same techniques as in the 2D case: the approximation of the invariant curves by periodic orbits. In this example we explore the observables associated to the invariant curve such as the Lyapunov exponents and the distance between the unstable and the stable bundles. We want to point out that the numerical computation of the fractalization route presented in this thesis is quite challenging compared with the computations in the dissipative case, since the curves are not attractors but of saddle-type.

5.- Computer validations of FHIT.
In this chapter we present a methodology to perform computer-assisted proofs of FHIT using the functional settting of the invariance of a FHIT.

Our methodology represents a step forward from the results and numerical algorithms and experiments exposed in [HdlL06b, HdlL06c, HdlL07]. Hence, the invariance of a torus leads to a functional equation that fits in the framework of Newton-Kantorovich theorem [HdlL06b]. Therefore, starting with an approximate solution of the invariance equation, one can use rigorous interval arithmetics [Moo79, KM84] to verify the hypothesis of the constructive existence theorem, which consists in checking several a-posteriori bounds. The verification of such bounds leads to the proof of the existence (and local uniqueness) of a true solution of the invariance equation, and hence of the true invariant torus. Note that in these proofs the way in which approximate solutions are produced is not important.

For the examples of this thesis, we have used paper and pen, Fourier methods [HdlL07], or rational approximation of frequencies (computing periodic orbits of approximate periodically-forced systems) to obtain these approximate solutions. These numerical methods are tailored for the specific class of invariant tori considered here. See e.g. [BHV07, BOV97] for general numerical methods to compute normally hyperbolic invariant manifolds. Having accurate and efficient numerical methods is essential for producing approximations that verifies the validation test, and more important in cases in which the tori are on the verge of breakdown. An alternative topological method for validating the existence of invariant sets of normally hyperbolic type has been considered in [Cap09], which is based on the method of covering relations [ZG04]. These methods work for more general dynamical systems but cannot be used to prove (local) uniqueness of the invariant sets.

We apply the computer-assisted techniques in three challenging scenarios: the Harper map, the Heagy-Hammel route in the quasiperiodically forced logistic map, and in some examples presented in the chapter of the breakdown of invariant curves in area preserving skew products.

6.- Numerical tools.
In this chapter we briefly describe the most relevant numerical tools used throughout the thesis, such as the computation of the invariant tori using the periodic orbits technique, the computation of the invariant bundles associated to an invariant torus, and some aspects of the computations used in the computer-assisted proofs.

The thesis finishes with an appendix and a list of open questions. In the appendix we give some examples of 3D linear cocycles with Mather spectrum a fulfilled annulus but with no continuous invariant bundles. We included this here in order to give an example of the relation between the Mather spectrum of a cocycle with its invariant bundles. Finally, we present a list of open questions that we have asked throughtout the thesis, as possible future lines of research.

Chapter 1

Theoretical framework

In this chapter we introduce the theoretical framework of this thesis. This exposition is taylored for the needs of the thesis, although most of the results can be generalized, for example to Normally Hyperbolic Invariant Manifolds.

1.1 Fiberwise Hyperbolic Invariant Tori in skew products

A *skew product* over a rotation is a bundle map

$$\begin{array}{rccc} (F,\omega): & \mathbb{R}^n \times \mathbb{T} & \longrightarrow & \mathbb{R}^n \times \mathbb{T} \\ & (z,\theta) & \longrightarrow & (F(z,\theta), \theta+\omega) \end{array} , \tag{1.1}$$

where $\mathbb{T} := \mathbb{R}/\mathbb{Z}$, $\omega \in \mathbb{R}$ and $F\colon \mathbb{R}^n \times \mathbb{T} \to \mathbb{R}^n$ is continuous, $\mathcal{C}^1$ with respect z. $\mathbb{R}^n$ is called the fiber space and $\mathbb{T}$ the base space of the skew product.

Remark 1.1.1. In most of the examples worked throughout the thesis the skew products are analytic in both z and θ.

Remark 1.1.2. Most of what follows works also for other base manifolds and base dynamics. In particular for $\mathbb{T}^d$ and $\omega \in \mathbb{R}^d$.

Remark 1.1.3. If $\omega = \frac{p}{q} \in \mathbb{Q}$, every fiber is q periodic, and we can think of (F,ω) as a θ parametric family of maps in $(\mathbb{R}^n)^q$. This point of view will be useful in numerical computations.

Remark 1.1.4. If $\omega \in \mathbb{R} - \mathbb{Q}$, we say that the skew product is quasiperiodic.

The graph of a measurable section $K\colon \mathbb{T} \to \mathbb{R}^n$ of the bundle $\mathbb{R}^n \times \mathbb{T}$, $\mathcal{K} = \{(K(\theta),\theta) \,|\, \theta \in \mathbb{T}\}$, is a torus. We often abuse notation and refer to K as a torus, rather than a section or the parametrization of the torus $\mathcal{K}$. If the section K satisfies the functional equation

$$F(K(\theta),\theta) - K(\theta+\omega) = 0 \ , \tag{1.2}$$

then the torus $\mathcal{K}$ is invariant under (F,ω) and its inner dynamics is the rigid rotation ω.

Remark 1.1.5. When ω is irrational, the condition of a measurable invariant torus to be a graph is not restrictive. Its proof, see [HdlL06c], goes as follows: Let $\hat{K}$ be a map of $\mathbb{T}$ in $\mathbb{R}^n \times \mathbb{T}$, $\hat{K}(\phi) = \left(\hat{K}_z(\phi), \hat{K}_\theta(\phi)\right)$, that is invariant under the skew product (1.1). Then it is satisfied that

$$\begin{aligned} F(\hat{K}_z(\phi), \hat{K}_\theta(\phi)) &= \hat{K}_z(\phi+\omega) && (1.3)\\ \hat{K}_\theta(\phi) + \omega &= \hat{K}_\theta(\phi+\omega). && (1.4) \end{aligned}$$

Since ω is irrational (hence ergodic), the only measurable solutions of equation (1.4) are $\hat{K}_\theta(\phi) = \phi + a$, with $a \in \mathbb{R}$.

Remark 1.1.6. For the periodic case it can happen that an invariant torus is not a graph. This will be a key remark when dealing with the breakdown phenomena in chapter §2.

The invariance equation (1.2) can be rewritten in functional terms. Let $\mathcal{T}\colon \mathcal{C}^0(\mathbb{T}, \mathbb{R}^n) \to \mathcal{C}^0(\mathbb{T}, \mathbb{R}^n)$ be the operator defined as

$$\mathcal{T}(K)(\theta) = F(K(\theta-\omega), \theta-\omega) - K(\theta)\ . \tag{1.5}$$

K is an invariant torus for (F, ω) if and only if

$$\mathcal{T}(K)(\theta) = 0. \tag{1.6}$$

The operator (1.6) is differentiable, see [dlLO99], with Frechet derivative the (bounded) linear operator $\mathrm{D}\mathcal{T}(K) : \mathcal{C}^0(\mathbb{T}, \mathbb{R}^n) \longrightarrow \mathcal{C}^0(\mathbb{T}, \mathbb{R}^n)$ defined as

$$\mathrm{D}\mathcal{T}(K)\Delta(\theta) = \mathrm{D}_z F(K(\theta-\omega), \theta-\omega)\Delta(\theta-\omega) - \Delta(\theta)\ . \tag{1.7}$$

The nature of the solutions of (1.6), and of the linear operator $\mathrm{D}\mathcal{T}(K)$, is strongly related to the dynamical properties of the linearized dynamics around K. This is given by the vector bundle map

$$\begin{array}{rccc} (M,\omega): & \mathbb{R}^n \times \mathbb{T} & \longrightarrow & \mathbb{R}^n \times \mathbb{T} \\ & (v, \theta) & \longrightarrow & (M(\theta)v, \theta+\omega) \end{array}\ , \tag{1.8}$$

where $M\colon \mathbb{T} \to L(\mathbb{R}^n)$ is the *transfer matrix* $M(\theta) = \mathrm{D}_z F(K(\theta), \theta)$.

Define the *transfer operator* $\mathcal{M}$ associated to the vector bundle map (1.8) as the bounded linear operator $\mathcal{M} : \mathcal{C}^0(\mathbb{T}; \mathbb{R}^n) \to \mathcal{C}^0(\mathbb{T}; \mathbb{R}^n)$,

$$\mathcal{M}(\Delta)(\theta) = M(\theta-\omega)\Delta(\theta-\omega). \tag{1.9}$$

The relation between the dynamical properties of the linear cocycle (M, ω) and the spectral properties of its associated transfer operator $\mathcal{M}$ has been intensively studied in the literature, see e.g. [Mat68, SS74, HPS77, Mañ78, LS90, dlL93, CL99]. A key result is the following.

Theorem 1.1.7. *Let $(M, \omega) : \mathbb{R}^n \times \mathbb{T} \to \mathbb{R}^n \times \mathbb{T}$ be a linear skew product, and $\mathcal{M} : \mathcal{C}^0(\mathbb{T}; \mathbb{R}^n) \to \mathcal{C}^0(\mathbb{T}; \mathbb{R}^n)$ its associated transfer operator. The following two properties are equivalent:*

(a) *$\mathcal{M}$ is a hyperbolic operator, that is, its spectrum has empty intersection with the unit circle of the complex plane;*

(b) *(M,ω) is uniformly hyperbolic, that is, there exists a continuous decomposition of the vector bundle $\mathbb{R}^n \times \mathbb{T}$ in a Whitney sum $E^s \oplus E^u$ of two invariant bundles E^s and E^u, such that M restricted to E^u is invertible, and there exists constants $C > 0$ and $0 < \lambda < 1$ such that*

- *If $(v,\theta) \in E^s$ then $|M(\theta + (l-1)\omega) \cdots M(\theta)v| \leq C\lambda^l |v|$ for all $l \geq 0$;*
- *If $(v,\theta) \in E^u$ then $|M(\theta + l\omega)^{-1} \cdots M(\theta - \omega)^{-1}v| \leq C\lambda^{-l}|v|$ for all $l \leq 0$.*

We emphasize that, since $\mathrm{D}\mathcal{T}(K) = \mathcal{M} - \mathcal{I}$, the hyperbolicity property of the transfer operator $\mathcal{M}$ implies the invertibility of $\mathrm{D}\mathcal{T}(K)$ and hence, the applicability of the Implicit Function Theorem. Invariant tori satisfying these hyperbolicity properties are the main object of this thesis.

Definition 1.1.8. A *Fiberwise Hyperbolic Invariant Torus* (*FHIT* for short) of the system (1.1) is an invariant torus $K : \mathbb{T} \to \mathbb{R}^n$ that satisfies (1.2) and such that its corresponding transfer operator $\mathcal{M}$ is hyperbolic.

The invariant bundles E^s and E^u of the associated linear skew product (M,ω), see theorem 1.1.7, are called the stable and the unstable bundles, respectively. If E^u is the zero bundle, i.e. the spectrum of $\mathcal{M}$ is inside the unit circle, then we say that the torus K is a uniform (or hyperbolic) attractor. If E^s is the zero bundle, i.e. the spectrum of $\mathcal{M}$ is outside the unit circle, then the torus K is a uniform (or hyperbolic) repellor. Otherwise we say that the torus K is a saddle.

Remark 1.1.9. A consequence of the Implicit Function Theorem is that FHIT are robust with respect to perturbations of F. Perturbations of the dynamics of $\mathbb{T}$ are more delicate, more differentiability of the skew product is needed, see [HPS77].

About the regularity of FHIT, there is the following result [HdlL06c].

Theorem 1.1.10. *Given a $\mathcal{C}^r$ $r \geq 1$, in the z coordinate, skew product (F,ω), then all its FHIT are $\mathcal{C}^r$. Also, if (F,ω) is analytic, then the FHIT are analytic.*

1.2 Dynamics of linear cocycles

Because theorem 1.1.7, the study of the linear part of an invariant torus (1.8) gives information of the linear stability of the nearby orbits. With this purpose, throughout this section it is presented the dynamics of these particular skew products.

Notation 1.2.1. The linear skew product (1.8) will be called *linear cocycle*.

We define $M(\theta, k)$ by

$$\begin{cases} M(\theta+(k-1)\omega)\cdots M(\theta) & \text{if } k>0 \\ Id & \text{if } k=0 \\ M(\theta+k\omega)^{-1}\cdots M(\theta-\omega)^{-1} & \text{if } k<0 \end{cases}.$$

For $k<0$ we suppose that the matrices $M(\theta+j\omega)$, $j=-1,\ldots,k$, are all invertible.

The dynamics of (1.8) depends strongly on the invertibility of the tranfer matrix $M(\theta)$. Noninvertibility implies that the dynamics degenerates: there is no homeomorphism over the vector bundle $\mathbb{R}^n\times\mathbb{T}$, hence the dynamics collapses in a smaller vector bundle E' with fiber space of dimension n', $n'<n$. Also, due to the linear nature of a cocycle, the zero section $(0,\theta)$ is invariant under it and, if it is understood the dynamics of a point (v,θ), then it is understood the dynamics of its linear span $(\lambda v,\theta)$, $\lambda\neq 0$. This means that, if one casts aside the study of the rate of growth of the magnitude of the iterations of the vector v and only concerns on the study of the geometry of the invariant sets, one can study the *projective cocycle*

$$\begin{array}{rccc} \mathbb{P}(M,\omega)\colon & \mathbb{S}^{n-1}\times\mathbb{T} & \longrightarrow & \mathbb{S}^{n-1}\times\mathbb{T} \\ & (v,\theta) & \longrightarrow & \left(\dfrac{M(\theta)v}{||M(\theta)v||},\theta+\omega\right) \end{array}, \tag{1.10}$$

where $\mathbb{S}^{n-1}$ is the $n-1$ dimensional sphere.

Remark 1.2.2. Rigorously speaking, the term projective cocycle refers when the bundle space is $\mathbb{P}^{n-1}\times\mathbb{T}$, where $\mathbb{P}^{n-1}$ is the $n-1$ projective space, instead of $\mathbb{S}^{n-1}\times\mathbb{T}$, but the later is a 2-1 cover of the first one.

Remark 1.2.3. Considering the map (1.10) is helpful when one wants to give visual representations of the invariant subbundles of a given cocycle.

The Lyapunov exponents measure the average growth of the orbits. Their definition is:

Definition 1.2.4. Given $(v,\theta)\in\mathbb{R}^n\times\mathbb{T}$, its *forward Lyapunov exponent* is

$$\lambda^+(v,\theta)=\limsup_{k\to+\infty}\frac{1}{k}\log||M(\theta,k)v||, \tag{1.11}$$

and, if $M(\theta)$ is invertible, its *backward Lyapunov exponent* is

$$\lambda^-(v,\theta)=\limsup_{k\to-\infty}\frac{1}{|k|}\log||M(\theta,k)v||. \tag{1.12}$$

Remark 1.2.5. It is possible to give bounds of the forward and backward Lyapunov exponents. Let

$$\begin{aligned} L&=\max_{\theta\in\mathbb{T}}||M(\theta)|| \\ S&=\max_{\theta\in\mathbb{T}}\left|\left|M(\theta)^{-1}\right|\right| \end{aligned}.$$

Then, $\lambda^+(v,\theta)\leq L$ and $\lambda^-(v,\theta)\geq S^{-1}$.

An important result that summarizes both the average growth and the directions of a general point (v, θ) under the action of a cocycle is Oseledet's theorem, see e.g [Arn98].

Theorem 1.2.6. *Let (M, ω) be a linear cocycle on $\mathbb{R}^n \times \mathbb{T}$. There exists a full-measure set R in $\mathbb{T}$, invariant under the rotation $\theta \to \theta + \omega$, such that, for every (v, θ), with $\theta \in R$:*

1. *The sup limits in the definitions* (1.11), (1.12) *are in fact limits.*
2. *For fixed $\theta \in R$ and every v, the values attained by the limits $\lambda^+(v, \theta)$ and $\lambda^-(v, \theta)$ is a finite set $\{\lambda_1(\theta) > \cdots \lambda_k(\theta)\}$, with $k = k(\theta) \leq n$.*
3. *There is a measurable invariant splitting of $\mathbb{R}^n = \oplus_{1 \leq i \leq k} E^i_\theta$ such that for every non-zero v,*
   - *$\lambda^+(v, \theta) \leq \lambda_j(\theta)$ iff $v \in \oplus_{j \leq i \leq k} E^i_\theta$.*
   - *$\lambda^-(v, \theta) \geq \lambda_j(\theta)$ iff $v \in \oplus_{1 \leq i \leq j} E^i_\theta$.*
4. *The linear maps $\left(M(j, \theta)^T M(j, \theta)\right)^{\frac{1}{2j}}$ converge as $j \to +\infty$ to a linear map whose eigenvalues are $e^{\lambda_1(\theta)} > \cdots > e^{\lambda_k(\theta)}$. If we denote by $\hat{E}^i_\theta$ their respective eigenspaces, then for each $i = 1, \cdots, k$, it is satisfied that*

$$\hat{E}^i_\theta \oplus \cdots \oplus \hat{E}^k_\theta = E^i_\theta \oplus \cdots \oplus E^k_\theta.$$

Oseledet's theorem states, in a measure theoretical sense, the hyperbolicity conditions in theorem 1.1.7 but, in the study of FHIT, it is required a continuous version of the Oseledet's theorem: the vector bundle $\mathbb{R}^n \times \mathbb{T}$ decomposes in a continuous, not only measurable, Whitney sum $E^u \oplus E^s$.

Remark 1.2.7. Even in the case that there exists the continuous Whitney sum of invariant subbundles, each of these can have a filtration of subbundles E^i, as the ones stated in Oseledet's theorem, such that they are only measurable.

An important corollary of Oseledet's theorem is the (almost) independence of the Lyapunov exponents with respect θ:

Corollary 1.2.8. *In the quasiperiodic case, for almost every $v \in \mathbb{R}^n$ and $\theta \in \mathbb{T}$, the limits*

$$\lim_{k \to +\infty} \frac{1}{k} \log ||M(\theta, k)v||$$

and

$$\lim_{k \to -\infty} \frac{1}{|k|} \log ||M(\theta, k)v||$$

exist and are equal to λ_+, λ_-. They are called the maximal *(resp.* minimal*) Lyapunov exponents.*

Another important notion is the linear conjugacy between cocycles.

Definition 1.2.9. Two cocycles (M, ω) and (N, ω) are linear conjugated if there exists a matrix-valued map $P\colon \mathbb{R}/(2\mathbb{Z}) \longrightarrow GL(n, \mathbb{R})$ such that it is satisfied the cohomology equation

$$M(\theta)P(\theta) = P(\theta + \omega)N(\theta) \tag{1.13}$$

for all $\theta \in \mathbb{T}$.

Remark 1.2.10. The linear conjugacy P is defined as a matrix-valued map on $\mathbb{R}/(2\mathbb{Z})$, and not in $\mathbb{T}$, in order to conjugate non-orientable invariant subbundles.

With the linear conjugacy, it can be introduced the concept of *reducibility*.

Definition 1.2.11. A linear cocycle (M, ω) is *reducible* if it is conjugated to a linear cocycle (Λ, ω) with constant transfer matrix Λ. E is a *reducible subbundle* of (M, ω) if it is invariant and $(M_{|E}, \omega)$ is reducible. In addition, if $(M_{|E}, \omega)$ is reducible to a diagonal matrix, the elements of the diagonal are called the *Lyapunov multipliers* of the invariant subbundle E.

Remark 1.2.12. When a cocycle is reducible, its dynamics are very simple. It is the dynamics of a linear map.

Remark 1.2.13. It can be proved that the absolute value of a Lyapunov multiplier is equal to the exponential of a Lyapunov exponent.

1.2.1 One dimensional cocycles

The dynamics of 1D cocycles are well understood. In this case, their transfer matrix are scalar-valued maps $M(\theta)$. Due to this particular form, the computation of the maximal (and unique) Lyapunov exponent is easy: using the Birkhoff Ergodic Theorem the Lyapunov exponent is equal to

$$\int_{\mathbb{T}} \log |M(\theta)| d\theta.$$

The study of the dynamics is splitted in two cases, when M vanishes at some point θ_0 or when it never vanishes. If it vanishes at some point θ_0, then the cocycle is not invertible everywhere. If it never vanishes, then the cocycle is invertible everywhere and its inverse is well-defined. Also, for the invertible case there is a classical result, see for example [Pui04b], that says that, under a diophantine hypothesis on ω, 1D cocycles are reducible. We present here a proof because we will use it in numerical computations.

Proposition 1.2.14. *Let $(M, \omega)\colon \mathbb{R}\times\mathbb{T} \longrightarrow \mathbb{R}\times\mathbb{T}$ be an analytic 1D cocycle, with invertible transfer matrix M and with ω diophantine, that is, there exist $\tau > 2$ and $C > 0$ such that, for every $k \in \mathbb{Z} - \{0\}$,*

$$\left|e^{2\pi i k\omega} - 1\right| > \frac{C}{|k|^\tau}. \tag{1.14}$$

Then it is reducible, that is, there exist a constant $\bar{M} \neq 0$ *and an analytic map* $P\colon \mathbb{T} \longrightarrow \mathbb{R}$, $P(\theta) \neq 0$ *for all* θ*, such that it is satisfied*

$$M(\theta)P(\theta) = P(\theta+\omega)\bar{M}.$$

Proof. Without loss of generality, we suppose that the transfer matrix $M\colon \mathbb{T} \longrightarrow \mathbb{R}$ is always positive. We want to find a positive analytic map $P\colon \mathbb{T} \longrightarrow \mathbb{R}$ and a positive constant $\bar{M}$ such that they satisfy

$$M(\theta)P(\theta) = P(\theta+\omega)\bar{M}. \tag{1.15}$$

Taking logarithms in the scalar equation (1.15) we obtain the functional equation

$$p(\theta+\omega) - p(\theta) = m(\theta) - \bar{m}, \tag{1.16}$$

where $p(\theta) = \log P(\theta)$, $m(\theta) = \log M(\theta)$ and $\bar{m} = \log \bar{M}$.

Let $p(\theta) = \sum_{k\in\mathbb{Z}} p_k e^{2\pi i k\theta}$ and $m(\theta) = \sum_{k\in\mathbb{Z}} m_k e^{2\pi i k\theta}$. Equation (1.16) says that the Fourier coefficients of both both $p(\theta)$, the unknown, and $m(\theta)$ must satisfy

$$p_k = \frac{m_k}{e^{2\pi i k\omega} - 1}.$$

Using the diophantine condition (1.14) we obtain that the modulus of the Fourier coefficients p_k are bounded above by

$$\frac{|m_k||k|^\tau}{C},$$

which implies that p_k are the coefficients of an analytic function.

To finish, $P(\theta) = e^{p(\theta)}$ is the desired analytic function. □

1.2.2 Two dimensional cocycles

In the recent years there has been many advances to understand the dynamical properties of 2D cocycles, see e.g. [HP06, AK06, AB07, BF06].

We discuss here cocycles with constant determinant 1. In this case, the maximal, λ_+, and minimal, λ_-, Lyapunov exponents satisfy $\lambda_+ = -\lambda_-$. In this case it is costumary to speak of the Lyapunov exponent, which refers to the maximal one. One way to classify these cocycles is with respect the value of their Lyapunov exponent:

- Positive Lyapunov exponent: Oseledet's theorem 1.2.6 asserts that there exists an invariant measurable Whitney sum of 1D bundles $E^u \oplus E^s$, with corresponding Lyapunov exponent λ_+, λ_-. If this Whitney sum is continuous, the cocycle is called *uniformly hyperbolic*, otherwise *non-uniformly hyperbolic*. In the uniform case (and ω diophantine) we have that the cocycle is reducible to a diagonal matrix, see proposition 1.2.14. In the non-uniform case, the dynamics of it is very complicated, with the apperance of Strange-Nonchaotic Attractors in the corresponding projective cocycle (1.10), see e.g. [Her83, HP06].

- Zero Lyapunov exponent: The dynamics of the cocycle are not exponential contracting nor expanding and, due to the Oseledet's theorem 1.2.6, we have that it is possible that there does not exist any (non-trivial) invariant measurable subbundle.

  Special cases of these cocycles are the parabolic case, with transfer matrix

  $$\begin{pmatrix} 1 & a(\theta) \\ 0 & 1 \end{pmatrix},$$

  and the elliptic case, with transfer matrix

  $$\begin{pmatrix} \cos(2\pi\theta) & -\sin(2\pi\theta) \\ \sin(2\pi\theta) & \cos(2\pi\theta) \end{pmatrix}.$$

We proceed now to study the homotopic invariants of 2D cocycles.

Definition 1.2.15. Let (M, ω) be a 2D cocycle with a continuous 1D invariant bundle, parameterized by $v\colon \mathbb{R}/(2\mathbb{T}) \longrightarrow \mathbb{R}^2$, $v(0) = v(2)$, and let $e_m\colon \mathbb{R}/(2\mathbb{T}) \longrightarrow \mathbb{R}^2$, $e_m(\theta) := (\cos(\pi m\theta), \sin(\pi m\theta))$. The *index* of the invariant bundle v is the half integer $\frac{m}{2}$ such that e_m and v are homotopically equivalent.

If a cocycle (M, ω) is homotopic to the identity, that is, there exists a continuous map $\gamma\colon [0,1] \longrightarrow \mathcal{C}^0(\mathbb{T}, SL(2,\mathbb{R}))$, such that $\gamma(0) = M$ and $\gamma(1) = Id$, then, considering the projective cocycle (1.10), we can construct its *lift* as a continuous map $f\colon \mathbb{R}\times\mathbb{T} \longrightarrow \mathbb{R}\times\mathbb{T}$. Then, with the help of this lift we can define the *fibered rotation number* associated to it, see [JM82, Her83, JS06, BJ09].

Definition 1.2.16. Consider a 2D cocycle (M, ω) homotopic to the identity with lift $f\colon \mathbb{R}\times\mathbb{T} \longrightarrow \mathbb{R}\times\mathbb{T}$. Then, its *fibered rotation number* is defined as the limit

$$\rho(M, \omega) = \lim_{k\to\infty} \frac{f^k(x,\theta)}{k}, \tag{1.17}$$

where $f^k(x,\theta) = f^{k-1}(f(x,\theta), \theta+\omega)$, $k > 0$ and $f^1(x,\theta) = f(x,\theta)$.

Some remarkable properties of the fibered rotation number are:

- The limit (1.17) is independent of the initial point (x,θ) and it is well-defined modulus 1.
- The fibered rotation number is a continuous function in both M and ω.
- If the cocycle (M,ω) has a continuous invariant bundle, then its fibered rotation number satisfies that

  $$\rho(M,\omega) = \frac{m\cdot\omega}{2},$$

  where m is the index of the invariant bundle.

  Figure 1.1 shows two invariant bundles with different index.

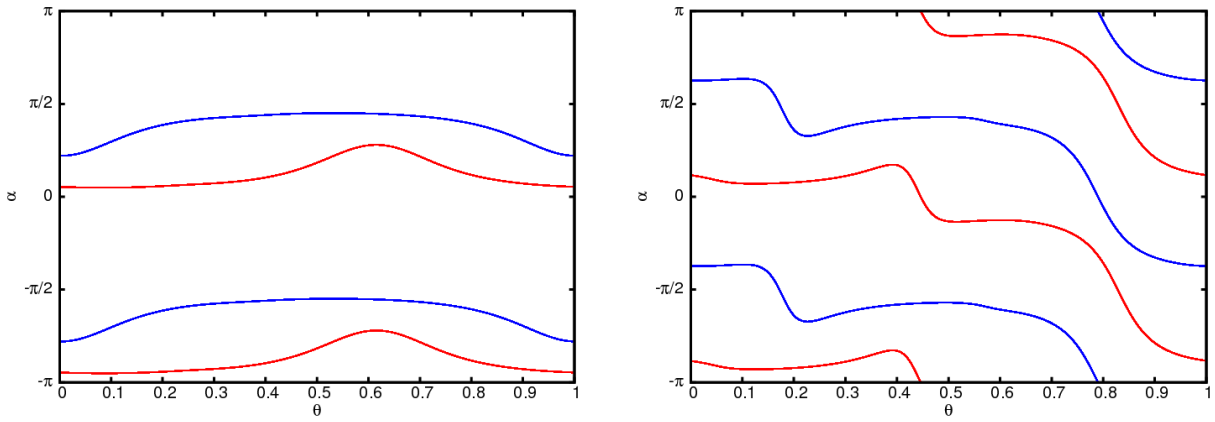

(a) Index = 0. (b) Index = −1/2.

Figure 1.1: The unstable (red) and stable (blue) bundles of two 1D invariant bundles of two cocycles with different index. Note that in the left figure the bundles are orientable, while in the right one they are non-orientable.

1.2.3 Higher dimensional cocycles

As we saw in the previous subsections, a key point to understand how the dynamics of a cocycle is organized is to know the number, dimensions and homotopy of the invariant subbundles. As the dimension of the vector bundle $\mathbb{R}^n$ increases, the possible combinations that arise increase and it is more difficult to give a full description of the classification.

An important tool for higher dimensional cocycles is the *index* of a 1D invariant bundle: the space of homotopical equivalent 1D bundles is $\mathbb{Z}/2$. This can be seen as follows: If one parameterize a 1D bundle as a map

$$v\colon \mathbb{T} \longrightarrow \mathbb{S}^{n-1}, \tag{1.18}$$

$n > 2$, then one has that, if we think that the torus $\mathbb{T}$ is the closed interval $[0, 1]$ with its endpoints identified, v is a continuous map with the possible exception of a discontinuity at 0. At 0 one has two possibilities: $v(0) = -v(1)$ or $v(0) = v(1)$. If we restrict to the case of $v(0) = v(1)$, the other one can be studied performing a 2-1 cover of the subbundle at $\mathbb{T}$. We have that the classification up to homotopy of invariant subbundles is equivalent to study continuous maps of the form (1.18), this is just the study of the fundamental group of the $n-1$ spheres, which is trivial. The $\mathbb{Z}/2$ term comes from the distiction between continuous parameterizations or antipodal parameterizations at 0.

Another tool for studying a n dimensional cocycle (M, ω) is its *adjoint cocycle*: this cocycle has as 1D invariant bundles the $(n-1)$ dimensional invariant bundles of the original cocycle. Its transfer matrix is $M(\theta)^{adj}$.

1.3 Spectral theory of transfer operator over rotations

In this section we describe in more detail the spectral properties of the transfer operator associated to a linear cocycle [Mat68, CL99]. Most of this theory is covered in [HdlL05]. Since we present properties of spectral theory of linear bounded operators, a good reference to keep in mind is [Kat95].

As we saw in section 1.1, a characterization of an invariant torus of a skew product to be FHIT is that its transfer operator $\mathcal{M}$, defined as a bounded operator acting on the Banach space $\mathcal{C}^0(\mathbb{T}, \mathbb{C}^n)$, has not the unit circle in the spectrum.

One important property of transfer operators is to understand their continuity property with respect perturbations in both the matrix-valued map M and the rotation vector ω. We assert that it is continuous with respect perturbations of the matrix-valued map M but not continuous on the rotation vector ω, see [HdlL05].

Notation 1.3.1. The spectrum of a transfer operator will be called M spectrum, in honor to the paper [Mat68].

The M spectrum, depending on the nature of rotation ω, the spectrum has a lot of central symmetries.

Theorem 1.3.2. *Let $\mathcal{M}$ be a transfer operator. Then,*

- *If ω is irrational, then its spectrum is rotational invariant, that is, if λ is in the spectrum and $\alpha \in \mathbb{R}$, then $e^{i\alpha}\lambda$ is in the spectrum.*
- *If ω is rational, $\omega = \frac{p}{q}$, and λ is in the spectrum, then $e^{2\pi i k\cdot\omega}\lambda$ is in the spectrum for all $k \in \mathbb{Z}$.*

Theorem 1.3.2 says that the spectrum of the transfer operator is formed by an union of annuli centered at 0. If the transfer matrix $M(\theta)$ is not invertible for some θ, then one of the annuli is a full disk containing 0.

Notation 1.3.3. We will denote by $\mathcal{A}_{\lambda,\mu}$ the annulus centered at 0 with inner radius λ and outer radius μ, that is,

$$\mathcal{A}_{\lambda,\mu} = \{z \in \mathbb{C} | \lambda \leq |z| \leq \mu\}.$$

Another interesing property of the spectrum of a transfer operator is that the whole spectrum is Weyl spectrum, that is, if λ is in the spectrum, then there exists a sequence of continuous sections v_k, with $||v_k|| = 1$ such that

$$\lim_{k\to\infty} ||\mathcal{M}_\omega v_k - \lambda v_k|| = 1.$$

With the annuli characterization of theorem 1.3.2 we can state the following theorem, which asserts $\mathcal{C}^r$ regularity to invariant bundles.

Theorem 1.3.4. *Let $\mathcal{M}$ be a transfer operator, with $\mathcal{C}^r$ transfer matrix, $r \geq 0$, and let λ, μ be real numbers. Assume that the spectrum does not intersect the annulus $\mathcal{A}_{\lambda,\mu}$.*

Then, $\mathbb{R}^n \times \mathbb{T}$ splits in a $\mathcal{C}^r$ Whitney sum $E^{<\lambda} \oplus E^{>\mu}$ that satisfies

- *If $(v,\theta) \in E^{<\lambda}$ then $|M(\theta+(l-1)\omega)\cdots M(\theta)v| \leq C\lambda^l|v|$ for all $l \geq 0$;*
- *If $(v,\theta) \in E^{>\mu}$ then $|M(\theta+l\omega)^{-1}\cdots M(\theta-\omega)^{-1}v| \leq C\mu^{-l}|v|$ for all $l \leq 0$,*

for a given $C > 0$.

A consequence of theorem 1.3.4 is that the stable and unstable bundles of a FHIT are as smooth as the linear cocycle associated to the FHIT.

1.4 Quasiperiodically discrete Schrödinger operators

In this section we review the notions on (discrete) Schrödinger operators that will be used throughout the thesis. For a general exposition on the subject, see [Pui04b, Bou05].

Definition 1.4.1. A *quasiperiodically (discrete) Schrödinger opearator* is a linear bounded operator H acting on $\ell^2(\mathbb{Z})$ of the following form

$$(Hx)_n = x_{n+1} + V(\theta_0 + n\omega)x_n + x_{n-1},$$

where $V\colon \mathbb{T} \longrightarrow \mathbb{R}$ is a contiuous periodic function and ω is irrational.

Some properties of a Schrödinger operator are:

- It is a self-adjoint operator on $\ell^2(\mathbb{Z})$.
- Its spectrum lies on the real line.

The localization and the characterization of the spectrum of a Schrödinger operator can be performed by finding generalized solutions of the following eigenvalue problem:

$$x_{n+1} + V(\theta_0 + n\omega)x_n + x_{n-1} = Ex_n. \tag{1.19}$$

Note that, if $(x_k)_{k\in\mathbb{Z}}$ is a solution of (1.19), then $(x_k, x_{k-1})_{k\in\mathbb{Z}}$ is an orbit of the linear cocycle, acting on $\mathbb{R}^2 \times \mathbb{T}$, with transfer matrix

$$M_E(\theta) = \begin{pmatrix} E - V(\theta) & -1 \\ 1 & 0 \end{pmatrix}. \tag{1.20}$$

The following result is due to Johnson [Joh83].

Theorem 1.4.2. *E is in the resolvent set of a quasiperiodic discrete Schrödinger operator if, and only if, the cocycle with transfer matrix* (1.20) *is uniformly hyperbolic.*

Another important tool associated to a Schrödinger operator is the *Integrated Density of States (IDS)* function. This function is defined as the limit

$$N(x) = \lim_{|N_2 - N_1| \to \infty} \frac{\#\left\{E \in \mathrm{Spec}(H_{[N_1,N_2]}) : E \leq x\right\}}{|N_2 - N_1|},$$

where $H_{[N_1,N_2]} = Q_{[N_1,N_2]} H Q_{[N_1,N_2]}$, with $Q_{[N_1,N_2]}$ the projection operator acting on $\ell^2(\mathbb{Z})$:

$$(Q_{[N_1,N_2]} v)_k = \begin{cases} v_k & \text{if } N_1 \leq k \leq N_2 \\ 0 & \text{otherwise} \end{cases}.$$

Some properties of the IDS function, see [Bou05], are:

- $N(\mathbb{R}) = [0, 1]$.
- N is monotone increasing.
- N is constant outside the spectrum.
- $x \in \mathrm{Spec}(H)$ if and only if $N(x) \notin \frac{1}{2}\left((\omega\mathbb{Z})/\mathbb{Z}\right)$.
- The fibered rotation number ρ of the associated cocycle of the Schrödinger operator satisfies that

$$\rho = N(x) \pmod 1.$$

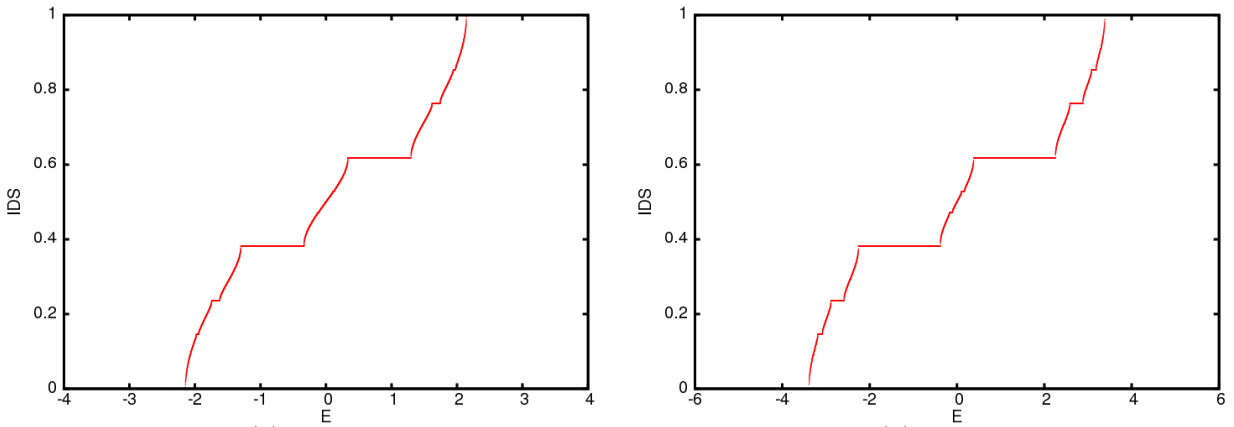

(a) $\lambda = 1$. (b) $\lambda = 3$.

Figure 1.2: Visual example of the Integrated Density of States for the quasiperiodic discrete Schrödinger operator with $V(\theta) = \lambda \cos(2\pi\theta)$ for different values of λ.

Chapter 2

Numerical study of breakdown of FHIT in area preserving skew products

In this chapter we present three different scenarios of bifurcation of FHIT in one-parameter families of quasiperiodically forced area preserving skew product systems. These bifurcations are: the smooth bifurcation, the non-smooth breakdown and the folding breakdown. We explore these bifurcations by approximating the quasiperiodic solutions by periodic orbits, see chapter §5 for the numerical methods used for these computations. For all the rational approximations we compute different observables, like the (maximal) Lyapunov exponent, minimum distance of the invariant bundles and the maximal FK eigenvalue (defined below). We compute these observables and observe different behaviours between different bifurcations. Also, these rational approximations give us some hints of a renormalization phenomenon behind all these bifurcations.

2.1 Introduction

The bifurcations that we study in this chapter are universal. However, to study their characteristics, we present them in an explicit model. These bifurcations are:

The smooth bifurcation, well-known in the literature, see e.g. [BHS96, HdlL07], is characterized by a smooth transition from a FHIT to an *elliptic curve*, which is surrounded by 2D tori. As the parameter approaches the bifurcation value, its Lyapunov exponent, and the maximum and minimum distance between its invariant bundles, goes to zero.

The non-smooth breakdown, first studied in [HdlL07] in a different model, goes as follows: as the parameter approaches the bifurcation value, the curve becomes more wildly: at the breakdown its analycity is broken and it generates sharp peaks. The Lyapunov exponent is positive in the breakdown and, while the minimum distance between the invariant bundles goes to zero, the maximum distance between them stays far from zero. After the breakdown,

numerics suggest that there is no continuous invariant curve, but a hyperbolic object.

The folding breakdown is a new mechanism of destruction of FHIT and shares some similarities with the non-smooth breakdown: the Lyapunov exponent is positive and the minimum distance between the invariant bundles is zero, while the maximum distance is positive. After the breakdown there is, for every partial convergent ω_n of the irrational rotation ω of the skew product, an invariant curve, which is not a graph, but it is hyperbolic in almost every point. As ω_n goes to ω, numerics suggest that these *folded* invariant curves converge, in the Hausdorff sense, to a hyperbolic invariant object which is not even a mesurable graph.

To describe these types of bifurcations, we consider the following *quasiperiodic forced standard map*

$$\begin{cases} \bar{x} &= x + \bar{y} \\ \bar{y} &= y - \dfrac{\kappa}{2\pi}\sin(2\pi x) - \varepsilon\sin(2\pi\theta) \\ \bar{\theta} &= \theta + \omega \pmod 1 \end{cases} . \tag{2.1}$$

Throughout all the chapter, we fix $\omega = \dfrac{\sqrt{5}-1}{2}$, the golden mean.

When $\kappa > 0$ and $\varepsilon = 0$, (2.1) has

$$\left\{ \left(\frac{1}{2}, 0, \theta \right) \right\}, \quad \theta \in \mathbb{T} \tag{2.2}$$

as FHIT. For every different scenario, we fix κ and continue the solution (2.2) with respect ε. Since for $\varepsilon = 0$ the invariant curve is constant, so the transfer matrix is constant and has positive eigenvalues, the fibered rotation number of the curve is 0. Then, while we continue (2.2), the fibered rotation number of the invariant curves for $\varepsilon > 0$ is also zero.

Remark 2.1.1. The skew product (2.1) is analytic, so its FHIT are analytic curves.

Remark 2.1.2. We want to emphasize that, although we show different bifurcations for some values of the parameter κ, every bifurcation is produced in an open set of the parameter κ. This is discussed at the end of the chapter.

The orbits of (2.1), $\{(x_n, y_n, \theta_n)\}_{n\in\mathbb{Z}}$, satisfy

$$x_{n+1} - 2x_n + \frac{\kappa}{2\pi}\sin(2\pi x_n) + x_{n-1} + \varepsilon\sin(2\pi\theta_n) = 0, \tag{2.3}$$

with $y_{n+1} = x_{n+1} - x_n$ and $\theta_n = \theta_0 + n\omega$. The form (2.3) is very useful from the theoretical point of view: an invariant curve of the quasiperiodically forced standard map can be represented as the graph of the function $x\colon \mathbb{T} \longrightarrow \mathbb{R}$. Then, the y coordinate of the invariant curve is just $y(\theta) = x(\theta) - x(\theta - \omega)$. Throughout all the chapter, we denote by $x(\theta)$ the invariant curves of the quasiperiodically forced standard map.

It is easy to see that the solutions of (2.3) are the stationary orbits of the gradient flow

$$\dot{x}_n = x_{n+1} - 2x_n + \frac{\kappa}{2\pi}\sin(2\pi x_n) + x_{n-1} + \varepsilon\sin(2\pi\theta_n), \tag{2.4}$$

defined in $\ell^\infty(\mathbb{Z})$. This gradient flow is called *(generalized) FK model*. It is a generalization of the FK model studied in, e.g. [MMS89, Har98, Gol01], and satisfies that it has equilbrium states of the potential

$$H(x,\theta_0) = \sum_{n\in\mathbb{Z}} \frac{1}{2}(x_{n+1}-x_n)^2 - \frac{\kappa}{4\pi^2}\cos(2\pi x_n) + \varepsilon \sin(2\pi(\theta_0+n\omega))x_n. \tag{2.5}$$

Remark 2.1.3. Given a fixed point of the FK model (2.3), its linearization at the fixed point is a discrete Schrödinger operator. The spectrum of the linearization of the fixed point will be called *FK spectrum*, and the upper bound of the FK spectrum will be called *maximal FK eigenvalue*. The computation of both the FK spectrum and maximal FK eigenvalue is the same as for a Schrödinger operator, and it is discussed in chapter §5.

As we observed above, the continued curves has zero fibered rotation number, which means that the FK spectrum lies on the negative real axis. This implies that they are attracting fixed points of (2.3). By the theory exposed in chapter §1, these curves will remain FHIT until they loose their attracting nature as ixed points of the gradient flow.

Remark 2.1.4. All the numerical computations have been done using the periodic orbits technique, see chapter §5 for further details. Also, when the periodic orbits technique does not work, we have used the FK model, equation (2.3), to compute the invariant curves, or objects. Note that integration of points under the flow only converge to objects that has zero fibered rotation number, which correspond to fixed points of the flow that are (exponentially) attracting.

Remark 2.1.5. All the computations shown throughout the chapter have been done for every partial convergent less than 10^7. We have compared them and obtained that there are no significant differences, otherwise we state the differences in the text. Hence, when we show a computation, we fix a partial convergent but the results are not significantly altered if we change the rational approximation.

2.2 Smooth bifurcation

This scenario is characterized by the transition of a FHIT to an elliptic curve: a curve surrounded by 2D tori. This is analogous to the bifurcation of a hyperbolic fixed point to an elliptic fixed point in an area preserving map. As the ε parameter approaches the bifurcation value, the Lyapunov exponent and the minimum and maximum distance between the invariant bundles approach zero. This means that the M spectrum of the curve, which is two concentric circles before the bifurcation, collides with the unit circle at the bifurcation value. See figure 2.1 for a schematic example of these spectra.

The example we present here appears when we fix $\kappa = 0.3$ and let ε increase from 0 to the critical value, $\varepsilon_c \simeq 1.336405501779$, where the transition from the hyperbolic curve to the elliptic curve is predicted.

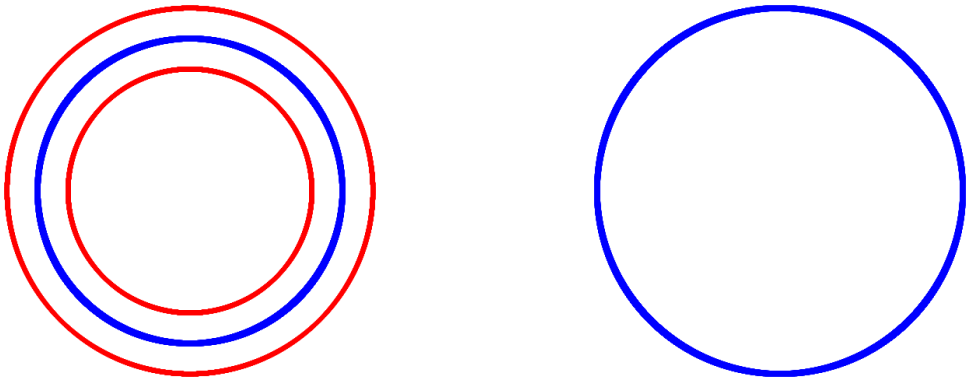

(a) Before the breakdown. (b) At the breakdown.

Figure 2.1: Schematic representation of the M spectrum before and at the smooth bifurcation. The blue circle is the unit circle.

2.2.1 Smooth bifurcation prediction and behaviour of the observables

For every partial convergent of the golden mean with its denominator between 30 and 6000000, we computed the critical ε_c where the transtition occurs, see table 2.1. The stopping criterion used for the computation of the table is when the Lyapunov exponent associated to the invariant curve, Λ, reaches values close to 10^{-5}. We observe in the table that the minimum distance between the unstable and stable bundles, and the maximal FK eigenvalue are close to zero. Also, from the table we can observe that these critical values converge to a value, $\varepsilon_\infty \simeq 1.336405501779$, which corresponds to the critical value of the transition of the curve in the quasiperiodic case. This convergence can be seen in figure 2.2. See also figure 2.3 for a visualitzation of the Lyapunov exponent, the minimum distance and the maximal FK eigenvalue near the bifurcation.

Remark 2.2.1. In table 2.2 we compute the Aitken's accelerations for the ten smallest rational approximations. Note that for the first Aitken's value we have 1.336405518559, which is remarkably close to the predicted $\varepsilon_\infty \simeq 1.336405501779$. Also note that in the third column in table 2.2, where the ratios of the differences of successive critical values ε_c is computed, stabilize to a value around $-3.819646318413\text{e-}01$. This gives us some hints that a renormalization phenomena occurs in this bifurcation.

In figure 2.4 it is shown several invariant curves with their invariant bundles for different values of ε near the bifurcation. We can observe that the smoothness of the invariant curve is not altered by the bifurcation, and that the invariant bundles collide in a smooth manner: the minimum and the maximum distance between them goes to zero as the parameter approaches the critical value.

As it is shown in figure 2.3, the Lyapunov exponent and the minimum distance between the invariant bundles behave as a square root, while the maximal FK eigenvalue behaves as

Numerator	Denominator	ε_c	Λ_c	Min. distance bundles	Maximal FK eigenvalue
21	34	1.337116464139e+00	1.001554423143e-05	1.351271083732e-05	-8.191906526917e-05
34	55	1.336134004543e+00	1.000015153835e-05	1.346752043618e-05	-3.139655053411e-05
55	89	1.336509211252e+00	1.002209673142e-05	1.350210958267e-05	-1.200925695392e-05
89	144	1.336365889419e+00	1.001111955774e-05	1.347936190104e-05	-4.592312325257e-06
144	233	1.336420632577e+00	1.000443207011e-05	1.347004461652e-05	-1.755244171632e-06
233	377	1.336399722423e+00	1.001430096021e-05	1.348469835971e-05	-6.707900204526e-07
377	610	1.336407709373e+00	1.001413695578e-05	1.346750951558e-05	-2.563625457696e-07
610	987	1.336404658626e+00	1.002286815786e-05	1.349215446674e-05	-9.797347490005e-08
987	1597	1.336405823909e+00	1.000689329833e-05	1.344036250397e-05	-3.741414883618e-08
1597	2584	1.336405378812e+00	1.001797837066e-05	1.342920110933e-05	-1.432927092537e-08
2584	4181	1.336405548829e+00	1.000404366461e-05	1.332652297059e-05	-5.501689816081e-09
4181	6765	1.336405483894e+00	1.000347073019e-05	1.326684499819e-05	-2.199635376624e-09
6765	10946	1.336405508672e+00	1.002218031994e-05	1.379965879994e-05	-9.385985322296e-10
10946	17711	1.336405499166e+00	1.000256977348e-05	1.447973793508e-05	-3.411742654369e-10
17711	28657	1.336405502778e+00	1.002214602726e-05	1.462385133238e-05	-1.766698752743e-10
28657	46368	1.336405501396e+00	1.002470259471e-05	1.463563241355e-05	-1.877197064459e-10
46368	75025	1.336405501924e+00	1.001932440478e-05	1.462792435003e-05	-1.387034486385e-10
75025	121393	1.336405501722e+00	1.002709270530e-05	1.463926522626e-05	-1.033728658076e-10
121393	196418	1.336405501800e+00	1.000905447889e-05	1.461291542170e-05	-6.257323548197e-11
196418	317811	1.336405501769e+00	1.002594316172e-05	1.463758218722e-05	-1.563603468910e-10
317811	514229	1.336405501781e+00	1.002278489014e-05	1.463297484791e-05	-5.088747201381e-11
514229	832040	1.336405501777e+00	1.001539899705e-05	1.462217708561e-05	-6.257323548197e-11
832040	1346269	1.336405501779e+00	1.001124898032e-05	1.461612238140e-05	-6.148299647177e-11
1346269	2178309	1.336405501779e+00	1.000158995030e-05	1.460202934921e-05	-6.192175661111e-11
2178309	3524578	1.336405501779e+00	1.000525427725e-05	1.460721668447e-05	-6.257323548197e-11
3524578	5702887	1.336405501779e+00	1.000384543790e-05	1.460531692387e-05	-6.257323548197e-11

Table 2.1: Critical ε_c where the smooth bifurcation occurs, with other observables.

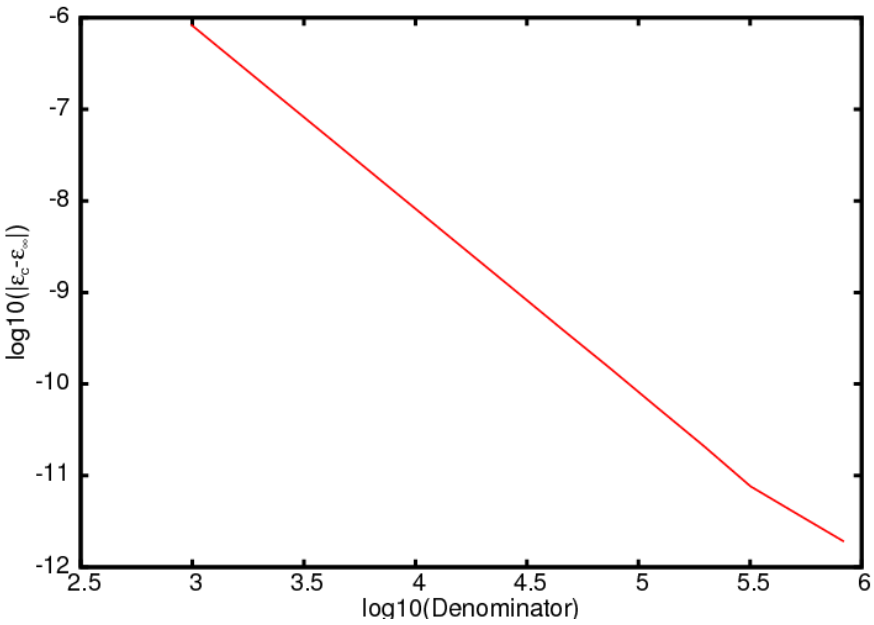

Figure 2.2: Graph of ε_c with respect the rational approximations.

Numerator	Denominator	Ratio convergence	Aitken's accel.
55	89	-3.819054851656e-01	1.336405518559e+00
89	144	-3.819809967525e-01	1.336405503724e+00
144	233	-3.819596590822e-01	1.336405502123e+00
233	377	-3.819683587215e-01	1.336405501874e+00
377	610	-3.819651347217e-01	1.336405501834e+00
610	987	-3.819664512905e-01	1.336405501815e+00
987	1597	-3.819665264814e-01	1.336405501859e+00
1597	2584	-3.819646318413e-01	1.336405501847e+00
2584	4181	-3.819779819878e-01	1.336405501735e+00
4181	6765	-3.819358748000e-01	1.336405502142e+00

Table 2.2: In the second column there is the q_n denominators of the partial convergents used to compute the third and fourth columns. In the third column there is the ratios of convergence between successive critical ε_n. These ratios are computed using the formula $\frac{\varepsilon_n - \varepsilon_{n-1}}{\varepsilon_{n-1} - \varepsilon_{n-2}}$. In the fourth column there is the Aitken's acceleration of the critical ε_n corresponding to the denominator q_n. These are computed using the formula $\frac{\varepsilon_n \varepsilon_{n-2} - \varepsilon_{n-1}^2}{\varepsilon_n - 2\varepsilon_{n-1} + \varepsilon_{n-2}}$.

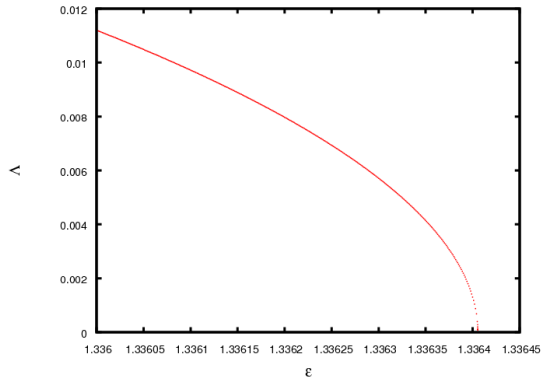

(a) Lyapunov exponent.

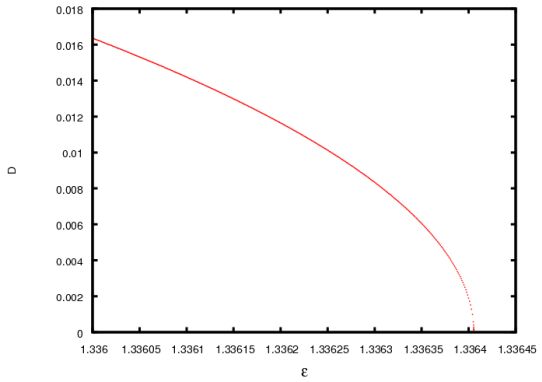

(b) Minimum distance function.

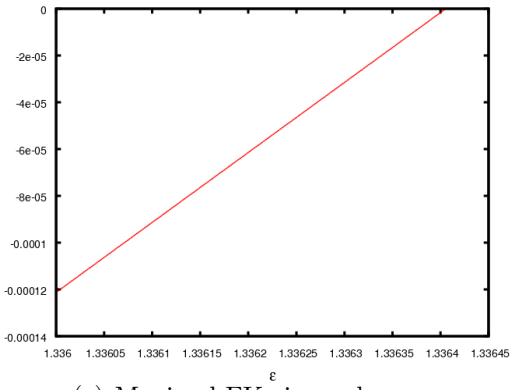

(c) Maximal FK eigenvalue.

Figure 2.3: Observables values along the continuation of the FHIT for $\omega_n = \frac{46368}{75025}$.

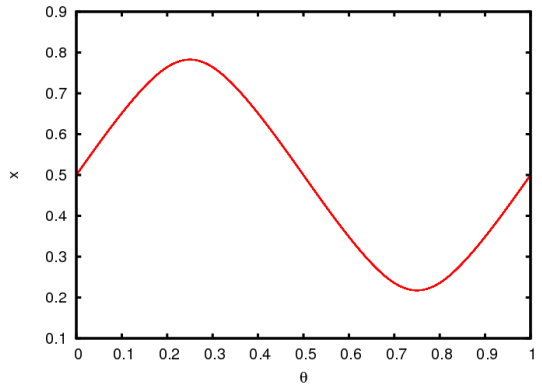

(a) $\kappa = 0.3$, $\varepsilon = 1$.

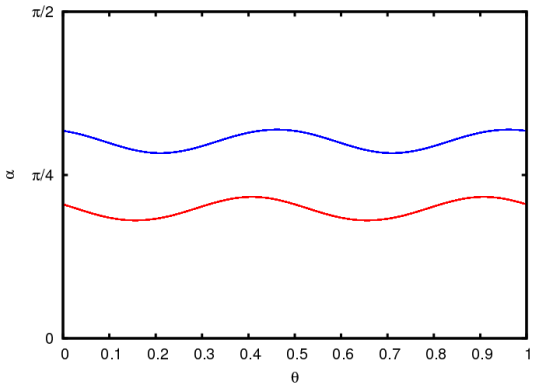

(b) $\kappa = 0.3$, $\varepsilon = 1$.

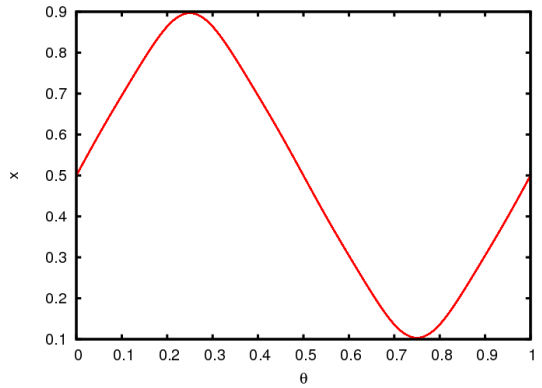

(c) $\kappa = 0.3$, $\varepsilon = 1.33$.

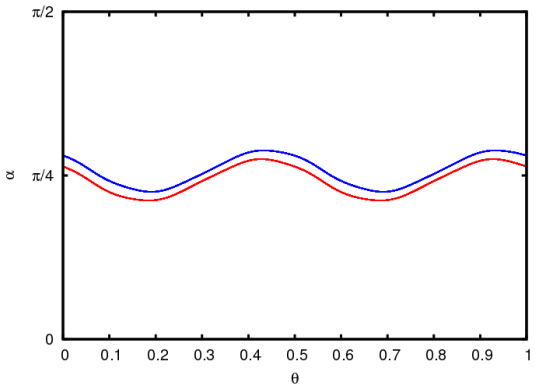

(d) $\kappa = 0.3$, $\varepsilon = 1.33$.

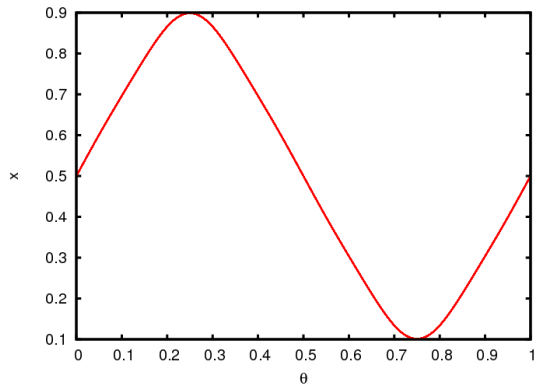

(e) $\kappa = 0.3$, $\varepsilon = 1.336$.

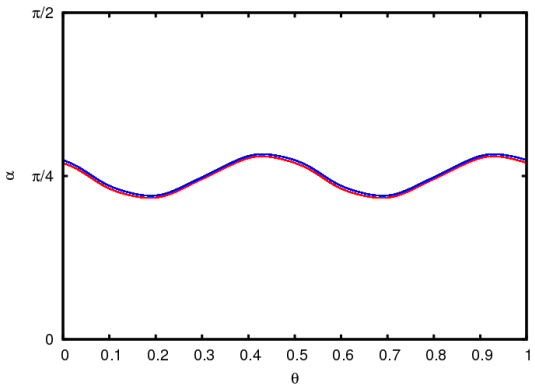

(f) $\kappa = 0.3$, $\varepsilon = 1.336$.

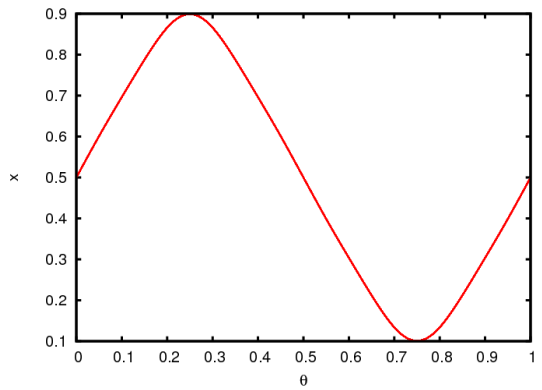

(g) $\kappa = 0.3$, $\varepsilon = 1.3364$.

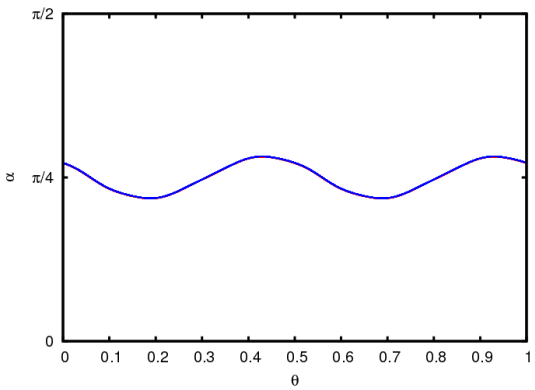

(h) $\kappa = 0.3$, $\varepsilon = 1.3364$.

Figure 2.4: Invariant curves (left) and their invariant bundles (right) with $\omega_n = \frac{46368}{75025}$, near the smooth bifurcation.

a line. To check these behaviours, for every partial convergence between 700 and 6000000 and for every of these three observables, we performed a fit, using the `fit` utility of `gnuplot`, of the data of these observables with the supposed behaviour. The Lyapunov exponent isn fitted by the function

$$\Lambda = b(\varepsilon_c - \varepsilon)^{\frac{1}{2}}$$

wher Λ is the Lyapunov exponent, ε_c is the critical value of the parameter and b is a constant. In table 2.3 it is shown the output of the fit that corresponds to the Lyapunov exponent. For the computation of that table we let b and ε_c be the variables to fit. Similarly, the fitting for the minimum distance function is done using formula

$$D = b(\varepsilon_c - \varepsilon)^{\frac{1}{2}}$$

where D represents the minimum distance, see table 2.4. Also, the fitting for the maximal FK eigenvalue is done using formula

$$\lambda_{max} = b(\varepsilon_c - \varepsilon)$$

where λ_{max} represents the maximal FK eigvalue, see table 2.5.

Remark 2.2.2. Note that the ε_c predicted by the fitting outputs are close to the ones that comes from table 2.1.

Numerator	Denominator	ε_c	b
610	987	1.336404648094	0.556222197926
987	1597	1.336405813488	0.556222790393
1597	2584	1.336405368166	0.556222750560
2584	4181	1.336405538051	0.556222984995
4181	6765	1.336405473608	0.556222434246
6765	10946	1.336405498023	0.556222850865
10946	17711	1.336405488936	0.556222446033
17711	28657	1.336405492169	0.556222846314
28657	46368	1.336405490786	0.556222845242
46368	75025	1.336405491413	0.556222743564
75025	121393	1.336405491405	0.556222544689
121393	196418	1.336405491089	0.556222949529
196418	317811	1.336405491160	0.556222845531
317811	514229	1.336405491271	0.556222743449
514229	832040	1.336405491066	0.556222949507
832040	1346269	1.336405491169	0.556222845534
1346269	2178309	1.336405491168	0.556222845538
2178309	3524578	1.336405491169	0.556222845534
3524578	5702887	1.336405491168	0.556222845538

Table 2.3: Fitting results for the Lyapunov exponent.

Numerator	Denominator	ε_c	b
610	987	1.336404609742	0.812315016364
987	1597	1.336405775314	0.812317480289
1597	2584	1.336405329278	0.812317409677
2584	4181	1.336405498697	0.812318777507
4181	6765	1.336405436044	0.812315111960
6765	10946	1.336405459064	0.812317878350
10946	17711	1.336405451365	0.812315144669
17711	28657	1.336405453222	0.812317804204
28657	46368	1.336405451840	0.812317799402
46368	75025	1.336405452820	0.812317120221
75025	121393	1.336405453498	0.812315795749
121393	196418	1.336405451783	0.812318492295
196418	317811	1.336405452214	0.812317799545
317811	514229	1.336405452677	0.812317119547
514229	832040	1.336405451761	0.812318492133
832040	1346269	1.336405452223	0.812317799568
1346269	2178309	1.336405452222	0.812317799566
2178309	3524578	1.336405452222	0.812317799587
3524578	5702887	1.336405452222	0.812317799500

Table 2.4: Fitting results of the minimum distance function.

Numerator	Denominator	ε_c	b
610	987	1.336404972751	-0.299010813617
987	1597	1.336405935817	-0.299011407883
1597	2584	1.336405413180	-0.299011409504
2584	4181	1.336405553503	-0.299011697212
4181	6765	1.336405477894	-0.299010983678
6765	10946	1.336405497893	-0.299011544526
10946	17711	1.336405487284	-0.299010987410
17711	28657	1.336405489775	-0.299011541984
28657	46368	1.336405488141	-0.299011544429
46368	75025	1.336405488717	-0.299011396760
75025	121393	1.336405488722	-0.299011115705
121393	196418	1.336405488313	-0.299011647254
196418	317811	1.336405488394	-0.299011517917
317811	514229	1.336405488543	-0.299011370895
514229	832040	1.336405488294	-0.299011635593
832040	1346269	1.336405488422	-0.299011497471
1346269	2178309	1.336405488421	-0.299011493162
2178309	3524578	1.336405488421	-0.299011494552
3524578	5702887	1.336405488421	-0.299011494513

Table 2.5: Fitting results for the maximal FK eigenvalue.

Remark 2.2.3. In [HdlL07] there is also numerical explorations of this bifurcation in the context of Schrödinger operators and area preserving skew products. These numerical explorations are done using Fourier methods to compute the invariant tori, see chapter §5. They observe that the Lyapunov exponent and minimum distance function behave as a square root.

2.2.2 After the smooth bifurcation

After the bifurcation, the invariant curve is as smooth as before the breakdown, but its invariant unstable and stable bundles have dissapeared: the curve is no more hyperbolic, see figure 2.8. There are 2D tori around it. Figure 2.5 shows a section, for $\theta = 0$, where it can be seen these 2D tori surrounding the invariant curve. Hence, in the bifurcation the invariant curve is still smooth but the dynamics of its associated cocycle is conjugated to a constant cocycle with transfer matrix of the form

$$\begin{pmatrix} 1 & a \\ 0 & 1 \end{pmatrix} \tag{2.6}$$

with $a \neq 0$. This conjugacy property is in accordance with the general theory, see [Pui04a].

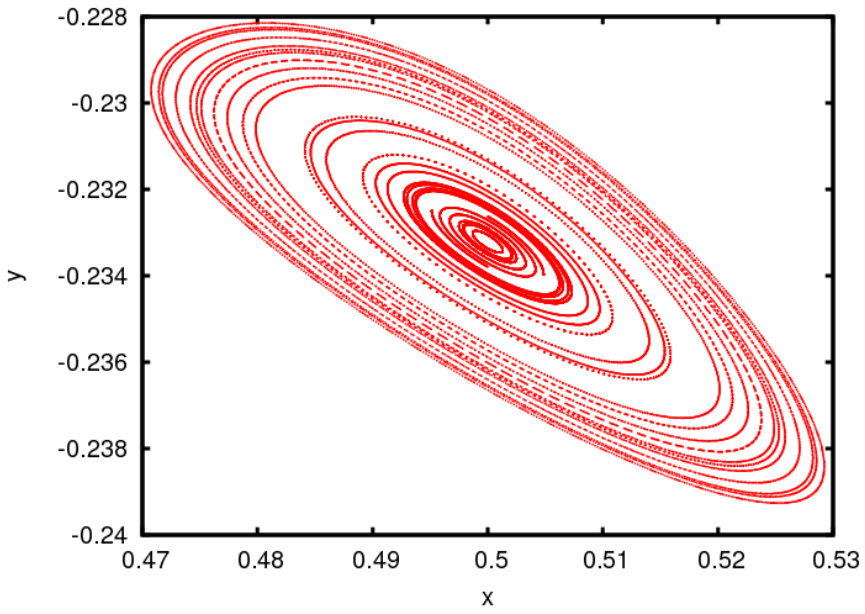

Figure 2.5: Neighbourhood of the torus after the transition. Section $\theta = 0$.

In figure 2.6 we plot the first and second derivative of the invariant curves for $\varepsilon = 1.3364$ (before the breakdown) and for $\varepsilon = 1.3365$ (after the breakdown). We observe in this figure that the first and second derivatives are continuous before and after the breakdown. Also, in figure 2.7 we can see the graphs of the maximum of the first and second derivatives of the invariant curves with respect ε near the breakdown.

Remark 2.2.4. We observe that the graph of the second derivative in figure 2.7 seems to have a vertical asymptote in the breakdown value, but this is a numerical phenomenon: as ε approaches the breakdown value, the system gets more singular because the condition number, of the linear system that has to be solved to compute the derivatives, increases.

If ε is increased up to 1.44 we observe, see figure 2.8, that the invariant curve bifurcates to a FHIT with invariant bundles with non-trivial homotopy (hence the fibered rotation number is different from zero). To see this bifurcation from elliptic curve to FHIT curve, we compute the upper 10% of the FK spectrum, with respect ε, before and after the breakdown, see figure 2.9. In this figure we can see that, after the breakdown, when the spectrum crosses the blue line, a part of the spectrum crosses the zero line, which means that for some ε values, the invariant curve is not a FHIT. In fact, KAM theory predicts that there is a Cantor set of ε such that the invariant curves are elliptic, see [JS96] and references therein. Increasing further ε, we observe that in the FK spectrum there is an open gap, where $\varepsilon = 1.44$ is in it, hence the invariant curve is FHIT.

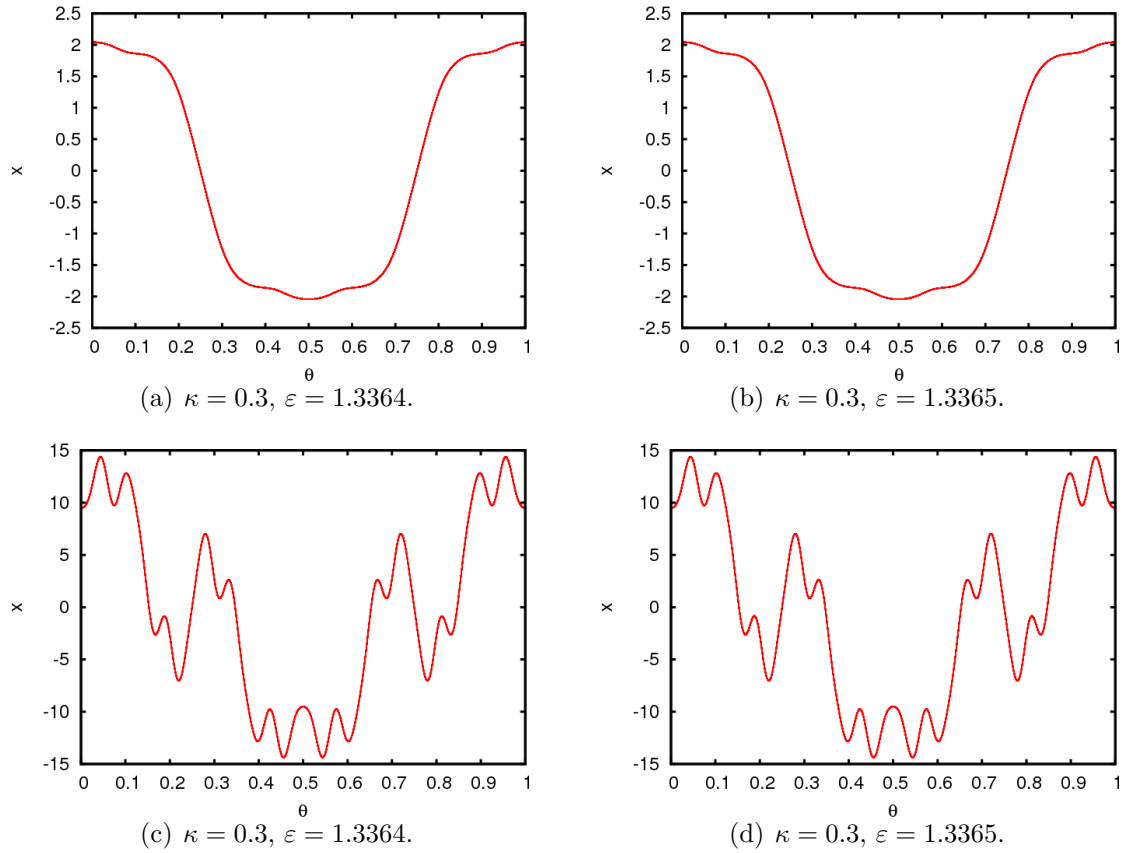

(a) $\kappa = 0.3$, $\varepsilon = 1.3364$.

(b) $\kappa = 0.3$, $\varepsilon = 1.3365$.

(c) $\kappa = 0.3$, $\varepsilon = 1.3364$.

(d) $\kappa = 0.3$, $\varepsilon = 1.3365$.

Figure 2.6: First derivative, $x'(\theta)$, (left) and second derivative, $x''(\theta)$, (right) of the invariant curve, with $\omega_n = \frac{46368}{75025}$, at ε values before and after the smooth bifurcation. Note that there are no significant changes.

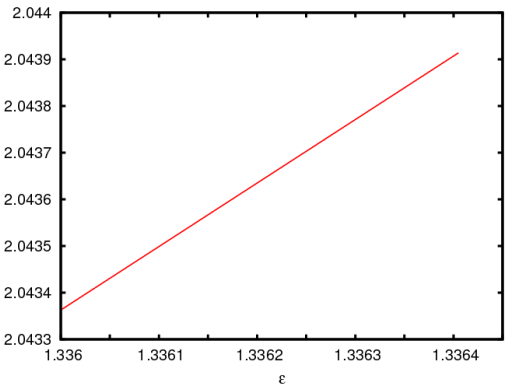

(a) Graph of the maximum of the first derivative for $\kappa = 0.3$.

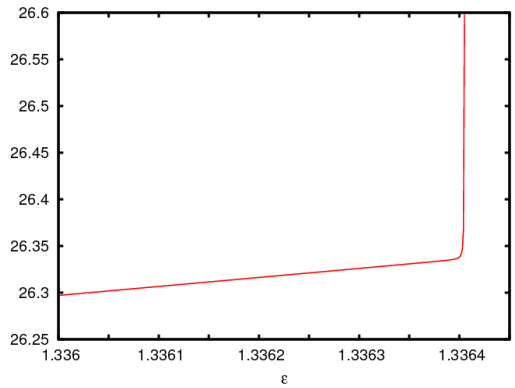

(b) Graph of the maximum of the second derivative for $\kappa = 0.3$.

Figure 2.7: Graphs of the derivatives with respect ε near the smooth bifurcation. These are computed with $\omega_n = \frac{2178309}{3524578}$.

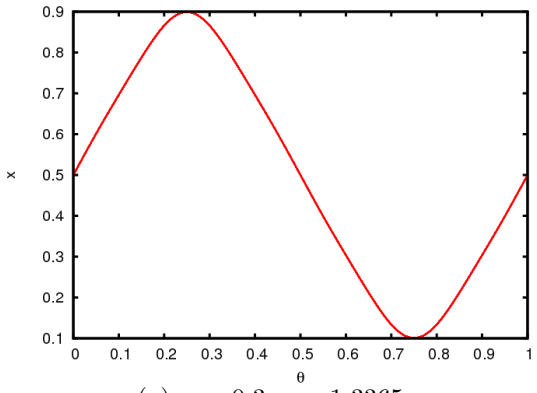

(a) $\kappa = 0.3$, $\varepsilon = 1.3365$.

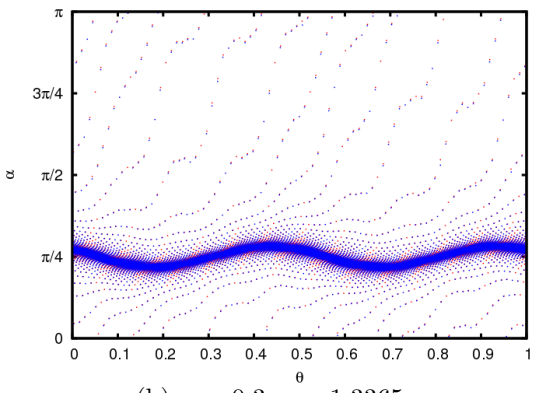

(b) $\kappa = 0.3$, $\varepsilon = 1.3365$.

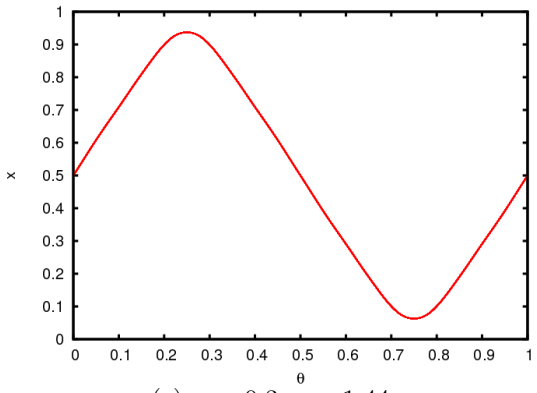

(c) $\kappa = 0.3$, $\varepsilon = 1.44$.

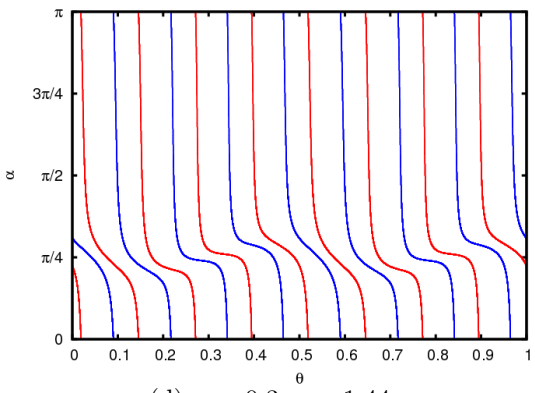

(d) $\kappa = 0.3$, $\varepsilon = 1.44$.

Figure 2.8: Invariant curves (left) and their invariant subbundles (right) with $\omega_n = \frac{46368}{75025}$, after the smooth bifurcation.

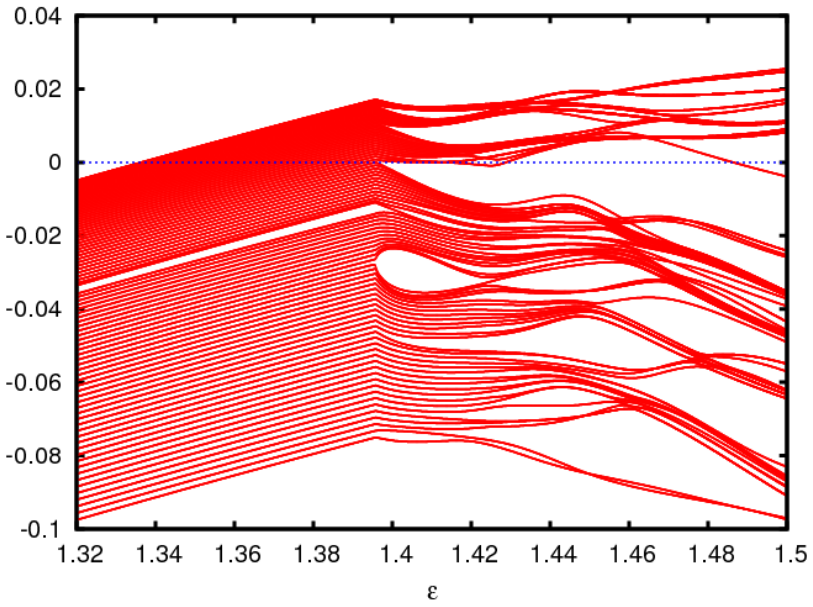

Figure 2.9: 10% of the FK spectrum for $\kappa = 0.3$.

2.3 Non-smooth breakdown

In this scenario, the invariant curve bifurcates in a non-smooth manner: the Lyapunov exponent is positive at the breakdown, and the invariant bundles collided non uniformly: the minimum distance between them goes to zero but the maximum distance stays positive. The spectral implications of this dynamical behaviour is that the M spectrum, which is an union of two circles before the breakdown, collides forming an annulus containing the unit circle, see figure 2.10. About the regularity of the invariant curves, it is observed that, as the parameter approaches the breakdown, the curve, which is always analytic when it is a FHIT, starts to develop peaks. Numerics suggests that at the breakdown, the curve has peaks, which means that the first derivative in the breakdown is a bounded but not a continuous curve, while the supremum norm of the second derivative goes to infinity.

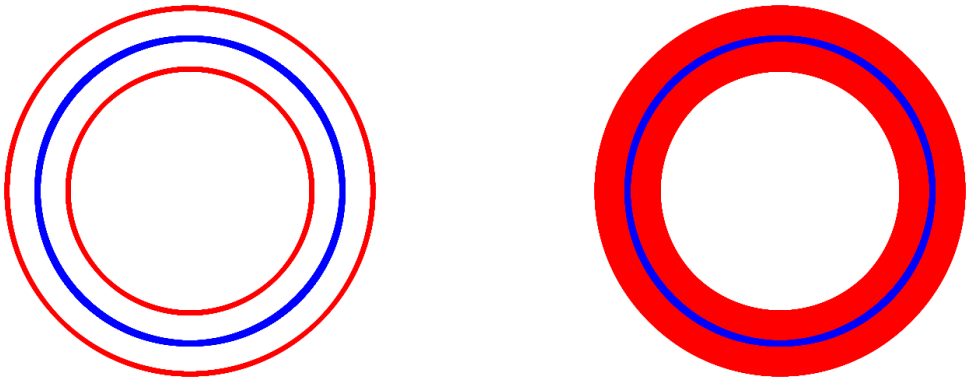

(a) Before the breakdown. (b) At the breakdown.

Figure 2.10: Schematic representation of the M spectrum before and at the non-smooth breakdown.

The non-smooth breakdown is observed when we fix $K = 1.3$ and increase ε form 0 to $\varepsilon_c \simeq 1.235275526763$.

2.3.1 Non-smooth breakdown prediction and behaviour of the observables

The ε parameter value where the breakdown occurs is computed with the periodic orbits with denominator between 30 and 6000000. All the critical parameter values obtained can be seen in table 2.6. The stopping criterion used for the computation of this table is when the periodic orbits method, used to compute the periodic curves, stops to work, see remark 2.3.1. In this table we can see that the Lyapunov exponent at every periodic approximation of ω is bigger than zero and that it stabilizes at a value around 0.36402. In figure 2.11 we observe the convergence of the critical parameter value ε_c and the Lyapunov exponent Λ_c compared with the computed one with denominator 5702887. Since the convergence of the

Lyapunov exponent is not linear, the Aitken method does not improve the convergence, see table 2.7.

Remark 2.3.1. An interesting phenomenon that occurs in this scenario, in contrast with the other two described in this chapter, is that, when the parameter value increases and approaches the breakdown value, the numerical method used to compute the approximate invariant curves, the periodic orbits method, stops to work: it cannot be continued any periodic orbit after the breakdown. When it stops, the minimum distance between the invariant bundles is close to zero, so we can conclude that the breakdown occurs near where the numerical method stops. As we will see at the end of the section, using the gradient flow we can continue the invariant curve after the breakdown and obtain a non-continuous object. This suggests that after the breakdown there is no longer a continuous curve, but a hyperbolic invariant object, which cannot be a measurable graph due to the discussion of invariant graphs in chapter §1.

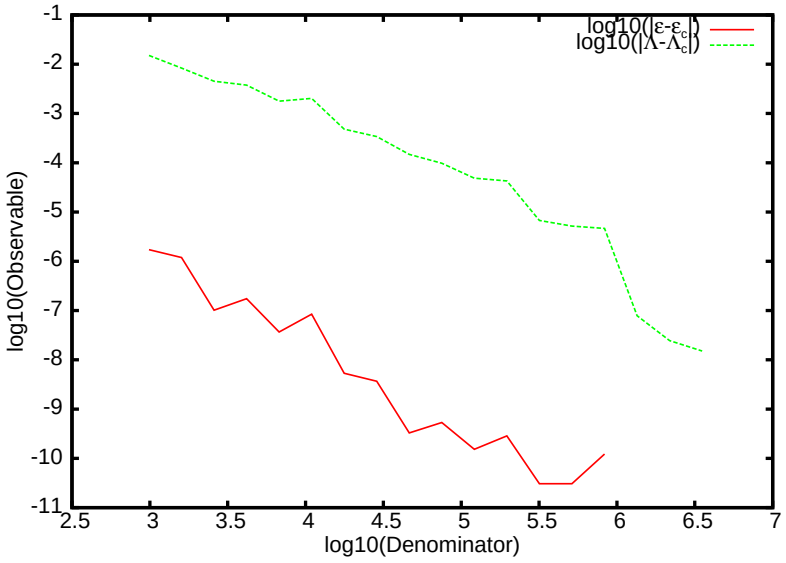

Figure 2.11: Graphs of ε_c and Λ_c with respect the rational approximations.

Figure 2.12 shows the curve and its invariant bundles for several values of ε near the non-smooth breakdown. Observe that the graphs of the invariant curves develop sharp edges as the ε parameter approaches the breakdown, while the invariant bundles collide in a non-smooth manner. The graphics suggest that the non-smooth collision of the bundles goes as follows: there is a θ_0 for which the invariant bundles approach, also for all the $\theta_0 + k\omega$ with $k \in \mathbb{Z}$, while for the others θ_0 the invariant bundles remain separated.

Near the breakdown we compute the first and second derivatives of the invariant curve, see figure 2.13. This figure suggests that the first derivative of the invariant curve at the

Numerator	Denominator	ε_c	Λ_c	Min. distance bundles	Maximal FK eigenvalue
21	34	1.245929101563e+00	1.297425889308e-06	1.624632311487e-04	-1.904991222545e-08
34	55	1.235843390365e+00	5.618454219392e-08	3.058808317746e-09	-1.267702226885e-10
55	89	1.235660986124e+00	1.494489210460e-01	1.692086337712e-08	-7.777938361445e-09
89	144	1.235242766740e+00	2.359487052485e-01	6.986546363663e-07	-6.368223694153e-07
144	233	1.235331500728e+00	2.882846312958e-01	7.949667780726e-07	-7.253765618931e-07
233	377	1.235287343112e+00	3.168961545237e-01	4.652990608366e-07	-4.244199361353e-07
377	610	1.235302711538e+00	3.049254898214e-01	5.041007734574e-07	-4.598972736857e-07
610	987	1.235277250097e+00	3.489439679897e-01	7.497097436193e-07	-6.836321144051e-07
987	1597	1.235276717863e+00	3.557026992143e-01	1.024610514543e-06	-9.343407853404e-07
1597	2584	1.235275424968e+00	3.595111521184e-01	1.135780689942e-06	-1.035559398587e-06
2584	4181	1.235275700525e+00	3.602738607483e-01	1.168753562819e-07	-1.065744465247e-07
4181	6765	1.235275563425e+00	3.622590579554e-01	4.621220353051e-07	-4.214122719930e-07
6765	10946	1.235275611145e+00	3.620060220809e-01	8.999767668882e-07	-8.205344784073e-07
10946	17711	1.235275532096e+00	3.635551895604e-01	1.024348491696e-06	-9.338589635296e-07
17711	28657	1.235275530445e+00	3.636943452632e-01	3.365367119423e-07	-3.068770615077e-07
28657	46368	1.235275526435e+00	3.638870047138e-01	7.081796308261e-07	-6.456146365962e-07
46368	75025	1.235275527297e+00	3.639374391000e-01	4.382728830965e-07	-3.995482399683e-07
75025	121393	1.235275526916e+00	3.639865193607e-01	5.796290794002e-07	-5.283894329891e-07
121393	196418	1.235275527050e+00	3.639923516709e-01	1.399960817827e-06	-1.276344119105e-06
196418	317811	1.235275526794e+00	3.640283527370e-01	1.669205835441e-06	-1.521908047984e-06
317811	514229	1.235275526794e+00	3.640299051017e-01	1.098403263455e-06	-1.001410189871e-06
514229	832040	1.235275526885e+00	3.640304407708e-01	3.435790705053e-06	-3.132437996100e-06
832040	1346269	1.235275526763e+00	3.640351613225e-01	2.156145434417e-06	-1.965834228109e-06
1346269	2178309	1.235275526763e+00	3.640350580754e-01	2.005720892150e-06	-1.828711110273e-06
2178309	3524578	1.235275526763e+00	3.640350977167e-01	2.058332760679e-06	-1.876686292234e-06
3524578	5702887	1.235275526763e+00	3.640350826454e-01	1.971014985890e-06	-1.796938400122e-06

Table 2.6: Critical ε_c where the non-smooth breakdown occurs, with other observables.

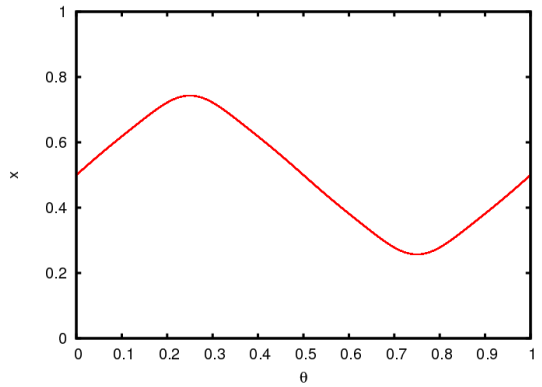

(a) $\kappa = 1.3$, $\varepsilon = 1$.

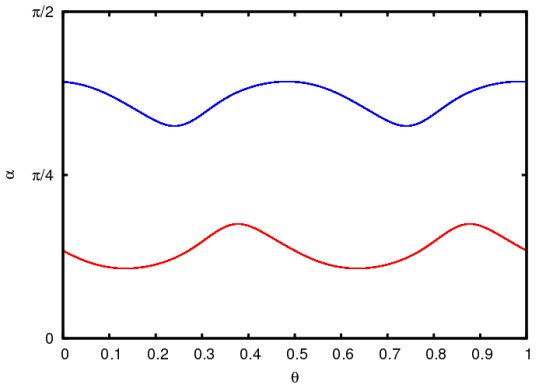

(b) $\kappa = 1.3$, $\varepsilon = 1$.

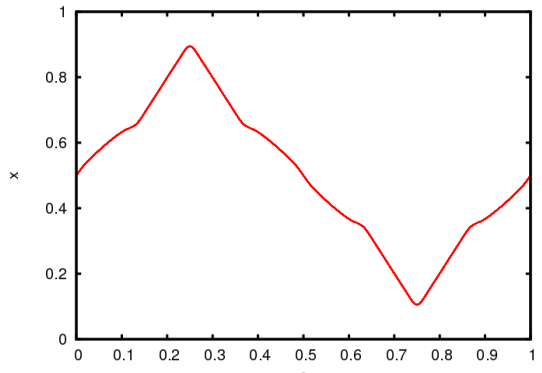

(c) $\kappa = 1.3$, $\varepsilon = 1.23$.

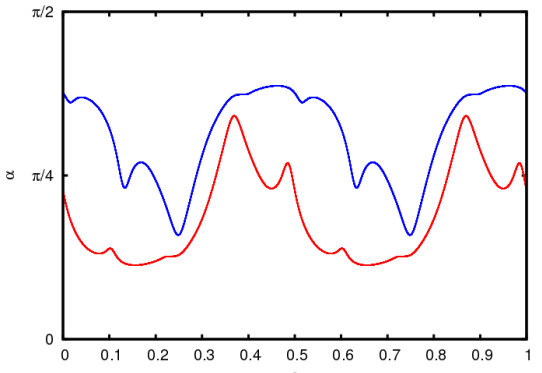

(d) $\kappa = 1.3$, $\varepsilon = 1.23$.

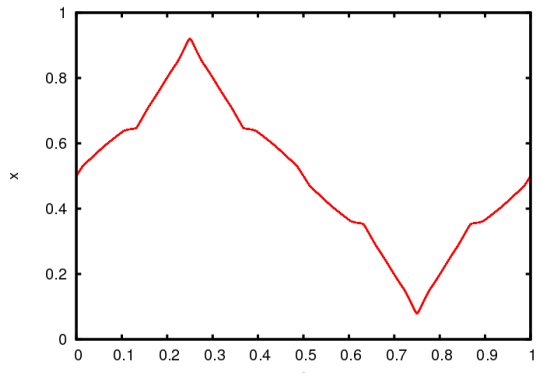

(e) $\kappa = 1.3$, $\varepsilon = 1.235$.

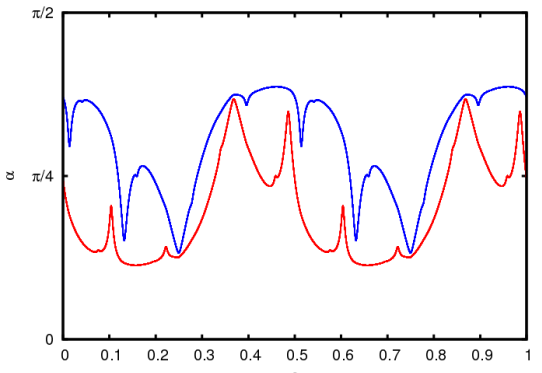

(f) $\kappa = 1.3$, $\varepsilon = 1.235$.

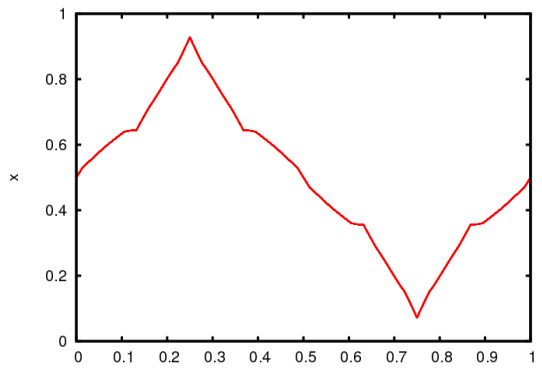

(g) $\kappa = 1.3$, $\varepsilon = 1.235275$.

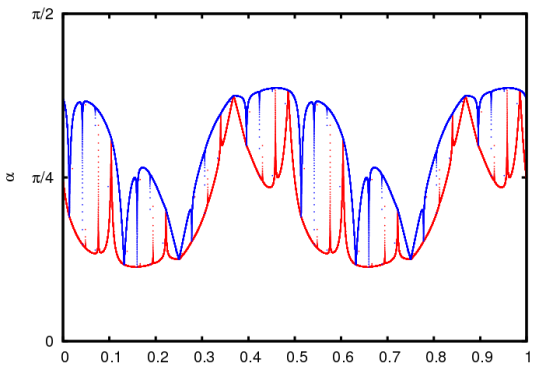

(h) $\kappa = 1.3$, $\varepsilon = 1.235275$.

Figure 2.12: Invariant curves (left) and their invariant bundles (right) with $\omega_n = \frac{46368}{75025}$, near the non-smooth breakdown.

Numerator	Denominator	Ratio convergence	Aitken's accel.
55	89	1.808541192710e-02	1.235657626508e+00
89	144	2.292816108434e+00	1.235984480997e+00
144	233	-2.121709117542e-01	1.235315969279e+00
233	377	-4.976403824778e-01	1.235302015937e+00
377	610	-3.480356703739e-01	1.235298743720e+00
610	987	-1.656737136610e+00	1.235293127808e+00
987	1597	2.090353767277e-02	1.235276706501e+00
1597	2584	2.429183210842e+00	1.235277622460e+00
2584	4181	-2.131315382136e-01	1.235275652188e+00
4181	6765	-4.975392979390e-01	1.235275609154e+00

Table 2.7: In the second column there is the q_n denominators of the partial convergents used to compute the third and fourth columns. In the third column there is the ratios of convergence between successive critical ε_n. These ratios are computed using the formula $\frac{\varepsilon_n-\varepsilon_{n-1}}{\varepsilon_{n-1}-\varepsilon_{n-2}}$. In the fourth column there is the Aitken's acceleration of the critical ε_n corresponding to the denominator q_n. These are computed using the formula $\frac{\varepsilon_n\varepsilon_{n-2}-\varepsilon_{n-1}^2}{\varepsilon_n-2\varepsilon_{n-1}+\varepsilon_{n-2}}$.

breakdown is bounded but not continuous, while the supremum norm of the second derivative of the invariant curve is infinite. Also, in figure 2.14 it is shown the maximum of the first and second derivative of the invariant curve with respect the parameter ε. As we observe, the first derivative remains bounded as ε approaches ε_c, while the second derivative, which is plotted in $\log_{10}$ scale, reaches values of order 10^6 near the breakdown.

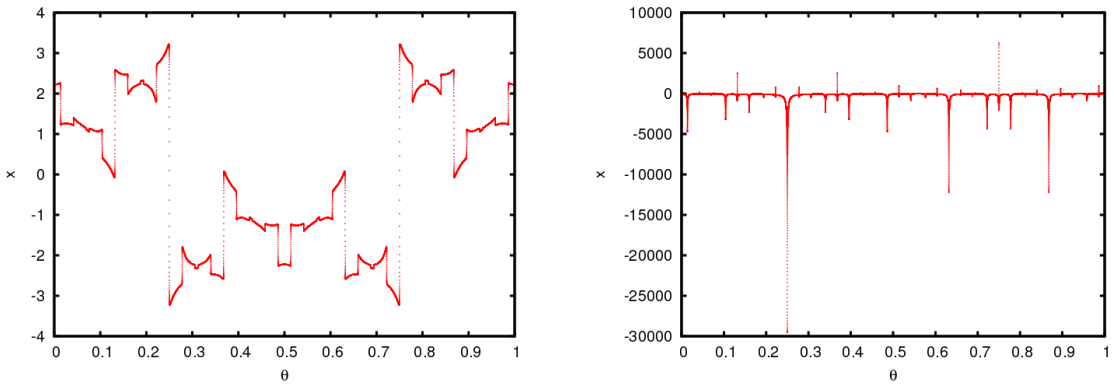

(a) $\kappa = 1.3$, $\varepsilon = 1.235275$. (b) $\kappa = 1.3$, $\varepsilon = 1.235275$.

Figure 2.13: First derivative, $x'(\theta)$, (left) and second derivative, $x''(\theta)$, (right) of the invariant curve, with $\omega_n = \frac{46368}{75025}$, at a ε value near the non-smooth breakdown.

In the left pictures of figure 2.15, we can observe the graph of the Lyapunov exponent, minimum distance between the invariant bundles and the maximal FK eigenvalue. As we observe, these three graphs behave as a square root with respect to the difference $(\varepsilon_c - \varepsilon)$. In the right pictures of figure 2.15 we plot the graphs of this three observables as a func-

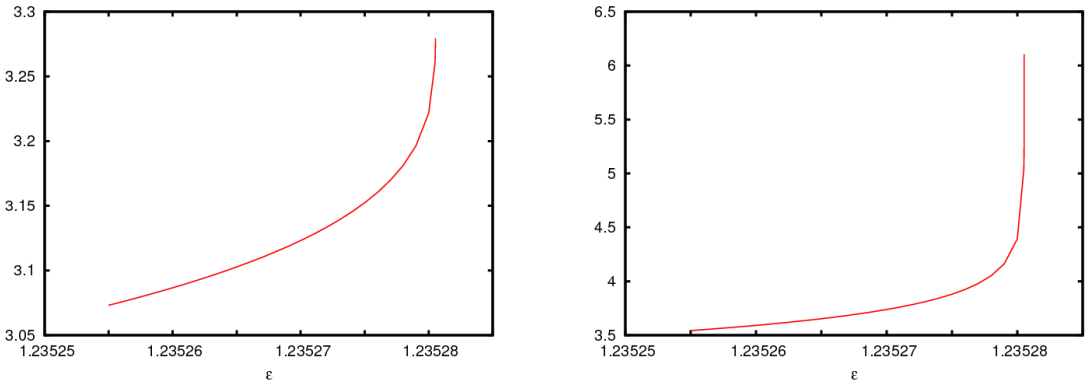

(a) Graph of the maximum of the first derivative for $\kappa = 1.3$.

(b) Graph of the maximum of the second derivative for $\kappa = 1.3$. The y axis is in $\log_{10}$ scale.

Figure 2.14: Graphs of the derivatives with respect ε near the non-smooth breakdown. These are computed with $\omega_n = \frac{2178309}{3524578}$.

tion of $\sqrt{\varepsilon_c - \varepsilon}$. These plots are straight lines, which strenghten the hypothesis that these observables behave as square root near the breakdown.

From the last paragraph and the right plots in figure 2.15 we conclude that the observables behave linearly with respect $\sqrt{\varepsilon_c - \varepsilon}$. We perform, for both three observables and with the help of the `fit` function in `gnuplot`, a fit in order to check this behaviour.

In table 2.8 we can see the fit for the Lyapunov exponent by the function

$$\Lambda = b(\varepsilon_c - \varepsilon)^{\frac{1}{2}} + c,$$

where Λ represents the Lyapunov exponent and ε_c is the parameter when the transition occurs. We can observe that the coefficients stabilize as the denominator of the partial convergent increases. As we can observe, the predicted ε_c from table 2.8 agrees in nine digits with the predicted one via the periodic orbits method, see table 2.6.

Remark 2.3.2. This square root behaviour is also supported by the figure 2.16, where it is shown the largest 10% of the FK spectrum of the invariant curve with respect ε.

In table 2.9 we can see the fit for the minimum distance function by the function

$$D = b(\varepsilon_c - \varepsilon)^{\frac{1}{2}},$$

where D represents the minimum distance function and ε_c is the parameter when the transition occurs. We can observe that the coefficients stabilize as the denominator of the partial convergent increases.

In table 2.10 we can see the fit for the maximal FK eigenvalue by the function

$$\lambda_{max} = b(\varepsilon_c - \varepsilon)^{\frac{1}{2}},$$

where λ_{max} represents the maximal FK eigenvalue and ε_c is the parameter when the transition occurs. We can observe that the coefficients stabilize as the denominator of the partial convergent increases.

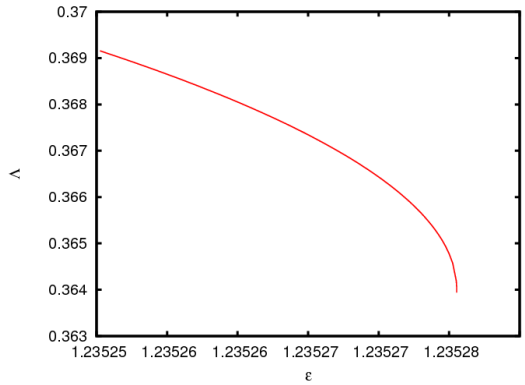

(a) Lyapunov exponent

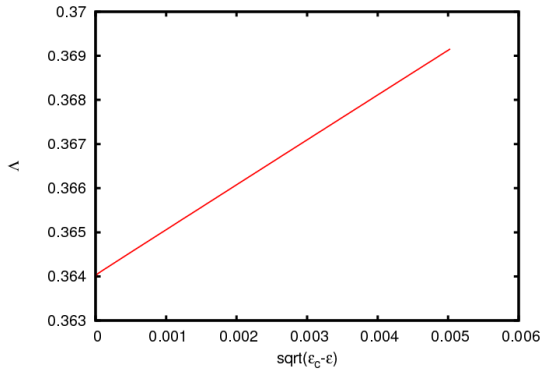

(b) Lyapunov exponent.

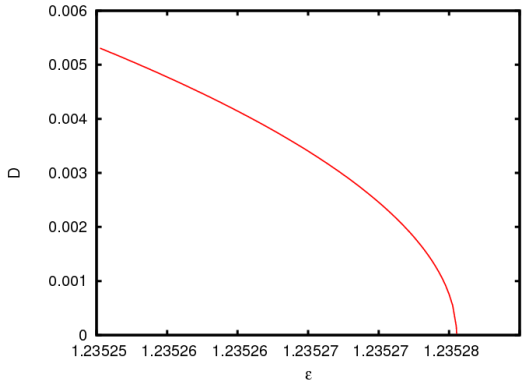

(c) Minimum distance function.

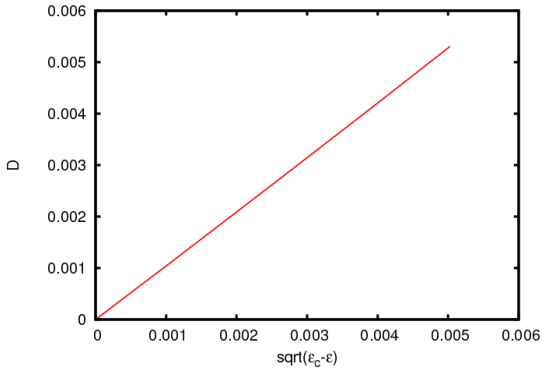

(d) Minimum distance function.

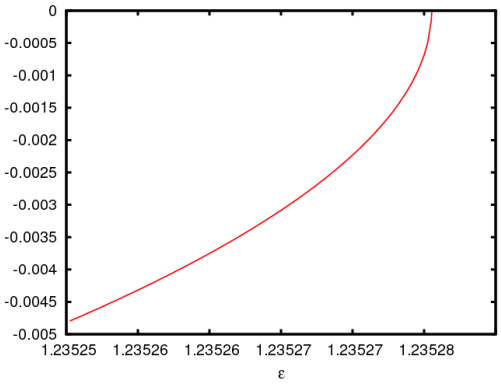

(e) Maximal FK eigenvalue.

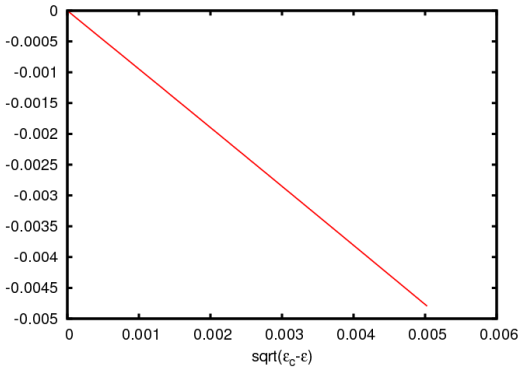

(f) Maximal FK eigenvalue.

Figure 2.15: Observables values along the continuation of the FHIT, for $\omega_n = \frac{46368}{75025}$, with respect ε (left) and $\sqrt{\varepsilon_c - \varepsilon}$ (right).

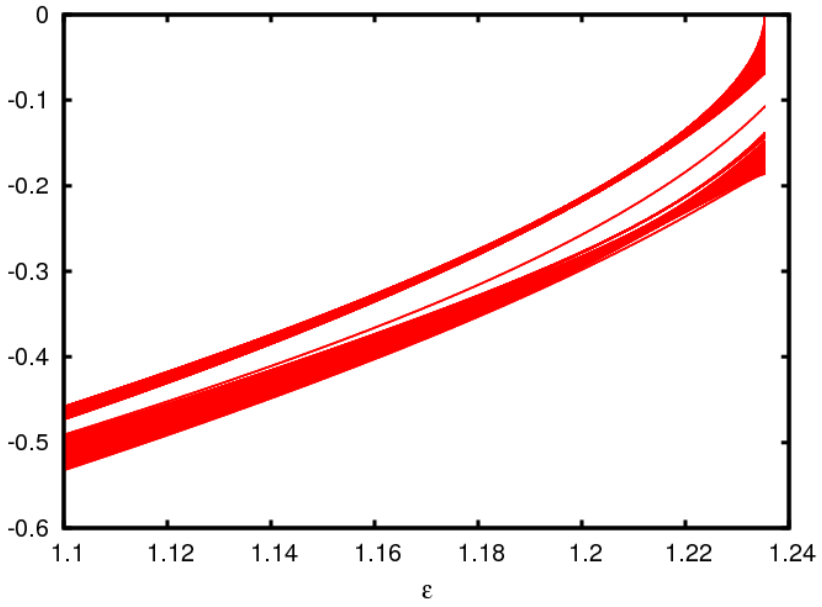

Figure 2.16: 10% of the FK spectrum $\kappa = 1.3$.

Numerator	Denominator	ε_c	b	c
610	987	1.235288815166	1.929669458707	0.357544193075
987	1597	1.235281946637	1.526950323123	0.360893528244
1597	2584	1.235278385603	1.229168286572	0.362734799711
2584	4181	1.235277490525	1.157315948767	0.363193088486
4181	6765	1.235276208604	1.058313749228	0.363779854479
6765	10946	1.235276280966	1.064594421607	0.363746597568
10946	17711	1.235275581642	1.019477491017	0.364025480278
17711	28657	1.235275542553	1.017224302358	0.364040261930
28657	46368	1.235275522252	1.016160124872	0.364047143474
46368	75025	1.235275522001	1.016116585456	0.364047413765
75025	121393	1.235275518825	1.015961014535	0.364048445972
121393	196418	1.235275521711	1.016106198080	0.364047480712
196418	317811	1.235275519175	1.015975011753	0.364048348125
317811	514229	1.235275519171	1.015974330284	0.364048352564
514229	832040	1.235275519258	1.015979242831	0.364048320566
832040	1346269	1.235275519149	1.015973192000	0.364048359942
1346269	2178309	1.235275519149	1.015973227541	0.364048359711
2178309	3524578	1.235275519149	1.015973213917	0.364048359800
3524578	5702887	1.235275519149	1.015973219061	0.364048359766

Table 2.8: Asymptotic results for the Lyapunov exponent.

Numerator	Denominator	ε_c	b
610	987	1.235277152315	1.056001847578
987	1597	1.235276640525	1.055413884515
1597	2584	1.235275348478	1.055268792719
2584	4181	1.235275624530	1.055251607346
4181	6765	1.235275482652	1.055394199957
6765	10946	1.235275529557	1.055420883306
10946	17711	1.235275451808	1.055397307119
17711	28657	1.235275454727	1.055260078205
28657	46368	1.235275443715	1.055487201439
46368	75025	1.235275451622	1.055263477838
75025	121393	1.235275444138	1.055485301404
121393	196418	1.235275451354	1.055263987843
196418	317811	1.235275446541	1.055408494124
317811	514229	1.235275446537	1.055408808805
514229	832040	1.235275446531	1.055409095999
832040	1346269	1.235275446528	1.055408979609
1346269	2178309	1.235275446527	1.055408986226
2178309	3524578	1.235275446528	1.055408987355
3524578	5702887	1.235275446527	1.055408988530

Table 2.9: Asymptotic results for the minimum distance function.

Numerator	Denominator	ε_c	b
610	987	1.235277200502	-0.954220310320
987	1597	1.235276678661	-0.953935339891
1597	2584	1.235275386162	-0.953798223236
2584	4181	1.235275661978	-0.953820133959
4181	6765	1.235275522440	-0.953874747343
6765	10946	1.235275569745	-0.953891294499
10946	17711	1.235275491357	-0.953865587789
17711	28657	1.235275492034	-0.953799887158
28657	46368	1.235275484453	-0.953900051972
46368	75025	1.235275488904	-0.953798772321
75025	121393	1.235275484880	-0.953900175317
121393	196418	1.235275488632	-0.953798572716
196418	317811	1.235275486059	-0.953864195082
317811	514229	1.235275486054	-0.953864187262
514229	832040	1.235275486047	-0.953864014288
832040	1346269	1.235275486044	-0.953864189964
1346269	2178309	1.235275486042	-0.953864191296
2178309	3524578	1.235275486043	-0.953864191180
3524578	5702887	1.235275486042	-0.953864189764

Table 2.10: Asymptotic results for maximal FK eigenvalue.

2.3.2 After the non-smooth breakdown

As we observed at remark 2.3.1 the numerical method used to continue the invariant curve that starts at $\varepsilon = 0$, stops near the breakdown parameter value. In order to check if there is still some invariant object we integrate the gradient flow (2.3) for $\kappa = 1.3$, $\varepsilon = 1.236$ and several partial convergents ω_n. A visual example of the invariant object with its invariant bundles can be seen in figure 2.17. This figure suggests that there is a (bounded) invariant object that remains after the breakdown, and that it is not a continuous invariant curve. Also, we compute its Lyapunov exponent, which is around 0.363. This positive Lyapunov exponent suggests that the invariant object is hyperbolic.

We want to point out several things about the invariant object that remains after the breakdown. First, we have tried to use this invariant object as an initial condition of the periodic orbits method, or variants of it, and we have not get any success, but we have evaluated it in the skew product and obtained a small error (around 10^{-12}). Second, the integration of the gradient flow only converges to attracting fixed points, so it can happen that after the breakdown, the invariant curve bifurcates to the invariant object described earlier and, maybe, to another ones, which will be not attracting fixed points of the gradient flow. With the tools that we have now we cannot say any more in this direction.

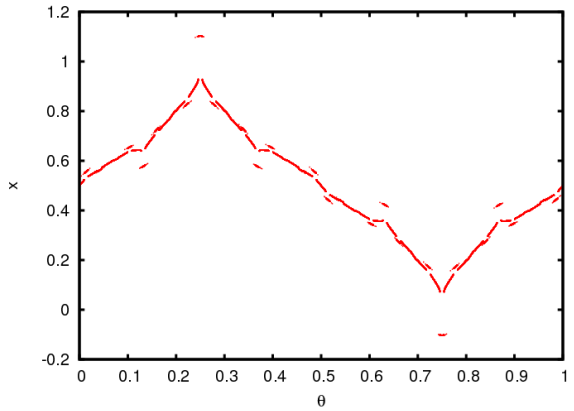

(a) $\kappa = 1.3$, $\varepsilon = 1.236$.

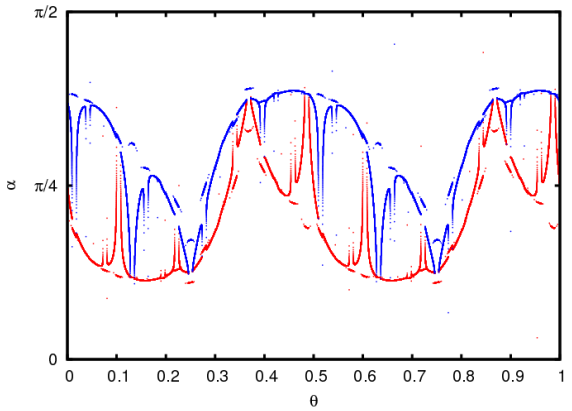

(b) $\kappa = 1.3$, $\varepsilon = 1.236$.

Figure 2.17: Invariant object (left) and its invariant bundles (right) with $\omega_n = \frac{46368}{75025}$, after the non-smooth breakdown.

2.4 Folding breakdown

This scenario is characterized by a transition from a uniformly hyperbolic curve to a non-uniformly hyperbolic object. As it happens in the non-smooth breakdown, as the parameter approaches the breakdown value, the Lyapunov exponent, and the maximum distance function between the invariant bundles, of the invariant curve stay far from zero, while the minimum distance goes to zero. This means that the M spectrum is an union of two circles before the bifurcation, while it is an annulus with the unit circle in it at the breakdown, see figure 2.18. It is also observed that, as the parameter approaches the critical value, the maximum slope of the invariant curve goes to infinity (this does not happen in the non-smooth breakdown).

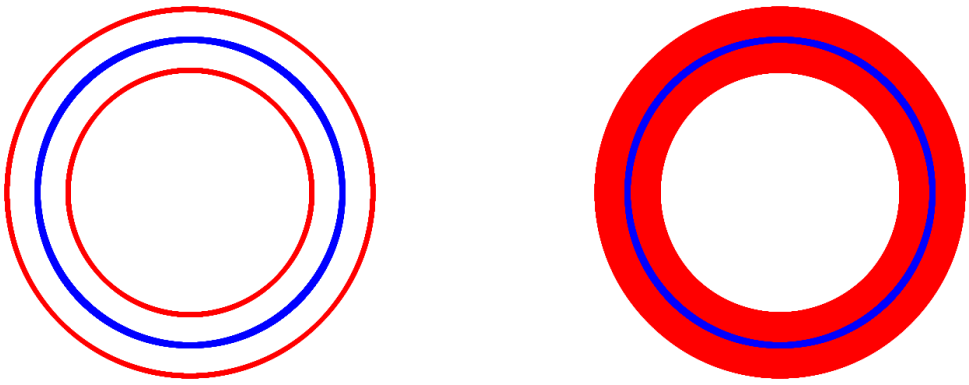

(a) Before the breakdown. (b) At the breakdown.

Figure 2.18: Schematic representation of the M spectrum before and at the folding breakdown.

After the critical value, the approximation of the invariant curve, which is computed using the periodic orbits method with rational rotation number ω_n, is no longer a graph with respect θ but it is a continuous curve with foldings. Numerics suggests that the folding invariant curves converge, as $\omega_n \to \omega$, to a non-smooth and non-uniformly hyperbolic invariant object.

Remark 2.4.1. Numerics suggests that there is a big difference between the invariant object after the non-smooth breakdown with the invariant object after the folding breakdown. The first one is, roughly speaking, the result of an invariant curve that has lost its continuity, while the second one is the limit, in the Hausdorff metric, of a sequence of (folding) smooth curves.

2.4.1 Folding breakdown prediction and behaviour of the observables

We compute the breakdown value of the invariant curves for rational approximations, ω_n, of the irrational rotation ω, with all the denominators between 30 and 6000000. This is shown in table 2.11. The stop criterion used for the computation of this table is that we stablish a threshold, 10^{-10}, for the absolute value of the maximal FK eigenvalue, or that the minimum distance between the invariant bundles is less than 10^{-4}. Observe in the table that the sequence of ε_c values for every partial convergent converges, while the Lyapunov exponents, which are sensibly bigger than zero, do not converge as good as in the smooth bifurcation or the non-smooth breakdown tables. For a visual example of these convergences, see figure 2.19. In this figure we observe that in the Lyapunov exponent's graph, there are some peaks, with period 3. These peaks corresponds to the rational approximations that has even denominator. In fact, from table 2.11 we can see that there are three families of rational approximations: the one with both odd numerator and denominator, the one with even numerator and odd denominator, and the last one with odd numerator and even denominator. These families converge exponentially to the critical value.

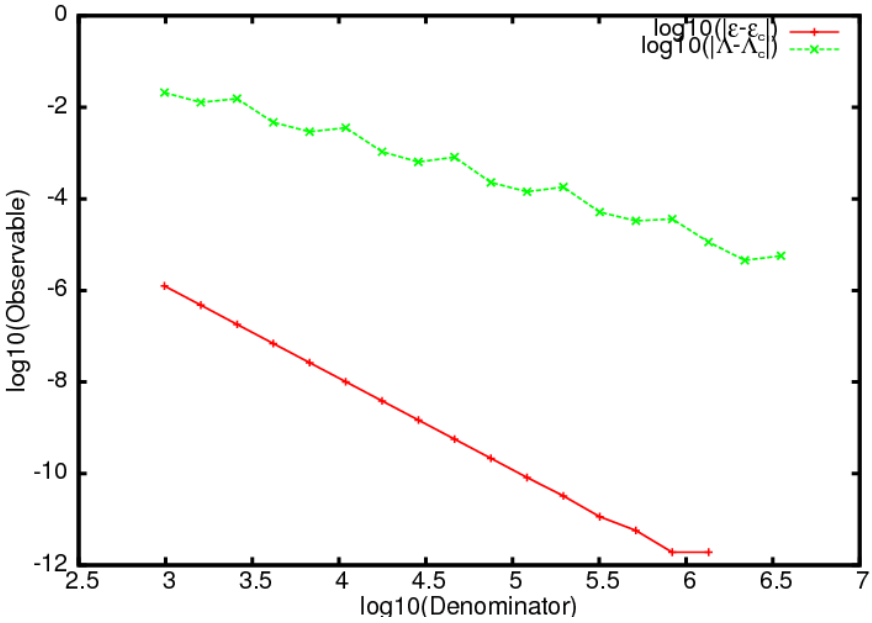

Figure 2.19: Exponential convergence of ε_c and Λ_c for the rational approximations.

Remark 2.4.2. In table 2.12 we compute the Aitken's accelerations for the ten smallest rational approximations. Note that for the third Aitken's value we have 1.275369505272, which is remarkably close to the predicted $\varepsilon_\infty \simeq 1.275369645795$. Also note that in the third column in table 2.12, where the ratios of the differences of successive critical values ε_c is computed, stabilize to a value around -3.819601904780e-01. This gives us some hints

Numerator	Denominator	ε_c	Λ_c	Min. distance bundles	Maximal FK eigenvalue
21	34	1.275275000001e+00	3.728914428544e-06	1.068649522428e-05	-1.979516600840e-05
34	55	1.274960875001e+00	8.282548508494e-04	3.005800253141e-08	-1.195985221859e-08
55	89	1.275521869573e+00	3.536738738393e-06	3.837818951524e-12	-2.480803462390e-11
89	144	1.275310907136e+00	4.595541154024e-08	5.615552467475e-11	-7.348717190325e-11
144	233	1.275392041663e+00	1.154422607770e-01	1.604050225978e-12	6.985940661336 4e-11
233	377	1.275361126840e+00	1.579042670030e-01	8.154144026661e-12	-5.231902964812e-11
377	610	1.275372946435e+00	1.407524200268e-01	2.659539255489e-12	-7.348717190325e-11
610	987	1.275368433366e+00	1.921692032124e-01	4.651334872818e-12	-3.600222294998e-11
987	1597	1.275370157442e+00	2.003111582607e-01	4.077904680599e-12	2.453399357783e-12
1597	2584	1.275369498937e+00	1.976576455716e-01	7.685019287606e-12	-7.348717190325e-11
2584	4181	1.275369750469e+00	2.084588182755e-01	5.267786207241e-12	-6.315325595056e-11
4181	6765	1.275369654394e+00	2.102109309722e-01	2.973121748794e-12	-4.407826029355e-11
6765	10946	1.275369691091e+00	2.095637343936e-01	4.351630167320e-12	-7.348717190325e-11
10946	17711	1.275369677074e+00	2.120715633719e-01	3.706368545408e-12	3.321154652800e-11
17711	28657	1.275369682428e+00	2.124990002425e-01	4.559241872925e-12	-5.604185782607e-11
28657	46368	1.275369680383e+00	2.123236273684e-01	2.733868686988e-12	-7.348717190325e-11
46368	75025	1.275369681163e+00	2.129114837748e-01	7.367051413353e-12	6.561715036885e-12
75025	121393	1.275369680866e+00	2.129965961807e-01	3.709199614121e-12	4.926236425154e-11
121393	196418	1.275369680980e+00	2.129581761024e-01	1.626754286832e-12	-7.348717190325e-11
196418	317811	1.275369680936e+00	2.130880463973e-01	3.116118474366e-12	-7.102393086431e-11
317811	514229	1.275369680954e+00	2.131065398902e-01	7.349676423018e-13	5.937708887920e-12
514229	832040	1.275369680946e+00	2.131033362522e-01	6.380229677915e-12	-7.348717190325e-11
832040	1346269	1.275369680950e+00	2.131282332785e-01	2.466915560717e-13	2.911693256642e-12
1346269	2178309	1.275369680948e+00	2.131350491452e-01	4.579225887368e-12	2.111785332978e-12
2178309	3524578	1.275369680948e+00	2.131338880111e-01	6.142142350284e-12	-7.348717190325e-11
3524578	5702887	1.275369680948e+00	2.131396029761e-01	5.545452985700e-12	-1.180713774194e-11

Table 2.11: Critical ε_c where the folding breakdown occurs, with other observables.

that a renormalization phenomenon occurs in this bifurcation. Compare also these ratios with the ones for the smooth bifurcation, table 2.2. The smooth bifurcation has a similar ratio: −3.819646318413e-01. They agree in 5 digits! We will explore this coincidence at the end of the chapter.

Numerator	Denominator	Ratio convergence	Aitken's accel.
55	89	-1.785895970348e+00	1.275162244534e+00
89	144	-3.760507629195e-01	1.275368559504e+00
144	233	-3.845922927548e-01	1.275369505272e+00
233	377	-3.810316593481e-01	1.275369656351e+00
377	610	-3.823277633985e-01	1.275369677339e+00
610	987	-3.818293702019e-01	1.275369680425e+00
987	1597	-3.820184122584e-01	1.275369680876e+00
1597	2584	-3.819464726728e-01	1.275369680891e+00
2584	4181	-3.819740131899e-01	1.275369680853e+00
4181	6765	-3.819601904780e-01	1.275369681007e+00

Table 2.12: In the second column there is the q_n denominators of the partial convergents used to compute the third and fourth columns. In the third column there is the ratios of convergence between successive critical ε_n. These ratios are computed using the formula $\frac{\varepsilon_n-\varepsilon_{n-1}}{\varepsilon_{n-1}-\varepsilon_{n-2}}$. In the fourth column there is the Aitken's acceleration of the critical ε_n corresponding to the denominator q_n. These are computed using the formula $\frac{\varepsilon_n\varepsilon_{n-2}-\varepsilon_{n-1}^2}{\varepsilon_n-2\varepsilon_{n-1}+\varepsilon_{n-2}}$.

In figure 2.20 it is shown the graphs of the Lyapunov exponent, the minimum distance function and the maximal FK eigenvalue, with respect ε. We observe that the asymptotic behaviour of both the minimum distance and the maximal FK eigenvalue are straight lines. The Lyapunov exponent seems to behave as a straight line, but at a distance of 10^{-7} of the predicted breakdown, it turns down. This "*turn down*" phenomenon is observed in all the partial convergents computed. If we delete in the computation outputs of the asymptotics these turn downs, and we check the Lyapunov exponent, we obtain table 2.13, where it is shown the values of the ε where the maximum Lyapunov exponent is attained, and its value. We observe that these values converge.

Figure 2.21 shows several curves with their invariant bundles, for several values of ε, near the folding breakdown. Note that, as in the non-smooth breakdown, the invariant bundles collide in a non-smooth manner: the minimum distance between them goes to zero, while the maximum distance stays far from zero. Note also that maximum slope of the invariant curves increases as ε goes to ε_c. Figure 2.22 shows the graph of the first derivative of a curve near the breakdown, and also the graph, with respect ε, of the maximum, in absolute value, of the first and second derivatives.

Now, we check the asympotic behaviour of the minimum distance function between the invariant bundles and the maximal FK eigenvalue for all the partial convergents with denominator between 700 and 6000000, near the folding breakdown, using the `fit` utility in

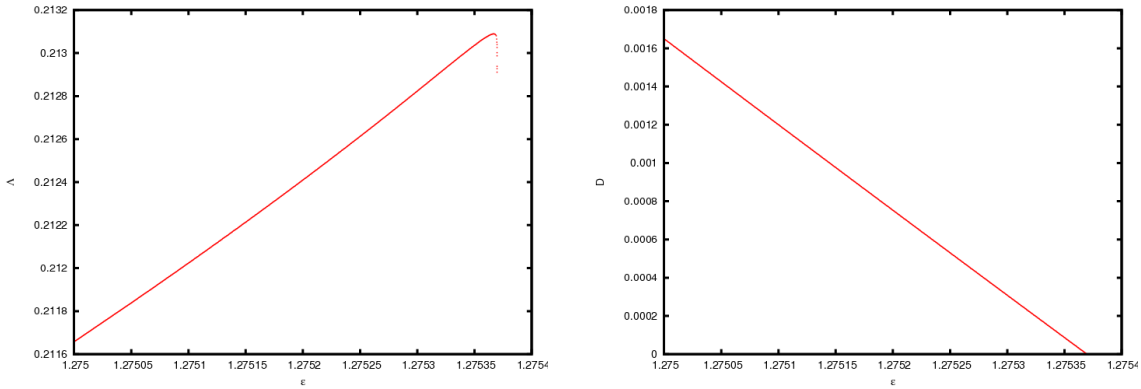

(a) Lyapunov exponent.

(b) Minimum distance function.

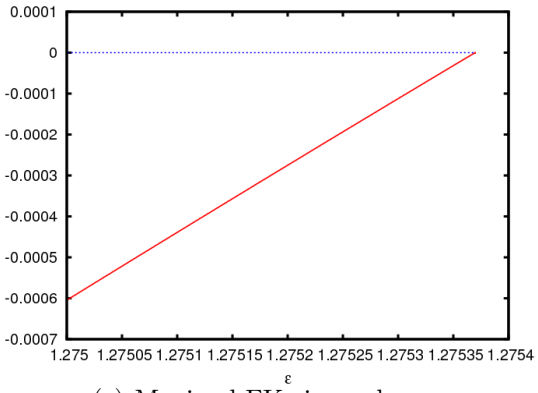

(c) Maximal FK eigenvalue.

Figure 2.20: Observables values along the continuation of the FHIT, for $\omega_n = \frac{46368}{75025}$, with respect ε.

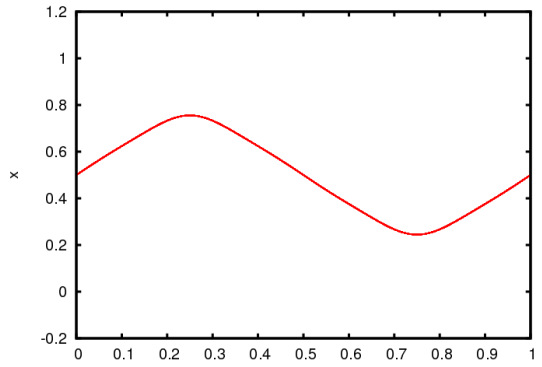

(a) $\kappa = 1.05$, $\varepsilon = 1$.

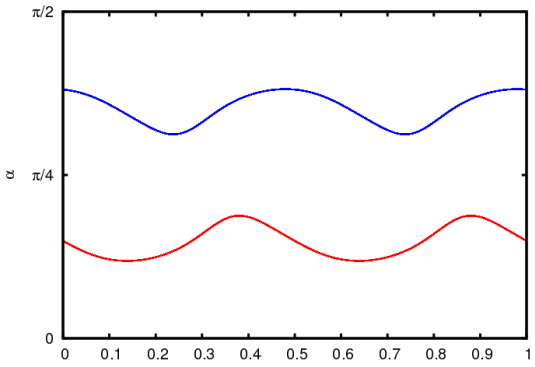

(b) $\kappa = 1.05$, $\varepsilon = 1$.

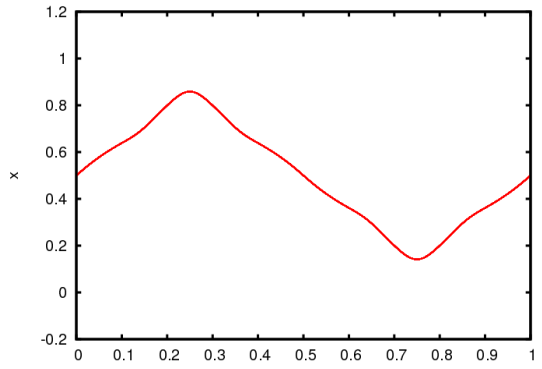

(c) $\kappa = 1.05$, $\varepsilon = 1.2$.

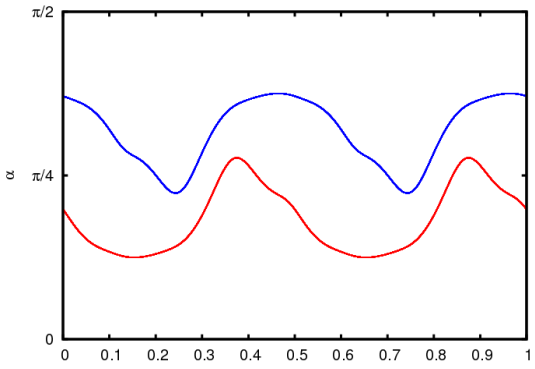

(d) $\kappa = 1.05$, $\varepsilon = 1.2$.

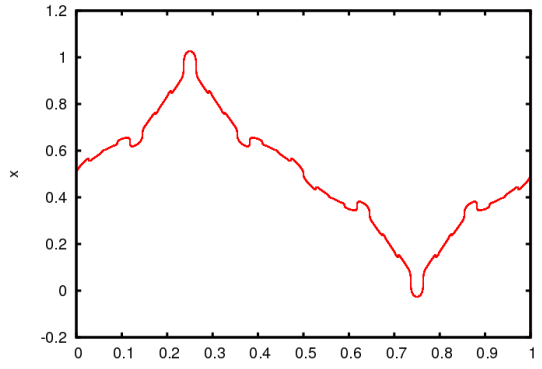

(e) $\kappa = 1.05$, $\varepsilon = 1.275$.

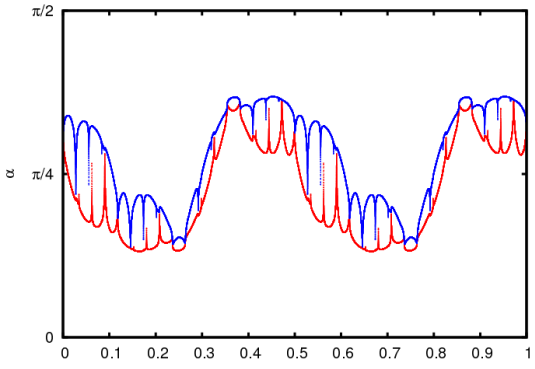

(f) $\kappa = 1.05$, $\varepsilon = 1.275$.

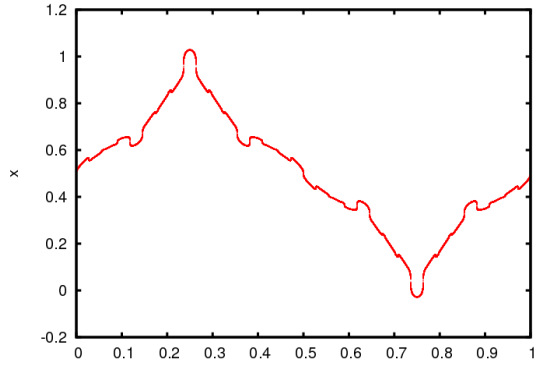

(g) $\kappa = 1.05$, $\varepsilon = 1.27536$.

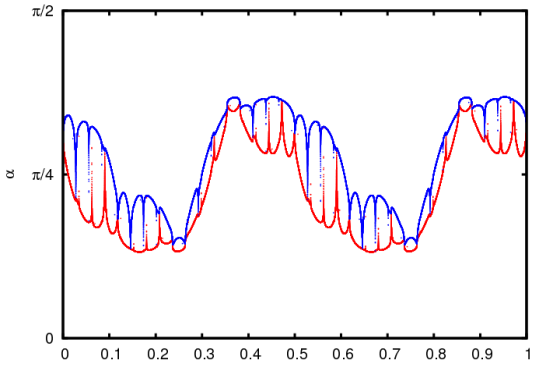

(h) $\kappa = 1.05$, $\varepsilon = 1.27536$.

Figure 2.21: Invariant curves (left) and their invariant bundles (right) with $\omega_n = \frac{46368}{75025}$, near the folding breakdown.

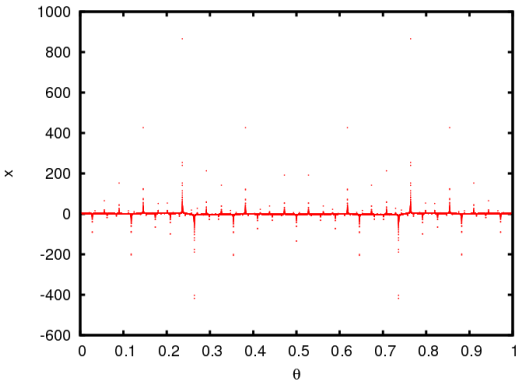

(a) First derivative of the invariant curve near the folding breakdown, at $\kappa = 1.05$, $\varepsilon = 1.2753$.

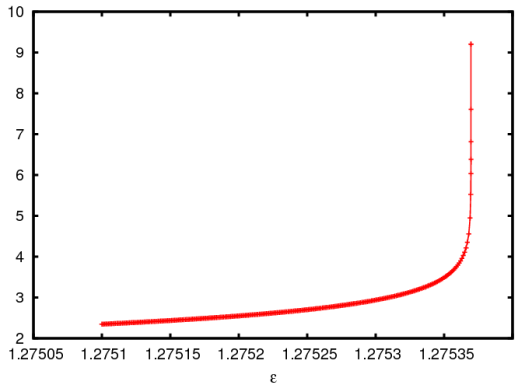

(b) Maximum first derivative graph, with respect ε, near the folding breakdown. The y axis is in $\log_{10}$ scale.

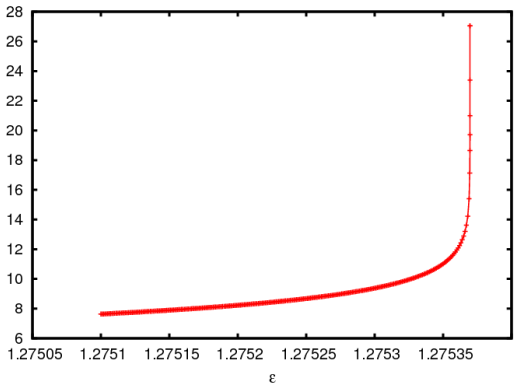

(c) Maximum second derivative graph, with respect ε, near the folding breakdown. The y axis is in $\log_{10}$ scale.

Figure 2.22: Several observables of the slope of the invariant curves near the folding breakdown for $\omega_n = \frac{46368}{75025}$.

Numerator	Denominator	ε_c	Lyapunov exponent (Λ_{max})
610	987	1.275083958017e+00	2.108429272589e-01
987	1597	1.275204213745e+00	2.115915668887e-01
1597	2584	1.275159345875e+00	2.112945336131e-01
2584	4181	1.275311766260e+00	2.124532060962e-01
4181	6765	1.275335002973e+00	2.126878887107e-01
6765	10946	1.275326254133e+00	2.125960450347e-01
10946	17711	1.275357100737e+00	2.129479723452e-01
17711	28657	1.275362058471e+00	2.130159603950e-01
28657	46368	1.275360180282e+00	2.129895177453e-01
46368	75025	1.275366854014e+00	2.130893283669e-01
75025	121393	1.275367953197e+00	2.131081071591e-01
121393	196418	1.275367535275e+00	2.131008283938e-01
196418	317811	1.275369032450e+00	2.131281047798e-01
317811	514229	1.275369282852e+00	2.131331570864e-01
514229	832040	1.275369187468e+00	2.131312030813e-01
832040	1346269	1.275369530475e+00	2.131384884700e-01
1346269	2178309	1.275369588334e+00	2.131398235506e-01
2178309	3524578	1.275369566264e+00	2.131393079536e-01
3524578	5702887	1.275369645795e+00	2.131412232005e-01

Table 2.13: Critical ε_c where the maximum Lyapunov exponent is attained.

`gnuplot`.

Remark 2.4.3. We do not report here the asympotic behaviour of the Lyapunov exponent because we have not succeed in it, but we have checked that it does not behave as a straight line nor a square root.

For the minimum distance function, see table 2.14, we fit it by

$$D = b(\varepsilon_c - \varepsilon),$$

where D represents the distance function and ε_c the parameter when the breakdown occurs. We have fitted the unknowns b and ε_c.

For the maximal FK eigenvalue, see table 2.15, we fit it by

$$\lambda_{max} = b(\varepsilon_c - \varepsilon),$$

where λ_{max} represents the maximal FK eigenvalue and ε_c the parameter when the breakdown occurs. We fit the unknowns b and ε_c.

Observe that for both fits, the ε_c output of the fittings are quite close, 10^{-5}, to the predicted ones in table 2.13.

2.4.2 After the breakdown

We continue, for several partial convergents $\omega_n = \frac{p_n}{q_n}$, the periodic orbits and observe that after the folding breakdown, see figure 2.23, they seem to lie in non-continuous graphs. Note

Numerator	Denominator	ε_c	b
610	987	1.275367829229	4.463266843647
987	1597	1.275369536726	4.463704574507
1597	2584	1.275368900023	4.463256748918
2584	4181	1.275369130518	4.463658585980
4181	6765	1.275369041732	4.463518677682
6765	10946	1.275369081206	4.463471195378
10946	17711	1.275369064192	4.463524474433
17711	28657	1.275369075722	4.463412797824
28657	46368	1.275369070598	4.463468509886
46368	75025	1.275369065080	4.463582934842
75025	121393	1.275369155710	4.460062859984
121393	196418	1.275369085165	4.462876191439
196418	317811	1.275369269885	4.453430397976
317811	514229	1.275369252625	4.453079249422
514229	832040	1.275369260816	4.453132010334
832040	1346269	1.275369227714	4.453108188694
1346269	2178309	1.275369220222	4.453186851665
2178309	3524578	1.275369223086	4.453154179539
3524578	5702887	1.275369213184	4.453279780334

Table 2.14: Asymptotic results for the minimum distance function with fixed $c = 1$.

Numerator	Denominator	ε_c	b
610	987	1.275367445362	-1.634832182121
987	1597	1.275369142326	-1.635098982192
1597	2584	1.275368519395	-1.634829330986
2584	4181	1.275368736620	-1.635070297522
4181	6765	1.275368652437	-1.634986350489
6765	10946	1.275368693651	-1.634958109968
10946	17711	1.275368674751	-1.634989921593
17711	28657	1.275368690177	-1.634923147442
28657	46368	1.275368683110	-1.634956475394
46368	75025	1.275368673622	-1.635024859910
75025	121393	1.275368678483	-1.634990518571
121393	196418	1.275368678595	-1.634990523948
196418	317811	1.275368683660	-1.634956536199
317811	514229	1.275368673415	-1.635024823993
514229	832040	1.275368673409	-1.635024821106
832040	1346269	1.275368678563	-1.634990539575
1346269	2178309	1.275368678563	-1.634990515450
2178309	3524578	1.275368678567	-1.634990502790
3524578	5702887	1.275368678564	-1.634990524231

Table 2.15: Asymptotic results for the maximal FK eigenvalue with fixed $c = 1$.

also that discontinuites are also present in the invariant bundles. The periodic orbits showed in figure 2.23 have, as θ coordinates, $\theta_k = 0 + k\omega_n$, $k = 0, \ldots, q_n - 1$.

Remark 2.4.4. The plots in figure 2.23 show that, for different values of ω_n, the periodic orbits resemble each other but, if for a fixed partial convergent ω_n, the graph has a discontinuity then, due to the periodicity of the skew product, it has q_n discontinuities. This implies that the number of discontinuities differ for different partial convergents.

In the pictures of figure 2.23 we observe that in some of the discontinuities it seems that there is a middle point between the extrema of the discontinuities, see figure 2.24 for a magnification of this phenomena. If, for these computations, there is an invariant curve and we continue these periodic points, which are computed for $\theta_0 = 0$, with respect θ_0, then we must obtain a closed curve. These continuations, with respect θ_0, are shown in figures 2.25 and 2.26. As we observe in these figures, the continuation of the periodic orbits with respect the parameter θ_0 leads to a closed curve, which is invariant, but it is not a graph of a function with respect θ: it has turnings. As we mentioned above, if there is a turning then, due to the periodicity of the system, the number of turnings must be a multiple of q_n. Also, as we observe in figures 2.25 and 2.26, as it is increased the denominator q_n of the partial convergent, it is obtained a sequence of invariant curves which are close to each other. This leads to conjecture that, as q_n goes to infinity, these converge, in the Hausdorff sense, to an invariant object, which cannot be the graph of a measurable function, see remark 1.1.5 in chapter §1.

Remark 2.4.5. From figures 2.25 and 2.26 we can observe that the width of the turnings does not depend on the denominator q_n. See also figure 2.27, where it is shown a superposition of three turnings for three different partial convergents. This implies that for a fixed θ_0, as q_n increases, the number of points on the folding curve, with θ cordinate equal θ_0, increases (without upper bound).

Remark 2.4.6. The computation of the continuation method of the periodic orbits with respect θ_0, for low values of the denominator q_n, is quite simple and the classical continuation method, see [Sim90], can be used. For moderate values of q_n, for example 6765 and above, the classical continuation method does not work, due to huge amount of memory required, hence we perform the continuation using the Newton's method explained in chapter 5. The initial seed used for the computation of the periodic orbit at $\theta_0 + \Delta$ is the periodic orbit at θ_0. To compute the turnings of the curves, we also use the information of the curvatures of the periodic points with respect the parameter θ_0 at three consecutive values of it.

As pointed in remark 2.4.6, we can only compute using the classical continuation method, the folding curves for low values of the period q_n. For all q_n between 55 and 377 we have computed the folding curves, continuing form $\theta = 0$ to $\theta = 1$. With these computations, we also compute the parameterization of the folding curves with respect the arclength, see figure 2.28. Note that the arclength of the curves increases as q_n increases. See table 2.16 for the arclength of the folding curves for these partial convergents.

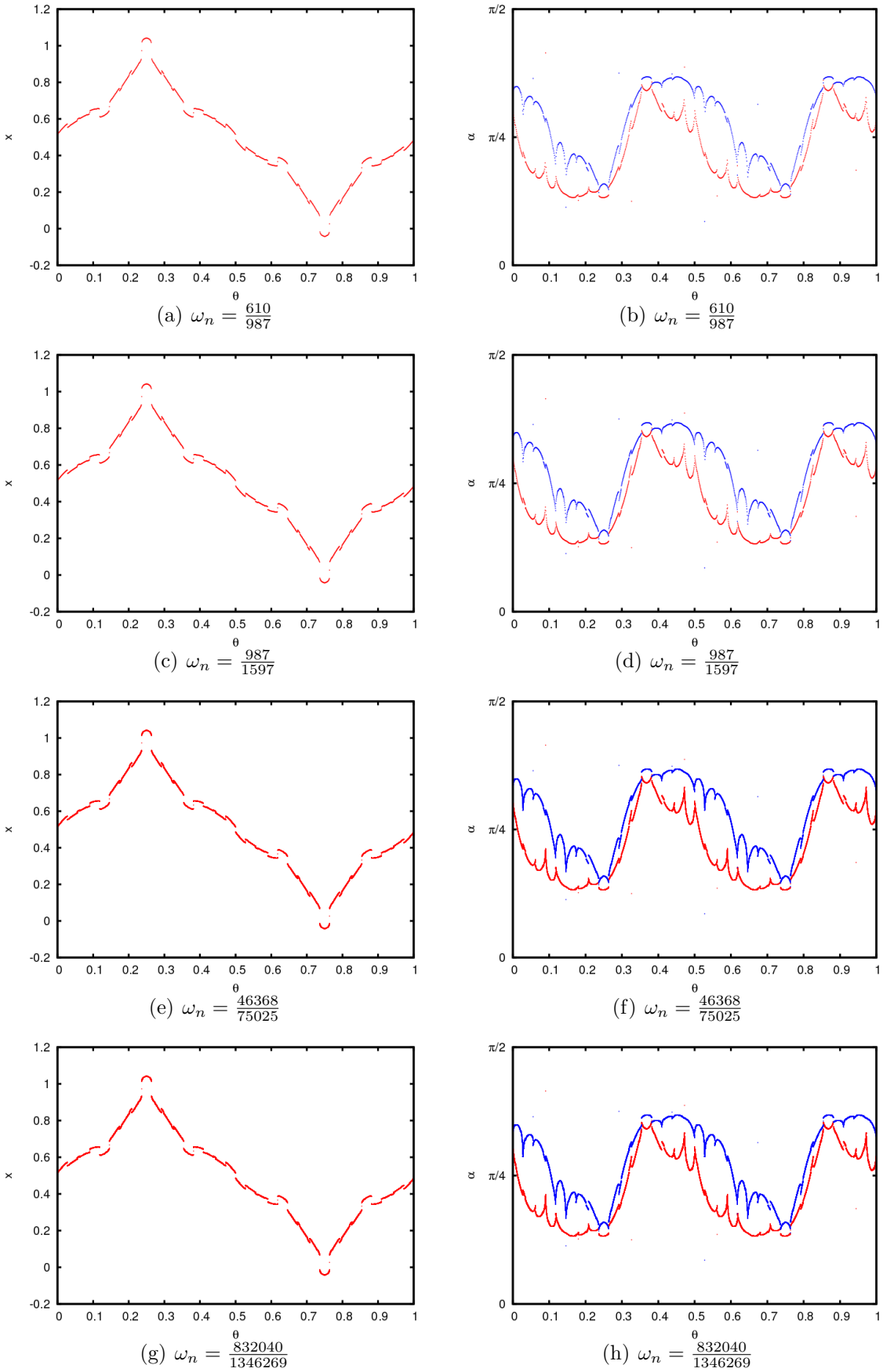

(a) $\omega_n = \frac{610}{987}$ (b) $\omega_n = \frac{610}{987}$

(c) $\omega_n = \frac{987}{1597}$ (d) $\omega_n = \frac{987}{1597}$

(e) $\omega_n = \frac{46368}{75025}$ (f) $\omega_n = \frac{46368}{75025}$

(g) $\omega_n = \frac{832040}{1346269}$ (h) $\omega_n = \frac{832040}{1346269}$

Figure 2.23: Periodic orbits (left) and their invariant bundles (right), with different rational approximation. The parameters are $\kappa = 1.05$, $\varepsilon = 1.28$ and $\theta_0 = 0$.

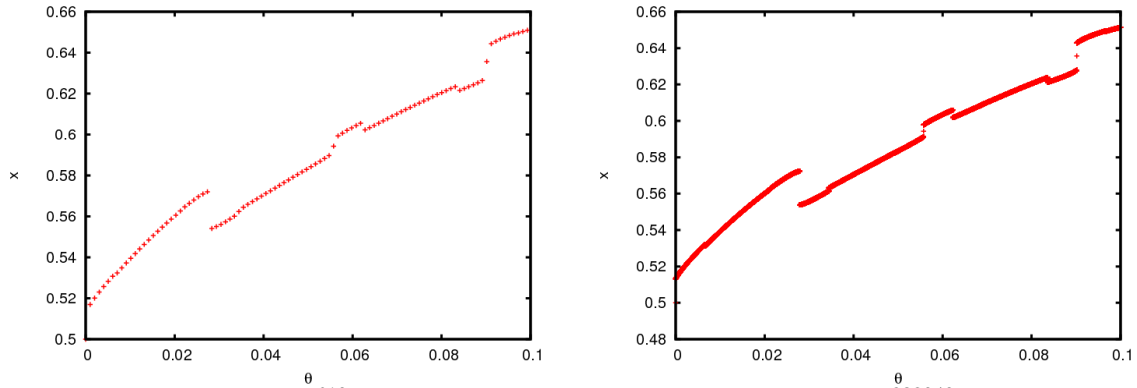

(a) $\omega_n = \frac{610}{987}$ (b) $\omega_n = \frac{832040}{1346269}$

Figure 2.24: Magnification of the periodic orbits for some of the partial convergents showed there. The parameters are $\kappa = 1.05$, $\varepsilon = 1.28$ and $\theta_0 = 0$.

Numerator	Denominator	Arclength
21	34	3.063197728351e+00
34	55	4.120121806595e+00
55	89	4.504743647041e+00
89	144	4.304636200438e+00
144	233	7.031692452759e+00
233	377	9.590577699228e+00

Table 2.16: Arclength of the folding curves for different $\omega_n = \frac{p_n}{q_n}$ for the parameter values $\kappa = 1.05$ and $\varepsilon = 1.28$.

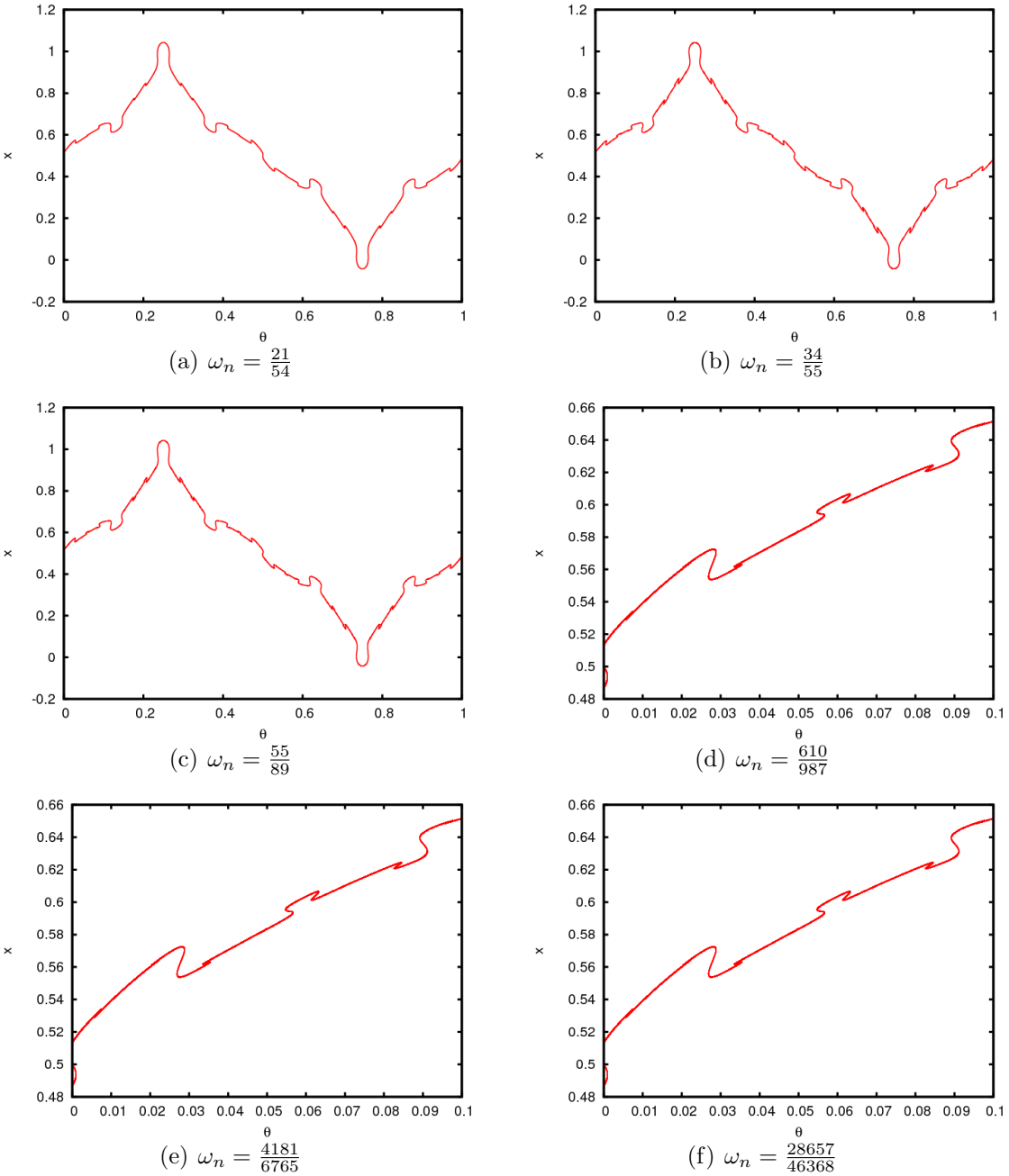

(a) $\omega_n = \frac{21}{54}$ (b) $\omega_n = \frac{34}{55}$

(c) $\omega_n = \frac{55}{89}$ (d) $\omega_n = \frac{610}{987}$

(e) $\omega_n = \frac{4181}{6765}$ (f) $\omega_n = \frac{28657}{46368}$

Figure 2.25: Folding curves computed for several partial convergents for the parameter values $\kappa = 1.05$ and $\varepsilon = 1.28$.

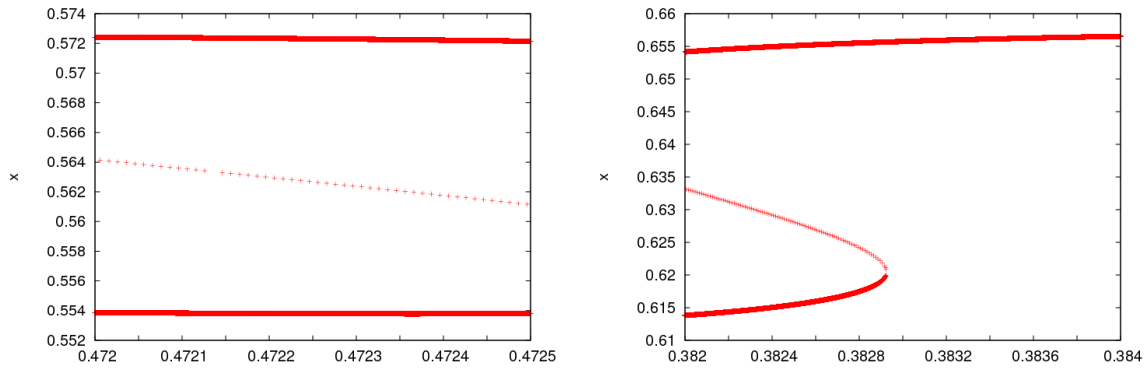

(a) $\omega_n = \frac{832040}{1346269}$ (b) $\omega_n = \frac{832040}{1346269}$

(c) $\omega_n = \frac{3524579}{5702887}$ (d) $\omega_n = \frac{5702887}{9227465}$

Figure 2.26: Folding curves computed for several partial convergents for the parameter values $\kappa = 1.05$ and $\varepsilon = 1.28$.

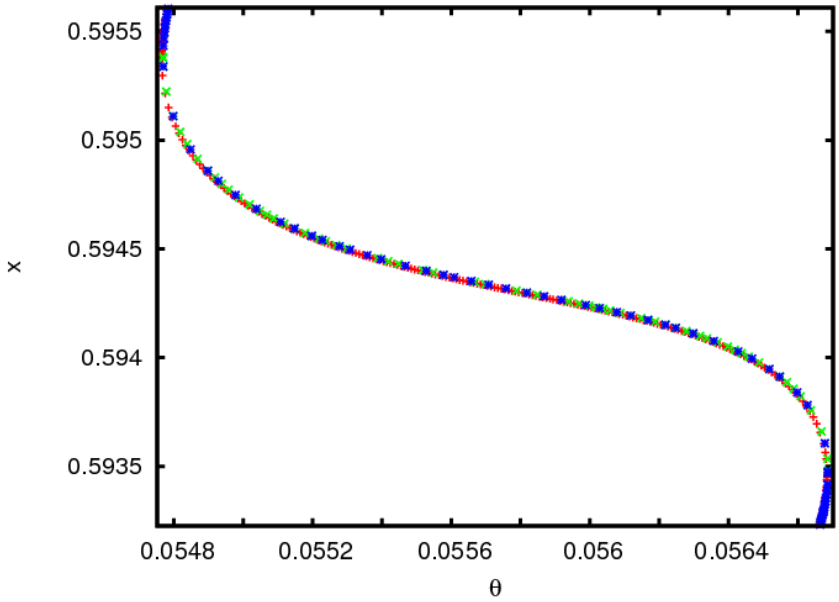

Figure 2.27: Magnification of a superposition of three folded curves for the partial convergents $\frac{610}{987}$ (red), $\frac{4181}{6765}$ (green) and $\frac{28657}{46368}$ (blue). Note that the width of the three turnings are almost the same.

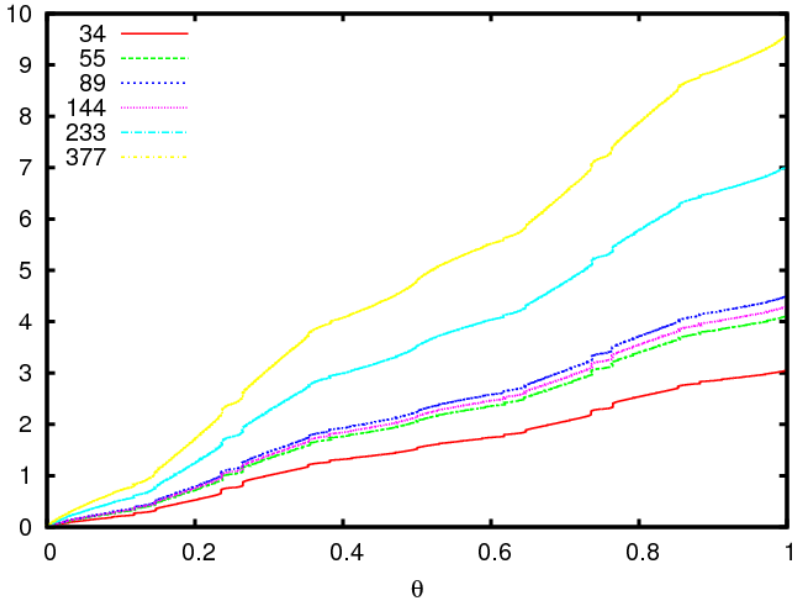

Figure 2.28: Graphs of the arclenght (y axis) with respect θ for different values of $\omega_n = \frac{p_n}{q_n}$.

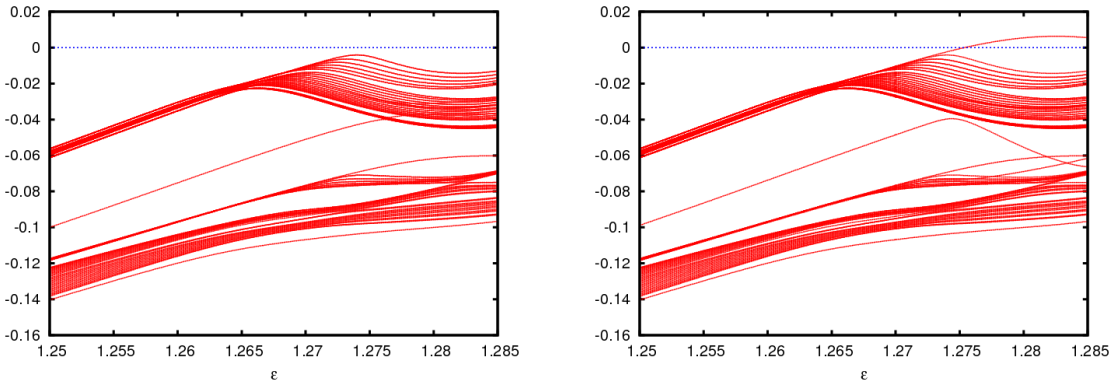

(a) $\theta_0 = 0$. (b) $\theta_0 = \frac{1}{2 \cdot 987}$.

Figure 2.29: 10% of the FK spectrum $\kappa = 1.05$ with respect ε, computed for the partial convergent $\omega_n = \frac{610}{987}$ and with different θ_0.

In terms of the stability properties of the periodic orbits, as stationary solutions of the gradient flow (2.4), we observed that it depends on the θ_0 that we choose to compute the periodic orbit. Figure 2.29 shows the biggest 10% of the FK spectrum for two different θ_0. Note that for $\theta_0 = 0$ all the spectrum lies on the negative axis, while for $\theta_0 = \frac{1}{2q_n}$ there is some part of the spectrum on the postive real axis. We performed this computation for several rational approximations and observed the same phenomenon for each of them. Also, we observed that the number of positive eigenvalues of the FK spectrum, for $\theta_0 = \frac{1}{2q_n}$, is the integer part of $\frac{N}{q_n}$, where $N \times N$ are the dimensions of the tridiagonal matrix used as an approximation of the discrete Schrödinger operator, the linear part of the gradient flow, used to compute the stability of the periodic point.

The numerical computations explained during this section suggest that, for a fixed rational approximation ω_n, the creation of the folding curves can be explained as follows: Before the folding breakdown, all the periodic points have their FK spectrum at the negative real axis, so all of them are attracting fixed points of the gradient flow. After the breakdown, some of the periodic orbits have some part of the FK spectrum positive, while other periodic orbits have all the FK spectrum negative. This suggests that, for a fixed θ_0, there is a bifurcation from one periodic orbit to three periodic orbits, one of them with positive FK spectrum. In conclusion, for a fixed θ_0 and rational approximation ω_n, the folding bifurcation can be read as a pitchfork bifurcation of an attracting fixed point of the gradient flow. Also, we conjecture that the invariant object, that is the Hausdorff limit of the folding curves for rational convergents, is a pitchfork bifurcation of the gradient flow for the irrational rotation ω.

Folding breakdown in other skew products:

We also explored other skew products than the one worked in this chapter and we found

that there are also folding bifurcations in other 2D skew products. For example, we explored the quasiperiodic standard map forced with other perturbations of θ, like

$$\begin{cases} \bar{x} &= x + \bar{y} \\ \bar{y} &= y - \dfrac{\kappa}{2\pi}\sin(2\pi x) - \varepsilon\left(\sin(2\pi\theta) + 0.1\sin(4\pi\theta)\right) \\ \bar{\theta} &= \theta + \omega \pmod 1 \end{cases} .$$

For this example, with $\kappa = 0.8$, there are folding curves. Figure 2.30 shows a picture for one of these foldings.

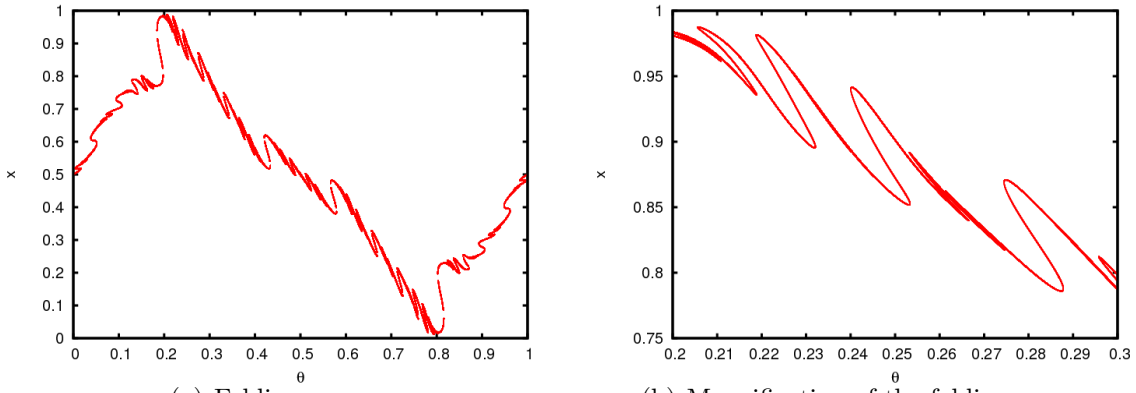

(a) Folding curve. (b) Magnification of the folding curve.

Figure 2.30: Folding curve for $\omega_n = \frac{610}{987}$. The parameter values are $\kappa = 0.8$ and $\varepsilon = 1.27$.

Also, we explored the quasiperiodic standard map with two frequencies

$$\begin{cases} \bar{x} &= x + \bar{y} \\ \bar{y} &= y - \dfrac{\kappa}{2\pi}\sin(2\pi x) - \varepsilon\left(\sin(2\pi\theta_1) + \sin(2\pi\theta_2)\right) \\ \bar{\theta_1} &= \theta_1 + \omega_1 \pmod 1 \\ \bar{\theta_2} &= \theta_2 + \omega_2 \pmod 1 \end{cases} ,$$

and found that, for $\omega_1 = \sqrt{2} - 1$, $\omega_2 = \sqrt{3} - 1$, $\kappa = 0.7$ and $\varepsilon = 0.772$, there exists a folding torus. See figure 2.31 for a visual example of it. Note that there are holes in the torus, which means that there has been a folding breakdown of it.

We suspect that, generically, the folding bifurcation occurs in all skew products that has a gradient flow associated to it. We plan in the future to attack this problem.

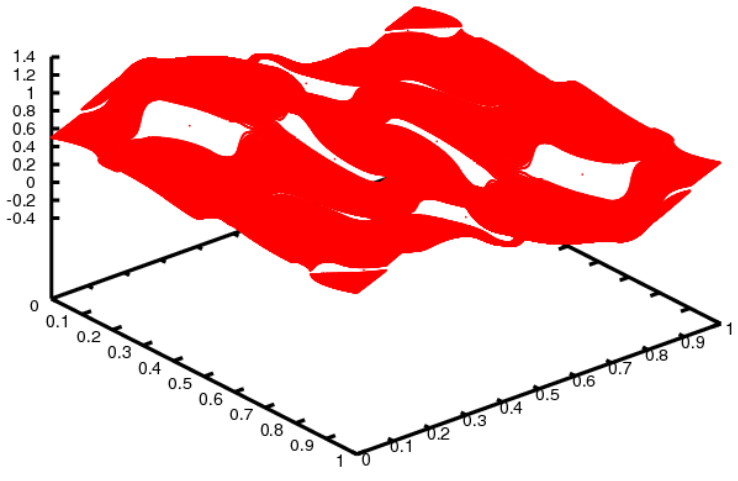

Figure 2.31: Invariant torus with two frequencies computed with rational approximation of the rotation vector $\left(\frac{485269}{1171543}, \frac{857629}{1171543}\right)$, and with parameter values $\kappa = 0.7$ and $\varepsilon = 0.772$.

2.5 Summary

We saw in this chapter a numerical exploration of three different types of bifurcations of FHIT. In table 2.17 we summarize the breakdowns, comparing and contrasting before, at, and after the breakdown for different observables.

Before breakdown.

	Min dist B.	Max dist B.	Lyap. exp.	M spec	FK spec	T. smooth	B. smooth
Smooth	> 0	> 0	> 0	Thin	< 0	Yes	Yes
Non-smooth	> 0	> 0	> 0	Thin	< 0	Yes	Yes
Folding	> 0	> 0	> 0	Thin	< 0	Yes	Yes

At breakdown.

	Min dist B.	Max dist B.	Lyap. exp.	M spec	FK spec	T. smooth	B. smooth
Smooth	$= 0$	$= 0$	$= 0$	Thin	$= 0$	Yes	Yes
Non-smooth	$= 0$	> 0	> 0	Thick	$= 0$	No	No
Folding	$= 0$	> 0	> 0	Thick	$= 0$	No	No

After breakdown.

	Min dist B.	Max dist B.	Lyap. exp.	M spec	FK spec	T. smooth	B. smooth
Smooth	$= 0$	$= 0$	$= 0$	Thin	> 0	smooth	smooth
Non-smooth	> 0	> 0	> 0	?????	< 0	non-mes	non-mes
Folding	> 0	> 0	> 0	Thin	> 0	non-mes	non-mes

Table 2.17: Summary of the observables behaviour of the three different breakdowns. The first column is the minimum distance between the invariant bundles, the second one is the maximum distance between invariant bundles, the third is the Lyapunov exponent, the fourth is the M spectrum, the fifth is the FK spectrum, the sixth is the smoothness of the invariant curve, and the seventh is the smoothness of the invariant bundles.

We computed the region, in the 2 parameter space (ε, κ), where there exists a FHIT. This is shown in figure 2.32. We highlight some parts of the figure. These are:

- The region **A** is the uniformly hyperbolic region, where the FHIT exists.
- The curve **B** is where the smooth bifurcation occurs. After this curve there are elliptic curves.
- The region **D** where the folding curves exists. Figure 2.33 shows a folding curve for a different κ and ε parameter values.
- The curve **E** is where the non-smooth breakdown occurs. After this curve there are no continuous invairant curves.

Remark 2.5.1. We could not characterize the type of breakdown that occurs in the curveis **C**. The numerics does not work properly on this part of the frontier and we do not have any clue of what happens there. We plan to come back to this problem on the future.

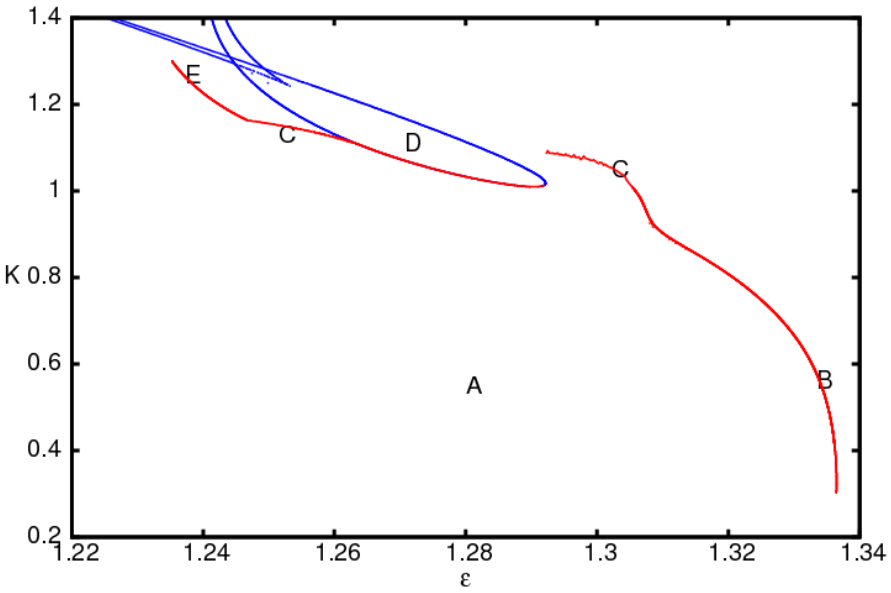

Figure 2.32: Boundary of the hyperbolic region for $\omega_n = \frac{6765}{10946}$.

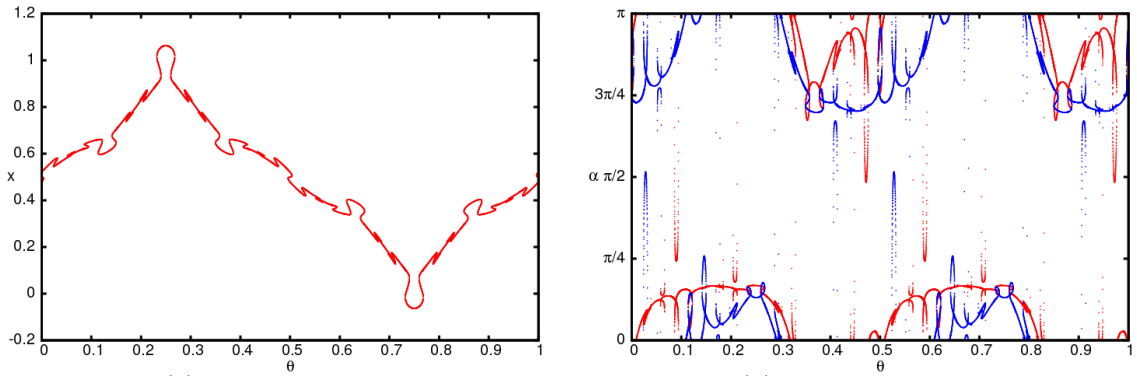

(a) Invariant curve. (b) Invariant bundles.

Figure 2.33: Invariant curve and its invariant bundles for $\omega_n = \frac{987}{1597}$. The parameter values are $\kappa = 1.102377$ and $\varepsilon = 1.272629$.

In figure 2.32 we observe that the curve **B**, smooth bifurcation, and the boundary of the region **D**, folding breakdown, are smooth. These smooth curves give some hints that a renormalization process is behind the breakdowns. Also, in the numerics described in these bifurcations, see tables 2.2 and 2.12, we observed that the Aitken's acceleration work

properly for the critical ε values, and that the ratios of the differences between successive critical ε values are similar, around -3.8196e-01. During the description of the breakdowns, we suggested that this gives some hints on a behind (but unknown) renormalization process. In order to strengthen this renormalization conjecture, we have computed, for other κ values and for both the smooth bifurcation and folding breakdown, these observables. We have obtained that for both the smooth and the folding bifurcations the Aitken's acceleration produces good estimates of the critical ε and that the ratios of the differences between successive critical ε are close to -3.8196e-01. These ratios are shown in table 2.18.

Remark 2.5.2. Note that -3.8196e-01 is close to the number $\frac{2}{\sqrt{5}+3} \simeq 3.81966011250$e-01.

Type bifurcation	κ	Ratios
Folding	1.02	-3.819608065480e-01
Folding	1.03	-3.819565612617e-01
Folding	1.07	-3.819696922783e-01
Smooth	0.4	-3.819670229269e-01

Table 2.18: Ratios of the differences between successive critical ε for different κ with different type of breakdown.

Chapter 3

The conservative fractalization route

The fractalization route is a mechanism of transition to chaos in a quasiperiodic system, in which an invariant curve gets increasingly wrinkled until it stops being a smooth curve. In this chapter we describe this mechanism in a completely different context: in quasiperiodically forced volume preserving skew products. With the help of M spectrum we unify, following the theoretical lines in [JT08], the explanation of this fractalization mechanism.

3.1 Introduction

The fractalization route was first observed in noninvertible dissipative systems in the pioneer work of Kaneko [Kan84], see also [Kan86, NK96, DRP04], where they observe that an attracting curve of the driven logistic map gradually wrinkles as the forcing parameter is increased, while no collision with other invariant object is observed. [Kan84] suggests that, as the forcing parameter is increased, there is a route from a smooth attracting curve to a Strange Nonchaotic Attractor (a non-smooth invariant object that is a minimal attractor with negative Lyapunov exponent), and then to a Strange Attractor (a non-smooth invariant object that is a minimal attractor with positive Lyapunov exponent). However, a more refined numerical exploration, see [HS05], suggests that when the Lyapunov exponent is negative there is an invariant continuous curve, and that the maximum slope of the (smooth) attracting curve increases as the Lyapunov exponent goes to zero. Hence, the *Strange Object* appears when the Lyapunov exponent reaches zero. In [HdlL07, JT08] it is suggested that a possible explanation of this breakdown phenomenon goes as follows: before the breakdown, at some value of the forcing parameter, the transfer operator associated to the invariant curve looses its invertibility: its M spectrum is a disk, with its radius the Lyapunov multiplier. Then, as the forcing parameter is increased, the M spectrum approaches the unit circle (the Lyapunov exponent goes to zero), meanwhile, the attracting curve is smooth but its maximal slope increases as the forcing parameter increases. The breakdown is produced when the M spectrum, which is a disk, collides with the unit circle. Then the smooth curve bifurcates to a Strange Object. Figure 3.1 shows a diagram of the M spectra before

and at the breakdown. After the creation of the Strange Object, if the forcing parameter is increased, ther is a Strange Attractor, SA: a minimal attractor with positive Lyapunov exponent. This means that the M spectrum is a disk with radius bigger than 1, that is, it contains the unit circle.

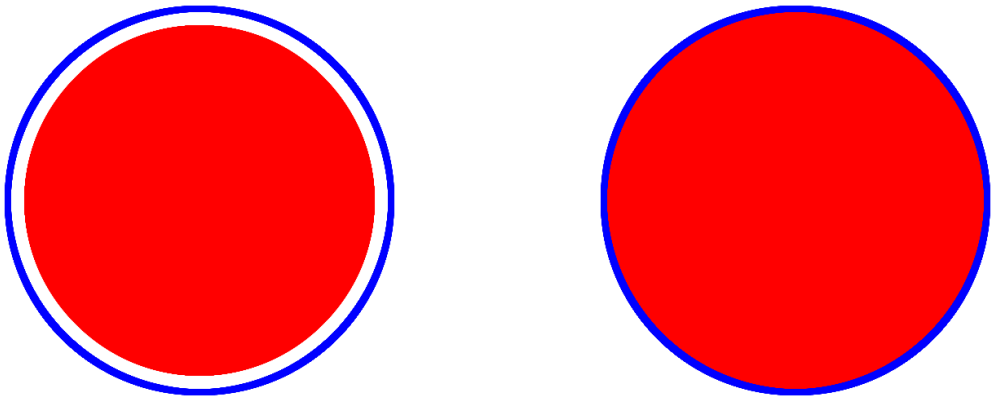

(a) Before breakdown. (b) At the breakdown.

Figure 3.1: Diagram of the M spectra for the dissipative 1D fractalization route. The unit circle is colored in blue.

The fractalization route has also been observed in dissipative higher dimensional skew product systems. For example, in quasiperiodically invertible dissipative systems, e.g. the rotating dissipative Henon map, see [SFKP96, KL04, HdlL07]. In this scenario, there is an attracting smooth curve with a 2D stable bundle. The role that plays the noninvertibility of the map, in the 1D case, is replaced by collisions of the 1D invariant subbundles (fast and slow stable subbundles). This implies that the M spectrum goes from an union of two concentric circles, when the 1D subbundles are smooth, to an annulus, when they are only measurable. Then, as the forcing value is increased, the invariant curve starts to wrinble, while the (maximal) Lyapunov exponent approaches zero. At zero Lyapunov exponent it is produced the Strange Object. This breakdown phenomenon can be interpreted, as in the case of noninvertible maps, in functional terms: the invariant curve has M spectrum an annulus with outer radius less than one before the breakdown. Then, at the breakdown the M spectrum, the annulus, has collided with the unit circle. Figure 3.1 shows a diagram of the M spectra before and at the breakdown.

In this chapter we describe a new fractalization route in a conservative 3D preserving skew product. This is the lowest dimension where it can occur. The invariant curve that we study is not an attracting curve, but a FHIT curve with stable and unstable bundles. The example goes as follows: when the forcing parameter is equal zero, the invariant curve is the graph of a constant function $K\colon \mathbb{T} \longrightarrow \mathbb{R}^3$. As the forcing parameter increases, and after several smooth transitions, the invariant curve has a 1D stable bundle and a 2D unstable bundle. The 2D unstable bundle decomposes in a continuous Whitney sum of 1D

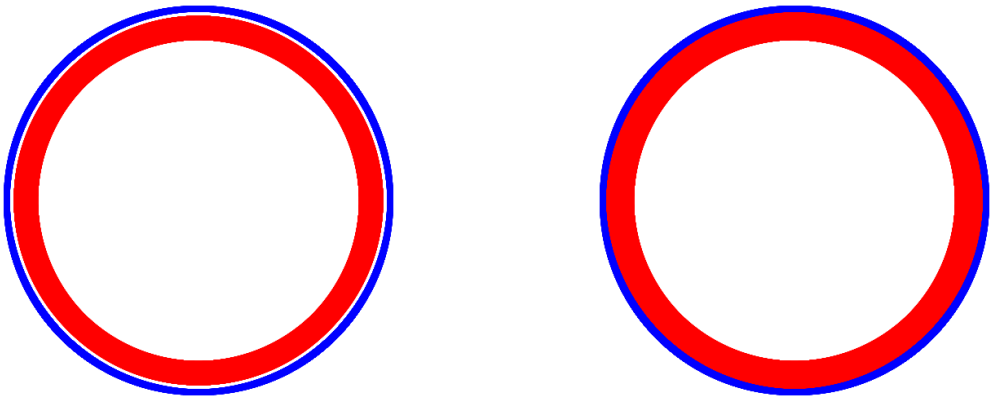

(a) Before breakdown. (b) At the breakdown.

Figure 3.2: Diagram of the M spectra for the dissipative 2D fractalization route. The unit circle is colored in blue.

subbundles (fast and slow unstable subbundles). This means that the M spectrum is an union of three circles, two of them with radius bigger than one. At some value of the forcing parameter, the two 1D unstable subbundles collide, forming a nonreducible 2D unstable bundle, which is the Whitney sum of two measurable non-continuous subbundles. Now, the M spectrum is the union of a circle, with radius less than one, with a thick annulus outside the unit circle. Then, as the forcing parameter is increased, the invariant curve starts to wrinkle, while the medium Lyapunov exponent, which is associated to the slow (measurable) unstable subbundle, goes to zero. The maximal and minimal Lyapunov exponents stay far from zero, hence the annulus part of the M spectrum has collided with the unit circle. Also, we observe that the distance between the stable and unstable bundles stays far from zero.

With the help of the numerical example presented in this chapter, and the theoretical arguments described above, we want to streghten the theoretical explanation of the fractalization route, which unifies both dissipative and conservative cases. To sum up, the fractalization route is a consequence of the collision, with the unit circle, of some annular part of the M spectrum. In this situation, the condition of fiberwise hyperbolicity fails and the torus can not be continued nor smoothly bifurcate.

Remark 3.1.1. We want to point out that the lowest dimension of a conservative skew product where the fractalization route could happen is three. This is because to have this type of breakdown, some part of the M spectrum must need to be an annulus. In one dimensions, the M spectrum is a full disk, so the skew product is not invertible along the curve. In two dimensions, if the M spectrum is an annulus and the invariant curve is FHIT, then it lies inside (resp. outside) the unit circle, which implies that the skew product is dissipative (resp. expansive).

We want to finish by comparing and contrasting the numerics used in this chapter. In the dissipative case, the classical method used in the literature, see e.g. [Kan84, Kan86,

NK96, DRP04, HdlL07, JT08, HS05], to compute attracting invariant curves is the iteration method; while in the conservative case, the computation that we perform is using the periodic orbits method, see chapter §5. As it is observed in [HS05, JT08], the iteration method has a big disadvantage: near the breakdown the invariant curve has big local expansion rates at some points and, due to the finite precision of the computations, the numerics generates bad approximations of the attracting sets. Without care, this generates false Strange sets instead of smooth curves. In the other hand, the computations of the hyperbolic curves done in this chapter does not suffer this pathology. This is because the periodic orbits method does not require the iteration of any map, so there are no possible local expansions nor accumulation of errors due to the finite precision of the computations.

Remark 3.1.2. In [CS10] they show how critical can be the computation of invariant curves using the classical iteration method. They compute an attracting curve in a quasiperiodically forced logistic map that, if the computations are performed in `double` precision, then the numerics gives as a result an (incorrect) strange set, but if the computations are performed in multiprecision arithmetics, then they obtain an extremely smooth and mild curve.

Remark 3.1.3. All the computations shown throughout the chapter has been done for every partial convergent less than 10^7. We compared them and obtained that there are no significant differences. Hence, when we show a computation, we fix a partial convergent but the results are not significantly altered if we change the rational approximation.

3.2 The studied model

The quasiperiodic nonlinear volume preserving system that we focus on is

$$\begin{cases} \bar{x} &= \dfrac{\kappa_1}{2\pi}\sin(2\pi x) + \dfrac{\kappa_2}{2\pi}\sin(2\pi y) + z - \varepsilon\sin(2\pi\theta) \\ \bar{y} &= x \\ \bar{z} &= y \\ \bar{\theta} &= \theta + \omega \pmod 1 \end{cases}, \tag{3.1}$$

where $\omega = \dfrac{1-\sqrt{5}}{2}$ is the inverse of the golden mean. We fix $\kappa_1 = 2.1$ and $\kappa_2 = 0.95$.

Remark 3.2.1. Before starting the detailed exposition of the fractalization route's example, we want to point out that we did an exploration of the skew product (3.1) for several values of the parameters κ_1, κ_2, and we found other different bifurcation phenomena: the smooth bifurcation and the non-smooth breakdown (see chapter §2 for a detailed exposition of these bifurcations in 2D skew products). We do not report them in this thesis due to the similarities with the 2D case.

The system (3.1) has the peculiarity that an invariant curve K is of the form $K(\theta) = (x(\theta), x(\theta-\omega), x(\theta-2\omega))$, where $x\colon \mathbb{T} \longrightarrow \mathbb{R}$ satisfies the functional equation

$$x(\theta+\omega) - \frac{\kappa_1}{2\pi}\sin(2\pi x(\theta)) - \frac{\kappa_2}{2\pi}\sin(2\pi x(\theta-\omega)) - x(\theta-2\omega) + \varepsilon\sin(2\pi\theta) = 0, \tag{3.2}$$

so, from now on, we will make an abuse of notation and denote by x the invariant curve.

For $\varepsilon = 0$ the system (3.1) has the constant FHIT $x(\theta) = 0$. It is a *saddle-focus*: its Lyapunov exponents are $\lambda_1 \simeq 0.95958961$ and $\lambda_2 = \lambda_3 \simeq -0.47979481$, so its stable bundle is 2D, with a complex pair of eigenvalues, and the unstable bundle is 1D. As this curve is continued via the parameter ε, it suffers several smooth transitions: some of them concerning only on the topology of its invariant bundles, others concerning its stability. To detect these transitions, we use the minimum distance between the invariant unstable and stable bundles, and the Lyapunov exponents of the 1D subbundles, see figure 3.3.

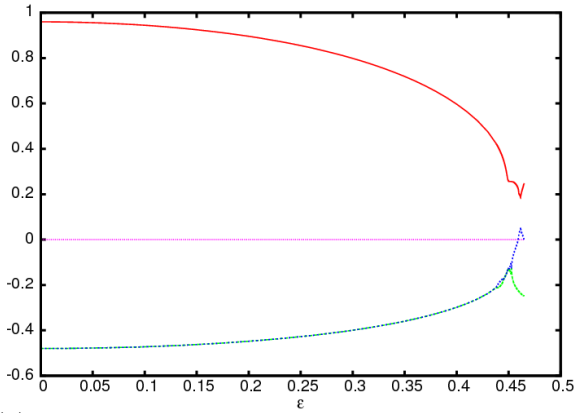

(a) Lyapunov exponents of the invariant curves, with respect to the parameter ε. The colors are: red (maximal), blue (medium), green (minimal).

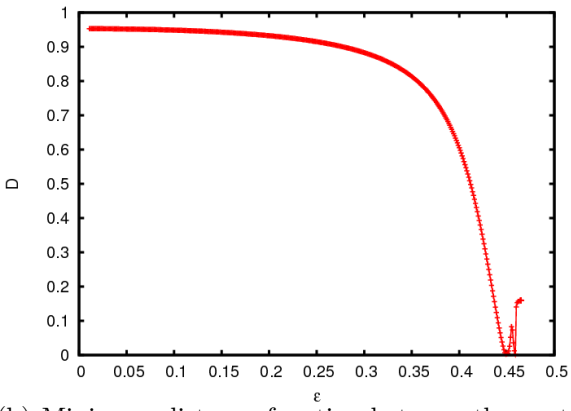

(b) Minimum distance function between the unstable and stable bundles.

Figure 3.3: Observables of the invariant curve. These are computed with partial convergent $\frac{46368}{75025}$.

The diagram of transitions can be summarized as follows:

1. From $\varepsilon = 0$ to $\varepsilon \simeq 0.459160$ the invariant curve has a 2D reducible stable bundle and 1D unstable bundle. Depending on the ε, the stable bundle is either of node-type (it decomposes into fast and slow stable subbundles) or is focus-type (it reduces to a matrix with complex conjugate eigenvalues). Figures 3.5 and 3.6 show some plots of node-type and focus-type. In figure 3.4 it is observed that the Lyapunov exponents have some open gaps. In these gaps is where the stable bundle is of node-type. In terms of the M spectrum, when the stable bundle is node-type means that the part of the spectrum associated to the bundle is the union of two circles, see subfigure 3.8(a), and when it focus-type means that the spectrum is a unique circle, see subfigure 3.8(b).

   From $\varepsilon \simeq 0.452905$ to $\varepsilon \simeq 0.459160$ the stable bundle is node-type with medium Lyapunov exponent approaching zero as ε approaches 0.459160. At this parameter value the invariant bundles has a smooth bifurcation: the slow stable subbundle bifurcates to the slow unstable subbundle.

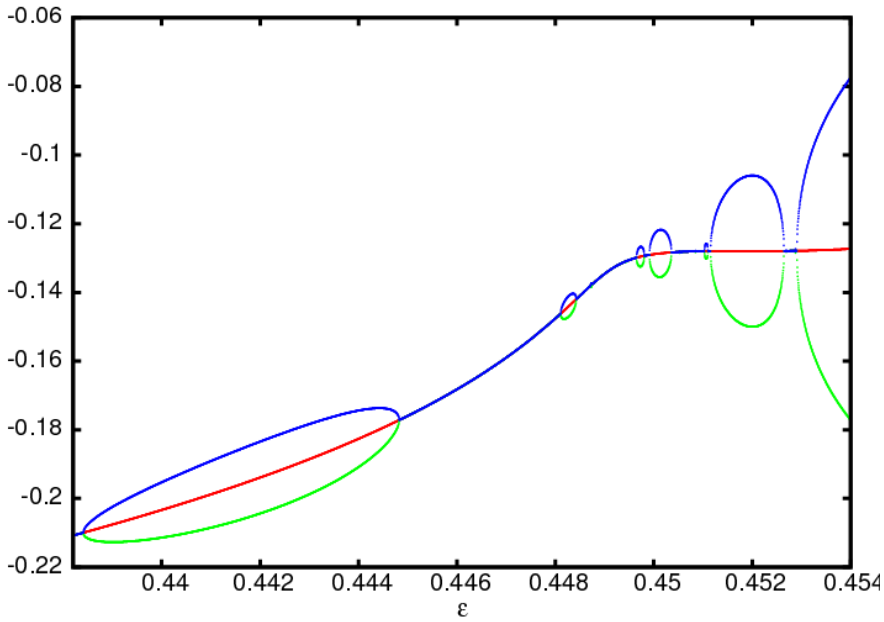

Figure 3.4: Magnification of the Lyapunov spectra for the parameter values $0.438 \leq \varepsilon \leq 0.454$. The colors are: blue (medium), green (minimal), red (the negative value of the half of the maximal exponent).

2. From $\varepsilon \simeq 0.459160$ to $\varepsilon \simeq 0.4598$ the unstable bundle is 2D reducible and the stable bundle is 1D. At $\varepsilon \simeq 0.4598$ the unstable bundle suffers a non-smooth transition: Its 1D subbundles collide in a non-smooth manner, while their Lyapunov exponents remain separated. Figure 3.7 shows this collision. This collision means that the M spectrum goes from an union of two circles, see subfigure 3.8(c), to an annulus, see subfigure 3.8(d).

3. From $\varepsilon \simeq 0.4598$ to $\varepsilon \simeq 0.4649$ the torus fractalizes: as ε increases, the invariant curve gets more wrinkled. The unstable bundle remains nonreducible, with different Lyapunov exponents, hence part of the M spectrum is an annulus. Figure 3.9 shows the invariant curve near the breakdown parameter $\varepsilon \simeq 0.4649$. The medium Lyapunov exponent goes to zero as ε increases, while the maximal and minimal Lyapunov exponents remain far from zero. This means that the M spectrum, which is an annulus, see subfigure 3.8(d), collides with the unit circle, see subfigure 3.8(e). Figure 3.10 shows the derivatives of the invariant curves near the breakdown. As ε increases the derivatives increases. See figure 3.13 for a graph in $\log_{10}$ scale of the maximum slope of the invariant curves with respect to the parameter ε. It can be observed that the maximum slope increases as the invariant curve fractalizes.

Remark 3.2.2. As it is said in the description of the bifurcation diagram, we predict that the fractalization route starts at $\varepsilon \simeq 0.4598$. Also, we compute the Medium Lyapunov

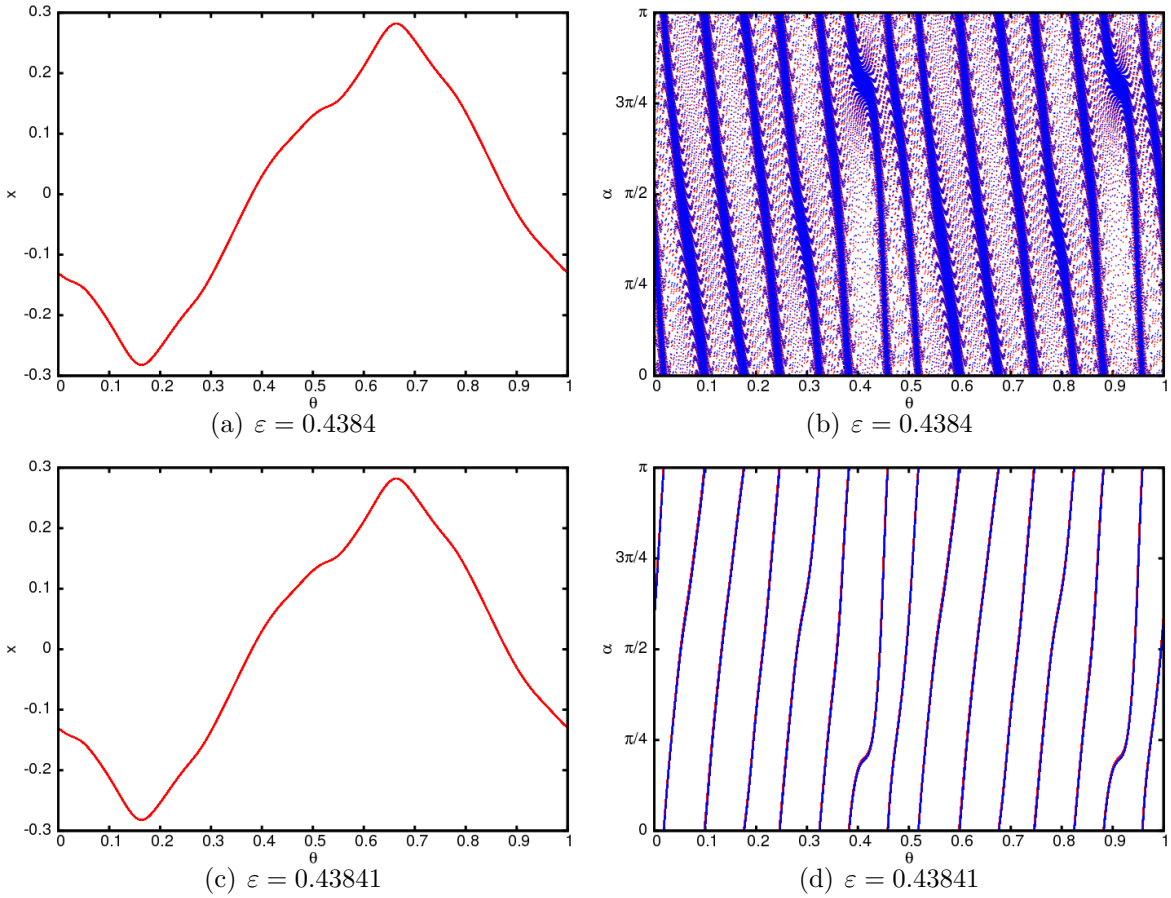

(a) $\varepsilon = 0.4384$ (b) $\varepsilon = 0.4384$

(c) $\varepsilon = 0.43841$ (d) $\varepsilon = 0.43841$

Figure 3.5: Invariant curves (left) and fast (red) and slow (blue) stable subbundles (right) for different values of ε. These are computed with partial convergent $\frac{196418}{317811}$. The fast and slow stable subbundles are plotted as a projection on the 2D stable bundle. See text for further details.

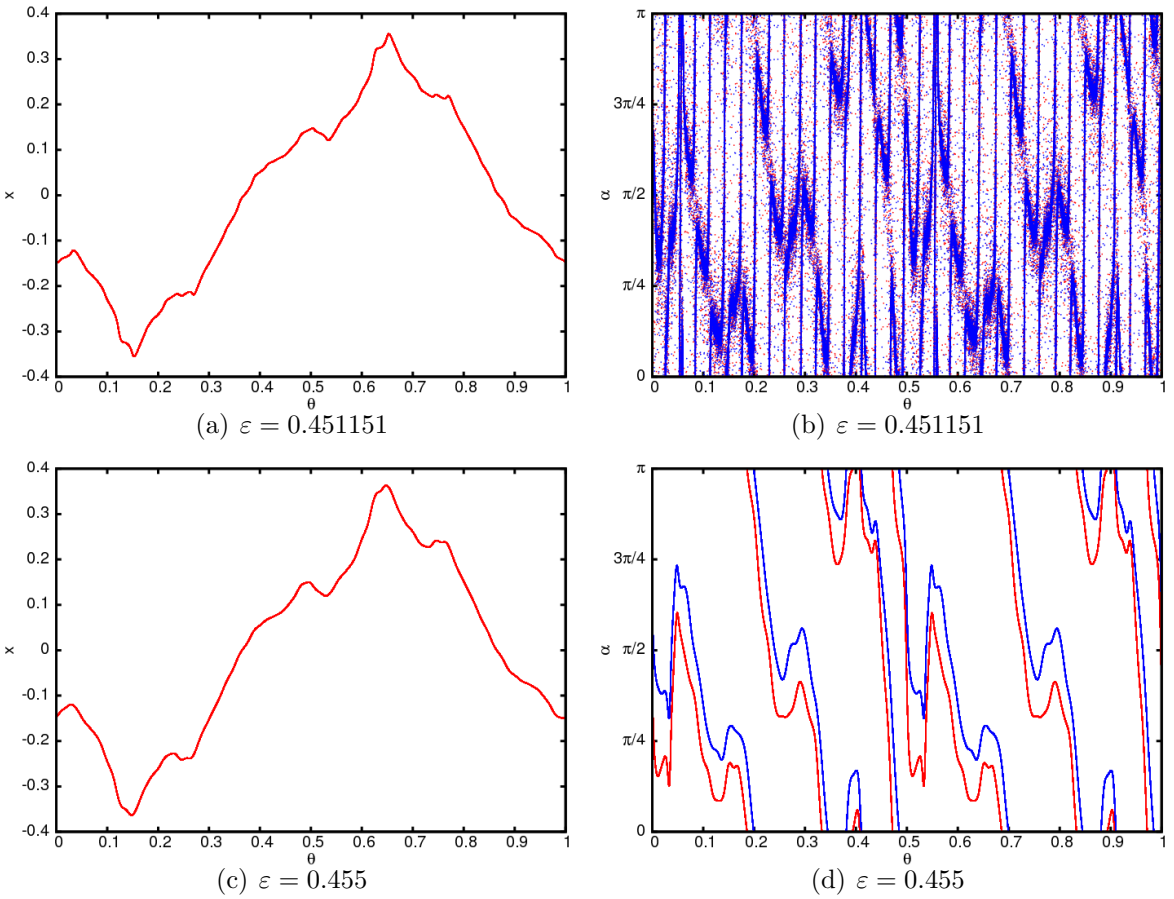

(a) $\varepsilon = 0.451151$ (b) $\varepsilon = 0.451151$

(c) $\varepsilon = 0.455$ (d) $\varepsilon = 0.455$

Figure 3.6: Invariant curves (left) and fast (red) and slow (blue) stable subbundles (right) for different values of ε. These are computed with partial convergent $\frac{196418}{317811}$. The fast and slow stable subbundles are plotted as a projection on the 2D stable bundle.

exponent's graph (see figure 3.11 for a visual example of it), for different values of the partial convergents, and checked that its behaviour is "*erratic*", which means that the curve is suffering the fractalization route, that is affecting also its regularity. Figure 3.12 shows the minimum distance function between the invariant unstable and stable bundles, with respect ε, near the breakdown. Note that this minimum distance function is always bigger than zero. This means that the invariant unstable and stable bundles do not merge. Also, we have computed several invariant curves for different values of ε near this regime (see figure 3.9) and with different partial convergents, and we have observed that as ε is increased, the wrinkle behaviour increase (although for all the parameter values ε before the non-smooth bifurcation the curves are all smooth). See also figure 3.10 for a visualization of the derivatives of the invariant curves near the breakdown.

3.3 Summary

We can summarize the fractalization breakdown with table 3.1. Compare this table with table 2.17 of the breakdowns described in chapter §2.

	Min dist B.	Max dist B.	Med. Lyap. exp.	M spec	T. smooth	B. smooth
Before breakdown	> 0	> 0	> 0	Thin	Yes	Yes
At breakdown	> 0	> 0	$= 0$	Thin	No	No

Table 3.1: Summary of the observables behaviour of the three different breakdowns. The first column is the minimum distance between the invariant bundles, the second one is the maximum distance between invariant bundles, the third is the medium Lyapunov exponent, the fourth is the M spectrum, the fifth is the smoothness of the invariant curve, and the sixth is the smoothness of the invariant bundles.

We showed in this chapter that an invariant curve with hyperbolic normal dynamics in a volume preserving skew product can fractalize as in the dissipative case. This numerical example strengthens the unified theoretical framework to understand the fractalization route in skew product systems. This framework is that, before the breakdown, there is a loosness of reducibility in an invariant bundle, which is the same that there is an annular part of the M spectrum. At the breakdown, the closest Lyapunov exponent to zero of the nonreducible invariant bundle collides with zero, which is the same that the annular part of the M spectrum collides with the unit circle.

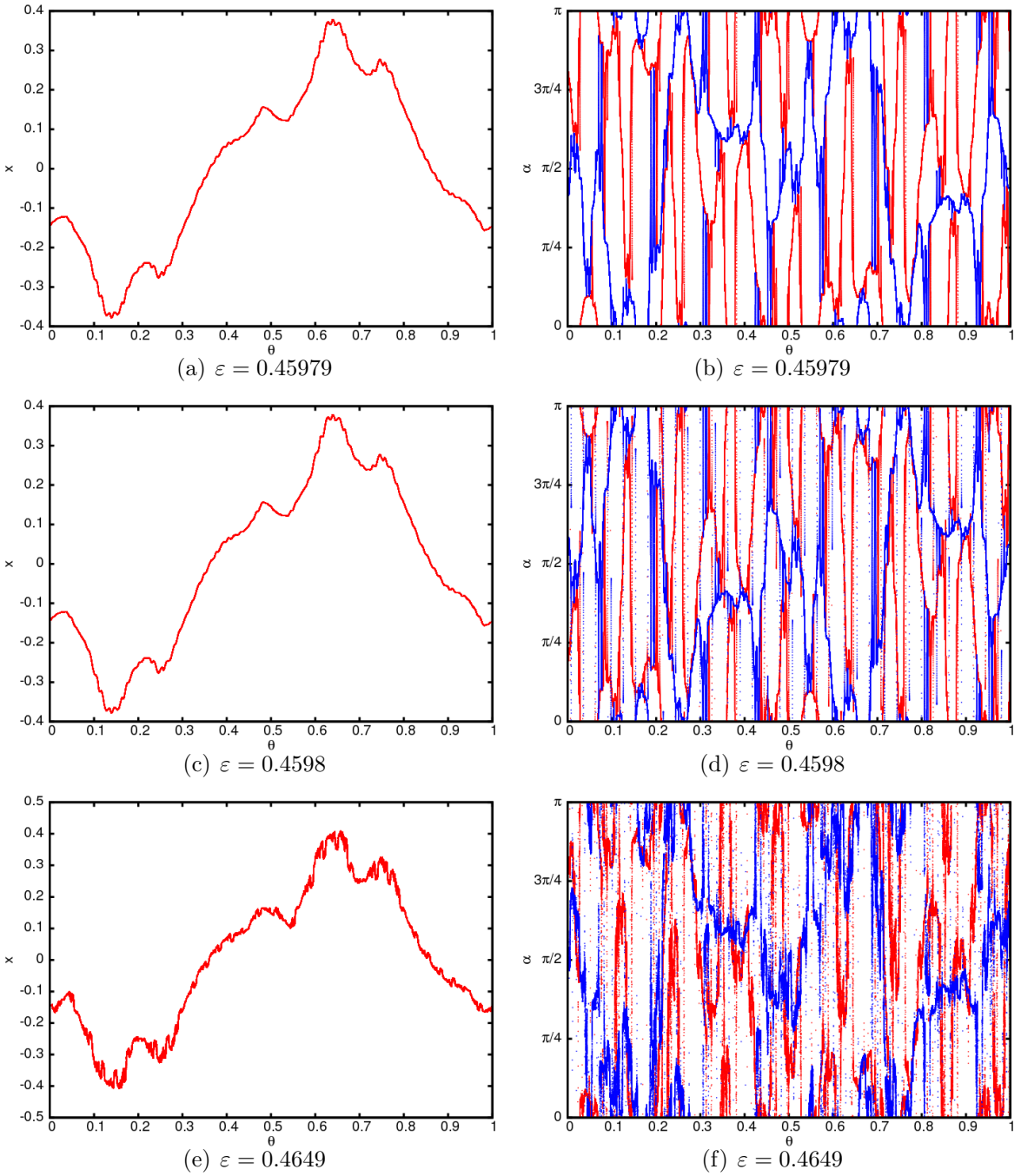

(a) $\varepsilon = 0.45979$ (b) $\varepsilon = 0.45979$

(c) $\varepsilon = 0.4598$ (d) $\varepsilon = 0.4598$

(e) $\varepsilon = 0.4649$ (f) $\varepsilon = 0.4649$

Figure 3.7: Invariant curves (left) and fast (red) and slow (blue) unstable subbundles (right) for different values of ε. These are computed with partial convergent $\frac{196418}{317811}$. The fast and slow unstable subbundles are plotted as a projection on the 2D unstable bundle.

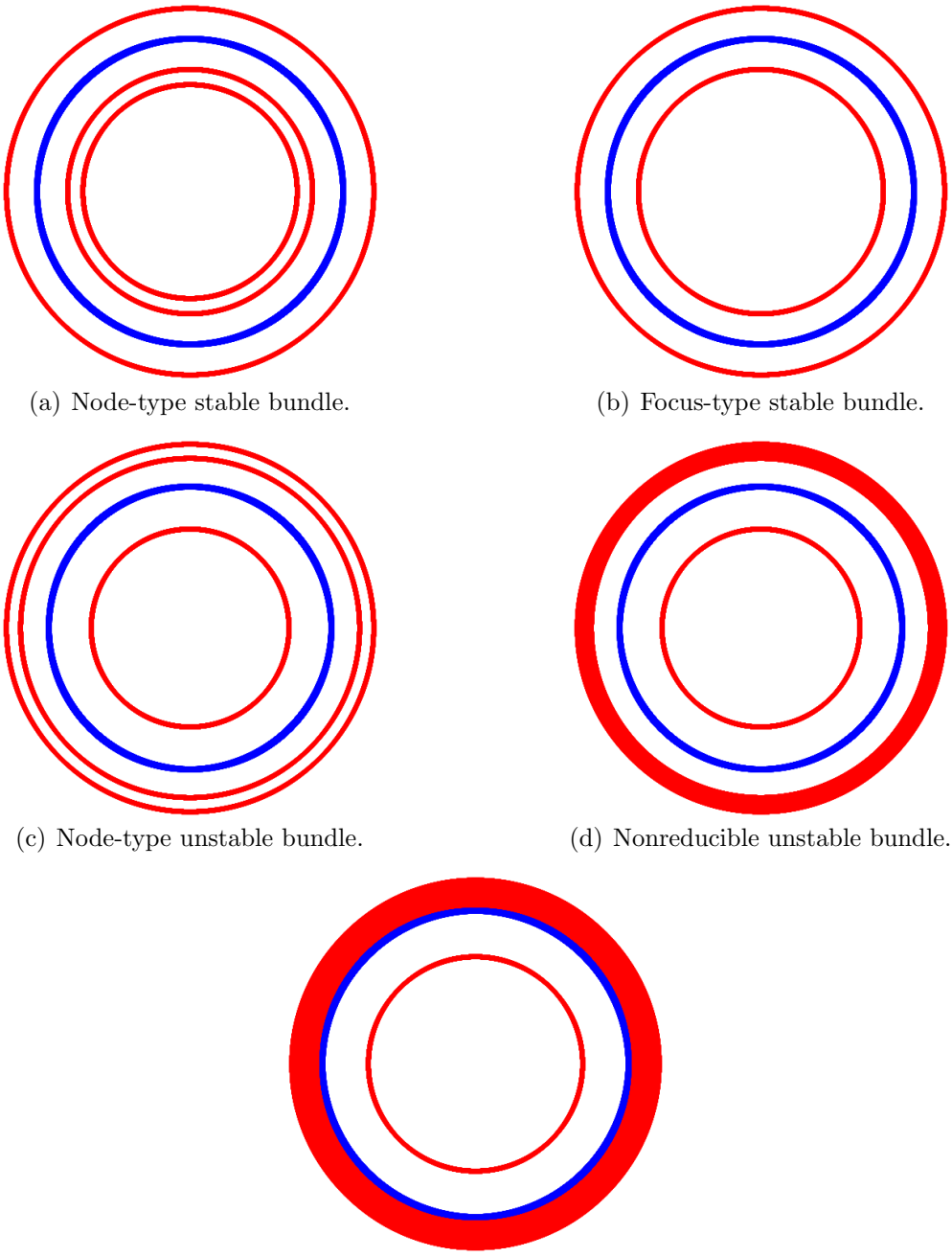

(a) Node-type stable bundle.

(b) Focus-type stable bundle.

(c) Node-type unstable bundle.

(d) Nonreducible unstable bundle.

(e) M spectrum at the breakdown.

Figure 3.8: Diagram of the M spectra for the different regimes of the bifurcation diagram. The blue circle is the unit circle.

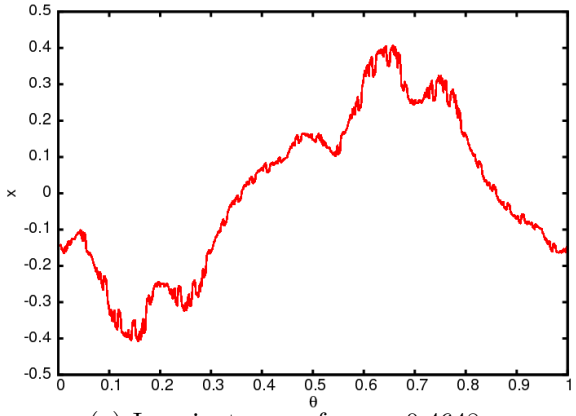

(a) Invariant curve for $\varepsilon = 0.4648$.

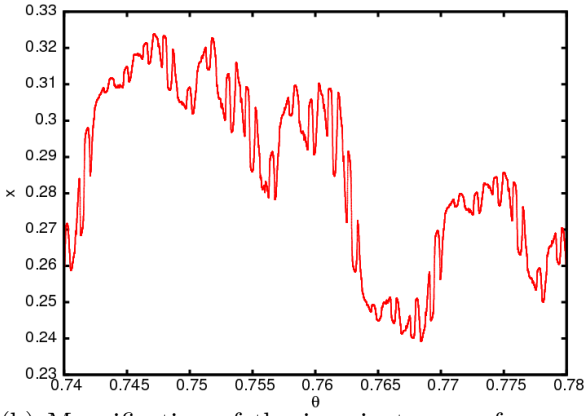

(b) Magnification of the invariant curve for $\varepsilon = 0.4648$.

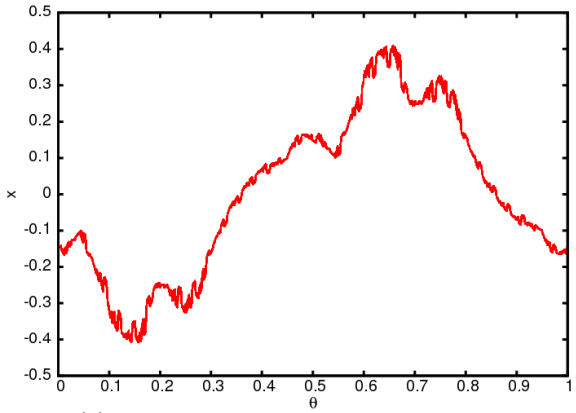

(c) Invariant curve for $\varepsilon = 0.464912$.

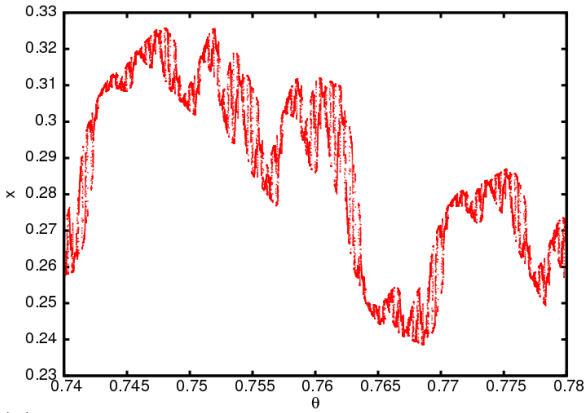

(d) Magnification of the invariant curve for $\varepsilon = 0.464912$.

Figure 3.9: Two (smooth) invariant curves near breakdown for the partial convergent $\frac{514229}{832040}$. Note that, as ε is increased, the curve is more wrinkled. Note that the invariant curves are a smooth curve, but very wrinkled, and, without the magnification, we cannot distinguish them.

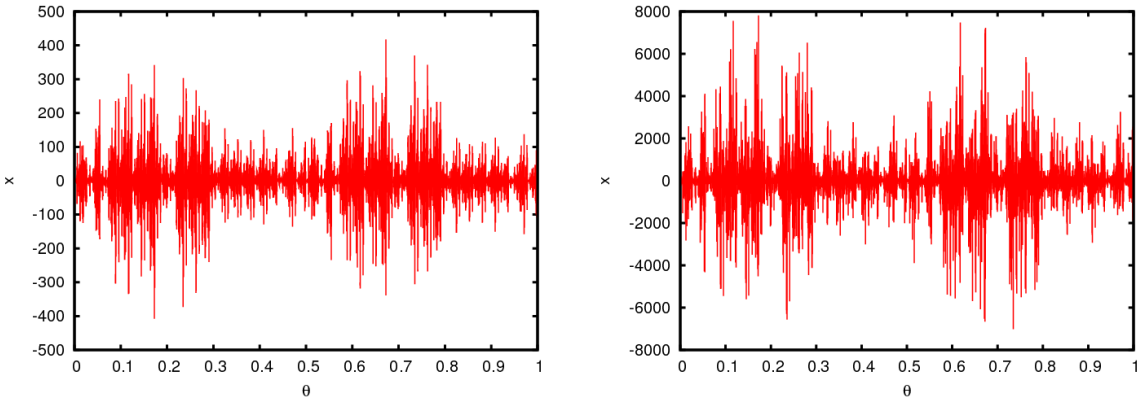

(a) $\varepsilon = 0.4648$ (b) $\varepsilon = 0.464912$

Figure 3.10: Derivatives of the invariant curves computed with partial convergent $\frac{46368}{75025}$ for different values of the ε parameter near the breakdown. Note that there is a slightly difference between the parameter ε but the magnitude of the derivatives differ a lot. See text for further details.

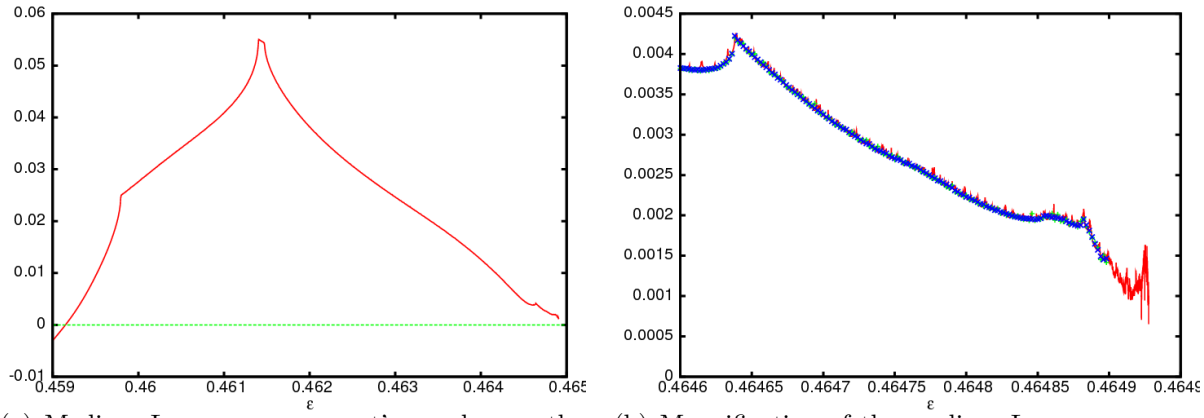

(a) Medium Lyapunov exponent's graph near the breakdown, computed with the partial convergent $\frac{46368}{75025}$. Note that at $\varepsilon \simeq 0.4598$ we can see a bump in it, where the one dimensional subbundles of the unstable bundle collide.

(b) Magnification of the medium Lyapunov exponent's graph near the breakdown, computed with several partial convergents: $\frac{46368}{75025}$ (red), $\frac{121393}{196418}$ (green), $\frac{514229}{832040}$ (blue).

Figure 3.11: Medium Lyapunov exponent's graphs for ε near the breakdown. These are computed with partial convergent $\frac{46368}{75025}$. See text for more details.

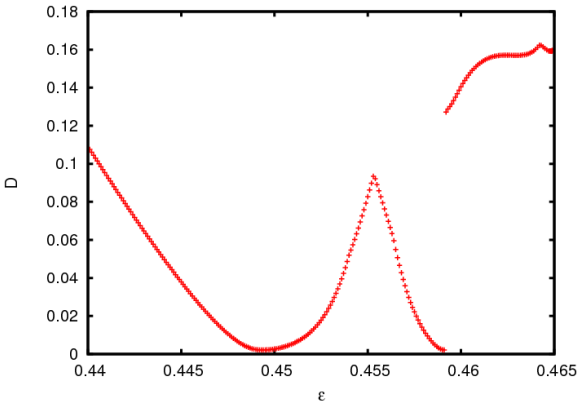

(a) Note that there is a discontinuity of the minimum distance function between the unstable and stable bundles at $\varepsilon = 0.45916$. At this parameter value there is the transition of the slow stable subbundle to the slow unstable subbundle.

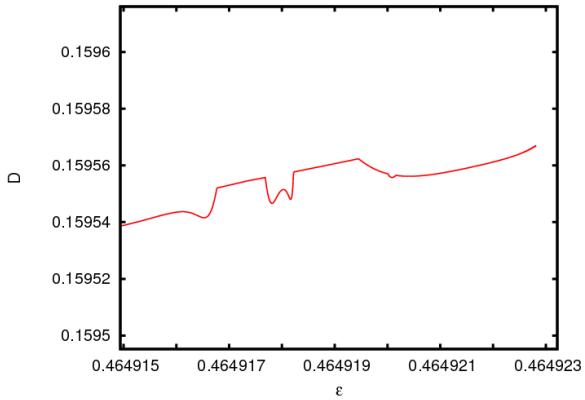

(b) Magnification of the minimum distance function near the breakdown. Note that it is bigger than zero.

Figure 3.12: Minimum distance between the invariant unstable and stable bundles near breakdown. This is computed with partial convergent $\frac{46368}{75025}$.

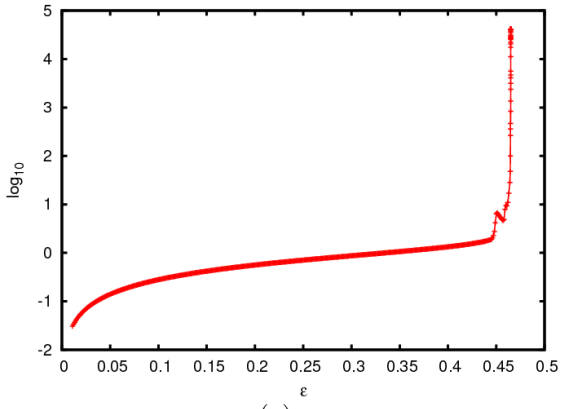

(a)

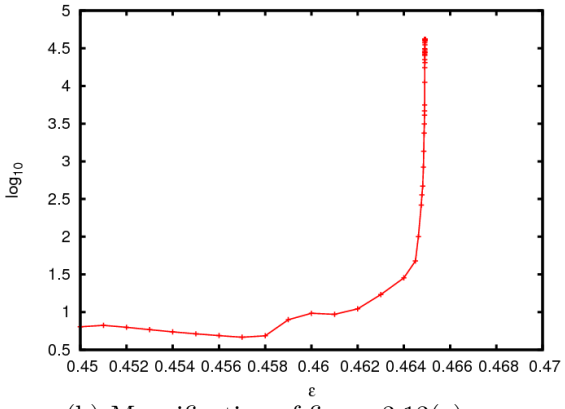

(b) Magnification of figure 3.13(a).

Figure 3.13: Maximum slope function of the invariant curve with respect ε computed with the partial convergent $\frac{514229}{832040}$. The y axis is in $\log_{10}$ scale. See text for further details.

Chapter 4

Computer-assisted proofs of FHIT

The goal of this chapter is to present a new methodology to provide rigorous proofs of the existence and (local) uniqueness of fiberwise hyperbolic invariant tori in quasiperiodically forced systems, even in cases in which the systems are very far from the perturbative regime and the tori are about to break. The methodology is based on the use of computers to verify the conditions of a taylored version of Newton-Kantorovich theorem [HdlL06b] for FHIT. We report the application of computer-assisted proofs of existence of invariant tori in three challenging scenarios.

The first scenario is the Harper map. This map arises in the study of the spectral properties of the Almost-Mathieu operator [HP06], a discrete Schrödinger operator. We develop computer-assisted proofs in several regimes of this map. This computer-assisted proofs will be a warm up for the next two scenarios because the invariant torus is known a priori and the validations concern only on the uniform hyperbolicity of the cocycles. We apply indirect arguments to prove the existence of SNA in the projective cocycle, analyzing different regions (gaps) of the parameter space and observing that the topology of the invariant bundles depend on the gaps [HP06, HdlL07]. We also show the dependence of the validations to the quality of the initial data, which in turn depends on the hyperbolicity constants.

The second scenario examined is the Heagy-Hammel route [HH94]. This is a period 2 attracting torus (appeared in a period doubling bifurcation) that collides with its companion repelling torus, producing a SNA. In this transition, the repelling torus is preserved, while the period 2 attracting torus is destroyed (and becomes a SNA). This situation has been observed in numerical experiments on a quasiperiodically driven logistic map, a noninvertible system. Interestingly, the role of noninvertibility in global bifurcations was already noted in [AK91, AKdlL07]. Noninvertibility is also a drawback in rigorous numerical computations, since it implies that the linear dynamics around the torus cannot be reduced to constant coefficients. Moreover, the unstable dynamics around the repelling torus has to be apparent on the period 2 attracting torus when both objects approach each other and, in the limit case, the closure of the SNA must contain some repelling orbits [Sta99]. Hence, even though

the normal dynamics around the period 2 attracting torus is attracting on average (the Lyapunov exponent is negative), it can be locally expanding. We overcome these computational problems by averaging the normal dynamics around the period 2 attracting torus. We prove that the period 2 attracting torus exists up to a relative distance which is less than $7.3 \cdot 10^{-4}$ of the estimated value of the breakdown. We emphasize that other collision mechanisms of formation of SNA have been studied both numerically and rigorously in the literature, such as the non-smooth versions of the saddle-node and pitchfork bifurcations [GFPS00, Jäg09, OWGF01].

The third scenario is a non-smooth breakdown of a saddle invariant torus, described in [HdlL07, HdlL06a], and in chapter §2, for a quasiperiodically driven standard map. Here, the stable and unstable bundles of a saddle torus approach each other in a complex way. In other words, their projectivizations show the typical collision mechanism of creation of SNA observed, e.g. in the Harper map [HP06, KS97]. Moreover, the corresponding Lyapunov multipliers are away from 1. We report this mechanism for a quasiperiodically forced standard map, and prove the existence of the saddle torus up to a bound that is at a relative distance less than $4.3 \cdot 10^{-7}$ from the estimated value of the breakdown.

All the validations presented here were tested with several types of computers working under several operating systems, although we report only the results obtained with a machine `Intel(R) Core(TM)2 Quad CPU Q9550 @ 2.83GHz` working under `Debian`, using one of the processors.

4.1 A validation theorem

In chapter §1 we saw the relation between hyperbolicity and the implementability of Newton's method. From theorem 1 in [HdlL06b], Newton's method for finding FHIT converges quadratically, provided that the initial approximations of the torus and its invariant bundles are accurate. The following is a reformulation of such a theorem, which is the theoretical core of the validations done in this chapter.

Notation 4.1.1. An *open strip* of the vector bundle $\mathbb{R}^n \times \mathbb{T}$ is the open set

$$D := \{(z, \theta) \in \mathbb{R}^n \times \mathbb{T} : \ z \in \mathcal{U}, \theta \in \mathbb{T}\},$$

where $\mathcal{U}$ is an open set of $\mathbb{R}^n$.

Theorem 4.1.2. *Let $\mathbb{R}^n \times \mathbb{T}$ be the trivial bundle over $\mathbb{T}$, endowed with the Finslered norm given by the maximum norm on each fiber. Let $F \colon D \subset \mathbb{R}^n \times \mathbb{T} \to \mathbb{R}^n$ be a continuous map defined in an open strip D, $\mathcal{C}^2$ with respect to z, and $\omega \in \mathbb{R}$, defining the skew product $(F, \omega) : D \to \mathbb{R}^n \times \mathbb{T}$.*

1.- *Assume we are given:*

1.1) *a continuous parametrization* $K\colon \mathbb{T} \to \mathbb{R}^n$ *of a torus* $\mathcal{K} \subset D$*;*

1.2) *two continuous matrix-valued maps* $P_1, P_2\colon \mathbb{T} \to \mathrm{L}(\mathbb{R}^n)$*;*

1.3) *a continuous block diagonal matrix-valued map* $\Lambda\colon \mathbb{T} \to \mathrm{L}(\mathbb{R}^n)$*,* $\Lambda(\theta) = \mathrm{diag}\,(\Lambda^s(\theta), \Lambda^u(\theta))$*, where* $\Lambda^s\colon \mathbb{T} \to \mathrm{L}(\mathbb{R}^{n_s})$ *and* $\Lambda^u\colon \mathbb{T} \to \mathrm{GL}(\mathbb{R}^{n_u})$*, with* $n = n_s + n_u$*.*

2.- *Let* $\rho, \sigma, \tau, \lambda, \hat{\lambda}$ *be positive constants such that:*

2.1) *For each* $\theta \in \mathbb{T}$*,* $R(\theta) = P_2(\theta + \omega)\,(F(K(\theta), \theta) - K(\theta + \omega)) \in \mathbb{R}^n$ *satisfies* $|R(\theta)| \leq \rho$*;*

2.2) *For each* $\theta \in \mathbb{T}$*,* $S(\theta) = P_2(\theta + \omega)\mathrm{D}F(K(\theta), \theta)P_1(\theta) - \Lambda(\theta) \in \mathrm{L}(\mathbb{R}^n)$ *satisfies* $|S(\theta)| \leq \sigma$*;*

2.3) *For each* $\theta \in \mathbb{T}$*,* $T(\theta) = P_2(\theta)P_1(\theta) - \mathrm{I}_n \in \mathrm{L}(\mathbb{R}^n)$ *satisfies* $|T(\theta)| \leq \tau$*;*

2.4) *For each* $\theta \in \mathbb{T}$*,* $\max\,(|\Lambda^s(\theta)|, |\Lambda^u(\theta)^{-1}|) \leq \lambda$*,* $|\Lambda(\theta)| \leq \hat{\lambda}$*;*

and assume that

2.5) $\lambda + \sigma + \tau < 1$*.*

3.- *Given a positive constant* r*, let* b, h *be positive constants such that:*

3.1) *For each* $(z, \theta) \in \mathbb{R}^n \times \mathbb{T}$ *with* $z = K(\theta) + P_1(\theta)v$ *and* $|v| \leq r$*, then* $(z, \theta) \in D$ *and* $B(z, \theta) = P_2(\theta + \omega)\mathrm{D}_z^2 F(z, \theta)\,[P_1(\theta)\cdot, P_1(\theta)\cdot] \in L^2(\mathbb{R}^n)$ *satisfies* $|B(z, \theta)| \leq b$*;*

3.2) $(1 - \lambda - \sigma - \tau)^{-2} b\rho \leq h$*;*

and assume that

3.3) $h < \frac{1}{2}$*.*

4.- *Assume also that the positive constants* r_0, r_1 *satisfy:*

4.1) $(1 - \lambda - \sigma - \tau)(1 - \sqrt{1 - 2h})b^{-1} \leq r_0 \leq r$*;*

4.2) $r_1 \leq (1 - \lambda - \sigma - \tau)(1 + \sqrt{1 - 2h})b^{-1}$ *and* $r_1 \leq r$*.*

Then, there exists a unique continuous map $K_*\colon \mathbb{T} \to \mathbb{R}^n$ *such that, for each* $\theta \in \mathbb{T}$*:*

a.1) $F(K_*(\theta), \theta) - K_*(\theta + \omega) = 0$*;*

a.2) $|P_1^{-1}(\theta)\,(K_*(\theta) - K(\theta))\,| \leq r_1$*.*

Moreover:

a.3) $|P_1^{-1}(\theta)\,(K_*(\theta) - K(\theta))\,| \leq r_0$.

5.- If, moreover, the positive constant μ satisfies:

5.1) $\lambda(1-\lambda^2)^{-1}(1-\tau)^{-1}(br_0 + \sigma + \hat{\lambda}\tau) \leq \mu < \frac{1}{4}$.

Then, there exist continuous matrix-valued maps $P_*\colon \mathbb{T} \to \mathrm{GL}(\mathbb{R}^n)$, $\Lambda_*\colon \mathbb{T} \to \mathrm{L}(\mathbb{R}^n)$, with $\Lambda_*(\theta) = \mathrm{diag}\,(\Lambda_*^s(\theta), \Lambda_*^u(\theta))$, where $\Lambda_*^s\colon \mathbb{T} \to \mathrm{L}(\mathbb{R}^{n_s})$ and $\Lambda_*^u\colon \mathbb{T} \to \mathrm{GL}(\mathbb{R}^{n_u})$, such that, for each $\theta \in \mathbb{T}$:

b.1) $P_*(\theta+\omega)^{-1}\mathrm{D}_z F(K_*(\theta),\theta)P_*(\theta) - \Lambda_*(\theta) = 0$;

b.2) $|P_1(\theta)^{-1}(P_*(\theta) - P_1(\theta))| \leq \frac{\mu}{\sqrt{1-4\mu}}$;

b.3) $|\Lambda_*(\theta) - \Lambda(\theta)| \leq \left(1 + \frac{\mu}{\sqrt{1-4\mu}}\right)(1-\tau)^{-1}(br_0 + \sigma + \hat{\lambda}\tau)$.

Remark 4.1.3. As a consequence of theorem 4.1.2, K_* parametrizes a FHIT, and the columns of P_* contain frames of its invariant bundles. Moreover, the convergence of Newton's method to K_* from K is quadratic.

Remark 4.1.4. From the results in [HdlL06c], the torus K_* is as smooth as the map F (including analytic).

Remark 4.1.5. The Finslered norm appearing in theorem 4.1.2 is the sup norm on each fiber. More general norms can be considered [HdlL06b], e.g. the Lyapunov metric adapted to the hyperbolic splitting. Instead of considering adapted metrics, theorem 4.1.2 considers adapted frames.

Remark 4.1.6. The norm of the second differential (in the coordinates of the adapted frame P_1), is bounded by b for all points in the strip

$$\bar{D}_{P_1}(K, r) = \{(z, \theta) \mid |P_1^{-1}(\theta)(z - K(\theta))| \leq r\}.$$

This bound b (and subsequently h) depends obviously on the radius r of the strip. A first choice is taking $2(1-\lambda-\sigma-\tau)^{-1}\rho \leq r$, that ensures (if $h < \frac{1}{2}$) that $r_0 \leq r$, assumption that appears in 3.3). We can also tune r (making it smaller) in order to improve the *error radius* r_0 and the *uniqueness radius* r_1.

Remark 4.1.7. One can state a similar theorem using norms with higher regularities (e.g. $\mathcal{C}^r$, Sobolev, analytic). In this thesis we have only considered (and implemented) validations using $\mathcal{C}^0$ norms. Hence, although the FHIT K_* is as smooth as the skew product and the bundles are as smooth as its differential, we only measure the distance of the invariant objects to the approximately invariant objects using $\mathcal{C}^0$ norms. We plan to come back to this problem in the future.

Remark 4.1.8. Theorem 4.1.2 also works if $\mathbb{T}$ is replaced by a general compact metric space, and $\omega : \mathbb{T} \to \mathbb{T}$ is replaced by a general homeomorphism. However, the fiberwise hyperbolic invariant graph K_* obtained will be in general less regular than F.

4.2 Implementation of the validation algorithm

In this section we explain implementation issues of computer validations of FHIT in skew products over rotations, based on Theorem 4.1.2. Since the base manifold of the skew product is a torus, and the base dynamics is a rotation, we use Fourier polynomials to approximate the periodic functions to modelize the components of the approximate invariant tori and bundles of the input data for the algorithm. We emphasize that other dynamics and/or other manifolds would lead to other types of approximations, such as simplices, splines, etc.

The core of the implementation is a set of routines to rigorously manage periodic functions and enclose them in Fourier polynomials plus error intervals. These are what we refer to as the Fourier models. For a brief and concise exposition on the definition, properties and rigorous manipulations of Fourier models, see chapter §5.

The validating computer program has to verify, from an approximately invariant torus and approximately invariant stable and unstable bundles (e.g. computed numerically or using perturbative arguments), all the hypotheses of Theorem 4.1.2. Notice that the checking has to be done only once. Since we will apply the computer programs in situations in which tori are about to break, see sections §4.3, §4.4 and §4.5, we prioritize the accuracy over the speed of the computations.

4.2.1 Validation of FHIT

Here we show how theorem 4.1.2 can be implemented, via Fourier models, in order to validate some initial data as a good approximation of a FHIT and its invariant subbundles for a given continuous skew product $(F, \omega) : D \subset \mathbb{R}^n \times \mathbb{T} \to \mathbb{R}^n \times \mathbb{T}$, $\mathcal{C}^2$ with respect to z.

We assume that we can effectively compute the enclosures of the components of the compositions of $F(z, \theta)$, $\mathrm{D}_z F(z, \theta)$ and $\mathrm{D}_z^2 F(z, \theta)$ with Fourier models. That is, we can substitute z by a (vector) Fourier model $\hat{K}$, if for each $\theta \in [0, 1]$, $\hat{K}(\theta) \subset D_\theta$ (a fact that can be rigorously checked by using interval arithmetics).

0) Compute, e.g. numerically or using perturbative arguments, the trigonometric polynomial approximations of an invariant torus (K), the adapted frame (P_1) and its inverse (P_2), and the dynamics on the invariant bundles ($\Lambda = \mathrm{diag}(\Lambda^s, \Lambda^u)$).

Fix the order m of the Fourier models throughout the rigorous computations of the validation algorithm. The results at each operation of Fourier models will be m-enclosed.

Remark 4.2.1. The order m of the Fourier models that we choose to represent rigorously the initial data depends on the invariant torus, its invariant bundles and the quality of the uniform hyperbolicity of them. A rule to fix it is to perform a study of the decay of the coefficients of the Fourier expansion of the initial data and choose m in order that all the Fourier coefficients that are discarded are below a given threshold (e.g. 10^{-6} is a

good threshold). As a rule of thumb, with this methodology we ensure that the error, in supremum norm, between the numerical computed initial data and the Fourier model is below the threshold.

The validation algorithm mimics the statement of theorem 4.1.2. Here are the steps:

1) From the input data, derive the Fourier models $\hat{K}$, $\hat{P}_1$, $\hat{P}_2$, $\hat{\Lambda} = (\hat{\Lambda}^s, \hat{\Lambda}^u)$.

2) Compute the upper bounds $\rho, \sigma, \tau, \lambda, \hat{\lambda}$ by enclosing the Fourier models $\hat{R}$, $\hat{S}$, $\hat{T}$, $\hat{\Lambda}^s$, $\hat{\Lambda}^u$, $(\hat{\Lambda}^u)^{-1}$. Check (using interval arithmetic) if $\lambda + \sigma + \tau < 1$. If not, the torus is not validated (and the algorithm stops).

3) Given r (for instance, an upper bound of $2(1 - \lambda - \sigma - \tau)^{-1}\rho$, see remark 4.1.6), compute upper bounds b and h. Since we use maximum norms, we compute the Fourier model $\hat{B} = B(\hat{K} + \hat{P}_1 [-r, r]^n, \cdot)$ of the bilinear map $B(z, \theta)$ for points (z, θ) in the strip $\bar{D}_{P_1}(K, r)$ and, hence, b is an upper bound of the maximum norm of $\hat{B}(\theta)$ for all points in $[0, 1]$. Once we compute h, check (using interval arithmetic) if $h < \frac{1}{2}$. If not, the torus is not validated (and the algorithm stops).

4) Compute (an upper bound of) the error radius $r_0 \geq (1 - \lambda - \sigma - \tau)\ (1 - \sqrt{1 - 2h})b^{-1}$ and (a lower bound of) the uniqueness radius $r_1 \leq (1 - \lambda - \sigma - \tau)\ (1 + \sqrt{1 - 2h})b^{-1}$. Check if $r_0 \leq r$. If not, the torus is not validated (and the algorithm stops).

   Then, the torus is validated, meaning that there is a unique invariant torus K_* in the strip $\bar{D}_{P_1}(K, r_1)$. Moreover, the torus K_* is contained in the strip $\bar{D}_{P_1}(K, r_0)$.

5) Compute the upper bound of μ using $\sigma, \tau, \lambda, \hat{\lambda}$. Check if $\mu < \frac{1}{4}$. If not, the normal dynamics of the validated torus is not validated (and the algorithm stops). Compute the upper bounds $\frac{\mu}{\sqrt{1-4\mu}} \leq \rho_P$ and $\left(1 + \frac{\mu}{\sqrt{1-4\mu}}\right)(1 - \tau)^{-1}(br_0 + \sigma + \hat{\lambda}\tau) \leq \rho_\Lambda$.

   Hence, the normal dynamics on the torus and the invariant subbundles are validated: they are at a distance of less than ρ_Λ, ρ_P from the ones given by the initial data.

4.2.2 Validation of a family of FHIT

Here we show the procedure to validate the existence of a family of FHIT of a one-parameter family of skew products $(F_t, \omega) : D \subset \mathbb{R}^n \times \mathbb{T} \to \mathbb{R}^n \times \mathbb{T}$, with parameter $t \in [a, b]$.

Consider the interval $[a, b] = I \cup J$, where I and J are closed intervals, and let K_i, $P_{1,i}$, $P_{2,i}$ and Λ_i for $i = I, J$ be the initial data of the validation algorithm for the (interval) skew products (F_i, ω). In order to check that the corresponding validated tori belong to the same family we proceed as follows.

0) Apply the validation algorithm explained in subsection §4.2.1 to the (interval) skew products (F_i, ω), $i = I, J$. Besides the Fourier models corresponding to the initial data, $\hat{K}_i$, $\hat{P}_{1,i}$, $\hat{P}_{2,i}$ and $\hat{\Lambda}_i$, the validation algorithm produces bounds $\rho_i, \sigma_i, \tau_i, r_{0,i}, r_{1,i}, h_i$.

1) Construct the Fourier model $\hat{E}_{I,J} = \hat{P}_{2,J} \cdot \left(\hat{K}_J - \left(\hat{K}_I + \hat{P}_{1,I} \cdot [-r_{0,I}, r_{0,I}]^n \right) \right)$. Check if

$$\|\hat{E}_{I,J}\| \leq (1 - \tau_J) r_{1,J}. \tag{4.1}$$

If this holds, the two initial data approximate the same family of FHIT, if not, this family has not been validated.

4.3 Example 1: upper bounds of the spectrum of 2 dimensional Schrödinger operators

In this section we report quantitative computer validations of existence of gaps of the spectrum of the Almost-Mathieu operator [Las95, Dam09], which is a discrete Schrödinger operator. These quantitative validations give lower bounds of the Lebesgue measure of some open gaps of this operator, which are used to give rigorous upper bounds of the Lebesgue measure of the spectrum. These results are used to test the efficiency of the validation algorithms, because we know a priori what is the Lebesgue measure of the spectrum of the operator. Also, the proofs of the open gaps in the spectrum is used to prove indirectly the existence of SNA in the projective cocycle associated to the operator.

The validations use the fact, see chapter §1, that a real number E is in the resolvent of the operator if and only if the linear cocycle associated to this energy is uniformly hyperbolic. We also compare the quality of the outputs of the validations with respect the type of breakdown of hyperbolicity.

It is important to remark that this first example does not use all the theory developed in the validation algorithm: we are using the fact that we know a priori which is the invariant torus, the zero section $K(\theta) = 0$. Hence, the validation algorithm reduces only to prove that the upper bounds σ, λ and τ of theorem 4.1.2 satisfy $\sigma + \lambda + \tau < 1$, because the upper bound ρ is exactly zero and the skew product where we work on is linear, which means that its second differential is also exactly zero.

4.3.1 Numerical exploration of the spectrum of the Almost-Mathieu operator

The Almost-Mathieu operator is defined as the bounded linear operator, acting on $\ell^2(\mathbb{Z})$,

$$(Hx)_n = x_{n+1} + L \cos\left(2\pi(\theta_0 + n\omega)\right) x_n + x_{n-1}. \tag{4.2}$$

We fix ω the golden mean.

Remark 4.3.1. As pointed out in chapter §1, this operator does depend on θ_0, but nor its spectral set nor the hyperbolic nature of its solutions depend on θ_0.

As described in chapter §1, the "eigenvalue" problem of the operator (4.2) is equivalent to see that the linear cocycle, the *Harper map*, defined as

$$\begin{array}{rccc}(M,\omega)\colon & \mathbb{R}^2\times\mathbb{T} & \longrightarrow & \mathbb{R}^2\times\mathbb{T}\\ & (v,\theta) & \longrightarrow & (M(\theta)v,\theta+\omega)\end{array}, \tag{4.3}$$

with transfer matrix

$$M(\theta)=\begin{pmatrix}E-L\cos(2\pi\theta) & -1\\ 1 & 0\end{pmatrix},$$

is uniformly hyperbolic, that is, the Harper map (4.3) has continuous invariant unstable and stable bundles. See [KS95, KS97, MOW00, HP06] for numerical and theoretical explorations of this linear cocycle. We will work with this linear cocycle with L values 1 and 3.

The linear cocycle satisfies, because ω is diophantine, that if it is uniformly hyperbolic and its invariant bundles are orientable, then the invariant bundles can be parameterized by continuous vector-valued maps $v_s\colon \mathbb{T}\longrightarrow\mathbb{R}^2$ (stable bundle) and $v_u\colon \mathbb{T}\longrightarrow\mathbb{R}^2$ (unstable bundle) that satisfies

$$M(\theta)v_i(\theta)=\lambda_i v_i(\theta),\ i=u,s,$$

where λ_i are the Lyapunov multipliers associated to the invariant bundles. If the invariant bundles are not orientable, we can use the "*double-cover trick*", see [HdlL06c]: the invariant bundles are orientable for the linear cocycle

$$\begin{array}{rccc}(\bar{M},\frac{\omega}{2})\colon & \mathbb{R}^2\times\mathbb{T} & \longrightarrow & \mathbb{R}^2\times\mathbb{T}\\ & (v,\theta) & \longrightarrow & \left(M(2\theta)v,\theta+\frac{\omega}{2}\right)\end{array}.$$

Remark 4.3.2. We use the double-cover trick to validate the non-orientable invariant bundles.

The spectrum and the dynamics of the cocycle (4.3) are binded by the following theorem [BJ02].

Theorem 4.3.3. *The Almost-Mathieu operator satisfies that the Lyapunov exponent of the Harper map* (4.3)*, with fixed L and energy E, is bigger than*

$$\max\left\{0,\log\left(\frac{L}{2}\right)\right\},$$

with equality only if E is in the spectrum.

With theorem 4.3.3 we can see that the Lyapunov exponent approaches zero as E approaches the spectrum when $L=1$, while for $L=3$ the Lyapunov exponent is always bigger than $\log\left(\frac{3}{2}\right)\simeq 0.4054651081$. See also [Avi09] for a discussion of these two regimes. Hence, these two L regimes are a good example to test what happens to the validation algorithm near different types of hyperbolicity breakdown.

As described in chapter §1, for a fixed L, this operator has associated an Integrated Density of States function, see figure 4.1. This function is defined on the real line and it is

monotone increasing, and stricly increasing only on the spectrum of the operator, so in its resolvent is constant. With the help of this function, which is computed using the numerical techniques described in chapter §5, we can detect numerically the open gaps of the Almost-Mathieu operator. See tables 4.1 and 4.2 for the first ten biggest gaps of this operator for $L = 1$ and $L = 3$. From the general theory described in chapter §1, E is in the resolvent (in a gap) if the IDS at E is equal $\frac{k\omega}{2} \pmod 1$, $k \in \mathbb{Z}$. These k are used to label the gaps in tables 4.1 and 4.2.

Remark 4.3.4. The orientability of the invariant bundles is related to the value of k. When k is an even integer, then the invariant bundles are orientable, otherwise they are non-orientable.

Remark 4.3.5. The IDS helps us to detect SNA in the dynamics of the projective cocycle of (4.3). If $L = 3$ (the Lyapunov multiplier is always bigger than 1) and $E_1 < E_2$ satisfy that they are in open gaps with different k label, then there exists an intermediate E_*, $E_1 < E_* < E_2$, such that E_* is in the spectrum of the Almost-Mathieu operator. Hence, by Oseledet's theorem, see chapter §1, at E_* the invariant bundles are only measurable, so the SNA is the measurable unstable bundle, that is an attractor in the projective cocycle.

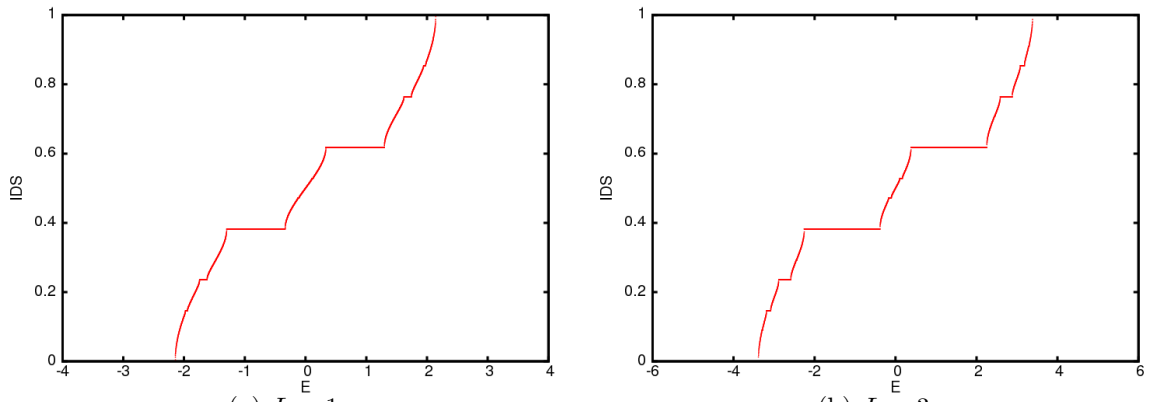

(a) $L = 1$. (b) $L = 3$.

Figure 4.1: Integrated Density of States of the Almost-Mathieu operator for different L values.

A result that we use in order to contrast the accuracy of the validation results with the theory is the following, see [Las95].

Theorem 4.3.6. *For every irrational ω and for a fixed L, the Lebesgue measure of the spectrum of the Almost-Mathieu operator is exactly*

$$|4 - 2\,|L||\,.$$

Remark 4.3.7. For ω irrational and $L \neq 0$, the spectrum of this operator has a very complicated structure: it is a Cantor set. This was proved in [BS82, Pui04a, AJ09].

spec. gap	left	right	width
0	2.144103733062e+00	$+\infty$	-
∞	$-\infty$	-2.144103733062e+00	-
1	3.350514793395e−01	1.297606544494e+00	0.962555065154
-1	-1.297606544494e+00	-3.350514793395e−01	0.962555065154
2	-1.743300521850e+00	-1.619954509735e+00	0.123346012115
-2	1.619954509735e+00	1.743300521850e+00	0.123346012115
3	1.943385314941e+00	1.977029056549e+00	0.033643741608
-3	-1.977029056549e+00	-1.943385314941e+00	0.033643741608
4	-1.239519195556e−01	-1.062295761108e−01	0.017722343444
-4	1.062295761108e−01	1.239519195556e−01	0.017722343444

Table 4.1: $L = 1$. Numerical approximation of the measure of the spectrum 2.013673.

spec. gap	left	right	width
0	3.386230716705e+00	$+\infty$	-
∞	$-\infty$	-3.386230716705e+00	-
1	3.833788871765e−01	2.252360553741e+00	1.868981666564
-1	-2.252360553741e+00	-3.833788871765e−01	1.868981666564
2	-2.882815551757e+00	-2.585066146850e+00	0.297749404907
-2	2.585066146850e+00	2.882815551757e+00	0.297749404907
3	3.081375732421e+00	3.185926513671e+00	0.104550781250
-3	-3.185926513671e+00	-3.081375732421e+00	0.104550781250
4	-1.703894042968e−01	-1.026932334899e−01	0.067696170806
-4	1.026932334899e−01	1.703894042968e−01	0.067696170806

Table 4.2: $L = 3$. Numerical approximation of the measure of the spectrum 2.094505.

Figure 4.2 shows the Lyapunov exponent function and the minimum distance function of these two regimes, $L = 1, 3$. Also, figures 4.3 and 4.4 show examples of the invariant bundles in these two regimes. We can observe in subfigures 4.3(c) and 4.3(d) a visual example of invariant bundles for $L = 1$ which are (numerically) on the spectrum of the Almost-Mathieu operator. Compare these with the subfigure 4.4(d), where the invariant bundles for $L = 3$ have also collided, but in a non-smooth manner.

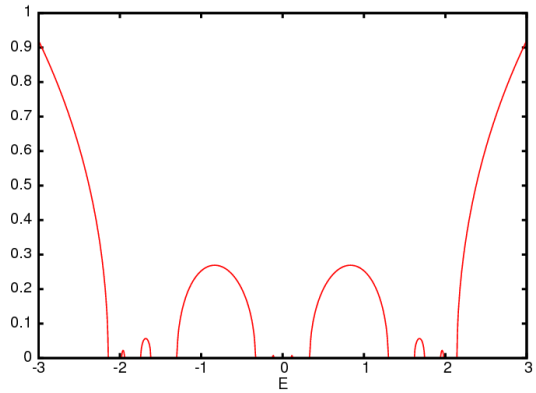

(a) Lyapunov exponent. $L = 1$.

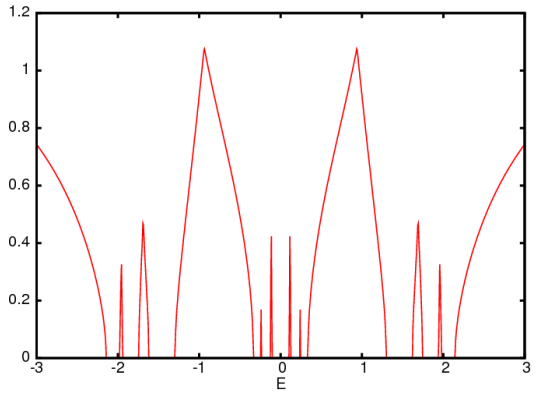

(b) Minimum distance function. $L = 1$.

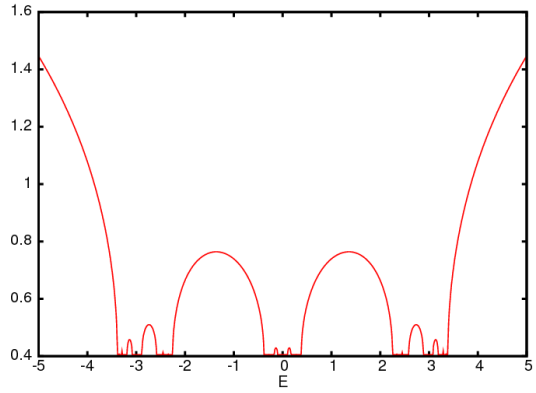

(c) Lyapunov exponent. $L = 3$.

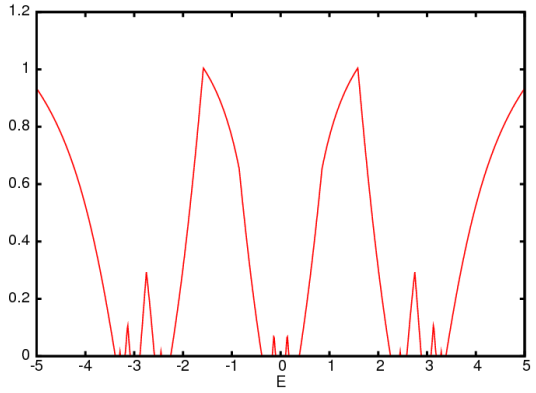

(d) Minimum distance function. $L = 3$.

Figure 4.2: Lyapunov exponent function and minimum distance function between the invariant bundles for $L = 1$ and $L = 3$.

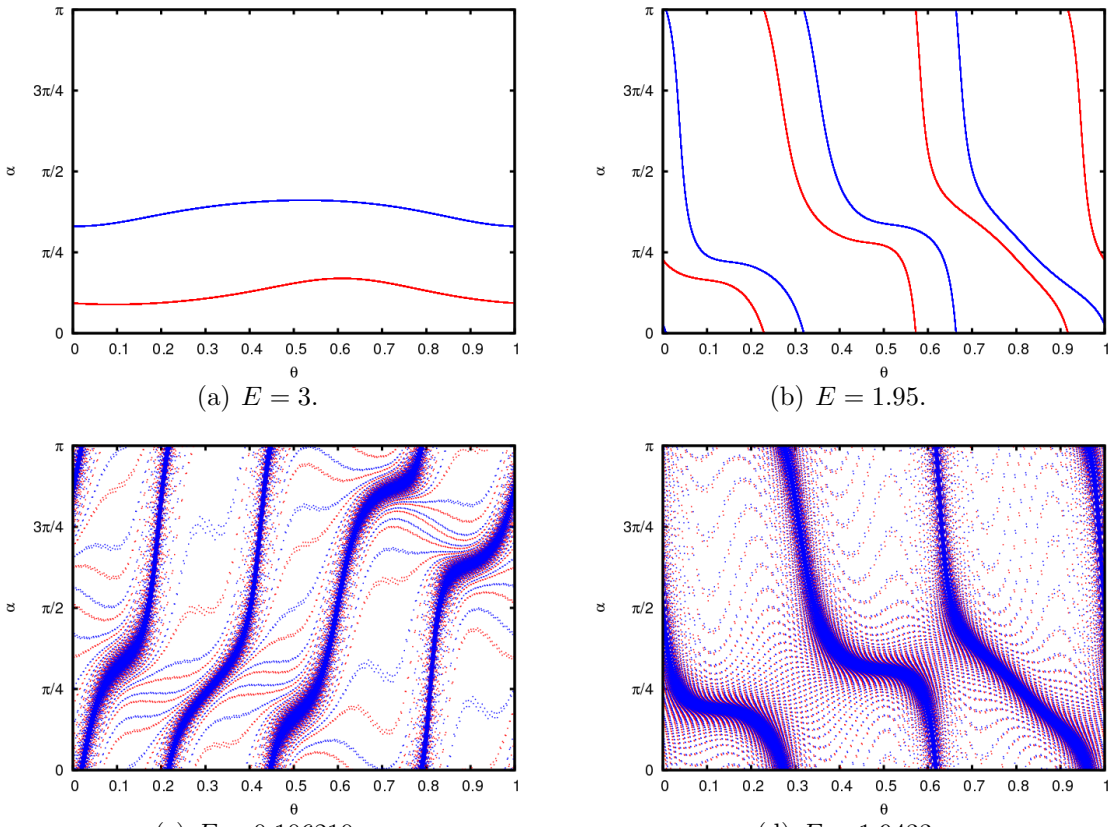

(a) $E = 3$. (b) $E = 1.95$.

(c) $E = 0.106210$. (d) $E = 1.9433$.

Figure 4.3: Unstable bundles (red) and stable bundles (blue) for $L = 1$ and different E values.

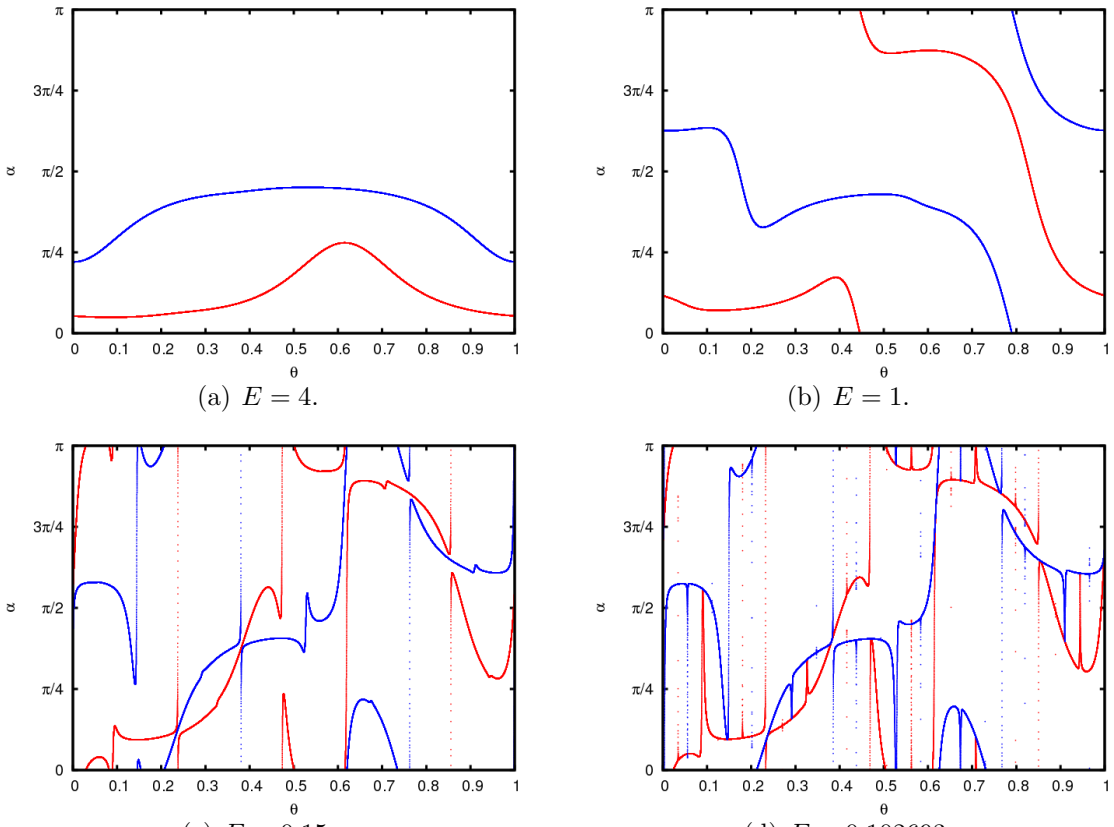

(a) $E = 4$. (b) $E = 1$.

(c) $E = 0.15$. (d) $E = 0.102693$.

Figure 4.4: Unstable bundles (red) and stable bundles (blue) for $L = 3$ and different E values.

4.3.2 Computer validations

Motivated by the previous numerical study, we proceed to show the validation results obtained for both the $L = 1$ and $L = 3$ regime. The goal of the validations presented here is to show the main differences between the validation algorithms when they are applied in regimes ($L = 1$) where the hyperbolicity is destroyed when the Lyapunov exponent is zero, and regimes ($L = 3$) when the Lyapunov exponent is positive. With the help of the validations we can give rigorous upper bounds of the Lebesgue measure of the spectrum of the Almost-Mathieu operator and, as pointed out in remark 4.3.5, for $L = 3$ we prove indirectly the existence of SNA in the projective cocycle of the linear cocycle associated to the Almost-Mathieu operator.

Remark 4.3.8. We perform the validations for the Almost-Mathieu operator because, as stated in the previous numerical study, the measure of the spectrum is well-known. However, the same validation technique can be applied in any (quasiperiodic) discrete Schrödinger operator in order to localize the gaps of the spectrum and to give upper bounds of its measure.

The validations for $L = 1$ are done with a number of 100 modes, while the validations for $L = 3$ with a number of 1500 modes. This is because, at $L = 1$, there is no need of a lot of Fourier modes in order to give to the validation algorithm a good approximation of the invariant bundles (the matrix-valued maps P_1 and P_2), while in the $L = 3$, as E approaches the boundary of a gap of the spectrum, the number of Fourier modes to modelize the initial data increases.

Remark 4.3.9. The computation of the invariant bundles differ a lot with respect the value of L. To compute the invariant bundles for $L = 1$ for energies E near the spectrum, the non-rigorous algorithm needs a lot of iterates to perform the computations because the Lyapunov multiplier is close, in absolute value, to 1. In the other hand, this phenomenon is not present for $L = 3$, because the Lyapunov exponent is, in absolute value, bigger than 1.

The first thing we validate are the ten biggest gaps of the spectrum for both L parameters. For an example of the output of the validation algorithm, see table 4.3. These validations can be seen in tables 4.4 and 4.5. The **bold** numbers are the ones that differ with the numerical values predicted in tables 4.1 and 4.2. From the validation tables we can obtain that a rigorous upper bound of the measure is of the spectrum for $L = 1$ is 2.013**735** and a rigorous upper bound for $L = 3$ is 2.**12634**. For both L, theorem 4.3.6 predicts that the Lebesgue measure of the spectrum is 2. Note that for $L = 1$ the prediction of the upper bounds of the measure of the spectrum is more accurate. This is because we can reach energies closer to the spectrum because the number of Fourier modes does not increase as the energies approach the spectrum.

To see the dependence of the quality of the validations with respect the number of Fourier modes used to modelize the initial data, we run the validation algorithm for $L = 3$ and $E = 3.3864$ for different number of Fourier modes, see table 4.6. We can observe

L	Energy E	σ	τ	λ	μ	ρ_Λ
1	-0.106239	2.483091e-07	2.322641e-07	9.999361e-01	3.760928e-03	4.824094e-07
1	-0.123942	3.887487e-07	3.296118e-07	9.998938e-01	3.380968e-03	7.208412e-07
1	2.144104	7.404575e-10	3.658449e-10	9.994621e-01	1.028292e-06	1.106500e-09
3	-0.104500	3.247660e-02	2.335234e-02	6.617801e-01	8.169597e-02	7.629253e-02
3	-0.161900	5.664570e-07	2.997832e-08	6.564044e-01	7.059915e-07	6.121279e-07
3	-2.585400	1.325050e-01	1.011495e-01	6.620383e-01	3.740879e-01	–

Table 4.3: Examples of the outputs of the validation algorithm for several energies in both L regimes. Note that the quality of the validations differ on the value of L.

spec. gap	left	right	width
0	2.144104**4**e+00	$+\infty$	
∞	$-\infty$	-2.144104**4**e+00	
1	3.350540e−01	1.297605e+00	0.962551
-1	-1.297605e+00	-3.350540e−01	0.962551
2	-1.743**299**e+00	-1.619956e+00	0.123343
-2	1.619955e+00	1.743**299**e+00	0.123343
3	1.943388e+00	1.977027e+00	0.033639
-3	-1.977027e+00	-1.943388e+00	0.033639
4	-1.239**425**e−01	-1.062**390**e−01	0.0177**035**
-4	1.062**390**e−01	1.239**425**e−01	0.0177**035**

Table 4.4: Validated gaps for $L = 1$. See text for further details.

spec. gap	left	right	width
0	3.386**300**e+00	$+\infty$	
∞	$-\infty$	-3.386**300**e+00	
1	3.8**40000**e−01	2.25**1850**e+00	1.86**7850**
-1	-2.25**1850**e+00	-3.8**40000**e−01	1.86**7850**
2	-2.882**000**e+00	-2.585**400**e+00	0.29**6600**
-2	2.585**400**e+00	2.882**000**e+00	0.29**6600**
3	3.08**2720**e+00	3.18**4000**e+00	0.10**1280**
-3	-3.18**4000**e+00	3.08**2720**e+00	0.10**1280**
4	-1.**619000**e−01	-1.**045000**e−01	0.0**57400**
-4	1.**045000**e−01	1.**619000**e−01	0.0**57400**

Table 4.5: Validated gaps for $L = 3$. See text for further details.

in this table that the quality of the validations increases as the number of Fourier modes increases. We want to point out that there is a threshold for the number of Fourier modes and, when this threshold is exceeded, then the quality of the validations decreases because the intervalar rounding error affects the computations.

modes	σ	τ	μ	ρ_Λ
1000	4.450523e-02	3.715832e-02	1.220098e-01	1.226678e-01
1050	2.502640e-02	2.148061e-02	6.856729e-02	6.363466e-02
1100	1.435212e-02	1.252136e-02	3.932783e-02	3.522698e-02
1150	7.662255e-03	6.660096e-03	2.082827e-02	1.827918e-02
1200	4.243660e-03	3.635333e-03	1.140599e-02	9.911308e-03
1250	2.445562e-03	2.159715e-03	6.678007e-03	5.774756e-03
1300	1.304042e-03	1.178295e-03	3.604592e-03	3.107328e-03
1350	7.158839e-04	6.485635e-04	1.980802e-03	1.704750e-03
1400	3.775534e-04	3.484195e-04	1.055612e-03	9.076539e-04
1450	2.006238e-04	1.822298e-04	5.556880e-04	4.775617e-04
1500	1.118179e-04	9.869580e-05	3.046152e-04	2.617224e-04
1550	6.501144e-05	5.415003e-05	1.713850e-04	1.472327e-04
1600	4.262203e-05	3.465038e-05	1.108558e-04	9.522767e-05
1650	2.470572e-05	2.060447e-05	6.517422e-05	5.598363e-05

Table 4.6: Dependency of the validations with respect the number of modes for $L = 3$, $E = 3.3864$. For all the validations, the value of λ is 0.658855383393.

4.4 Example 2: computer validations for noninvertible skew products

In this section we report computer validations of existence of invariant tori for a noninvertible map, the quasiperiodically driven logistic map. Special emphasis is put on *validation of non-reducible tori* for values close to their breakdown. Note that in this context, the concept of non-reducible torus is equivalent to the noninvertibility of the transfer at some points of the torus.

4.4.1 Numerical exploration of invariant curves in the quasiperiodically driven logistic map

The *driven logistic map* is defined as the skew product

$$\begin{array}{rccl}(F,\omega)\colon & \mathbb{R}\times\mathbb{T} & \longrightarrow & \mathbb{R}\times\mathbb{T} \\ & (z,\theta) & \longrightarrow & (a(1+D\cos(2\pi\theta))z(1-z),\theta+\omega)\end{array}, \tag{4.4}$$

where $\omega=\frac{1}{2}(\sqrt{5}-1)$; and a and D are parameters. We will fix $D=0.1$ and let $a>0$ vary. This map has been the target of several numerical studies: see for example [AKdlL07, HH94], where the authors explore numerically the creation of SNA (Strange Non-chaotic Attractor) via collision of period 2 attracting curves and a repelling curve. After the collision, the period 2 attracting curve has bifurcated to a SNA while the repelling curve is still a smooth curve. This mechanism is known as the Heagy-Hammel route.

In figure 4.5(a) appears the bifurcation diagram (with respect to a) of the invariant objects, while in figure 4.5(b) appears the corresponding Lyapunov multipliers. A particularly simple case is the zero-curve $x_a(\theta)=0$, for which the Lyapunov multiplier can be analytically computed (see e.g. [JT08]): $\Lambda(a)=\frac{a}{2}\left(1+\sqrt{1-D^2}\right)$. Hence, for $D=0.1$, the zero-curve is attracting if $a<2(1+\sqrt{0.99})^{-1}$ and repelling if $a>2(1+\sqrt{0.99})^{-1}\simeq 1.002512$.

Now, let's explain the other invariant curves and their bifurcations, labelled in figure 4.5(b). This is done through a numerical exploration.

A) $a\in(0,1.002512)$: There is a reducible repelling curve. As $a\to 0$ this curves tends to $\frac{a-1}{a}$, and its Lyapunov multiplier approaches 2. As $a\to 1.002512$ this curve tends to 0.

B) $a\in(1.002512,1.854419)$: There is a reducible attracting curve with positive Lyapunov multiplier ($0<\Lambda<1$). This curve comes from a transcritical bifurcation between the zero-curve $x(\theta)=0$ and the repelling curve of region A.

C) $a\in(1.854419,2.406952)$: There is a non-reducible attracting curve, that is, its transfer matrix vanishes at some points. This curve belongs to the same family of the curve of region B.

D) $a \in (2.406952, 3.141875)$: There is a reducible attracting curve with negative Lyapunov multiplier ($-1 < \Lambda < 0$). This curve also belongs to the same family of curves of regions B and C.

E) $a \in (3.141875, 3.271383)$: The attracting curve of region D ends in a period doubling bifurcation. In region E, there is a period 2 attracting curve and a period 1 repelling curve (see figures 4.6(a) and 4.6(b) for the corresponding Lyapunov multipliers). For values $a \in (3.141875, 3.17496)$ the period 2 attracting curve is reducible and for values $a \in (3.17496, 3.271383)$ it is non-reducible.

At a near 3.271383 the period 2 attracting curve collides in a non-smooth way with the repelling curve, bifurcating to a SNA (Heagy-Hammel fractalization route). Figures 4.7(a) and 4.7(b) show these invariant objects before and after the bifurcation.

F) $a \in (3.271383, \infty)$: The repelling curve exists for all these values. The SNA *seems to persist* for values in $a \in (3.271383, 3.2746)$, and afterwards it *apparently bifurcates* into a SA (Strange Attractor), with Lyapunov multiplier bigger than 1.

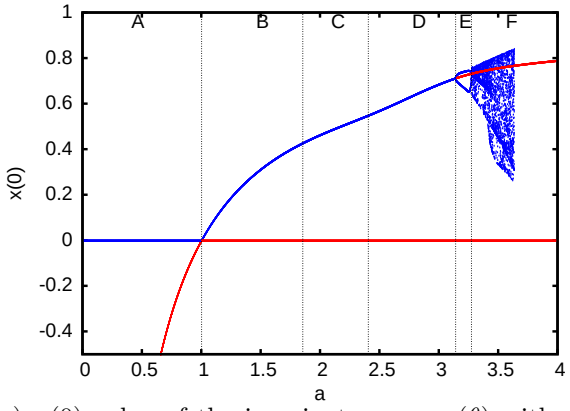

(a) $x(0)$ value of the invariant curves $x(\theta)$ with respect to parameter a. The red color represents a repelling curve and the blue color an attracting object.

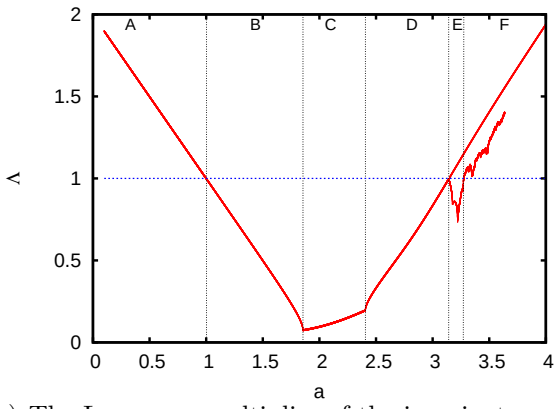

(b) The Lyapunov multiplier of the invariant curves.

Figure 4.5: Bifurcation diagram of the invariant curves and their Lyapunov multipliers, with respect to parameter a. See text for further details.

4.4.2 Numerical computation of the initial data

In this section, we describe how to compute the initial data K, P_1, P_2, Λ for attracting curves of the noninvertible 1D skew product (F, ω). Similar methods can be applied for repelling

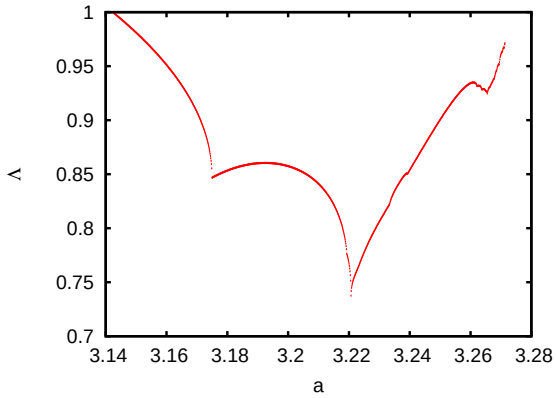

(a) Lyapunov multiplier of the period 2 attracting curve in region E. The peaks correspond to variations of the number of zeroes of the transfer cocycle [JT08].

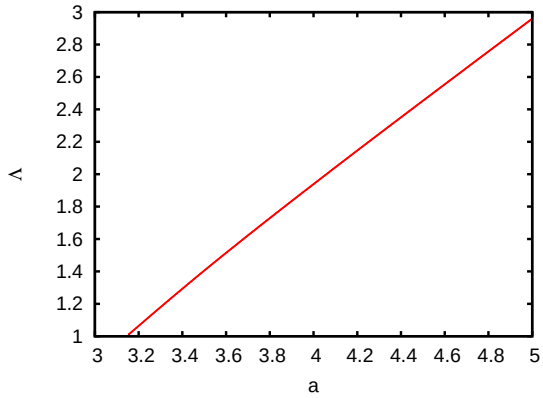

(b) Lyapunov multiplier of the repelling curve in regions E and F. There is no trace of the non-smooth E-F bifurcation of the period 2 attracting companion around $a = 3.271$.

Figure 4.6: Lyapunov multipliers of the invariant and periodic curves, with respect to parameter a.

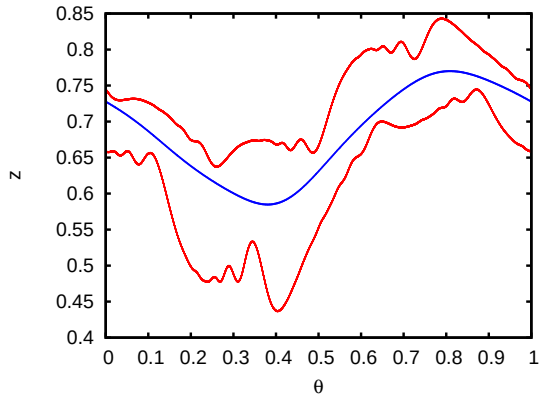

(a) Invariant curves for $a = 3.24$. The red curves is the period 2 attractor, the blue curve is the repellor.

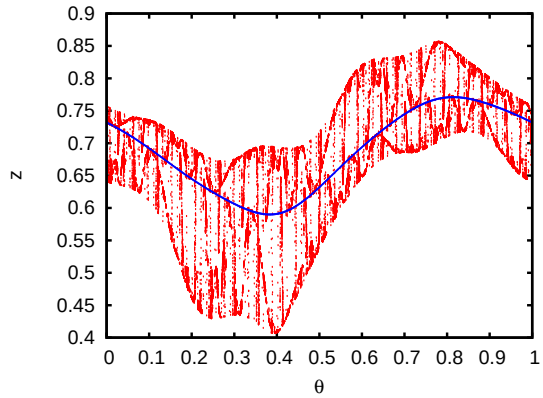

(b) Invariant objects for $a = 3.272$. The red object is the SNA, the blue curve is the repellor.

Figure 4.7: Graphical representation of the Heagy-Hammel route. See text for further details.

curves, by using a right inverse of the map (i.e., one of the branches of the inverse of (F, ω)). We will also present methods to deal with noninvertible transfer matrices.

The approximately invariant torus K can be computed using the simple iteration algorithm, since the invariant torus is attracting. The number of iterations needed to obtain a good approximation depends heavily on the modulus of the Lyapunov multiplier. In our computations, the number of iterations does not exceed 10^{10} simple iterations.

More challenging is the computation of the initial data P_1, P_2, Λ, since even though the transfer matrix M is contracting "on average", it can be locally expanding. The condition of invertibility of the transfer matrix plays a key role in this computation. We have considered two methods in order to overcome these computational problems.

Lyapunov metric This is a general construction when dealing with uniform hyperbolicity [Ano69]. In the 1D case, for an uniformly attracting torus with transfer matrix M and Lyapunov multiplier λ, this metric is given by $|v|_\theta = |L(\theta)v|$, where $L : \mathbb{T} \to [1, \infty)$ is the continuous function

$$L(\theta) = \sum_{j=0}^{\infty} \frac{1}{\bar{\lambda}^j} |M(\theta + (j-1)\omega) \cdots M(\theta)|, \tag{4.5}$$

where $1 > \bar{\lambda} > |\lambda| + \varepsilon$, for sufficiently small $\varepsilon > 0$. Instead of considering this Lyapunov metric, we consider the transformations $P_1(\theta) = \frac{1}{L(\theta)}$ and $P_2(\theta) = L(\theta)$. Hence, we define the continuous function

$$\Lambda(\theta) = P_2(\theta + \omega) M(\theta) P_1(\theta) = \operatorname{sgn}(M(\theta)) \left(\frac{L(\theta) - 1}{L(\theta)} \right) \bar{\lambda}, \tag{4.6}$$

where $\operatorname{sgn}(\cdot)$ is the sign function. Then, $|\Lambda(\theta)| \leq \bar{\lambda} < 1$ for all $\theta \in \mathbb{T}$.

Reducibility and almost reducibility to constant coefficients The goal of the reducibility method is to reduce the transfer matrix to a constant Λ, which satisfies

$$M(\theta) P_1(\theta) = P_1(\theta + \omega) \Lambda, \tag{4.7}$$

for a suitable transformation $P_1(\theta) \neq 0$. If $M(\theta)$ is invertible for all $\theta \in \mathbb{T}$, this equation is solved by taking logarithms and solving small the small divisor equations obtained by matching the Fourier coefficients, see chapter §1.

If $M(\theta)$ has zeroes, equation (4.7) has no continuous solutions. Hence, we can not reduce $M(\theta)$ to constant coefficients. To overcome this difficulty, we consider the modified equation

$$(M(\theta)^2 + \varepsilon \eta(\theta)) P_1(\theta)^2 = P_1(\theta + \omega)^2 \lambda_\varepsilon^2, \tag{4.8}$$

for a suitable function $\eta \colon \mathbb{T} \to [0, 1]$ and a sufficiently small $\varepsilon > 0$.

One choice for the function η is $\eta(\theta) = 1 - \left(\frac{M(\theta)}{||M||_{\mathcal{C}^0}} \right)^2$. This function achieves its maximum value, 1, when the transfer matrix vanishes and decays rapidly outside its zeroes.

Notice that

$$\lambda_\varepsilon^2 = exp\left(\int_{\mathbb{T}} \log(M(\theta)^2 + \varepsilon\eta(\theta))d\theta\right), \tag{4.9}$$

hence we consider $\varepsilon > 0$ such that $|\lambda_\varepsilon| < 1$ (notice that $|\lambda_0| < 1$).

By defining

$$\Lambda(\theta) = \frac{M(\theta)}{\sqrt{M(\theta)^2 + \varepsilon\eta(\theta)}}\lambda_\varepsilon \ ,$$

we obtain that $P_1, P_2 = P_1^{-1}$ and Λ satisfy equation

$$P_2(\theta + \omega)M(\theta)P_1(\theta) = \Lambda(\theta) \ .$$

Remark 4.4.1. $\Lambda(\theta)$ and $M(\theta)$ have the same sign and the same number of zeros.

Remark 4.4.2. In numerical computations these equations are solved by matching Fourier coefficients up to a finite order, even though the analytical solution of small divisors equations involve the smoothness of the transfer matrix and diophantine properties of the rotation ω. These are intermediate computations to produce initial data to be validated by our computer programs.

Numerical comparison of both methods The Lyapunov metric method and the almost reducibility method have been tested, among others, for the period 2 attracting curve of the quasiperiodically driven logistic map, with $D = 0.1$ and $a = 3.250$. In this case, the transfer matrix is noninvertible, hence nonreducible to constant. See figure 4.8 to check differences between the two methods. In figure 4.8(a) we can see that the dynamics of the linear cocycle is locally expanding in some regions (but it is globally contracting), while in figures 4.8(e) and 4.8(c) the linear cocycles are locally and globally contracting. Notice that the Fourier coefficients of the reduced matrix $\Lambda(\theta)$, figure 4.8(d), decay slowly when using the Lyapunov metric method, while they decay exponentially fast when using the almost reducibility method, figure 4.8(f).

4.4.3 Computer validations

Motivated by the previous numerical study, see subsection §4.4.1, we have validated the invariant curves appearing in the bifurcation diagram in figure 4.5(a), up to values of a close to the smooth bifurcations A-B (transcritical) and D-E (period doubling) and the non-smooth bifurcation E-F. We report here in detail the existence of the repellor in regions E and F, and the existence of the period 2 attracting curve near the non-smooth bifurcation E-F.

Invariant curves in regions A, B, C and D have been validated using no more than 20 Fourier modes. The validations near the smooth bifurcations have been performed obtaining results similar to the ones reported below for the repellor.

To summarize the validations that we will present in detail, we have:

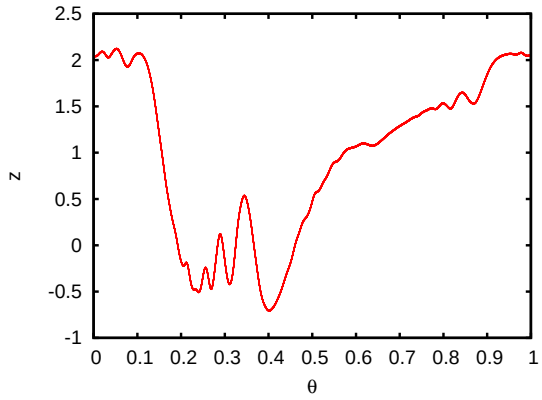

(a) Transfer matrix $M(\theta)$.

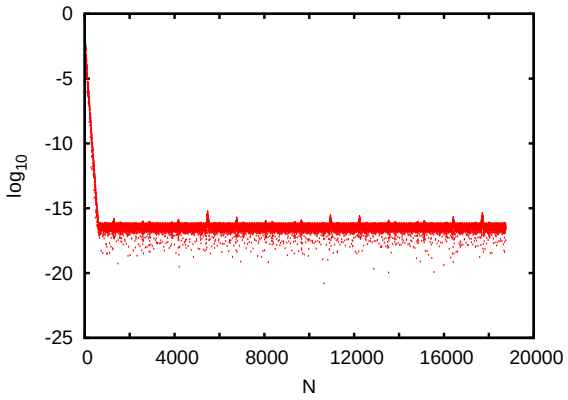

(b) Modes of the transfer matrix $M(\theta)$.

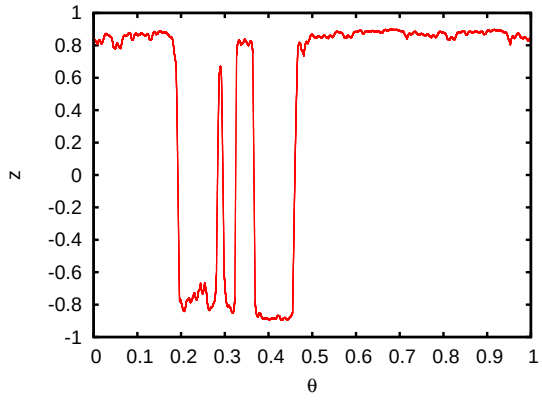

(c) Reduced matrix $\Lambda(\theta)$, computed via Lyapunov metric method.

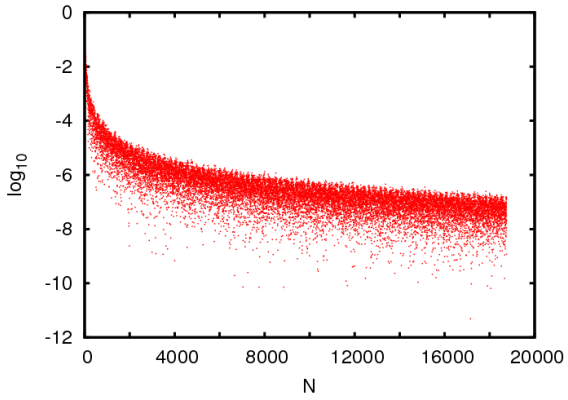

(d) Modes of the reduced matrix $\Lambda(\theta)$, computed via Lyapunov metric method.

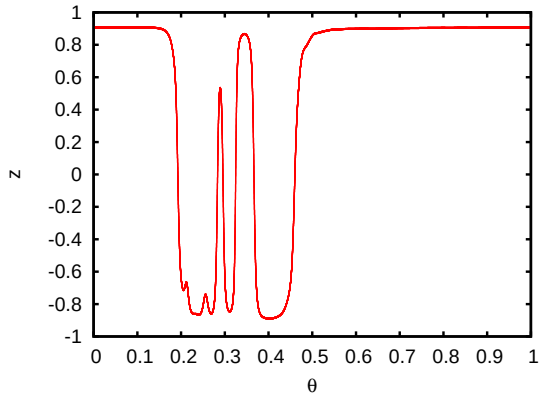

(e) Reduced matrix $\Lambda(\theta)$, computed via almost-reducibility method.

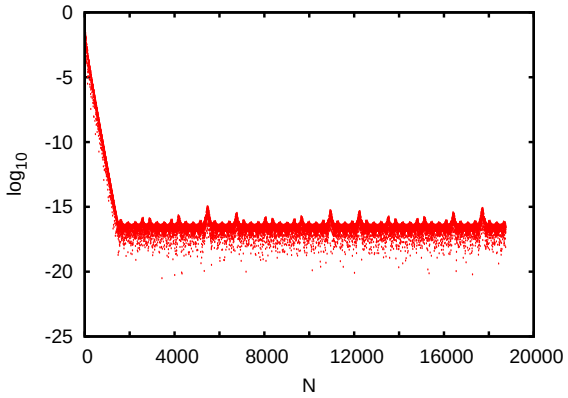

(f) Modes of the reduced matrix $\Lambda(\theta)$, computed via almost-reducibility method.

Figure 4.8: Graphical comparison of the computed reduced $\Lambda(\theta)$ of the period 2 attracting curve, for $a = 3.25$ and $D = 0.1$.

Proposition 4.4.3. *1. For the range of parameters $a \in (3.157065, \infty)$ of the system (4.4) there exists a continuous family of invariant repellor curves.*

2. For every parameter $a = 3.265, 3.268, 3.269$ of the system (4.4) there exists a period 2 invariant attracting curve.

Validation of the repellor

Here we explain the validation of the repelling curve. First of all, we validate analytically the existence of this curve for $a \in (4.6, \infty)$ and then, via Computer Assisted Proofs, we validate it for $a \in (3.157065, 5)$ and check that the two families match.

Analytic validation For the analytic validation, it is convenient to consider the following right inverse of (F, ω):

$$\begin{array}{rccl} (G,\omega)\colon & \mathbb{R}\times\mathbb{T} & \longrightarrow & \mathbb{R}\times\mathbb{T} \\ & (z,\theta) & \longrightarrow & \left(\dfrac{1}{2}+\dfrac{1}{2}\sqrt{1-4\dfrac{z}{a(1+D\cos(2\pi(\theta-\omega)))}},\theta-\omega\right) \end{array} . \tag{4.10}$$

We apply the validation algorithm with the following initial datum: $K(\theta) = \frac{a-1}{a}$, $P_1(\theta) = P_2(\theta) = 1$, $\Lambda(\theta) = M(\theta) = \mathrm{D}_z G\left(\frac{a-1}{a}, \theta\right)$. In the following, we consider the bound

$$\Delta = \sqrt{1 - \frac{4(a-1)}{a^2(1-D)}} \, .$$

The constants $\rho = \frac{1}{2} - \frac{1}{a} - \frac{1}{2}\Delta$, $\sigma = \tau = 0$ and $\lambda = \hat{\lambda} = \frac{1}{a(1-D)\Delta}$ satisfy inequalities 2.1), 2.2), 2.3), 2.4) of the validation theorem 4.1.2. Inequality 2.5) is satisfied if $a > \frac{1}{(1-D)\Delta}$.

Choosing $r = \frac{2\rho}{1-\lambda}$, we obtain the upper bound of the second derivative 3.1) to be

$$b = \frac{2}{a^2(1-D)^2\left(1 - \frac{4\left(\frac{a-1}{a}+r\right)}{a(1-D)}\right)^{\frac{3}{2}}} \, ,$$

from which we obtain $h = (1-\lambda)^{-2} b\rho$. Fixing D, for $a > 0$ sufficiently big, we obtain $h < \frac{1}{2}$ and then there is a unique invariant torus close to initial data K. In particular, for $D = 0.1$, we obtain the crude lower bound $a > 4.6$ (for which $h < 0.45$).

Computer validation After showing the existence of the repelling curve for values $a > 4.6$, we prove (computer-assisted) the existence of the family of the repelling curve for $3.157065 \leq a \leq 5$, starting at $a = 5$. This validation has been done, using expression (4.4), by computing the initial data using the algorithms presented in subsection §4.4.2 with 30 Fourier modes (This choice of number of modes is done in order to ensure that the discarded

modes are of magnitude less than 10^{-8}). We emphasize that the width of the intervals of validation shorten as they approach to the period doubling bifurcation value $a \simeq 3.143$. The algorithm stops when the width of the intervals is less that 10^{-6}, reaching $a = 3.157065$. See figure 4.9(a).

Remark 4.4.4. The algorithm stops at a distance $1.5 \cdot 10^{-2}$ of the predicted bifurcation value because the Lyapunov multiplier (bounded by λ) of the invariant curve goes to 1, where it undergoes a smooth bifurcation.

Remark 4.4.5. In this computation we apply the validation algorithm 2800 times and the time of computation is around 307 minutes. This means that each validation step, which consists in computing the initial data, validating the existence and uniqueness of a FHIT near it, and then, checking the matching, takes around 6.5 seconds.

In order to show how the upper bounds of the validation algorithm behave near the bifurcation value, we apply the validation algorithm for values $a = 3.16 + 0.01 \cdot j$, with $j = 0, \ldots, 184$, using 30 Fourier modes. The results are displayed in figures 4.9(b), 4.9(c) and 4.9(d).

Remark 4.4.6. Interestingly, while the numerically computed initial data is produced with a non-rigorous estimate of the error of order 10^{-14}, and although the validations are done using the `FILIB++` library, which operates with intervals in `double` precision, the rigorous error bounds achieve order 10^{-10}.

Validation of the period 2 attracting curve

The goal in this subsection is to validate period 2 attracting curves near the predicted non-smooth bifurcation value $a_* \approx 3.271$. To do so, we considered the 2 times composition of the driven logistic map (4.4):

$$\begin{array}{rccc} (F,\omega)^2\colon & \mathbb{R}\times\mathbb{T} & \longrightarrow & \mathbb{R}\times\mathbb{T} \\ & (z,\theta) & \longrightarrow & (F(F(z,\theta),\theta+\omega),\theta+2\omega) \end{array} . \tag{4.11}$$

First, we perform a numerical study of the regularity of the initial data: the torus K, the transformations P_1 and P_2, and the normalized cocycle Λ. Since the associated transfer matrix M is noninvertible, we use the almost-reducibility method to compute P_1, P_2 and Λ. Figure 4.10 shows with respect to parameter a, a numerical estimate of the maximum slope of the computed initial data. Note that P_1 is the initial datum with the biggest slope. For example, at $a = 3.265$ the slope of P_1 is $4.3 \cdot 10^4$, while the slopes of the torus and the normalized cocycle are $2.4 \cdot 10^1$ and $3.07 \cdot 10^3$, respectively. Notably, at $a = 3.269$ the slope of P_1 is $4.25 \cdot 10^6$. Hence, P_1 is used in order to determine the number of Fourier modes in the validation process, because it is the initial datum with the biggest Fourier coefficients. We choose the number of modes in order that the discarded ones are of magnitude less than 10^{-8}. Figure 4.11 shows the initial data K (and M), P_1 and Λ for $a = 3.265$ and $a = 3.269$. Notice that a small change in the value of a leads to a dramatic change in the initial data.

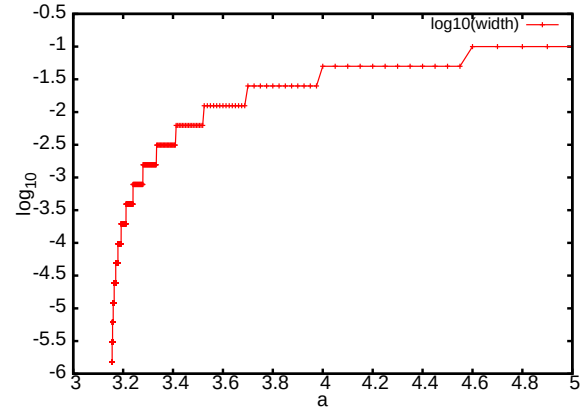

(a) Width of the intervals of the family validation.

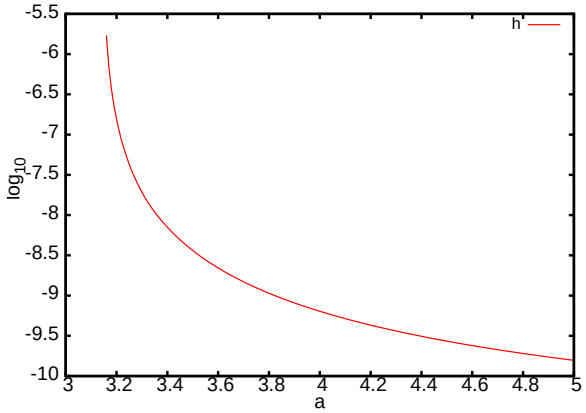

(b) h value of the validations.

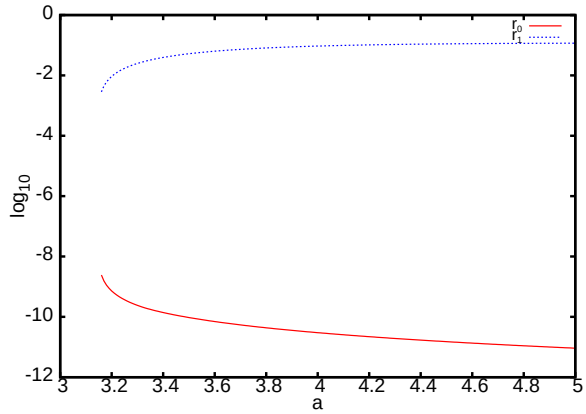

(c) r_0 and r_1 values of the validations.

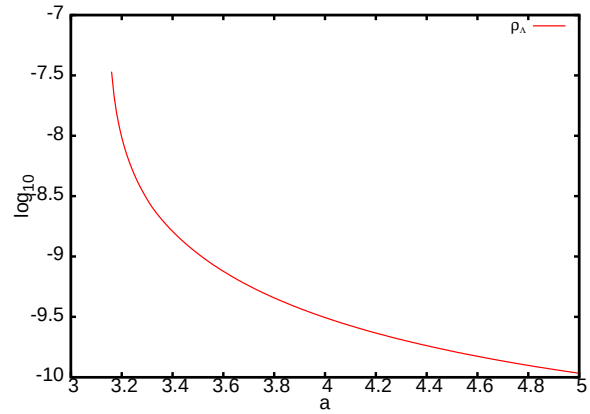

(d) ρ_Λ error values.

Figure 4.9: Data obtained of the validations of the repelling curve for $D = 0.1$.

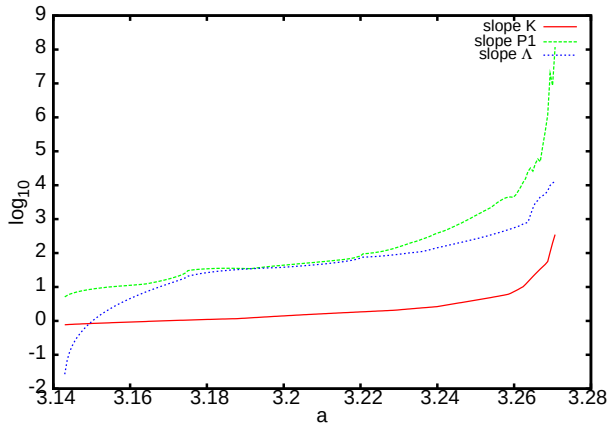

Figure 4.10: Maximum slopes of the period 2 attracting curve K (in red), its P_1 transformation (in green) and the normalized cocycle Λ (in blue), with respect to parameter a.

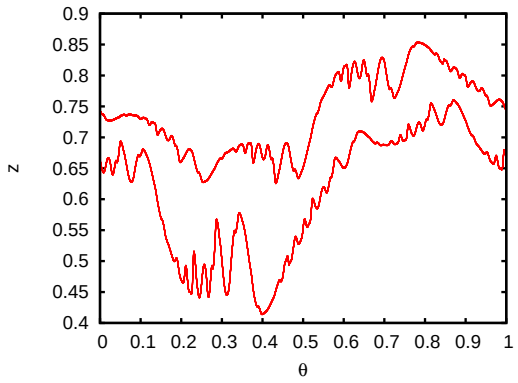

(a) Torus $K(\theta)$ and its image, for $a = 3.265$.

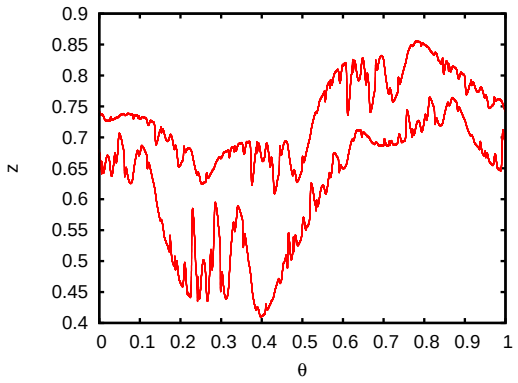

(b) Torus $K(\theta)$ and its image, for $a = 3.269$.

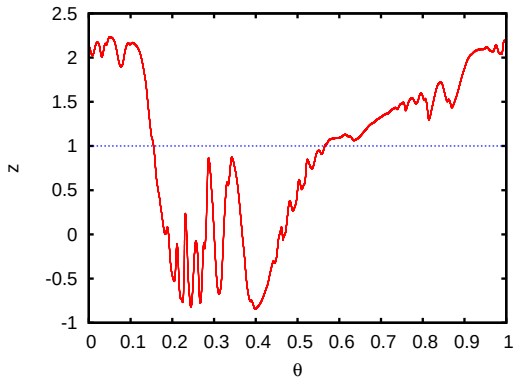

(c) Cocycle $M(\theta)$, for $a = 3.265$.

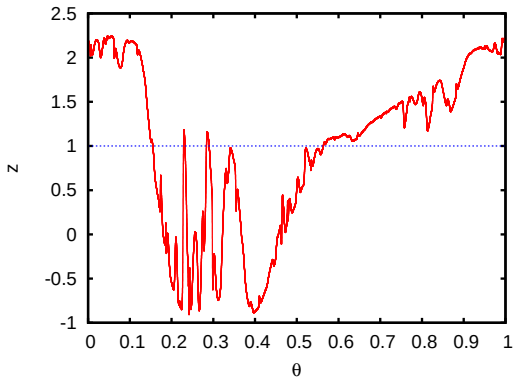

(d) Cocycle $M(\theta)$, for $a = 3.269$.

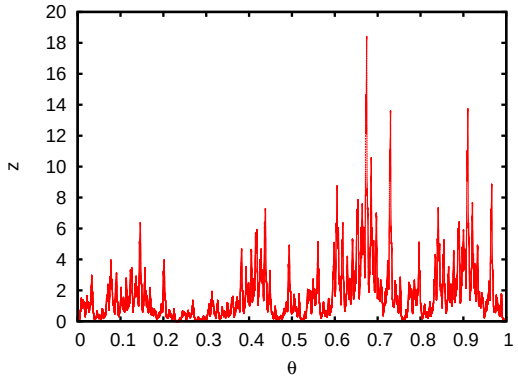

(e) Transformation $P_1(\theta)$, for $a = 3.265$.

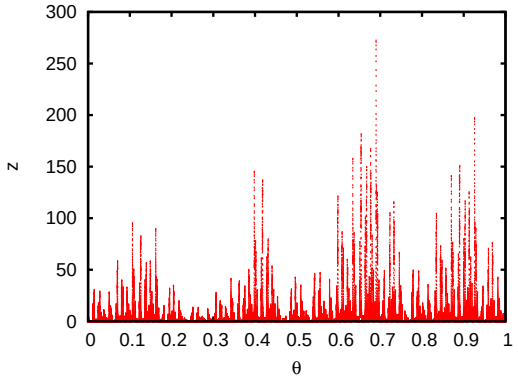

(f) Transformation $P_1(\theta)$, for $a = 3.269$.

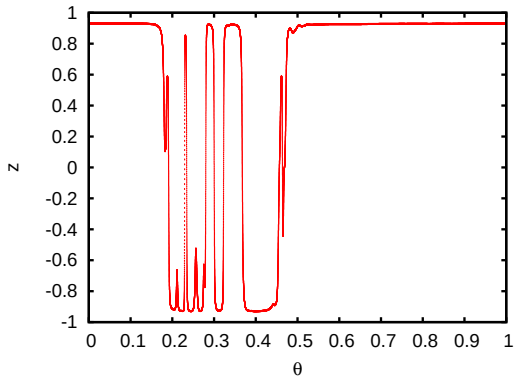

(g) Reduced cocycle $\Lambda(\theta)$, for $a = 3.265$.

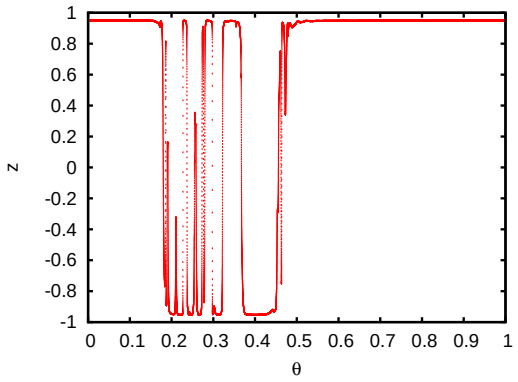

(h) Reduced cocycle $\Lambda(\theta)$, for $a = 3.269$.

Figure 4.11: Graphs of the initial data close to the breakdown of the period 2 curve.

The validation results for different values of the parameter a are shown in table 4.7. The initial data used as input are computed with high accuracy because at these parameter values, the period 2 attracting curve is near the repellor curve. Note also that in all these validations the time computation depends heavily on the regularity of the initial data, because less regularity implies the use of more Fourier modes to represent the initial data, which implies more computational time.

Remark 4.4.7. Note that in table 4.7, for the parameter value $a = 3.269$, we do not have an estimation of ρ_Λ. This is because the validation algorithm can not compute it due to the fact that the upperbound μ, see point 5.2) of theorem 4.1.2, is bigger than $\frac{1}{4}$. This means that, although we could validate the existence (and local uniqueness) of the period 2 invariant torus, we could not validate the distance between the initial data Λ_0 and the transfer operator of the truly invariant torus of the system.

a	3.265	3.268	3.269
h	3.046383e-05	2.248226e-03	4.203495e-01
r_0	5.365990e-09	1.701127e-07	3.635973e-06
ρ_Λ	5.815762e-03	4.542701e-04	-
order	3000	17000	27000
time (minutes)	5	130	361

Table 4.7: Validation results of the period 2 invariant torus of the driven logistic map for different values of **a** close to breakdown.

4.5 Example 3: computer validations on the verge of the hyperbolicity breakdown of a saddle torus

In this section we report computer validations of existence of saddle tori on the verge of their hyperbolicity breakdown for a quasiperiodically forced standard map. This phenomenon was described in [HdlL07, HdlL06a] for similar models. See also chapter §2 for a detailed exposition of this phenomenon.

4.5.1 Two bifurcation scenarios of saddle tori in the quasiperiodically forced standard map

The *quasiperiodically forced standard map* is the map $(F, \omega) : \mathbb{T} \times \mathbb{R} \times \mathbb{T} \to \mathbb{T} \times \mathbb{R} \times \mathbb{T}$ defined as

$$\begin{cases} \bar{x} &= x + \bar{y} \\ \bar{y} &= y - \frac{\kappa}{2\pi} \sin(2\pi x) - \varepsilon \sin(2\pi\theta) \\ \bar{\theta} &= \theta + \omega \end{cases} , \tag{4.12}$$

where we fix $\omega = \frac{1}{2}(\sqrt{5} - 1)$.

Remark 4.5.1. This map has been studied extensively in chapter §2. See this chapter for a detailed description of it.

For every $\kappa > 0$, there exists a family $K_\varepsilon(\theta)$ of FHIT (saddle type), with $\varepsilon \in (-\varepsilon_c, \varepsilon_c)$, such that $K_0(\theta) = \left(\frac{1}{2}, 0\right)$. Notice that $K_{-\varepsilon}(\theta) = -K_\varepsilon(\theta)$. An interesting problem is to approach as closely as possible the limiting value ε_c, the critical parameter value, and study the obstructions to fiberwise hyperbolicity.

Remark 4.5.2. Since (4.12) is area preserving, the product of the Lyapunov multipliers associated to the 1-dimensional stable and unstable subbundles is equal to 1. Then, by an abuse of notation, we refer by the Lyapunov multiplier to the maximal Lyapunov multiplier.

We perform a numerical exploration and we find that the bifurcation mechanism around ε_c depends on κ. Here we report two main examples, see also chapter §2 for a detailed exposition of these and other phenomena:

1. For low values of κ, e.g. $\kappa = 0.3$ with $\varepsilon_c \approx 1.3364054$, there is a smooth bifurcation: the hyperbolicity is broken down because the Lyapunov multiplier goes to 1 as ε goes to ε_c, but the invariant subbundles collide smoothly.

2. For high values of κ, e.g. $\kappa = 1.3$ with $\varepsilon_c \approx 1.2352755$, there is a non-smooth bifurcation: the hyperbolicity is broken down because the invariant bundles collide non-uniformly as ε goes to ε_c, and the Lyapunov multiplier stays far from 1.

See figures 4.12 and 4.14 for a graphical representation of the invariant tori and their invariant subbundles, represented by the angle α that form them with the positive semi-axis

$x > 0$, near these two bifurcations. Notice the difference between these two bifurcations: in the smooth one the invariant subbundles collide uniformly, while in the nonsmooth one the invariant subbundles collide creating sharp peaks in the collisions. Figures 4.13 and 4.15 show the Lyapunov multipliers and minimum distance between the invariant subbundles as a function of ε. Note also that, depending on the bifurcation scenario, these observables behave asymptotically differently. For a more detailed explanation of these phenomena see [HdlL07].

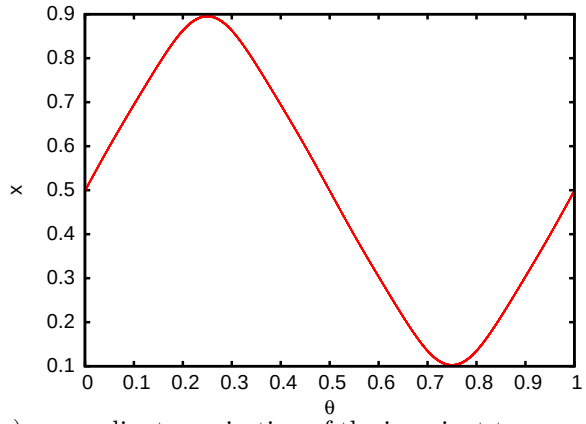

(a) x-coordinate projection of the invariant torus. $\varepsilon = 1.33$.

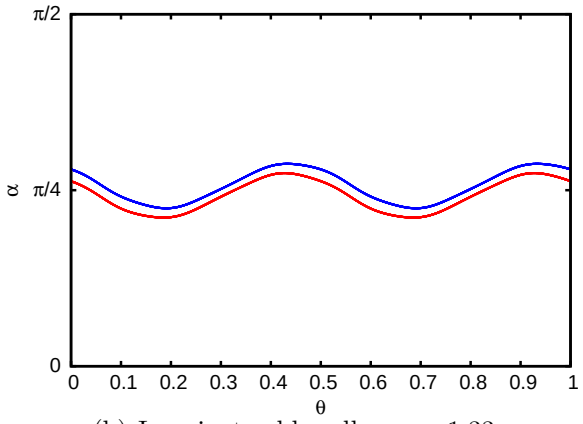

(b) Invariant subbundles. $\varepsilon = 1.33$.

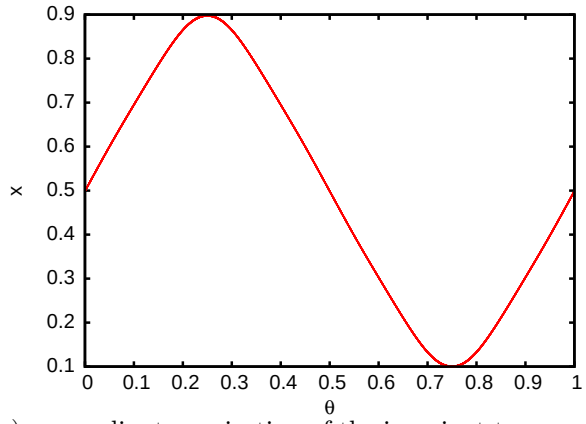

(c) x-coordinate projection of the invariant torus. $\varepsilon = 1.3364$.

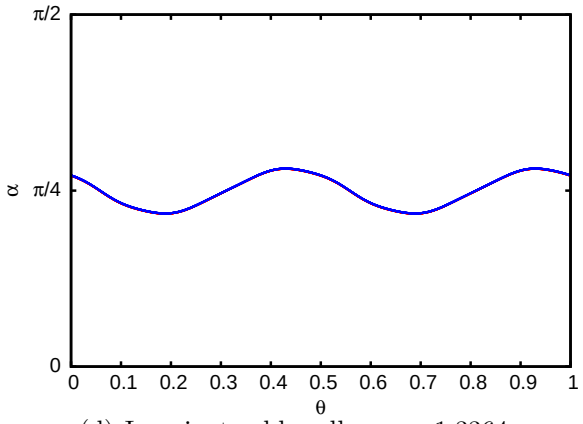

(d) Invariant subbundles. $\varepsilon = 1.3364$.

Figure 4.12: Smooth bifurcation: invariant torus and its subbundles for $\kappa = 0.3$ near the bifurcation value $\varepsilon_c \approx 1.3364054$.

Numerical estimate of the breakdown value In both examples, we compute the invariant tori and their invariant bundles, and estimate the critical values ε_c, using the different Fourier methods of [HdlL06b] and computing periodic orbits for rational approximations $\frac{p}{q}$ of the rotation number ω. These methods produce similar results. Table 4.8 reports the

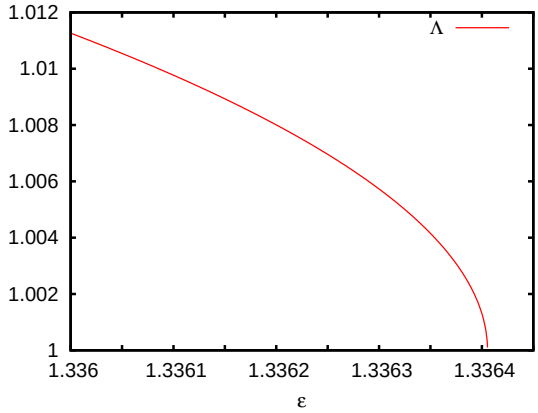

(a) Lyapunov multiplier as a function of ε.

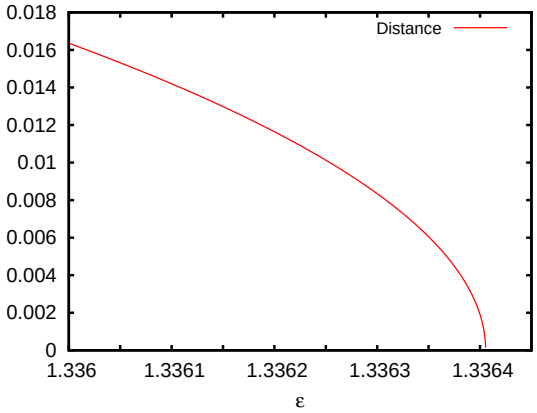

(b) Minimum distance between subbundles.

Figure 4.13: Smooth bifurcation: observables for $\kappa = 0.3$ near the bifurcation value $\varepsilon_c \approx 1.3364054$. See text for further details.

results using rational approximations of ω with $\kappa = 1.3$.

p	q	ε_c	Λ_c
610	987	**1.235277**250097	**1.41**7569758833
987	1597	**1.235276**717863	**1.42**7183182503
1597	2584	**1.235275**424968	**1.43**2628905747
2584	4181	**1.235275**700525	**1.43**3722000980
4181	6765	**1.2352755**63425	**1.43**6571048918
6765	10946	**1.235275**611145	**1.43**6207590892
10946	17711	**1.2352755**32096	**1.43**8434241268
17711	28657	**1.2352755**30445	**1.43**8634421523
28657	46368	**1.23527552**6435	**1.43**8911614742
46368	75025	**1.23527552**7297	**1.43**8984187196
75025	121393	**1.23527552**6916	**1.439**054814648
121393	196418	**1.23527552**7050	**1.439**063207687
196418	317811	**1.2352755267**94	**1.4391**15016429
317811	514229	**1.2352755267**94	**1.4391**17250462
514229	832040	**1.23527552**6885	**1.4391**18021353
832040	1346269	**1.235275526763**	**1.43912**4814800
1346269	2178309	**1.235275526763**	**1.43912**4666214
2178309	3524578	**1.235275526763**	**1.43912472**3263
3524578	5702887	**1.235275526763**	**1.43912470**1574

Table 4.8: Critical ε_c, computed with double precision, where the transition occurs and the associated Lyapunov multiplier Λ_c for each of the partial convergent of the golden mean with denominator less than $6 \cdot 10^6$. $\kappa = 1.3$. The bold digits represent the coincident digits, with respect to the values obtained for the biggest denominator.

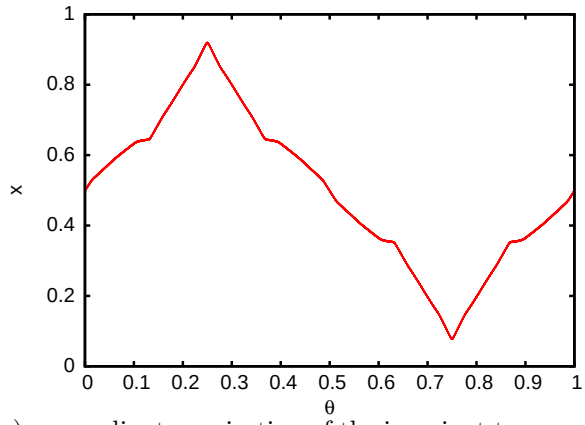

(a) x-coordinate projection of the invariant torus. $\varepsilon = 1.235$.

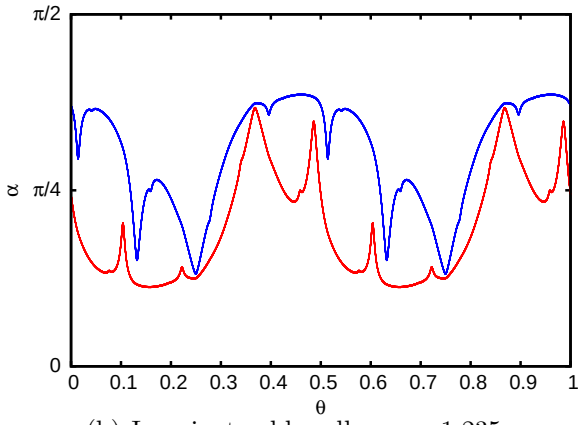

(b) Invariant subbundles. $\varepsilon = 1.235$.

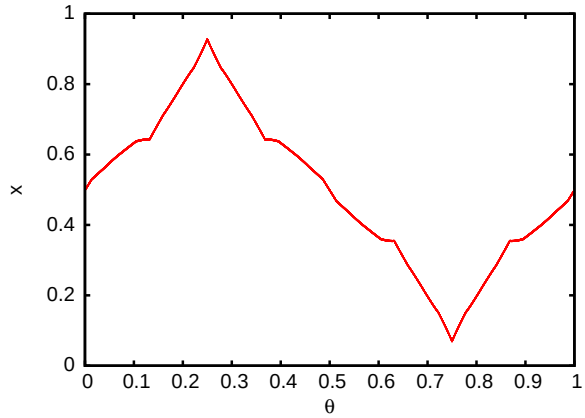

(c) x-coordinate projection of the invariant torus. $\varepsilon = 1.235275$.

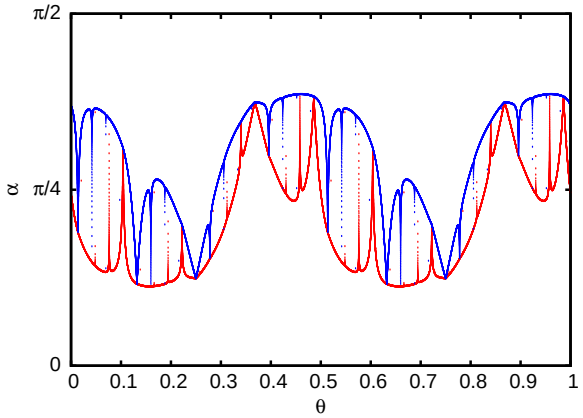

(d) Invariant subbundles. $\varepsilon = 1.235275$.

Figure 4.14: Nonsmooth bifurcation: invariant torus and its subbundles for $\kappa = 1.3$ near the bifurcation value $\varepsilon_c \approx 1.2352755$. See text for further details.

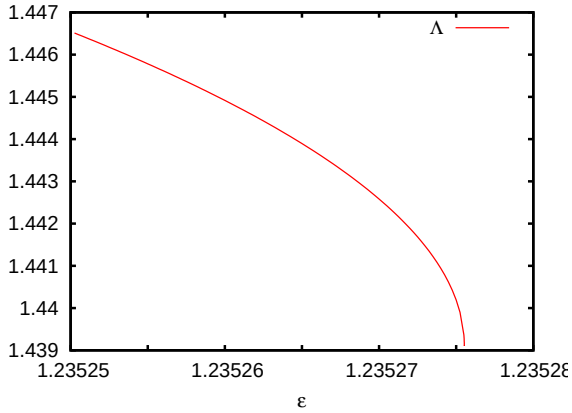

(a) Lyapunov multiplier as a function of ε.

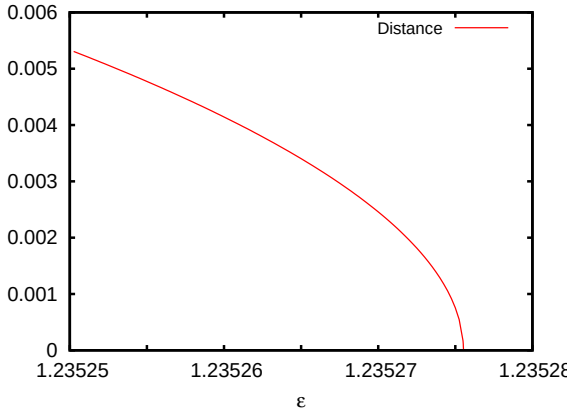

(b) Minimum distance between subbundles.

Figure 4.15: Nonsmooth bifurcation: observables for $\kappa = 1.3$ near the bifurcation value $\varepsilon_c \approx 1.2352755$.

4.5.2 Computer Validations

In this section we report computer validations of the invariant tori for the non-smooth bifurcation scenario, for $\kappa = 1.3$ with $\varepsilon_c = 1.2352755$. This is a challenging example because the invariant subbundles near the bifurcation are quite wild (SNA behavior in the projectivized cocycle, see [HP06]). Thousands of Fourier modes are needed in order to obtain good initial data for the validation algorithm.

Remark 4.5.3. In the smooth bifurcation scenario, the initial data required in order to obtain successful validations near the bifurcation value need no more than one hundred Fourier modes. For $\kappa = 0.3$, we validate the FHIT for $\varepsilon = 1.3364$, which is at a relative distance of $3 \cdot 10^{-4}$ from the estimated bifurcation value $\varepsilon_c \approx 1.3364054$.

To summarize the validations that we will present in detail, we have:

Proposition 4.5.4. *1. For the range of parameters $\varepsilon \in [0, 1.073969]$ of the system (4.12) there exists a continuous family of local uniqueness invariant saddle curves.*

2. For the parameters $\varepsilon = 10^{-2}j$, $j = 0, \ldots, 123$ of the system (4.12) there exists local unique invariant saddle curves.

3. For every parameter $\varepsilon = 1.235270, 1.235273, 1.235275$ of the system (4.12) there exists a local unique invariant saddle curve.

4.5.3 Validations

In a first run, we validate tori K_ε for values of ε in a grid of step size $\leq 10^{-2}$ of the parameter interval $[0, 1.2351]$. Note that the difference between the predicted breakdown value ε_c and the last validation $\varepsilon = 1.2351$ is less than of order $1.8 \cdot 10^{-4}$. The results of this first run are

reported in figure 4.16. We observe that, as ε increases, the upper bounds of the validation algorithm h and r_0, which measure the quality of the approximate invariant torus, increase, while the lower bound of r_1, which measures the size of the uniqueness strip, decreases. We also observe that the upper bounds μ and ρ_Λ, which measure the quality of the approximate invariant bundles, increase. The number of Fourier modes required in the validations goes from 0 to 1280.

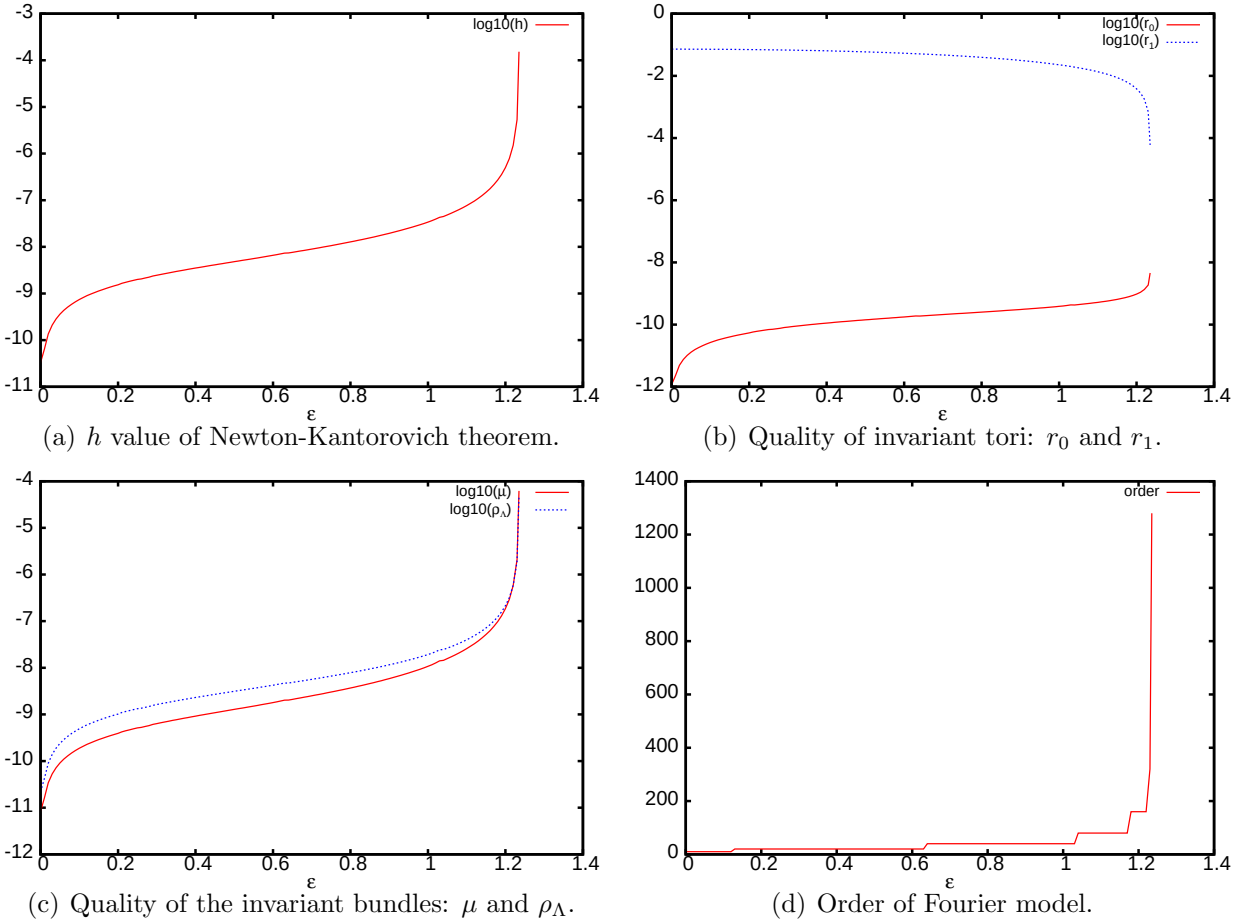

(a) h value of Newton-Kantorovich theorem.

(b) Quality of invariant tori: r_0 and r_1.

(c) Quality of the invariant bundles: μ and ρ_Λ.

(d) Order of Fourier model.

Figure 4.16: Data output obtained from the validations of the invariant tori and their invariant bundles for $\kappa = 1.3$ with respect to ε. See text for further details.

In order to illustrate the validation algorithm for families of FHIT, we use it to validate the whole family in the parameter interval $\varepsilon \in [0, 1.073969]$, with Fourier models of order 100. The main problem if we try to validate the family further is that the width of the parameter intervals required in the algorithm is too small, of order 10^{-6}.

Remark 4.5.5. A possible way, not developed in this chapter, to refine the validation algorithm for families of FHIT is to reformulate it in terms of Fourier-Taylor models, where one can expand the Fourier coefficients of the initial data with respect to the parameters of

the family in Taylor polynomials. The authors plan to come back to this issue in the near future.

In a final run, we validate the initial data for the values $\varepsilon = 1.235270, 1.235273, 1.235275$, with Lyapunov multipliers $\Lambda = 1.442582, 1.441463, 1.440193$, respectively, in order to check the applicability of the validation algorithm extremely close to the non-smooth bifurcation. The obtained results are shown in table 4.9. Note that the difference between 1.235275 and the predicted bifurcation value, 1.2352755, is less than $5.3 \cdot 10^{-7}$.

ε	1.235270	1.235273	1.235275
h	2.853269e-03	8.140590e-03	8.928078e-02
r_0	1.302039e-07	2.490723e-07	1.035418e-06
r_1	9.100589e-05	6.069352e-05	2.107294e-05
μ	1.825306e-03	5.188943e-03	3.841927e-02
ρ_Λ	1.370355e-03	3.900239e-03	2.985134e-02
order	5802	7918	27692
time (minutes)	103	154	1094

Table 4.9: Validation results of invariant tori of the quasiperiodically forced standard map for three ε values near the predicted breakdown. Note that the order of the Fourier models and the time of validation, increase as ε increase.

4.6 Final comments

A moral of this chapter is that good numerics lead to successful validations. Notably, knowledge of the dynamics around the torus is an important ingredient for an accurate numerical computation.

An issue is the precision (`single, double, long double, multiple`) of the interval package. The one used, `FILIB++`, is `double` precision. This, of course, has its limitations, and if we want to validate invariant tori more precisely, then we will need a multiprecision library, but the procedure for validate the invariant tori remains the same. An example where a multiprecision library is needed is [CS10].

The computational time of the validation algorithms depends heavily on the regularity of the initial data, and hence, their number of Fourier modes. The most time-consuming computations with Fourier models are the product and the evaluation. Although the times reported in this chapter correspond to computations with a single processor, we have also used the library `OpenMP` (see [CJvdP07]) in order to have parallel computations (by distributing the product and evaluation routines on the processors).

The models worked out in this chapter have simple analytic expressions. But our validation algorithms can be applied to more general models, as long as we are capable of evaluating the map (and its first and second derivatives). For instance, for a skew product flow, we can consider its Poincaré map with the variationals [BM98, WZ07].

Chapter 5

Numerical tools

In this chapter we present the notable computer tools used in the thesis: computation of invariant tori via the periodic orbits method, computation of the invariant bundles and Lyapunov exponents of a linear cocycle, computation of the fibered rotation number and spectrum of a Schrödinger operator, and rigorous manipulation of Fourier models for the computer-assisted proofs of FHIT. Other numerical techniques, like integration of ODEs [Sim90], or computation of Fast Fourier Transforms (which are done with the C package `FFTW`, see [FJ05]), used in the thesis are not discussed in this chapter because they are quite standard and are not in the main focus of the thesis.

Remark 5.0.1. In few pages we summarize the codes we developed, which are of considerable length. We estimate that there are around 500.000 lines of code.

5.1 Computation of invariant tori in quasiperiodic skew products

In this thesis we compute two types of tori: attracting tori in dissipative systems and saddle type tori in area, and volume, preserving skew product systems of the form

$$\begin{array}{rccc} (F,\omega): & \mathbb{R}^n \times \mathbb{T} & \longrightarrow & \mathbb{R}^n \times \mathbb{T} \\ & (z,\theta) & \longrightarrow & (F(z,\theta), \theta+\omega) \end{array}, \tag{5.1}$$

where ω is an irrational number and F is differentiable enough, even analytic. The invariance equation of an invariant torus $z\colon \mathbb{T} \longrightarrow \mathbb{R}^n$ is

$$F(z(\theta),\theta) = z(\theta+\omega). \tag{5.2}$$

For the computation of an attracting torus, we use the iteration method: Given an initial point (z_0,θ_0), near the invariant torus, iterate it forwards a fixed amount of times N. After these iterations, the point is near the invariant torus, so iterating another fixed amount of times, the orbit described by it approximates the torus.

For the computation of saddle type tori the iteration method does not work, due the hyperbolic nature of the objects, hence it is needed more refined techniques to compute them. In the literature there are several methods to numerically compute them. These methods can be splitted in two big families:

5.1.1 Fourier's method:

To solve (1.2) write down the torus z via its Fourier series as

$$z(\theta) = \sum_{k \in \mathbb{Z}} z_k e^{2\pi \mathbf{i} k \theta}$$

and try to find the unknowns z_k. As we are dealing with a numerical problem we truncate the Fourier series as a finite sum of terms with index $|k| < N$. Then, apply Newton's method for the non-linear system of equations with unknowns z_k. See [Jor01], [HdlL06b] for a discussion of several applications and variations of this method.

Remark 5.1.1. Fourier methods inspire the numerical tools used in the Computer-Assisted Proofs in chapter §4.

Remark 5.1.2. The Fourier's method is applied, in the form presented in [HdlL06b], in the computation of the initial data of the FHIT for the computer validations presented chapter §4.

5.1.2 Periodic orbits method:

Approximate the irrational number ω by a rational number $\hat{\omega} = \frac{p}{q}$ (a partial convergent) and replace the skew product (F, ω) by $(F, \hat{\omega})$. Since the invariant torus that we want to compute persists under small perturbations of the skew product, see chapter §1, an invariant torus of $(F, \hat{\omega})$ approximates an invariant torus of (F, ω), if q is large enough. Now, the invariant torus of $(F, \hat{\omega})$ is foliated by periodic orbits, so compute one of these periodic orbits.

Remark 5.1.3. The periodic orbits method is applied in the computation of the FHIT of chapters §2, §3 and §4. The periodic orbits method allows to "*compute*" the invariant objects that remain after the breakdown of the invariant tori.

Remark 5.1.4. One of the goals of the periodic orbits method is to give hints of renormalization. In this line, it has some similarities with the methods used in KAM context, see for example [Gre79, Har98], where KAM tori are computed by approximating them by the Birkhoff periodic orbits that surround them. The main difference of both methods is that, in KAM context, the computed periodic orbits does not belong to an invariant torus, while in the FHIT context, they belong to an invariant torus in a nearby skew product.

The error produced by the periodic orbits method can be estimated as follows: given a skew product (F, ω) and a rational approximation of ω, $\hat{\omega} = \frac{p}{q}$, let $z \colon \mathbb{T} \longrightarrow \mathbb{R}^n$ be an

invariant torus of the skew product $(F, \hat{\omega})$, computed by the peridic orbits method. Then, it is satisfied that $||F(z(\theta), \theta) - z(\theta + \hat{\omega})|| \leq \epsilon_1$. Hence, the error that produces z as a parameterization of an invariant torus of (F, ω) is

$$e = ||F(z(\theta), \theta) - z(\theta + \omega)|| = ||(F(z(\theta), \theta) - z(\theta + \hat{\omega})) + (z(\theta + \hat{\omega}) - z(\theta + \omega))|| \,.$$

Now, using $|\omega - \hat{\omega}| < \epsilon_2$ we have that

$$e \simeq \epsilon_1 + ||\mathrm{D}z(\theta)||\, \epsilon_2.$$

Remark 5.1.5. Since the irrational rotation ω is approximated by its partial convergents $\frac{p}{q}$, the difference $\left|\omega - \frac{p}{q}\right|$ is less than $\frac{1}{q^2\sqrt{5}}$, with equality only if ω is the golden mean, see [HW08].

Now, let's explain the algorithm: Fix the rational approximation $\hat{\omega} = \frac{p}{q}$ and $\theta_0 \in \mathbb{T}$. The goal is to compute the periodic points $z_0 = z(\theta_0), z_1 = z(\theta_0 + \hat{\omega}), \ldots, z_{q-1} = z(\theta_0 + (q-1)\hat{\omega}), z_q = z(\theta_0 + q\hat{\omega}) = z(\theta_0) = z_0$. This computation is done by applying Newton's method on the system of non-linear equations (shooting method)

$$\left\{ \begin{array}{rcl} F(z_{q-1}, \theta_0 + (q-1)\hat{\omega}) - z_0 &=& 0 \\ F(z_0, \theta_0) - z_1 &=& 0 \\ F(z_1, \theta_0 + \hat{\omega}) - z_2 &=& 0 \\ \vdots & & \\ F(z_{q-2}, \theta_0 + (q-2)\hat{\omega}) - z_{q-1} &=& 0 \end{array} \right. . \tag{5.3}$$

The main obstruction to solve (5.3) via Newton's method is the dimension of the system, which is nq, because, at each step, it is needed to solve a linear system with dimension $nq \times nq$, which is prohibitive, in terms of memory, for moderate values of q. We handle this problem by taking advantage of the sparseness nature of the system: it is applied a taylored version of `LU` method with row partial pivoting. That is, we apply the `LU` method with partial pivoting to $q \times q$ block-matrices of the form

$$\begin{pmatrix} x & 0 & & & \cdots & & x \\ x & x & 0 & & & & 0 \\ 0 & x & x & 0 & & & \\ & 0 & x & x & 0 & & \\ \vdots & & & \ddots & \ddots & & \\ 0 & & & & x & x & 0 \\ 0 & 0 & & \cdots & 0 & x & x \end{pmatrix}, \tag{5.4}$$

where the x's are the only non-zero $n \times n$ block-coefficients. Let's denote by A_0 the block-matrix (5.4), that is the 0th step of the `LU` factorization. Then, the block-coefficients of A_0 are

$$A_0(i,j) = \left\{ \begin{array}{ll} x & \text{if } j = i \text{ or } j = i - 1 \pmod q \\ 0 & otherwise \end{array} \right. .$$

After the first iteration of LU, the block-matrix A_1 has the form

$$\begin{pmatrix} x & x & 0 & & \cdots & & x \\ 0 & x & 0 & & & & x \\ 0 & x & x & 0 & & & 0 \\ & 0 & x & x & 0 & & \\ \vdots & & & \ddots & \ddots & & \\ 0 & & & & x & x & 0 \\ 0 & 0 & \cdots & & 0 & x & x \end{pmatrix}, \tag{5.5}$$

and after the second iteration, the block-matrix A_2 has the form

$$\begin{pmatrix} x & x & 0 & & \cdots & & x \\ 0 & x & x & 0 & & & x \\ & 0 & x & 0 & & & x \\ & 0 & x & x & 0 & & 0 \\ \vdots & & & \ddots & \ddots & & \\ 0 & & & & x & x & 0 \\ 0 & 0 & & \cdots & 0 & x & x \end{pmatrix}. \tag{5.6}$$

In general, after k iterations of LU, the block-coefficients of the matrix A_k are

$$A_k(i,j) = \begin{cases} x & \text{if } i < k, \text{ and } j = i, j = i+1, \text{ or } j = q-1 \\ x & \text{if } i = k, \text{ and } j = i, \text{ or } j = q-1 \\ x & \text{if } q > i > k, \text{ and } j = i \text{ or } j = i-1 \\ 0 & \textit{otherwise} \end{cases}.$$

Observe that the memory storage of the matrix A_k, at each step k, requires only q rows with three $n \times n$ non-zero coefficients. This implies that there is no need to store all the matrix A_0 for the computation of the LU method, but only q rows with 3 $n \times n$ non-zero coefficients.

Remark 5.1.6. The time computation depends linearly with respect nq. When n is equal 2 or 3, we have solved non-linear systems like 5.3 of order $q \simeq 10^7$ with less than 1 minute on a desktop computer.

Remark 5.1.7. In some examples, like the "*non-linear Schrödinger equations*" in chapters §2 and §3, we use this special "*non-linear Schrödinger*" structure to adapt the LU method to solve the system of non-linear equations (5.3).

We finish this subsection by showing how to compute the derivatives of an invariant torus $z\colon \mathbb{T} \longrightarrow \mathbb{R}^n$ of (5.1). Without loss of generality, we explain here the first derivative. This satisfies the equation

$$D_z F(z(\theta),\theta) z'(\theta) + D_\theta F(z(\theta),\theta) = z'(\theta+\omega). \tag{5.7}$$

Note that (5.7) is a linear equation that, if we implement it using a system like (5.3), we obtain that its matrix is the same as of the system (5.3) that arises when computing the invariant torus, and its independent term is the evaluations of $D_\theta F(z(\theta),\theta)$ at $\theta_k = \theta_0 + k\omega$ for $k = 0,\ldots,q-1$. Hence, we use the adapted `LU` method to solve this system.

5.2 Invariant bundles of linear cocycles and Lyapunov exponents

Let

$$\begin{array}{rccc}(M,\omega): & \mathbb{R}^n\times\mathbb{T} & \longrightarrow & \mathbb{R}^n\times\mathbb{T}\\ & (v,\theta) & \longrightarrow & (M(\theta)v,\theta+\omega)\end{array} \tag{5.8}$$

be a linear cocycle with invertible transfer matrix M. Here we describe how to compute its invariant bundles when ω is rational, $\frac{p}{q}$, because we are interested in the invariant bundles of the approximations of FHIT computed using the periodic orbits method described in the previous section. See [HdlL06b, HdlL07, PS10, PS11] for a collection of papers using similar techniques of the ones described here.

First, we present the 2D case and then, derive the 3D case.

5.2.1 2D cocycles:

The invariant unstable and stable bundles, if they exist, are 1D. Since the stable bundle is the unstable bundle under the action of the inverse of (5.8), we only detail here the computation of the unstable bundle.

Fix $(v_0,\theta_0)\in\mathbb{R}^2\times\mathbb{T}$ at random, with $||v_0||=1$, and fix N_{prev}, N_{max}, M (with $M<N_{max}$) and ϵ (tolerance) small. Denote by

$$\hat{v}_{k+1} = \frac{M(\theta_0+k\omega)\hat{v}_k}{L_k},$$

where $L_k = ||M(\theta_0+k\omega)\hat{v}_k||$, $\hat{v}_0 = v_0$.

Then, the algorithm for the computation of the unstable bundle goes as follows:

1. Iterate $N_{prev}q$ times the point $(\hat{v}_0,\theta_0)$ to obtain the point $(\hat{v}_{N_{prev}q},\theta_{N_{prev}q}) = (\hat{v}_{N_{prev}q},\theta_0)$.
2. Set $\lambda_0 = 0$.
3. Iterate, as in the first point, the point $(\hat{v}_{N_{prev}q},\theta_0)$. Compute also $\lambda_{k+1} = \lambda_k + \log(L_{k+N_{prev}q})$. After mq iterations, $1\le m\le N_{max}$, check if

$$\left|\frac{\lambda_{mq}}{mq} - \frac{\lambda_{(m-1)q}}{(m-1)q}\right| < \epsilon. \tag{5.9}$$

   Stop the algorithm when the condition (5.9) has been satisfied at least M times or when $k = N_{max}q$.

When the algorithm finishes, the q last iterations approximate the unstable bundle and $\frac{\lambda_{mq}}{mq}$ approximates the Lyapunov exponent.

Remark 5.2.1. This method resembles the power method used to compute leading eigenvalues of matrices.

Remark 5.2.2. The fibered rotation number associated to the unstable bundle can be computed at the same time as the computation of the Lyapunov exponent. At point 2. of the algorithm, we define a counter $R = 0$. Then, at point 3., every time we compute the unit vectors $\hat{v}_k$, we check if $\hat{v}_{k-1}\hat{v}_k < 0$, if so, we add one to R. Then, at the end of the algorithm, an approximation of the fibered rotation number is $\frac{R}{mq}$.

Remark 5.2.3. If one knows in advance that the Lyapnov exponent is near some value, say Λ, then one can choose as N_{prev} the integer part of $e^{\frac{1}{\Lambda}}$.

Remark 5.2.4. In general, we have obtained good results with the choice of $N_{max} = 10N_{prev}$, $M = \frac{N_{max}}{100}$ and $\epsilon = 10^{-6}$. We have observed that when the invariant bundles are continuous we can achieve errors of order $\epsilon \simeq 10^{-14}$.

5.2.2 3D cocycles:

The invariant unstable and stable bundles, if they exist, satisfy that the sum of their dimensions is 3. Without loss of generality, we suppose that the unstable bundle, E^u, is 2D and it is spanned by the invariant fast and slow unstable subbundles; and the stable bundle, E^s, is 1D.

The computation of the 2D unstable bundle is done using the same iteration scheme in the 2D case explained above with the adjoint cocycle explained in chapter §1. Also, the 2D invariant bundle that is spanned by the slow unstable subbundle and the stable bundle is computed by the iteration of the inverse of the 2 exterior cocycle.

The computation of the 1D stable bundle is done via the iteration of the inverse of the cocycle (5.8). Also, the 1D fast unstable subbundle is computed via the iteration method applied to the cocycle (5.8).

Finally, once the 2D invariant bundle E^u and the 2D invariant bundle, spanned by the slow unstable subbundle and the stable bundle, are computed, the slow unstable subbundle is simply the intersection of the former two.

5.3 Fibered rotation number and spectrum of Schrödinger operators

Here we describe the numerical computation of the fibered rotation number and the spectrum of Schrödinger operators. See [MMS89, Har98] and [Pui04b, PS10, PS11] for similar algorithms.

Let's denote by H be the Schrödinger operator

$$(Hx)_n = x_{n+1} + x_{n-1} + V(\theta_0 + n\omega)x_n, \tag{5.10}$$

where $V\colon \mathbb{T} \to \mathbb{R}$ is continuous and ω is irrational, and consider the truncated operator $H_{(N,M)}$, acting on $\mathbb{R}^{M-N}$, defined as

$$(H_{(N,M)}x)_n = \begin{cases} V(\theta_0 + n\omega)x_n + x_{n+1} & \text{if } n = 0 \\ x_{n-1} + V(\theta_0 + n\omega)x_n + x_{n+1} & \text{if } 0 < n < M - N - 1 \\ x_{n-1} + V(\theta_0 + n\omega)x_n & \text{if } n = M - N - 1 \end{cases} \tag{5.11}$$

This linear operator has, as matrix representation, a tridiagonal matrix with 1 in the sub-diagonals and $V(\theta_0 + n\omega)$ in the diagonal. Let's denote by the *averaged signature* of the matrix $H_{(N,M)}$ the number of eigenvalues less than 0 divided by $|N - M|$.

As we saw in chapter §1, the averaged signature of $H_{(N,M)}$, as $|N - M| \to \infty$, stabilizes and the limit is the fibered rotation number, up to a factor 2π, that is, the fibered rotation number is 2π times the signature.

In order to compute the fibered rotation number, we have used an algorithm based on the following theorem, see [GVL96]:

Theorem 5.3.1 (Sturm Sequence Property)**.** *Lets denote by T_r, where $r = M - N - 1$, the matrix $H_{(N,M)}$ and denote by T_s, $s < r$, its dominant $(s+1) \times (s+1)$ matrix. Lets denote by a_i the diagonal components of T_r. If we denote by Δ_s the determinant of T_s, there is the recursion formula*

$$\Delta_s = a_s\Delta_{s-1} - \Delta_{s-2} \tag{5.12}$$

where $\Delta_{-1} = 1$ and $\Delta_0 = a_0$.

Then the number of sign changes in the sequence

$$\{\Delta_{-1}, \Delta_0, \Delta_1, \ldots, \Delta_r\} \tag{5.13}$$

is equal to the signature of T_r.

This theorem can not be applied directly to the computation of the fibered rotation number due to numerical instabilities: Δ_s grows exponentially. In order to do applicable this theorem we control the growth of the determinants. To do this we use the fact that computing Δ_s, under the action of (5.12), is the same as computing it under the action of the cocycle with transfer matrix $A(\theta)$

$$\begin{pmatrix} V(\theta) & -1 \\ 1 & 0 \end{pmatrix},$$

where the initial data is $\theta = \theta_0$ and $v_0 = (\Delta_{-1}, \Delta_0)$, so $v_k = (\Delta_{k-1}, \Delta_k)$. Since we are only interested in the number of sign changes of (5.13), when iterating the cocycle we normalize by the norm.

To compute the spectrum we use the result, see chapter §1, that the spectrum are the λ's that the fibered rotation number of the Schrödinger operator $H - \lambda Id$ is increasing. So, the spectrum is computed by applied the previous method to compute fibered rotation numbers with combination of the bisection method with respect the variable λ.

Remark 5.3.2. All the spectra and fibered rotation numbers computed in chapter §2 are done by substituting ω in equation (5.10) by a partial convergent.

5.4 Rigorous manipulation of Fourier models

Here we detail the implementation of Fourier models, assuming the reader is familiar with interval computations [Moo66, Tuc11, Zgl]. In what follows, when we refer to as a interval we mean a compact interval. The result of an operation with intervals is an interval that encloses the result. This is what one can do when implementing interval operations in a computer.

Notation 5.4.1. Given an interval $J = [a, b]$, we denote $J^- = a, J^+ = b$. The modulus of an interval is $|J| = \max(|J^-|, |J^+|)$.

Remark 5.4.2. We have coded a `C++` package to manage rigorously Fourier models. The intervalar arithmetic is done with the help of the `fi-lib++` package, see [HK97].

Definition 5.4.3. A (one dimensional, real) *Fourier model* of order $m \geq 0$ is a couple $\hat{G} = (G(\theta), R)$, where

$$G(\theta) = A_0 + \sum_{k=1}^{m} \big(A_k \cos(2\pi k\theta) + B_k \sin(2\pi k\theta)\big)$$

is a trigonometric polynomial with interval *coefficients* $A_0, \ldots, A_m$, $B_1, \ldots B_m$, and the *remainder* $R = R(\hat{G})$ is an interval. Abusing notation, we denote $B_0 = \{0\}$, and for all $k > m$ we define $A_k = B_k = \{0\}$. We also mean by Fourier model of order -1 as an interval R.

We say that a continuous function $f\colon \mathbb{T} \to \mathbb{R}$ belongs to the Fourier model $\hat{G}$, denoted $f \in \hat{G}$, if for all $\theta \in \mathbb{T}$, $f(\theta) \in A_0 + \sum_{k=1}^{m} (A_k \cos(2\pi k\theta) + B_k \sin(2\pi k\theta)) + R$.

Let $\hat{G}, \hat{H}$ be two Fourier models. We say that $\hat{G}$ is enclosed by $\hat{H}$, $\hat{G} \subset \hat{H}$, iff for any continuous periodic function $f\colon \mathbb{T} \to \mathbb{R}$, $f \in G$ implies $f \in H$.

Given an interval J, the image of J under the Fourier model $\hat{G}$ is defined as $\hat{G}(J) = G(J) + R(\hat{G})$, where $G(J)$ is the interval image of J under the trigonometric polynomial with interval coefficients G. That is, $\hat{G}(J) = \{f(\theta) \in \mathbb{R} \mid f \in \hat{G}, \theta \in J\}$. The image of $\hat{G}$ is $\hat{G}([0, 1])$. The supremum norm is the non-negative number $||\hat{G}|| = |\hat{G}([0, 1])|$. An upper bound of the supremum norm is the ℓ^1-norm $||\hat{G}||_1 = |A_0| + \sum_{k=1}^{m} (|A_k| + |B_k|) + |R|$.

Remark 5.4.4. The computer implementation of $\hat{G}(J)$ obtains an enclosure E of the result, i.e. $\hat{G}(J) \subset E$. In order to avoid large overestimations, specially in cases in which the functions $f \in \hat{G}$ behave wildly, we consider suitable subdivisions $J = \bigcup_{i=1}^{n} J_i$ in subintervals J_i, computing the enclosures E_i of the $\hat{G}(J_i)$.

Definition 5.4.5. Let $\hat{G} = (G(\theta), R)$ be a Fourier model of order m, and $\ell \geq 0$. We define the ℓ-tail of $\hat{G}$ as $\hat{G}_{>\ell} = (G_{>\ell}(\theta), R)$, where $G_{>\ell}(\theta)$ is the intervalar Fourier polynomial $\sum_{k=\ell+1}^{m} (A_k \cos(2\pi k\theta) + B_k \sin(2\pi k\theta))$. We define the ℓ-enclosure of $\hat{G}$ as $\hat{G}_{\leq\ell} = (G_{\leq\ell}, \hat{G}_{>\ell}([0,1]))$, where $G_{\leq\ell}(\theta) = A_0 + \sum_{k=1}^{\ell} \left(A_k \cos(2\pi k\theta) + B_k \sin(2\pi k\theta)\right)$. Abusing notation, $\hat{G}_{>-1} = \hat{G}$, $\hat{G}_{\leq -1} = \hat{G}([0,1])$.

Given a d-variable function $\varphi(x_1, \ldots, x_d)$, and d Fourier models $\hat{G}_1, \ldots, \hat{G}_d$, we are interested in computing a Fourier model $\hat{H}$ enclosing the composition $\varphi \circ \hat{G}$, where $\hat{G} = (\hat{G}_1, \ldots, \hat{G}_d)$. That is, we want that, for all $\theta \in \mathbb{T}$, $\varphi(\hat{G}(\theta)) \subset H(\theta)$. We will consider here the case that φ is elementary (in the Liouville sense), that is we will assume the φ is a combination of finitely many arithmetic operations and compositions with simple functions (or intrinsic functions [RMB05]) such as the power function, the exponential function or the trigonometric functions.

The arithmetic operations with Fourier models are defined as follows. Addition and subtraction of two Fourier models $\hat{G}$ and $\hat{H}$ is defined componentwise:

$$\hat{G} + \hat{H} = (G(\theta) + H(\theta), R(\hat{G}) + R(\hat{H})) \ , \ \hat{G} - \hat{H} = (G(\theta) - H(\theta), R(\hat{G}) - R(\hat{H})).$$

If J is an interval, we define the multiplication of $\hat{G}$ with J as

$$J \cdot \hat{G} = (JG(\theta), JR).$$

The product of $\hat{G}$ and $\hat{H}$ is

$$\hat{G} \cdot \hat{H} = (G(\theta)H(\theta), G([0,1])R(\hat{H}) + H([0,1])R(\hat{G}) + R(\hat{G})R(\hat{H})).$$

In order to bound the order of the Fourier models through the operations in a computation, we in fact compute enclosures of the products. For instance, if $\hat{G}$ and $\hat{H}$ are two Fourier models of order m, their m-product is the m-enclosure of the product, i.e. $(\hat{G} \cdot \hat{H})_{\leq m}$.

Once we have defined the arithmetic operations with Fourier models, compositions with polynomials are straightforward. If $P(x) = C_0 + C_1 x + C_2 x^2 + \ldots + C_n x^n$ is a polynomial with interval coefficients, we compute the composition $P \circ \hat{G}$ using a Hörner scheme:

$$P(\hat{G}) = C_0 + \hat{G} \cdot \left(C_1 + \hat{G} \cdot \left(C_2 + \cdots + \hat{G} \cdot \left(C_{n-1} + C_n \cdot \hat{G}\right) \cdots\right)\right).$$

Since the order of the composition is n times the order m of $\hat{G}$, we usually substitute each product of Fourier models in the Hörner scheme by the corresponding m-product. Hence, we obtain an enclosure of order m of the composition of $\hat{G}$ with P.

Enclosures of the compositions of Fourier models with simple functions, such as the exponential, power function, logarithm, etc. can be performed with the aid of the corresponding Taylor polynomial approximations (and bounds of the Lagrange errors). We consider here the composition with the sine and cosine functions, which are the ones that appear in our examples.

Given $\ell > 0$, let $S_\ell(x)$, $C_\ell(x)$ be the Taylor polynomials of degree ℓ of the sine and cosine functions, respectively. Let

$$\hat{S}_\ell(x) = S_\ell(x) + \frac{[-1,1]}{(\ell+1)!}x^{l+1} \ , \hat{C}_\ell(x) = C_\ell(x) + \frac{[-1,1]}{(\ell+1)!}x^{l+1}$$

be the corresponding polynomials with Lagrange error bounds. Then, the compositions of (F, ω) with the sine and cosine functions are enclosed in

$$\begin{aligned}\sin_\ell(\hat{G}) &= \sin(A_0) \cdot \hat{C}_\ell(\hat{G}_{>0}) + \cos(A_0) \cdot \hat{S}_\ell(\hat{G}_{>0}) \ , \\ \cos_\ell(\hat{G}) &= \cos(A_0) \cdot \hat{C}_\ell(\hat{G}_{>0}) - \sin(A_0) \cdot \hat{S}_\ell(\hat{G}_{>0}) \ ,\end{aligned}$$

respectively. In computer implementations, the order ℓ of the Taylor polynomials is chosen such that $\left|\frac{1}{(l+1)!}(\hat{G}_{>0}[0,1])^{l+1}\right|$ is less than a given tolerance. We also use m-products in the intermediate computations.

Another operation used is the shift of a Fourier model $\hat{G} = (G(\theta), R)$ by an (interval) rotation ω. This is the Fourier model $S_\omega(\hat{G}) = (S(\theta), R)$, with $S(\theta) = A_0 + \sum_{k=1}^{m} (A'_k \cos(2\pi k\theta) + B'_k \sin(2\pi k\theta))$, where

$$A'_k = B_k \cos(2\pi k\omega) - A_k \sin(2\pi k\omega) \ , \ B'_k = A_k \cos(2\pi k\omega) + B_k \sin(2\pi k\omega).$$

Remark 5.4.6. For the validation algorithms, we also use vector and matrix Fourier models, that are implemented straightforwardly.

Appendix A

Strange Non-Chaotic Saddles in projective 3D cocycles

In this appendix we present two simple examples of 3D continuous linear cocycles which satisfy that their M spectrum are annuli containing the unit circle but they do not have continuous 1D bundles. This question was explored in the paper [Joh87], where the author found an example in the context of continuous linear cocycles with almost-periodic coefficients.

We want to point out that a 3D cocycle with positive Lyapunov exponent with no continuous 1D bundles has a Strange Non-Chaotic Saddle in its projective cocycle. This goes as follows: the 3D cocycle has three measurable 1D invariant bundles, one expanding, one contracting and one with Lyapunov exponent equal zero (central bundle). The central bundle is the Strange Non-Chaotic Saddle, because the planes that pass through it and both the expanding and contracting bundles are its unstable and stable bundles (in the projective cocycle). It is Strange because because it is only measurable and not continuous, it is non-Chaotic because its inner dynamics is quasiperiodic, and it is a Saddle because it has non zero Lyapunov exponents.

A.1 The symmetric cocycle

Let $A\colon \mathbb{T} \longrightarrow SL(2,\mathbb{R})$ be a matrix-valued map, and ω an irrational number. Consider the vector spaces $M(2,\mathbb{R})$, the space fo 2×2 matrices, and $M_s(2,\mathbb{R})$ the space of symmetric 2×2 matrices. Consider the 4D cocycle defined as

$$(\otimes A,\omega)\colon \begin{array}{ccc} M(2,\mathbb{R})\times\mathbb{T} & \to & M(2,\mathbb{R})\times\mathbb{T} \\ (G,\theta) & \to & (\bar{G},\theta+\omega) := (A(\theta)GA(\theta)^T,\theta+\omega) \end{array}. \tag{A.1}$$

Remark A.1.1. The notation $\otimes A$ comes from the fact that if we vectorize the matrix G, then the transfer matrix of the cocycle $(\otimes A,\omega)$ is the Kronecker product of the matrix-valued map A by itself [Hal74].

The cocycle $(\otimes A, \omega)$ has a first integral: the determinant. This is because the transfer matrix $A(\theta)$ has determinant equal 1. Also, $(\otimes A, \omega)$ leaves invariant the 1D subspace of skew-symmetric matrices $M_{sk}(2, \mathbb{R})$, which are of the form

$$\begin{pmatrix} 0 & d \\ -d & 0 \end{pmatrix}, \, d \in \mathbb{R}.$$

It is satisfied that $M(2, \mathbb{R})$ decomposes in the two invariant subspaces $M_s(2, \mathbb{R}) \oplus M_{sk}(2, \mathbb{R})$. Note that $M_s(2, \mathbb{R}) \cong \mathbb{R}^3$.

The following lemma relates the singular values of the iterations of the cocycles (A, ω) and $(\otimes A, \omega)$.

Lemma A.1.2. *If $a_n = \sigma_1(A(n, \omega))$ and $b_n = \sigma_2(A(n, \omega))$ are the singular values of the n-th iteration of the cocycle (A, ω), then the four singular values of the n-th iteration of $(\otimes A, \omega)$ are $a_n^2 \geq 1 = 1 \geq b_n^2$.*

Proof. This comes from the fact that, if we vectorize G, $vec(G)$, we have that the transfer matrix of the linear cocycle $(\otimes A, \omega)$ is the Kronecker's product $A(\theta) \otimes A(\theta)$. Then, using Oseledet's theorem, see chapter §1, and the basic properties of the Kronecker's product, the desired singular values are all products of two elements of the singular values of the matrix $A(n, \theta)$. □

With the help of Oseledet's theorem, see theorem 1.2.6 in chapter §1, and lemma A.1.2, we can connect the Lyapunov spectrum of the 2D cocycle (A, ω) with the Lyapunov spectrum of $(\otimes A, \omega)$.

Corollary A.1.3. *If Λ_1, Λ_2 are the Lyapunov exponents of the cocycle (A, ω), then $2\Lambda_1$, 0 and $2\Lambda_2$ are the Lyapunov exponents of the cocycle $(\otimes A, \omega)$.*

Now we can define the symmetric cocycle.

Definition A.1.4. The *symmetric cocycle* is the linear cocycle defined as $(\otimes A, \omega)$ restricted to the vector bundle $M_s(2, \mathbb{R}) \times \mathbb{T}$.

From now on, we will denote by $(\otimes A, \omega)$ the symmetric cocycle.

Remark A.1.5. By corollary A.1.3, the symmetric cocycle has Lyapunov exponents $2\Lambda_1$, 0 and $2\Lambda_2$, with $\Lambda_1 \geq 0$ and $\Lambda_2 \leq 0$.

A consequence of lemma A.1.2 and the general theory of Kronecker's products of cocycles described in [HdlL05] is the following result.

Corollary A.1.6. *(A, ω) is uniformly hyperbolic if and only if $(\otimes A, \omega)$ has an exponential trichotomy (also called uniform partial hyperbolic splitting): it has three invariant 1D sub-bundles, one with positive Lyapunov exponent, one with negative Lyapunov exponent, and one with zero Lyapunov exponent.*

A tool to undersand the dynamics of the symmetric cocycle is its associated *projective* cocycle. It is defined as the skew product

$$\begin{array}{rccc} \mathbb{P}(\otimes A,\omega)\colon & \mathbb{S}^2\times\mathbb{T} & \to & \mathbb{S}^2\times\mathbb{T} \\ & (G,\theta) & \to & \left(\dfrac{A(\theta)GA(\theta)^T}{||A(\theta)GA(\theta)^T||},\theta+\omega\right). \end{array} \tag{A.2}$$

Since the determinant of a matrix G is preserved under the action of $(\otimes A,\omega)$, we have that the sign (of the determinant) of the points on $\mathbb{S}^2$ is preserved under A.2, so there are three invariant sets on $\mathbb{S}^2$, see figure A.1:

- *Positive sign:* This set is diffeomorphic to a disjoint union of two open disks.
- *Negative sign:* This set is diffeomorphic to an open cylinder.
- *Zero sign:* this set is diffeomorphic to a disjoint union of two circles. These two circles come from the intersection of the cone, formed by the matrices with determinant zero, and the 2 sphere.

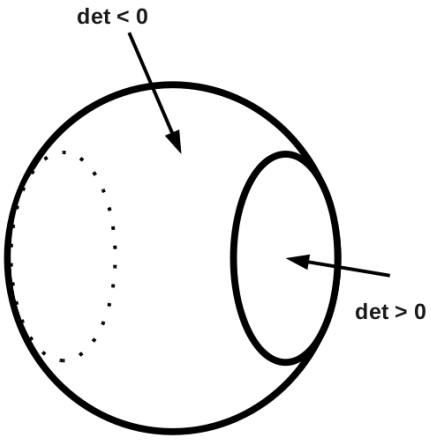

Figure A.1: Schematic representation of the invariant sets on $\mathbb{S}^2$ under the projective symmetric cocycle.

From the previous geometrical decomposition of the phase space in terms of the sign of the determinant, it can be proved that:

Lemma A.1.7. *Let $G\colon\mathbb{T}\longrightarrow\mathbb{R}^3$ be an invariant $1D$ bundle of $(\otimes A,\omega)$ with determinant different of 0 at some point θ_0, and let ω be irrational. Then there exists two $2D$ invariant bundles that, for each θ, contain $G(\theta)$ and are tangent to the cone of the determinant equal to 0. Moreover, if the determinant of G is negative, the two $2D$ invariant bundles are real, and if the determinant of G is positive, they are complex.*

Proof. First of all, let's introduce coordinates (a, b, c) in $M_s(2, \mathbb{R})$, which correspond to the matrix form

$$\begin{pmatrix} a & b \\ b & c \end{pmatrix}.$$

Note that the cone of determinant equals zero corresponds to the equation $ac - b^2 = 0$. Also, a plane tangent to the cone has equation $Aa + Bb + Cc = 0$, where the coefficients A, B and C satisfy that there exists a point (a_0, b_0, c_0) in the cone of determinant zero, i.e. $a_0c_0 - b_0^2 = 0$, such that $A = c_0$, $B = -2b_0$ and $C = a_0$.

Finally, if $G(\theta) = (g_1(\theta), g_2(\theta), g_3(\theta))$, then the two 2D invariant bundles that pass through $G(\theta)$ and are tangent to the cone of determinant zero have coefficients $A(\theta), B(\theta)$ and $C(\theta)$ of the form $A(\theta) = 1$, $B(\theta) = -2\sqrt{C(\theta)}$ and

$$C(\theta) = \left(\frac{g_2(\theta)}{g_1(\theta)} \pm \frac{\sqrt{g_2(\theta)^2 - g_1(\theta)g_3(\theta)}}{g_1(\theta)} \right)^2,$$

hence the 2D bundles are real if and only if the determinant of $G(\theta)$ is less than zero. □

From corollary A.1.6 we have that if (A, ω) is uniformly hyperbolic, then the cocycle $(\otimes A, \omega)$ is partially hyperbolic. One can ask what happens when (A, ω) is not uniformly hyperbolic. Since $(\otimes A, \omega)$ is not partially hyperbolic we have, by Oseledet's theorem, that the 1D contracting and expanding subbundles are not continuous but only measurable. Is the central subbundle, the one with associated zero Lyapunov exponent, continuous? The following theorem answers this question.

Theorem A.1.8. *Let ω be irrational and (A, ω) a 2D linear cocycle with positive Lyapunov exponent. Then the central subbundle of $(\otimes A, \omega)$ is continuous if and only if (A, ω) is uniformly hyperbolic.*

Proof. Let's prove that if (A, ω) is uniformly hyperbolic, then $(\otimes A, \omega)$ has a 1D continuous invariant subbundle with Lyapunov exponent equal 0:

Since (A, ω) is uniformly hyperbolic, there exist continuous matrix-valued maps $P\colon \mathbb{R}/(2\mathbb{Z}) \longrightarrow GL(2, \mathbb{R})$ and $\Lambda\colon \mathbb{R}/(2\mathbb{Z}) \longrightarrow GL(2, \mathbb{R})$, with

$$\Lambda(\theta) = \begin{pmatrix} \Lambda_1(\theta) & 0 \\ 0 & \Lambda_2(\theta) \end{pmatrix},$$

such that (A, ω) is conjugated to Λ through P, that is,

$$A(\theta)P(\theta) = P(\theta + \omega)\Lambda(\theta). \tag{A.3}$$

Note that, since $A(\theta)$ is in $SL(2, \mathbb{R})$,

$$\hat{\lambda}_i = \int_{\mathbb{T}} \log |\Lambda_i(\theta)| \, d\theta,$$

$i = 1, 2$, satisfy that $\hat{\lambda}_1 + \hat{\lambda}_2 = 0$.

Now, define $G(\theta) = P(\theta)RP(\theta)^T$, where

$$R = \begin{pmatrix} 0 & 1 \\ 1 & 0 \end{pmatrix}.$$

Using (A.3), it is easy to verify that

$$A(\theta)G(\theta)A(\theta)^T = \Lambda_1(\theta)\Lambda_2(\theta)G(\theta + \omega),$$

and, using $\hat{\lambda}_1 + \hat{\lambda}_2 = 0$, it is proved that $G(\theta)$ has Lyapunov exponent equal 0.

Let's prove now that if $(\otimes A, \omega)$ has a 1D continuous invariant subbundle, G, with zero Lyapunov exponent, then (A, ω) is uniformly hyperbolic:

Since ω is irrational and the determinant is preserved by $(\otimes A, \omega)$, the sign of the determinant remains constant along $G(\theta)$ with respect θ. There are three possible cases:

- *det* > 0: This case is not possible. If the determinant of $G(\theta)$ is positive, we have that the two 2D bundles that are tangent to the cone of determinant zero and pass through $G(\theta)$ are invariant and *complex*, see lemma A.1.7. Then, the two 1D *complex* subbundles that lie in the cone of determinant zero and belong to the 2D bundles, are invariant and conjugated one to the other. Hence, their Lyapunov exponents are equal. This implies that the maximal Lyapunov exponent of $(\otimes A, \omega)$ is zero, which implies that the Lyapunov exponent of (A, ω) is zero.

- *det* < 0: There are two (real) 2D invariant bundles that contain $G(\theta)$ and are tangent to the cone of determinant 0, see lemma A.1.7. The intersection of this two bundles with the cone creates another two (real) 1D invariant subbundles and, since G is continuous, they are continuous. Now, using the hypothesis that the Lyapunov exponent of (A, ω) is positive and corollary A.1.6, we have that (A, ω) is uniformly hyperbolic.

- *det* $= 0$: For every $G(\theta)$, the plane tangent to the cone of determinant 0 and that contains $G(\theta)$ generates a 2D invariant bundle. Because the Lyapunov exponent of (A, ω) is positive, this 2D invariant bundle contains another 1D invariant subbundle, which has non-zero Lyapunov exponent. Without loss of generality we will think that it has positive Lyapunov exponent. Since the dynamics constrained on this invariant 2D bundle is also a 2D cocycle and has one 1D continuous invariant subbundle an another that is measurable, then the measurable must be continuous also. Then, the other 1D invariant subbundle is constructed by the intersection of the other 2D invariant bundle that is tangent to the cone of determinant zero.

□

A.1.1 A numerical example of a symmetric cocycle without continuous 1D invariant bundles

Let (A_E, ω), with ω the golden mean, the linear cocycle with transfer matrix

$$A_E(\theta) = \begin{pmatrix} E - 3\cos(2\pi\theta) & -1 \\ 1 & 0 \end{pmatrix}.$$

(A_E, ω) is called the Harper map with parameter E, see chapter §4 for a more detailed description of this cocycle and its properties.

The Harper map satisfies that, for $E > E_c$, where $E_c \approx 3.386230716705$, is uniformly hyperbolic, while for $E = E_c$, it is not uniformly hyperbolic, but with positive Lyapunov exponent.

From the results of theorem A.1.8, the symmetric cocycle $(\otimes A_E, \omega)$ associated to the Harper map satisfies that for $E > E_c$, it has three 1D invariant subbundles, while for $E = E_c$ it has no 1D continuous invariant subbundles. Also, from the construction of theorem A.1.8, we observe that the central subbundle, for $E > E_c$, satisfies that it has negative determinant and it seems plausible that, as E approaches E_c, this determinant gets close to zero.

Remark A.1.9. We emphasize that the maximal Lyapunov exponent is just two times the Lyapunov exponent of the linear cocycle (A_E, ω) and, as a consequence of theorem A.1.8, the minimum distance between the 1D invariant subbundles is proportional to the determinant along the central subbundle.

Remark A.1.10. The symmetric cocycle $(\otimes A_E, \omega)$ has transfer matrix

$$\begin{pmatrix} (E - 3\cos(2\pi\theta))^2 & -2\,(E - 3\cos(2\pi\theta)) & 1 \\ (E - 3\cos(2\pi\theta)) & -1 & 0 \\ 1 & 0 & 0 \end{pmatrix}.$$

In order to see how the central subbundle of $(\otimes A_E, \omega)$ behaves as E approaches E_c, for a fixed E, we compute it using the projective cocycle (A.2). Also, we compute the minimum of the absolute value of the determinant along θ. Figure A.2 show the minimum of the absolute value of the determinant of the central bundle with respect E. As we observe in subfigure A.1.1, it seems that the minimum determinant goes to zero like a parabola, subfigure A.1.1 shows the square root of the minimum determinant with respect E. Observe that this subfigure is almost a straight line. In order to see that it is a straight line, we performed a fitting, using the `fit` function in `gnuplot`, and obtained that the square root of the minimum determinant is like

$$a \cdot (E - E_c),$$

where $a \approx 0.531769514695$.

Also, for several values of the parameter value E, near the critical value E_c, we compute the graphs of the determinant along the central bundle, see figure A.3. As we observe in

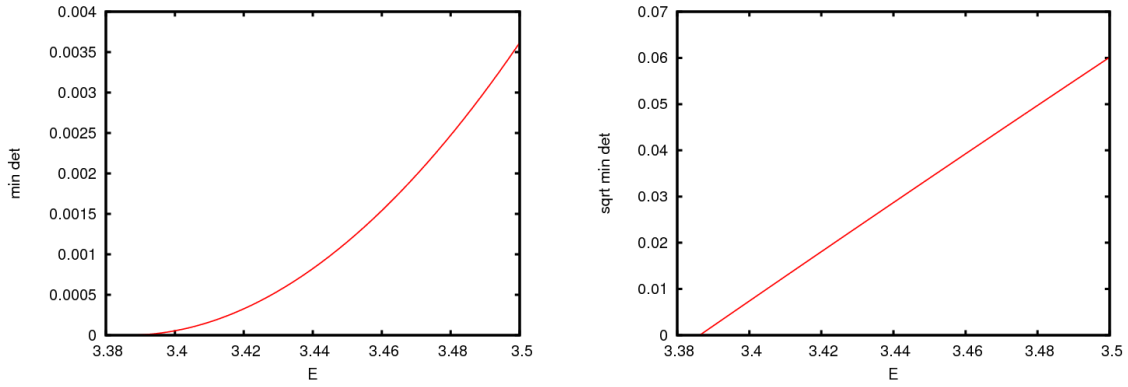

Figure A.2: Minimum of the absolute value of the determinant of the central subbundle with respect E (left) and the square root of it with respect E (right).

this figure, as E gets close to E_c, the determinant along the central subbundle approaches zero. This figure resembles the ones that are obtained when computing pinched SNA [Kel96, FKP06, Jäg07].

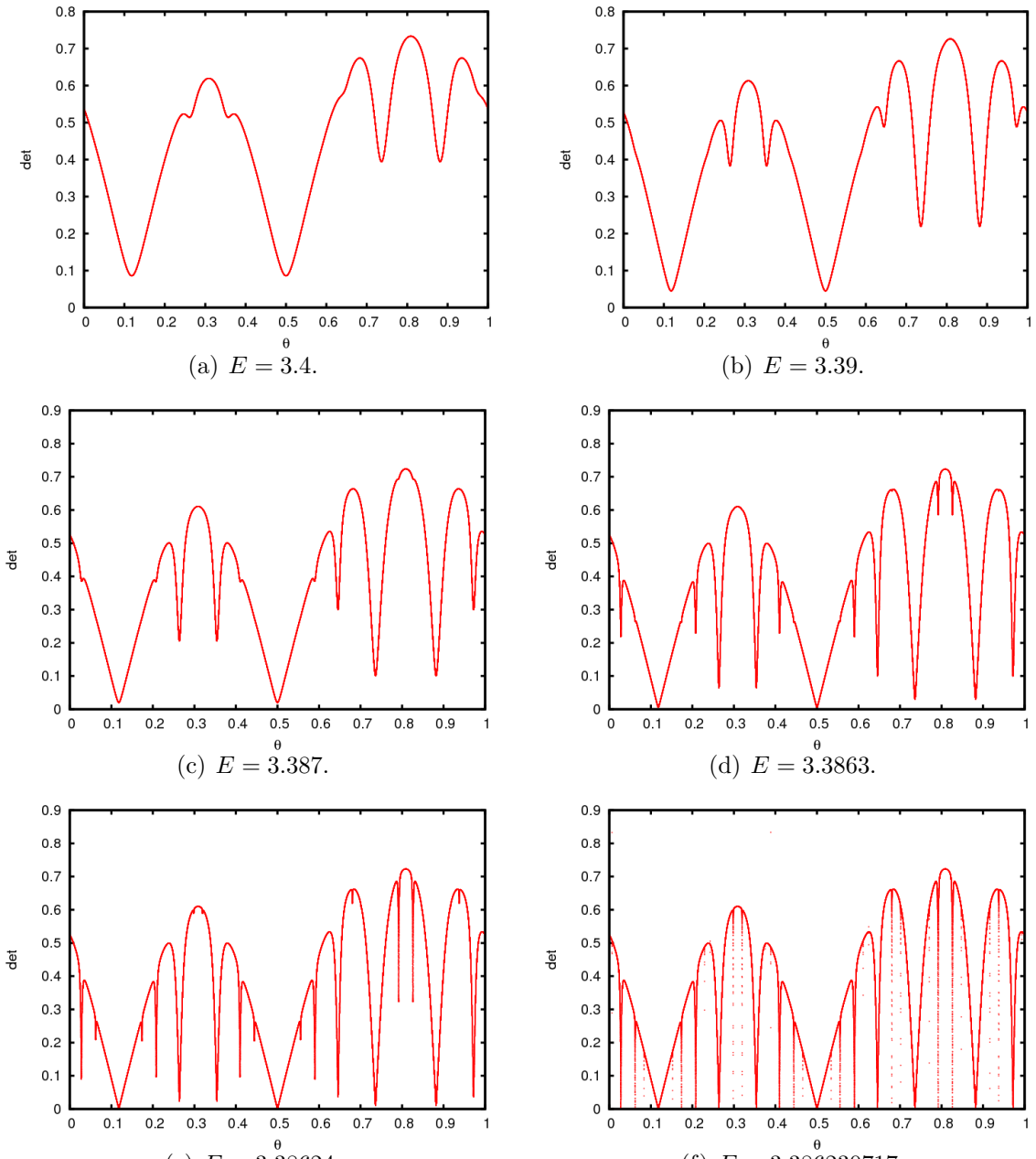

(a) $E = 3.4$. (b) $E = 3.39$.

(c) $E = 3.387$. (d) $E = 3.3863$.

(e) $E = 3.38624$. (f) $E = 3.386230717$.

Figure A.3: Absolute value of the determinant of the central subbundle with respect θ (x axis) for several values of E near E_c. On the y axis there is the $\frac{1}{4}$th power of the absolute value of the determinant.

A.2 Triangular linear cocycle

Let $(\hat{A}, \omega)$ be a 2D linear cocycle, with ω irrational, and let $b\colon \mathbb{T} \longrightarrow \mathbb{R}^2$ a continuous vector-valued map. The *triangular linear cocycle* is the 3D linear cocycle (A, ω) with transfer matrix

$$A(\theta) = \begin{pmatrix} \hat{A}(\theta) & b(\theta) \\ 0 & 1 \end{pmatrix}.$$

The triangular cocycle has the property that, for any vector-valued map b, its M spectrum is the union of the M spectrum of the cocycle (A, ω) with the unit circle. Also, the 2D bundle

$$E = \{((x, y, z), \theta) \,|z = 0\}$$

is invariant.

Proposition A.2.1. *If the M spectrum of $(\hat{A}, \omega)$ is an union of two circles that do not lie on the unit circle, then (A, ω) has a continuous invariant 1D bundle with associated zero Lyapunov exponent.*

Proof. If the M spectrum of $(\hat{A}, \omega)$ does not contain the unit circle, then the linear functional equation

$$\hat{A}(\theta)\hat{v}(\theta) + b(\theta) = \hat{v}(\theta + \omega)$$

has a continuous solution $\hat{v}\colon \mathbb{T} \longrightarrow \mathbb{R}^2$. Now, define the bundle $v(\theta) = (\hat{v}(\theta), 1)$. It is easy to see that this 1D bundle satisfies

$$A(\theta)v(\theta) = v(\theta + \omega).$$

□

Related to propostion A.2.1, we have the following result

Lemma A.2.2. *The 3D linear cocycle (A, ω) has a continuous 1D invariant bundle with zero Lyapunov exponent if and only if there exists a continuous $\hat{v}\colon \mathbb{T} \longrightarrow \mathbb{R}^2$ that solves the equation*

$$\hat{A}(\theta)\hat{v}(\theta) - \hat{v}(\theta + \omega) = -b(\theta).$$

Proof. Note that if $v\colon \mathbb{T} \longrightarrow \mathbb{R}^3$ is invariant under the linear cocycle (A, ω) and has zero Lyapunov exponent, then it satisfies

$$\begin{pmatrix} A(\theta) & b(\theta) \\ 0 & 1 \end{pmatrix} v(\theta) = \Lambda(\theta)v(\theta + \omega),$$

with

$$\int_{\mathbb{T}} \log|\Lambda(\theta)| d\theta = 0.$$

If we denote $v(\theta) = (\hat{v}(\theta), z(\theta))$, with $\hat{v}\colon \mathbb{T} \longrightarrow \mathbb{R}^2$ and $z\colon \mathbb{T} \longrightarrow \mathbb{R}$, then the zero Lyapunov exponent implies that the cohomology equation

$$z(\theta) = \Lambda(\theta) z(\theta + \omega)$$

has the only non-trivial solution $z(\theta) = 1$. Hence, $v(\theta)$ has the form $(\hat{v}(\theta), 1)$.

The other implication of the lemma is done in proposition A.2.1. □

Before stating the main theorem of this section, we want to remember a classical result in Functional analysis, see [Con00] for a general reference.

Theorem A.2.3. *Let $L\colon X \longrightarrow X$ be a bounded linear operator on a Banach space X. Then, z is in the Weyl spectrum of L, but not in the point spectrum, if and only if, there exists a residual set $B \in X$ such that the linear equation*

$$Lx - zx = b \tag{A.4}$$

has no solutions for $b \in B$. This is the same as saying that $L - zId$ is injective but $(L - zId)(X)$ is not closed in X.

Remark A.2.4. Remember that a residual set is the countable intersection of open dense sets, which is dense by Baire theorem.

Theorem A.2.5. *Let $(\hat{A}, \omega)$ be a non-uniformly hyperbolic 2D linear cocycle, i.e. its M spectrum is an annulus containing the unit circle. Then, there exists a residual set of $b\colon \mathbb{T} \longrightarrow \mathbb{R}^2$ in the Banach space of continuous vector-valued maps $\mathcal{C}^0(\mathbb{T}, \mathbb{R}^2)$, such that the triangular linear cocycle associated to $(\hat{A}, \omega)$ and b has no continuous 1D invariant subbundle with zero Lyapunov exponent.*

Proof. Given a vector-valued map $b\colon \mathbb{T} \longrightarrow \mathbb{R}^2$, we will denote by (A_b, ω) the triangular linear cocycle associated to $(\hat{A}, \omega)$ and b.

By lemma A.2.2, (A_b, ω) has a continuous 1D invariant subbundle if an only if the functional equation

$$\hat{A}(\theta - \omega) x(\theta - \omega) - x(\theta) = -b(\theta - \omega). \tag{A.5}$$

has a continuous solution $x\colon \mathbb{T} \longrightarrow \mathbb{R}^2$.

Equation A.5 is equation (A.4) for the transfer operator, $\hat{\mathcal{A}}$, associated to the linear cocycle $(\hat{A}, \omega)$, that is, $(\hat{\mathcal{A}} - Id)x = b$. Using the fact that the spectrum of a transfer operator, M spectrum, is equal to the Weyl spectrum, see chapter §1, that $(\hat{A}, \omega)$ is not uniformly hyperbolic, and using theorem A.2.3, we conclude that (A_b, ω) has no continuous 1D invariant subbundles with zero Lyapunov exponent for a residual set of b's. □

Open questions

In the course of our work we have solved some problems, but many questions have been raised. Here we present several of these questions and possible future lines of work.

- Study in detail the gradient flow and its fixed points that arise when studying FHIT in area preserving skew product systems. See chapter §2 for a detailed description of this flow.
- Study the renormalization properties of the breakdowns exposed in chapters §2 and §3.
- Does the folding breakdown, see chapter §2, appear in higher dimensional skew products with irrational rotation?
- What is the invariant object that remains after the fractalization route in volume preserving skew products like the one exposed in chapter §3?
- The gradient flow for the volume preserving skew product described in §3 does not work, but it is still possible to define a flow in $\ell^2(\mathbb{Z})$ which has as fixed points FHIT. Study the properties of this flow.
- Develop the theory to perform computer-assisted proofs of invariant tori, as explained in chapter §4, using not only the Banach space $\mathcal{C}^0$, but also other Banach spaces like $\mathcal{C}^r$, with $r > 0$, Sobolev spaces, analytic spaces...
- Develop the theory for the rigorous computer validation of FHIT in skew product systems where the dynamics on the base space $\mathbb{T}^d$ is not a rigid rotation but a more general diffeomorphism.
- Develop the theory for the rigorous computer validation of Normally Hyperbolic Invariant Tori in dynamical systems which are not skew product systems.
- Apply the Fourier models machinery for other problems. For example, for the validation of periodic orbits of dissipative PDEs. (This part is work in progress with professor Rafael de la Llave).
- Explain the pinched structure of the determinant of the central subbundle of the symmetric cocycle described in appendix §A.

Resum

El comportament a llarg termini d'un sistema dinàmic està organitzat pels seus objectes invariants. Per tant, és important entendre com aquests objectes invariants persisteixen sota pertorbacions del sistema, donar resultats de la seva existència, regularitat i dependència respecte paràmetres, i classificar les seves bifurcacions i mecanismes de trencament. En aquesta tesi, treballarem aquestes qüestions per a una classe particular de sistemes dinàmics i objectes invariants. Els sistemes que considerarem són els que estan forçats quasiperiòdicament, és a dir, acoplats a una rotació irracional, i els objectes invariants són tors invariants amb dinàmica irracional. Aquests tors surgeixen com a resposta del forçment quasiperiòdic i es representen geomètricament com a grafs dels angles de la rotació [Sta97]. Es sabut que la persistència (en un conjunt obert de paràmetres) de varietats invariants està fortament lligada al concepte d'hiperbolicitat normal [Fen72, HPS77, Mañ78, Sac65]. En aquesta tesi considerarem el concepte anàleg per als sistemes forçats quasiperiòdicament. Per tant, els tors invariants que tractarem són fibrats hiperbòlics (FHIT). Sense entrar en massa detall, un tor continu invariant està fibrat hiperbòlicament si hi ha una dicotomia en la linealització de la dinàmica al seu voltant: el fibrat normal es descomposa en fibrats estables i inestables a on la dinàmica es uniformement contractiva i repulsiva, respectivament. Cal notar que la dinàmica sobre el fibrat tangent està dominada per la dinàmica en el fibrat normal, ja que els exponents de Lyapunov són zero. Aquest fet implica que els tors fibrats hiperbòlics persisteixen (en un conjunt obert de paràmetres) i tenen el mateix grau de diferenciabilitat que el sistema [HdlL06c].

En particular, en aquesta tesi considerem exemples en els quals els tors bifurquen suaument i exemples a on els tors es trenquen. Un dels objectius principals és definir bons observables per a l'estudi dels diferents tipus de bifurcacions. Els fenoments de trencament de tors han sigut estudiats amb molta profunditat en la literatura, en el context d'Atractors Extranys no Caòtics (SNA), desde el seu descobriment [Her83, GOPY84]. En aquests articles un tor atractor suau bifurca en un objecte atractor amb geometria molt complicada (no és ni continu) però s'observa que la seva dinàmica interna és no caòtica, de fet, és quasiperiòdica. Aquest comportament d'objectes invariants ha sigut clau per a la física teòrica. Es considera que aquest és el preludi per a comportaments caòtics en els sistemes, i per tant hi ha hagut molts estudis tant numèrics com experimentals per a estudiar els mecanismes de formació dels SNA (vegeu [FKP06, PNR01] i les referències que allà s'esmenten). També hi ha hagut esforços teòrics per a explicar rigorosament com funcionen aquests mecanismes (vegeu per

exemple [BO96, Bje09, HP06, Jäg09, Kel96, Sta99, SS00]). Ara però, l'atenció que s'ha prestat als mecanismes de trencament de tors tipus sella, al contrari que els tors atractors, és força minsa. Aquests tors, amb les seves varietats invariants associades, són molt més difícils de calcular numèricament. En aquesta tesi hem estudiat, doncs, què passa després dels trencament, posant especial èmfasi en la natura geomètrica i dinàmica dels objectes que queden després del trencament.

També considerem en aquesta tesi la qüestió d'existència dels FHIT, fins i tots en casos on els tors són a prop de trencament. Aquí presentem un nova metodologia per a donar proves rigoroses, via Computer-Assisted Proofs (CAPs), de l'existència i unicitat (loca) de FHIT en sistemes forçats qüasiperiòdicament. Un punt clau per a fer CAPs és formular el problema d'invariància d'aquests objectes en termes funcionals [HdlL06c]. Aplicacions de CAPs usant eines funcionals en el camp dels sistemes dinàmics té una llarga història. Un dels precursors va ser la demostració de les conjectures de Feigenbaum en aplicacions unimodals [Lan82, Lan87], però també hi ha, per exemple, la demostració d'universalitat de les cascades de doblaments de periode en aplicacions que conserven àrea [EKW84], la prova de l'existència de l'atractor extrany de Lorenz [Tuc02], i, més recentment, l'existència de tors invariant crítics en sistemes Hamiltonians [Koc08]. Vegeu també el capítol 7 en el llibre [dlL01] i l'article de divulgació [KSW96]. Un denominador comú en totes aquestes demostracions és que es proposa un marc funcional per a l'objecte que es vol demostrar la seva existència, es troba una aproximació numèrica d'aquest, i després es demostra la seva existència d'una solució propera a l'aproximació. Tot això es fa usant que l'objecte a demostrar es pot parametritzar com un zero d'una equació funcional en un espai de Banach i veient que es compleixen condicions d'existència (usant per exemple mètodes estil Newton). Nosaltres, per a validar els FHIT, un espai natural de Banach és l'espai de funcions contínues periòdiques amb la norma del suprem. Resultats teòrics en [HdlL06c] ens aseguren a posteriori que els objectes validats seran tant diferenciables com el sistema skew product a on viuen. Cal notar que hi ha una diferència força gran entre els mètodes exposats en la literatura i el que aquí desenvolupem. Els primers tenen l'aventatge de que treballen amb operadors compactes, mentres que nosaltres treballem amb operadors acotats no compactes.

Resumint, la tesi es pot descompondre amb dos objectius principals: l'estudi dels possibles trencaments de FHIT i la demostració rigorosa d'aquests usant tècniques CAPs.

Aquesta tesi ha sigut organitzada en diferents capítols.

1.- Marc teòric dels FHIT.

En aquest capítol es descriu el marc tèoric dels FHIT i dels skew products quasiperiòdics. Aquests últims són aplicacions no lineals de la forma

$$\begin{array}{rccc} (F,\omega)\colon & \mathbb{R}^n \times \mathbb{T} & \longrightarrow & \mathbb{R}^n \times \mathbb{T} \\ & (z,\theta) & \longrightarrow & (F(z,\theta), \theta+\omega) \end{array}$$

a on ω és un nombre irracional. Un tor invariant és un graf d'una funció cont'inua $K\colon \mathbb{T} \longrightarrow$

$\mathbb{R}^n$ que satisfà l'equació d' invariancia

$$F(K(\theta),\theta) = K(\theta+\omega).$$

Direm que un tor invariant és FHIT si la seva dinàmica normal infinitessimal al voltant seu és uniformement hiperbòlica. És a dir, que el seu cocicle associat

$$\begin{array}{rccc}(D_zF,\omega)\colon & \mathbb{R}^n\times\mathbb{T} & \longrightarrow & \mathbb{R}^n\times\mathbb{T}\\ & (v,\theta) & \longrightarrow & (D_zF(K(\theta),\theta)v,\theta+\omega)\end{array}$$

deixa invariant una suma de Whitney de fibrats $E^u \oplus E^s$ tal que la seva dinàmica és exponencialment contractiva en E^s i exponencialment expansiva en E^u.

Es descriu breument la dinàmica lineal de cocicles. Aquesta descripció és necessària per entendre la dinàmica al voltant dels tors invariants.

També s'estudia les relacions dinàmiques i funcionals dels tors invariants, com per exemple l'espectre associat a un tor invariant.

Finalment s'introdueix el concepte d'operador de Schrödinger discret. Aquest serà de gran ajuda per a entendre les bifurcacions de tors hiperbòlics en sistemes que preserven àrea forçats qüasiperiòdicament.

2.- Trencament de FHIT en sistemes que preserven àrea forçats qüasiperiòdicament
En aquest capítol es descriuen i es comparen els diferents tipus de trencament de tors FHIT en sistemes que preserven àrea forçats qüasiperiòdicament. Aquests mecanismes són la bifurcació suau, el trencament no suau i el trencament per plegaments. Aquests trencaments han sigut estudiats numèricament usant el mètode de còmput dels tors invariants aproximant aquests per òrbites periòdiques. Per a cadascun dels trencaments hem estudiat el comportament de l'exponent de Lyapunov, la distància entre els fibrats invariants, etc.

La bifurcació suau, o bifurcació sella-el.líptic, és la transició d'un FHIT a un tor el.líptic, el qual té tors al voltant amb dimensió més alta. Tant l'exponent de Lyapunov com la distància mínima entre els fibrats va a zero quan la bifurcació es produeix. Aquesta bifurcació és ben entesa usant tècniques KAM, vegeu [BHS96].

El trencament no suau satisfà que la distància mínima entre els fibrats va a zero, però tant l'exponent de Lyapunov com la distància màxima entre els fibrats romanen positius quan la bifurcació té lloc. Això, aparentment, és contraintuitiu. També s'observa que el pendent del tor roman acotat quan es produeix la bifurcació, mentres que la seva derivada segona es dispara i va a infinit. Després de la bifurcació detectem que hi ha un objecte invariant que persisteix, però aquest no és un tor continu.

El trencament per plegaments comparteix algunes similituds amb el trencament no suau, com per exemple el comportament de la distància mínima entre els fibrats, l'exponent de Lyapunov i la distància màxima entre els fibrats. Ara però, s'observa que la derivada primera del tor es dispara prop del trencament i va cap a infinit. Després del trencament s'observa que, per a cada òrbita periòdica computada que aproximi el tor, aquesta no descriu el graf d'una funció, però és sobre una corba contínua. Això és degut a que la corba, foliada

d'òrbites periòdiques, té plegaments. S'observa també que si es canvia el nombre racional de la corba, les corbes amb plegaments són similars. Això ens fa conjecturar que quan la rotació és irracional, hi ha un objecte hiperbòlic, que no pot ser una corba mesurable, que roman invariant sota el skew product.

3.- Ruta de fractalització de FHT en sistemes skew product que preserven volum.
En aquest capítol presentem una nova ruta de fractalització de FHIT en sistemes skew product que preserven volum. Aquest tipus de trencament ha sigut observat en sistemes dissipatius, vegeu per exemple [Kan84, HdlL06a, JT08] però mai en sistemes conservatius. Aquí presentem un exemple en un skew product 3D que preserva volum. Veiem que el fenòmen de fractalització també esdevé. Amb l'ajuda d'aquest tipus de trencament en sistemes conservatius podem donar un un marc teòric unificat que engloba tant el cas conservatiu com el dissipatiu.

5.- Validació de FHIT via CAPs.
En aquest capítol presentem una nova metodologia per a fer CAPs de FHIT usant el marc funcional d'invariància d'aquests objectes. Aquesta metodologia representa un pas endavant dels resultats, tant teòrics com numèrics, presentats en els articles [HdlL06c, HdlL06b, HdlL07]. La metodologia podria ser descrita de la següent forma: Donada una aproximació del FHIT que es vol validar, aquest és modelat com una aplicació de l'espai de Banach de les funcions periòdiques usant tècniques intervalars, vegeu [Moo79, KM84] com a referència en anàlis intervalar. Després, s'usa aquest model per a validar l'existència d'una solució propera usant el teorema de Newton-Kantorovich adaptat al problema que estem treballant.

Aquesta metodologia és aplicada en diversos exemples: validació de cotes superiors de la mesura de l'espectre d'operadors de Schrödinger, validació de FHIT en sistemes no invertibles prop de trencament no suau i validació de FHIT en sistemes que preserven àrea.

6.- Eines numèriques.
En aquest capítol descrivim breument les eines numèriques més rellevants usades durant la tesi, com la computació de tors invariants en skew products, la computació dels seus fibrats invariants i alguns dels aspectes més tècnics relacionats en les CAPs del capítol 5.

La tesi acaba amb un apèndix i una llista de problemes oberts. En l'apèndix donem alguns exemples de cocicles 3D a on demostrem que no existeixen fibrats 1D continus, només mesurables. En la llista de problemes oberts donem possibles línies de recerca cara el futur.

Bibliography

[AB07] A. Avila and J. Bochi, *A uniform dichotomy for generic* $\mathrm{SL}(2,\mathbb{R})$ *cocycles over a minimal base*, Bull. Soc. Math. France **135** (2007), no. 3, 407–417.

[AJ09] A. Avila and S. Jitomirskaya, *The Ten Martini Problem*, Ann. of Math. (2) **170** (2009), no. 1, 303–342.

[AK91] R. A. Adomaitis and I. G. Kevrekidis, *Noninvertibility and the structure of basins of attraction in a model adaptive control system*, J. Nonlinear Sci. **1** (1991), no. 1, 95–105.

[AK06] A. Avila and R. Krikorian, *Reducibility or nonuniform hyperbolicity for quasiperiodic Schrödinger cocycles*, Ann. of Math. (2) **164** (2006), no. 3, 911–940.

[AKdlL07] R. A. Adomaitis, I. G. Kevrekidis, and R. de la Llave, *A computer-assisted study of global dynamic transitions for a noninvertible system*, Internat. J. Bifur. Chaos Appl. Sci. Engrg. **17** (2007), no. 4, 1305–1321.

[Ano69] D. V. Anosov, *Geodesic flows on closed Riemann manifolds with negative curvature.*, Proceedings of the Steklov Institute of Mathematics, No. 90 (1967). Translated from the Russian by S. Feder, American Mathematical Society, Providence, R.I., 1969.

[Arn98] L. Arnold, *Random dynamical systems*, Springer Monographs in Mathematics, Springer-Verlag, Berlin, 1998.

[Avi09] A. Avila, *Global theory of one-frequency Schrodinger operators I: stratified analyticity of the Lyapunov exponent and the boundary of nonuniform hyperbolicity*, Preprint, 2009.

[BF06] J. Bochi and B. Fayad, *Dichotomies between uniform hyperbolicity and zero Lyapunov exponents for* $\mathrm{SL}(2,\mathbb{R})$ *cocycles*, Bull. Braz. Math. Soc. (N.S.) **37** (2006), no. 3, 307–349.

[BHJ+03] H. W. Broer, H. Hanßmann, À. Jorba, J. Villanueva, and F. Wagener, *Normal-internal resonances in quasi-periodically forced oscillators: a conservative approach*, Nonlinearity **16** (2003), no. 5, 1751–1791.

[BHS96] H. W. Broer, G. B. Huitema, and M. B. Sevryuk, *Quasi-periodic motions in families of dynamical systems*, Lecture Notes in Mathematics, vol. 1645, Springer-Verlag, Berlin, 1996, Order amidst chaos.

[BHV07] H. W. Broer, A. Hagen, and G. Vegter, *Numerical continuation of normally hyperbolic invariant manifolds*, Nonlinearity **20** (2007), no. 6, 1499–1534.

[BJ02] J. Bourgain and S. Jitomirskaya, *Continuity of the Lyapunov exponent for quasiperiodic operators with analytic potential*, J. Statist. Phys. **108** (2002), no. 5-6, 1203–1218, Dedicated to David Ruelle and Yasha Sinai on the occasion of their 65th birthdays.

[BJ09] K. Bjerklöv and T. H. Jäger, *Rotation numbers for quasiperiodically forced circle maps-mode-locking vs. strict monotonicity*, J. Amer. Math. Soc. **22** (2009), no. 2, 353–362.

[Bje09] K. Bjerklöv, *SNA's in the quasi-periodic quadratic family*, Comm. Math. Phys. **286** (2009), no. 1, 137–161.

[BM98] M. Berz and K. Makino, *Verified integration of ODEs and flows using differential algebraic methods on high-order Taylor models*, Reliab. Comput. **4** (1998), no. 4, 361–369.

[BO96] Z. I. Bezhaeva and V. I. Oseledets, *On an example of a "strange nonchaotic attractor"*, Funktsional. Anal. i Prilozhen. **30** (1996), no. 4, 1–9, 95.

[Bou05] J. Bourgain, *Green's function estimates for lattice Schrödinger operators and applications*, Annals of Mathematics Studies, vol. 158, Princeton University Press, Princeton, NJ, 2005.

[BOV97] H. W. Broer, H. M. Osinga, and G. Vegter, *Algorithms for computing normally hyperbolic invariant manifolds*, Z. Angew. Math. Phys. **48** (1997), no. 3, 480–524.

[BS82] J. Béllissard and B. Simon, *Cantor spectrum for the almost Mathieu equation*, J. Funct. Anal. **48** (1982), no. 3, 408–419.

[Cap09] M. J. Capiński, *Covering relations and the existence of topologically normally hyperbolic invariant sets*, Discrete Contin. Dyn. Syst. **23** (2009), no. 3, 705–725.

[CJvdP07] B. Chapman, G. Jost, and R. van der Pas, *Using OpenMP: Portable Shared Memory Parallel Programming (Scientific and Engineering Computation)*, The MIT Press, October 2007.

[CL99] C. Chicone and Y. Latushkin, *Evolution semigroups in dynamical systems and differential equations*, Mathematical Surveys and Monographs, vol. 70, American Mathematical Society, Providence, RI, 1999.

[Con00] J. B. Conway, *A course in operator theory*, Graduate Studies in Mathematics, vol. 21, American Mathematical Society, Providence, RI, 2000.

[CS10] M. J. Capiński and C. Simó, *Computer Assisted Proof for Normally Hyperbolic Invariant Manifolds*, Preprint, 2010.

[Dam09] D. Damanik, *The spectrum of the Almost-Mathieu operator*, Preprint, 2009.

[dlL93] R. de la Llave, *Hyperbolic dynamical systems and generation of magnetic fields by perfectly conducting fluids*, Geophys. Astrophys. Fluid Dynam. **73** (1993), no. 1-4, 123–131, Magnetohydrodynamic stability and dynamos (Chicago, IL, 1992).

[dlL01] ———, *A tutorial on KAM theory*, Smooth ergodic theory and its applications (Seattle, WA, 1999), Proc. Sympos. Pure Math., vol. 69, Amer. Math. Soc., Providence, RI, 2001, pp. 175–292.

[dlLO99] R. de la Llave and R. Obaya, *Regularity of the composition operator in spaces of Hölder functions*, Discrete Contin. Dynam. Systems **5** (1999), no. 1, 157–184.

[DRP04] S. Datta, R. Ramaswamy, and A. Prasad, *Fractalization route to strange nonchaotic dynamics*, Phys. Rev. E **70** (2004), no. 4, 046203.

[EKW84] J.-P. Eckmann, H. Koch, and P. Wittwer, *A computer-assisted proof of universality for area-preserving maps*, Mem. Amer. Math. Soc. **47** (1984), no. 289, vi+122.

[Fen72] N. Fenichel, *Persistence and smoothness of invariant manifolds for flows*, Indiana Univ. Math. J. **21** (1971/1972), 193–226.

[FJ05] M. Frigo and S. G. Johnson, *The design and implementation of FFTW3*, Proceedings of the IEEE **93** (2005), no. 2, 216–231, Special issue on "Program Generation, Optimization, and Platform Adaptation".

[FKP06] U. Feudel, S. Kuznetsov, and A. Pikovsky, *Strange nonchaotic attractors*, World Scientific Series on Nonlinear Science. Series A: Monographs and Treatises, vol. 56, World Scientific Publishing Co. Pte. Ltd., Hackensack, NJ, 2006, Dynamics between order and chaos in quasiperiodically forced systems.

[GFPS00] P. Glendinning, U. Feudel, A. S. Pikovsky, and J. Stark, *The structure of mode-locked regions in quasi-periodically forced circle maps*, Phys. D **140** (2000), no. 3-4, 227–243.

[Gol01] C. Golé, *Symplectic twist maps*, Advanced Series in Nonlinear Dynamics, vol. 18, World Scientific Publishing Co. Inc., River Edge, NJ, 2001, Global variational techniques.

[GOPY84] C. Grebogi, E. Ott, S. Pelikan, and J. A. Yorke, *Strange attractors that are not chaotic*, Phys. D **13** (1984), no. 1-2, 261–268.

[Gre79] J. M. Greene, *A method for determining a stochastic transition*, J. Math. Phys. **20(6)** (1979), 1183–1201.

[GVL96] G. H. Golub and C. F. Van Loan, *Matrix computations*, third ed., Johns Hopkins Studies in the Mathematical Sciences, Johns Hopkins University Press, Baltimore, MD, 1996.

[Hal74] P. R. Halmos, *Finite-dimensional vector spaces*, second ed., Springer-Verlag, New York, 1974, Undergraduate Texts in Mathematics.

[Har98] A. Haro, *The Primitive Function of an exact symplectomorphism*, Ph.D. thesis, Universitat de Barcelona, Barcelona, Spain, July 1998.

[HdlL05] A. Haro and R. de la Llave, *Spectral theory and dynamical systems*, 2005.

[HdlL06a] ———, *Manifolds on the verge of a hyperbolicity breakdown*, Chaos **16** (2006), no. 1, 013120, 8.

[HdlL06b] ———, *A parameterization method for the computation of invariant tori and their whiskers in quasi-periodic maps: numerical algorithms*, Discrete Contin. Dyn. Syst. Ser. B **6** (2006), no. 6, 1261–1300 (electronic).

[HdlL06c] ———, *A parameterization method for the computation of invariant tori and their whiskers in quasi-periodic maps: rigorous results*, J. Differential Equations **228** (2006), no. 2, 530–579.

[HdlL07] ———, *A parameterization method for the computation of invariant tori and their whiskers in quasi-periodic maps: explorations and mechanisms for the breakdown of hyperbolicity*, SIAM J. Appl. Dyn. Syst. **6** (2007), no. 1, 142–207 (electronic).

[Her83] M.-R. Herman, *Une méthode pour minorer les exposants de Lyapounov et quelques exemples montrant le caractère local d'un théorème d'Arnol′d et de Moser sur le tore de dimension* 2, Comment. Math. Helv. **58** (1983), no. 3, 453–502.

[HH94] J. F. Heagy and S. M. Hammel, *The birth of strange nonchaotic attractors*, Phys. D **70** (1994), no. 1-2, 140–153.

[HK97] W. Hofschuster and W. Kraemer, *A Fast Public Domain Interval Library in ANSI C*, Proceedings of the 15th IMACS World Congress on Scientific Computation, Modelling and Applied Mathematics **2** (1997), 395–400.

[HP06] A. Haro and J. Puig, *Strange nonchaotic attractors in Harper maps*, Chaos **16** (2006), no. 3, 033127, 7.

[HPS77] M. W. Hirsch, C. C. Pugh, and M. Shub, *Invariant manifolds*, Lecture Notes in Mathematics, Vol. 583, Springer-Verlag, Berlin, 1977.

[HS05] A. Haro and C. Simó, *To be or not to be a SNA: That is the question*, Preprint, 2005.

[HW08] G. H. Hardy and E. M. Wright, *An introduction to the theory of numbers*, sixth ed., Oxford University Press, Oxford, 2008, Revised by D. R. Heath-Brown and J. H. Silverman, With a foreword by Andrew Wiles.

[Jäg07] T. H. Jäger, *On the structure of strange non-chaotic attractors in pinched skew products*, Ergodic Theory Dynam. Systems **27** (2007), no. 2, 493–510.

[Jäg09] ———, *Strange non-chaotic attractors in quasiperiodically forced circle maps*, Comm. Math. Phys. **289** (2009), no. 1, 253–289.

[JM82] R. A. Johnson and J. Moser, *The rotation number for almost periodic potentials*, Comm. Math. Phys. **84** (1982), no. 3, 403–438.

[Joh83] R. A. Johnson, *A review of recent work on almost periodic differential and difference operators*, Acta Appl. Math. **1** (1983), no. 3, 241–261.

[Joh87] ———, *The Oseledec and Sacker-Sell spectra for almost periodic linear systems: an example*, Proc. Amer. Math. Soc. **99** (1987), no. 2, 261–267.

[Jor01] A. Jorba, *Numerical computation of the normal behaviour of invariant curves of n-dimensional maps*, Nonlinearity **14** (2001), no. 5, 943–976.

[JS96] À. Jorba and C. Simó, *On quasi-periodic perturbations of elliptic equilibrium points*, SIAM J. Math. Anal. **27** (1996), no. 6, 1704–1737.

[JS06] T. H. Jäger and J. Stark, *Towards a classification for quasiperiodically forced circle homeomorphisms*, J. London Math. Soc. (2) **73** (2006), no. 3, 727–744.

[JT08] A. Jorba and J. C. Tatjer, *A mechanism for the fractalization of invariant curves in quasi-periodically forced 1-D maps*, Discrete Contin. Dyn. Syst. Ser. B **10** (2008), no. 2-3, 537–567.

[Kan84] K. Kaneko, *Fractalization of torus*, Progr. Theoret. Phys. **71** (1984), no. 5, 1112–1115.

[Kan86] ———, *Collapse of tori and genesis of chaos in dissipative systems*, World Scientific Publishing Co., Singapore, 1986.

[Kat95] T. Kato, *Perturbation theory for linear operators*, Classics in Mathematics, Springer-Verlag, Berlin, 1995, Reprint of the 1980 edition.

[Kel96] G. Keller, *A note on strange nonchaotic attractors*, Fund. Math. **151** (1996), no. 2, 139–148.

[KL04] S.-Y. Kim and W. Lim, *Universal mechanism for the intermittent route to strange nonchaotic attractors in quasiperiodically forced systems*, Journal of Physics A: Mathematical and General **37** (2004), no. 25, 6477.

[KM84] E. W. Kaucher and W. L. Miranker, *Self-validating numerics for function space problems*, Notes and Reports in Computer Science and Applied Mathematics, vol. 9, Academic Press Inc., Orlando, FL, 1984, Computation with guarantees for differential and integral equations.

[Koc08] H. Koch, *Existence of critical invariant tori*, Ergodic Theory Dynam. Systems **28** (2008), no. 6, 1879–1894.

[KS95] J. A. Ketoja and I. I. Satija, *Self-Similarity and Localization*, Phys. Rev. Lett. **75** (1995), no. 14, 2762–2765.

[KS97] ———, *Harper equation, the dissipative standard map and strange nonchaotic attractors: relationship between an eigenvalue problem and iterated maps*, Phys. D **109** (1997), no. 1-2, 70–80, Physics and dynamics between chaos, order, and noise (Berlin, 1996).

[KSW96] H. Koch, A. Schenkel, and P. Wittwer, *Computer-assisted proofs in analysis and programming in logic: a case study*, SIAM Rev. **38** (1996), no. 4, 565–604.

[Lan82] O. E. Lanford, III, *A computer-assisted proof of the Feigenbaum conjectures*, Bull. Amer. Math. Soc. (N.S.) **6** (1982), no. 3, 427–434.

[Lan87] ———, *Computer-assisted proofs in analysis*, Proceedings of the International Congress of Mathematicians, Vol. 1, 2 (Berkeley, Calif., 1986) (Providence, RI), Amer. Math. Soc., 1987, pp. 1385–1394.

[Las95] Y. Last, *Almost everything about the almost Mathieu operator. I*, XIth International Congress of Mathematical Physics (Paris, 1994), Int. Press, Cambridge, MA, 1995, pp. 366–372.

[LS90] Yu. D. Latushkin and A. M. Stëpin, *Weighted shift operators, the spectral theory of linear extensions and a multiplicative ergodic theorem*, Mat. Sb. **181** (1990), no. 6, 723–742.

[Mañ78] R. Mañé, *Persistent manifolds are normally hyperbolic*, Trans. Amer. Math. Soc. **246** (1978), 261–283.

[Mat68] J. N. Mather, *Characterization of Anosov diffeomorphisms*, Nederl. Akad. Wetensch. Proc. Ser. A 71 = Indag. Math. **30** (1968), 479–483.

[MMS89] R. S. MacKay, J. D. Meiss, and J. Stark, *Converse KAM theory for symplectic twist maps*, Nonlinearity **2** (1989), no. 4, 555–570.

[Moo66] R. E. Moore, *Interval analysis*, Prentice-Hall Inc., Englewood Cliffs, N.J., 1966.

[Moo79] ———, *Methods and applications of interval analysis*, SIAM Studies in Applied Mathematics, vol. 2, Society for Industrial and Applied Mathematics (SIAM), Philadelphia, Pa., 1979.

[MOW00] B. D. Mestel, A. H. Osbaldestin, and B. Winn, *Golden mean renormalization for the Harper equation: the strong coupling fixed point*, J. Math. Phys. **41** (2000), no. 12, 8304–8330.

[NK96] T. Nishikawa and K. Kaneko, *Fractalization of a torus as a strange nonchaotic attractor*, Phys. Rev. E **54** (1996), no. 6, 6114–6124.

[OWGF01] H. M. Osinga, J. Wiersig, P. Glendinning, and U. Feudel, *Multistability and nonsmooth bifurcations in the quasiperiodically forced circle map*, Internat. J. Bifur. Chaos Appl. Sci. Engrg. **11** (2001), no. 12, 3085–3105.

[PNR01] A. Prasad, S. S. Negi, and R. Ramaswamy, *Strange nonchaotic attractors*, Internat. J. Bifur. Chaos Appl. Sci. Engrg. **11** (2001), no. 2, 291–309.

[PS10] J. Puig and C. Simó, *Resonance tongues in the quasi-periodic hill-schrdinger equation with three frequencies*, Regular and Chaotic Dynamics (2010), 1–18.

[PS11] ———, *Resonance tongues and spectral gaps in quasi-periodic schrdinger operators with one or more frequencies. a numerical exploration*, Journal of Dynamics and Differential Equations (2011), 1–21.

[Pui04a] J. Puig, *Cantor spectrum for the almost Mathieu operator*, Comm. Math. Phys. **244** (2004), no. 2, 297–309.

[Pui04b] ———, *Reductibility of Quasi-Periodic Skew-Products and the Spectrum of Schrödinger Operators*, Ph.D. thesis, Universitat de Barcelona, Barcelona, Spain, April 2004.

[RMB05] N. Revol, K. Makino, and M. Berz, *Taylor models and floating-point arithmetic: proof that arithmetic operations are validated in cosy*, Journal of Logic and Algebraic Programming **64** (2005), no. 1, 135 – 154.

[Sac65] R. J. Sacker, *A new approach to the perturbation theory of invariant surfaces*, Comm. Pure Appl. Math. **18** (1965), 717–732.

[SFKP96] O. Sosnovtseva, U. Feudel, J. Kurths, and A. Pikovsky, *Multiband strange nonchaotic attractors in quasiperiodically forced systems*, Physics Letters A **218** (1996), no. 3-6, 255 – 267.

[Sim90] C. Simó, *On the Analytical and Numerical Approximation of Invariant Manifolds*, Modern Methods in Celestial Mechanics, Comptes Rendus de la 13ieme Ecole Printemps d'Astrophysique de Goutelas (France), 24-29 Avril, 1989. Edited by Daniel Benest and Claude Froeschle. Gif-sur-Yvette: Editions Frontieres, 1990., p.285 (1990).

[SS74] R. J. Sacker and G. R. Sell, *Existence of dichotomies and invariant splittings for linear differential systems. I*, J. Differential Equations **15** (1974), 429–458.

[SS00] R. Sturman and J. Stark, *Semi-uniform ergodic theorems and applications to forced systems*, Nonlinearity **13** (2000), no. 1, 113–143.

[Sta97] J. Stark, *Invariant graphs for forced systems*, Phys. D **109** (1997), no. 1-2, 163–179, Physics and dynamics between chaos, order, and noise (Berlin, 1996).

[Sta99] ———, *Regularity of invariant graphs for forced systems*, Ergodic Theory Dynam. Systems **19** (1999), no. 1, 155–199.

[Tuc02] W. Tucker, *A rigorous ODE solver and Smale's 14th problem*, Found. Comput. Math. **2** (2002), no. 1, 53–117.

[Tuc11] ———, *Validated Numerics: A Short Introduction to Rigorous Computations*, Princeton University Press, Princeton, NJ, To appear in 2011.

[WZ07] D. Wilczak and P. Zgliczyński, *C^r-Lohner algorithm*, `arXiv:0704.0720v1` (2007).

[ZG04] P. Zgliczyński and M. Gidea, *Covering relations for multidimensional dynamical systems*, J. Differential Equations **202** (2004), no. 1, 32–58.

[Zgl] P. Zgliczyński, *Computer assisted proofs in dynamics*, `http://www.ii.uj.edu.pl/~zgliczyn/cap07/cap07.htm`.